university of groningen

umcg

Medicine • Engineering

Magnetic Soft Robots toward Non-invasive Diagnosis and Therapy — Chen Wang

Magnetic Soft Robots
toward
Non-invasive Diagnosis and Therapy

Chen Wang

Invitation

You are cordially invited to attend the public defense of the PhD thesis entitled

MAGNETIC SOFT ROBOTS TOWARD NON-INVASIVE DIAGNOSIS AND THERAPY

By

Chen Wang

Monday
26 January 2026
14: 30 hrs

In the Aula of the Academy Building of the University of Groningen

Broerstraat 5, Groningen

Paranymphs:
Adriana Vasi
Yiling Zhang

MAGNETIC SOFT ROBOTS TOWARD NON-INVASIVE DIAGNOSIS AND THERAPY

Chen Wang

university of groningen

Magnetic soft robots toward non-invasive diagnosis and therapy

PhD thesis

to obtain the degree of PhD at the
University of Groningen
on the authority of the
Rector Magnificus Prof. J.M.A. Scherpen
and in accordance with
the decision by the College of Deans.

This thesis will be defended in public on

Monday 26 January 2026 at 14.30 hours

by

Chen Wang

born on 7 June 1994

Supervisors

Prof. S. Misra
Dr. V. K. Venkiteswaran

Assessment Committee

Prof. P. Breedveld
Prof. G.J.M. Tuijthof
Prof. A.G.P. Kottapalli

This work is part of the research project MAESTRO.

This work was supported by the European Research Council (ERC) under the European Union's Horizon 2020 Research and Innovation programme under grant 866494 project-MAESTRO, and financial support from the China Scholarship Council is acknowledged.

This dissertation has been approved by:

Prof. Dr. Sarthak Misra
Dr. Venkatasubramanian K. Venkiteswaran

Cover design: Chen Wang
Lay-out: Chuang Li
Printed by: Ipskamp

ISBN: 978-94-6536-034-8

Dedicated to my family

Samenvatting

Magnetische zachte robots zijn naar voren gekomen als veelbelovende platforms voor biomedische toepassingen, dankzij hun miniatuurformaat, mechanische flexibiliteit en draadloze aandrijfmogelijkheden. Hun vermogen om natuurlijke voortbeweging na te bootsen en zich te verplaatsen in krappe, dynamische en heterogene omgevingen maakt hen uitermate geschikt voor taken zoals gerichte medicijnafgifte, minimaal invasieve diagnostiek en interventies, en *in vivo* sensing. Recente studies hebben aangetoond dat deze systemen aanzienlijk potentieel bieden voor het realiseren van multimodale voortbeweging en het integreren van medische functionaliteiten. Niettemin vereist de klinische toepassing van deze systemen een meer diepgaande en systematische kennis van hun aanpassingsvermogen aan de omgeving, multifunctionaliteit en geïntegreerde sensorprestaties.

Dit proefschrift pakt deze uitdagingen aan door het ontwerp en de functionaliteit van magnetische zachte robots te verbeteren via een reeks toepassingsgerichte studies. **Hoofdstuk 2** richt zich op het schakelen van bewegingsmodi in complexe omgevingen onder eenvoudige magnetische aandrijving. Een op vin-golf geïnspireerde robot met amfibische voortbeweging wordt geïntroduceerd, die zowel droge oppervlakken als natte omgevingen kan doorkruisen met behulp van magnetisch aangedreven golvende poten. **Hoofdstuk 3** onderzoekt bio-geïnspireerde voortbeweging in combinatie met biologisch afbreekbare materialen voor medicijnafgifte. Een meersegmentige, afbreekbare robot wordt voorgesteld die door kronkelige lichaamsholten kan navigeren en medicatieladingen kan afgeven. **Hoofdstuk 4** behandelt de uitdaging van stabiele voortbeweging in biologische omgevingen. Hierin wordt een ringvormige robot met controleerbare oppervlaktehechting gepresenteerd, die manipulatie- en transporttaken uitvoert op met slijm beklede oppervlakken. Deze ontwikkelingen tonen aan hoe voortbewegingsstrategieën en materiaaleigenschappen synergetisch kunnen worden geïntegreerd om diverse biomedische toepassingen te ondersteunen.

Hoofdstukken 5 en **6** breiden de functionele reikwijdte van magnetische zachte robots verder uit. **Hoofdstuk 5** introduceert een dubbelresponsief systeem dat magnetische vormprogrammering combineert met temperatuur-geactiveerde activering. Dit maakt nauwkeurige controle mo-

gelijk over grijpen, loslaten en herconfiguratie — capaciteiten die bijzonder nuttig zijn voor medicijnafgifte. **Hoofdstuk 6** presenteert *SeroTab*, een gesensorde, inslikbare zachte robot voor *in vivo* pH-monitoring en het verzamelen van maagsappen. Met zijn op pinguïns geïnspireerde voortbeweging en hydrogel-gebaseerde sensortechnologie toont *SeroTab* succesvol realtime fysiologische monitoring en moleculaire diagnostiek aan in diermodellen. Deze studies onderstrepen het belang van het integreren van sensorische mogelijkheden in zachte robots om gesloten-luscontrole en autonome functie mogelijk te maken in complexe biologische omgevingen.

Tot slot vat **Hoofdstuk 7** de kernbevindingen van dit proefschrift samen, waarbij een toepassingsgedreven strategie wordt benadrukt voor het bevorderen van magnetische zachte robotica op het gebied van voortbeweging, functionaliteit en sensorisatie. Een belangrijke bijdrage is de succesvolle *in vivo* validatie van een volledig geïntegreerd zacht robotisch systeem, dat zijn potentieel aantoont voor fysiologische monitoring en therapeutische toepassingen binnen levende organismen. Deze prestatie markeert niet alleen een belangrijke stap richting klinische vertaling, maar vormt ook de basis voor de ontwikkeling van op ziekten gerichte zachte robots met klinisch relevante functionaliteiten. Door synthetische engineering te combineren met biologische inzichten, effent dit onderzoek de weg voor de volgende generatie van slimme, minimaal invasieve robotplatformen voor precieze diagnostiek en therapie.

Summary

Magnetic soft robots have emerged as promising platforms for biomedical applications owing to their miniature size, mechanical compliance, and wireless actuation capabilities. Their capacity to emulate natural locomotion and navigate through confined, dynamic, and heterogeneous environments positions them as ideal candidates for tasks such as targeted drug delivery, minimally invasive diagnostics and interventions, and *in vivo* sensing. Recent studies have demonstrated significant potential in achieving multimodal locomotion and integrating medical functionalities. Nevertheless, the clinical translation of these systems necessitates a more comprehensive understanding of their environmental adaptability, multifunctionality, and integrated sensing performance.

This dissertation addresses these challenges by advancing the design and functionality of magnetic soft robots through a series of application-oriented studies. **Chapter 2** focuses on motion mode switching in complex environments under simple magnetic actuation. A fin-wave-inspired robot with amphibious locomotion is introduced, capable of navigating both dry surfaces and wet environments using magnetically driven undulating legs. **Chapter 3** explores bioinspired locomotion combined with biodegradable materials for drug delivery. A multi-segmented, degradable robot is proposed, capable of navigating tortuous lumens and releasing drug payloads. **Chapter 4** addresses the challenge of stable locomotion in biological environments. It presents a ring-shaped robot with controllable surface adhesion, performing manipulation and transport tasks on mucus-lined surfaces. These developments illustrate how locomotion strategies and material functionalities can be synergistically integrated to enable diverse biomedical applications.

Chapters 5 and **6** expand the functional scope of magnetic soft robots. **Chapter 5** introduces a dual-responsive system combining magnetic shape programming with temperature-triggered actuation. This enables precise control over gripping, releasing, and reconfiguration—capabilities particularly useful for drug delivery. **Chapter 6** presents *SeroTab*, a sensorized, ingestible soft robot for *in vivo* pH monitoring and gastric fluid sampling. With its penguin-inspired locomotion and hydrogel-based sensing, *SeroTab*

successfully demonstrates real-time physiological monitoring and molecular diagnostics in animal models. These studies highlight the importance of integrating sensing capabilities into soft robots to enable closed-loop control and autonomous function in complex biological settings.

Finally, **Chapter 7** summarizes the core findings of this dissertation, emphasizing an application-driven strategy for advancing magnetic soft robotics in terms of locomotion, functionality, and sensorization. A key contribution is the successful *in vivo* validation of a fully integrated soft robotic system, demonstrating its potential for physiological sensing and therapeutic tasks within living organisms. This achievement not only marks a significant step toward clinical translation but also lays a foundation for the development of disease-targeted soft robots with clinically relevant functionalities. By bridging synthetic engineering with biological insight, this research paves the way for the next generation of smart, minimally invasive robotic platforms for precision diagnostics and therapy.

Contents

1

Introduction

1.1 Evolution of Magnetic Soft Robots

Biological systems, characterized by their inherent softness and adaptability, offer efficient strategies for interacting with complex environments, inspiring the development of a new class of machines: soft robots [1]. The term *soft* refers to the compliant materials used in constructing soft robotic bodies, which exhibit mechanical properties similar to those of biological tissues [2]. While Young's modulus is an idealized metric, it serves as a useful approximation of material stiffness: conventional robotic materials (e.g., metals, plastics) have moduli on the order of 10^9–10^{12} Pa, whereas soft non-linear elastic materials (e.g., skin, muscle) approximately range from 10^4–10^9 Pa [3]. Soft robots are thus defined as autonomous systems primarily composed of materials within this softer modulus range. Animals such as octopuses, squids, snakes, worms, and millipedes possess entirely soft bodies (Figure 1.1) [4], which enhance their adaptability and robustness, motivating the use of soft materials in robotics to enable capabilities like elongation, bending, twisting, squeezing, climbing, and growth [5].

In contrast to conventional rigid-bodied robots, which are primarily used in manufacturing and pose safety risks during human interaction, soft robots are constructed from intrinsically compliant materials (e.g., silicone rubbers) that deform upon impact and dissipate collision energy, thereby reducing the risk of injury and enabling safer, more adaptive physical interaction [2], [6]. Their compliant structures enable a greater number of degrees of freedom compared to hard-bodied counterparts, enhancing their

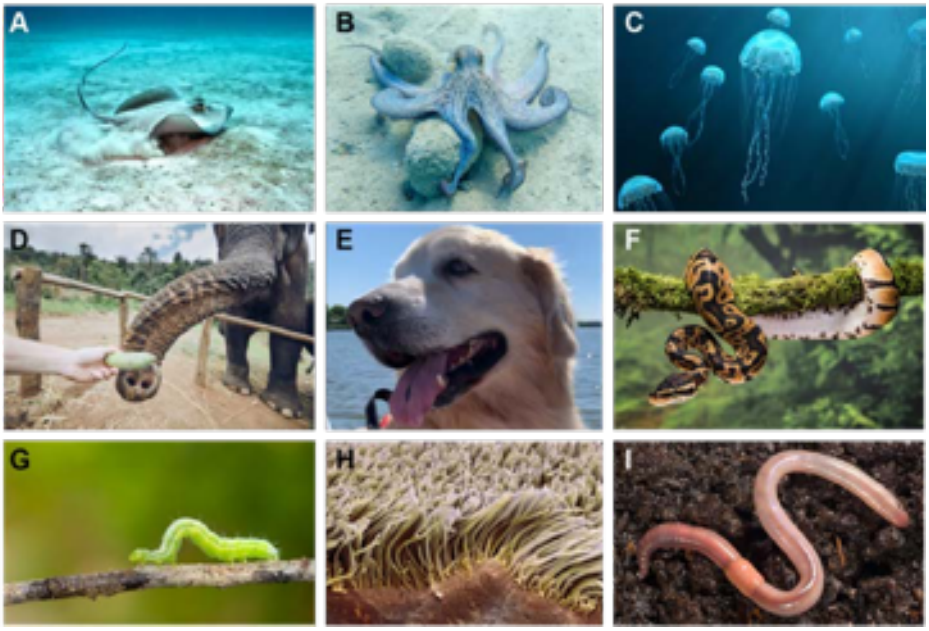

Figure 1.1: Examples of hydroskeletons and muscular hydrostats: (A) Fin-wave of stingray (©ThoughtCo.). (B) Octopus arms (©PADI). (C) Jellyfish swimming (©Getty Images). (D) Elephant trunk (©PanSci). (E) Mammalian tongue. (F) Snake (©Getty Images). (G) Inchworm (©2020 Carlos Pereira M/Shutterstock). (H) Cilia and flagella (©ThoughtCo.). (I) Earthworm (©Alamy).

adaptability and safety in complex environments (Figure 1.2) [3]. Notable examples of soft robots—including PneuNet grippers [7], octopus-inspired arms [8], GoQBot [9], quadrupedal soft robots [10], and the autonomous Octobot [11]—have demonstrated the potential of these systems to perform complex tasks such as adaptive grasping, morphological transformation, and autonomous locomotion. The use of such compliant materials enables safer interaction with humans, greater adaptability in object manipulation, and enhanced mobility across variable terrains. Soft robots thus hold great promise in a range of applications including medical devices, wearable assistive technologies, search-and-rescue missions, and autonomous exploration in unstructured environments [1]. To unlock their full potential, core robotic functions—such as sensing, actuation, computation, power storage, and communication—must be embedded within the soft material matrix,

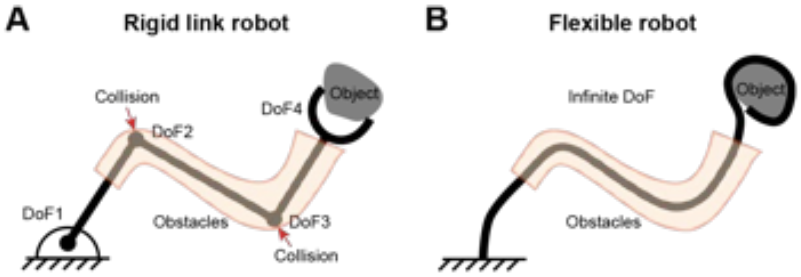

Figure 1.2: Comparison between (A) hard and (B) soft robots in terms of flexibility, manipulation capabilities, and load-bearing performance [3].

forming smart, multifunctional structures.

1.1.1 Magnetic Actuation: Enabling Wireless Manipulation

A critical first step in designing a soft robot is selecting an appropriate actuation method. Early demonstrations of soft robotic movement and functionality were primarily enabled by pneumatic, hydraulic, and electric actuators, which laid the foundation for the development of this field (Figure 1.3) [12]. However, despite increasing interest in biomedical and untethered applications, these conventional approaches present several critical limitations [13]. Fluid-driven systems such as pneumatic and hydraulic actuators, as well as tendon-driven mechanisms, typically require bulky external hardware and are heavily tethered [14], [15]. This significantly restricts their suitability for applications that demand compactness and autonomy, including implantable devices, targeted drug delivery, and minimally invasive surgical tools. Moreover, the inherent nonlinearity, large deformations, and mechanical complexity of soft structures, which often possess many passive degrees of freedom, pose substantial challenges for modeling and control [6], [16]. Traditional rigid-body control frameworks are often inadequate, emphasizing the need for new strategies tailored to compliant systems. In addition, conventional soft actuators are difficult to miniaturize, as their fabrication processes and reliance on pressurized systems are not conducive to operation at sub-millimeter scales [17], [18].

With continued advancements in materials and design, researchers have

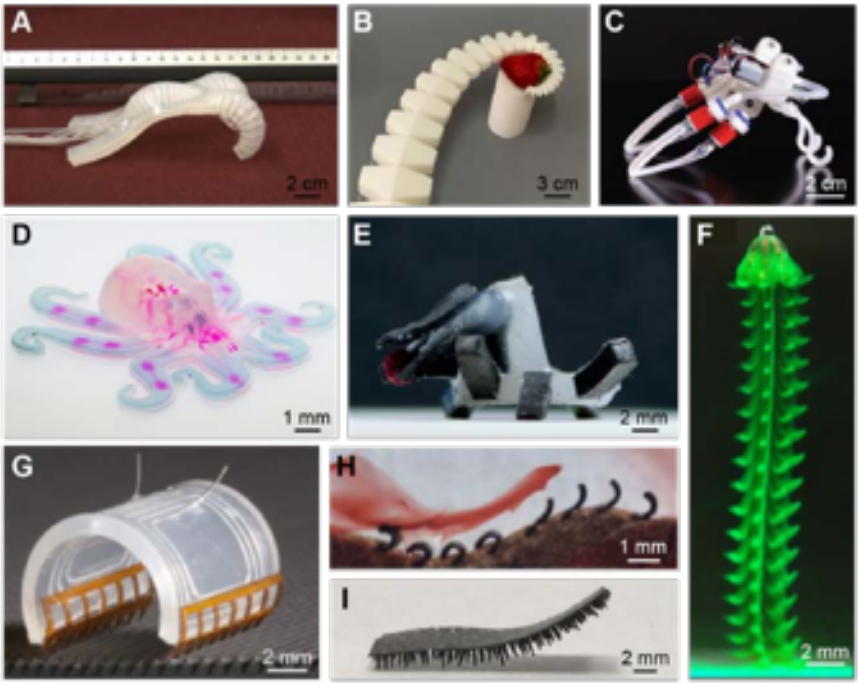

Figure 1.3: Soft robots inspired by a range of biological systems. (A) A multi-gait quadruped [19]. (B) Octopus arm-inspired soft gripper [20]. (C) A self-oscillating limb [21]. (D) Octopus-shaped robot with integrated fluidic system [11]. (E) A hexapod robot with six magnetic legs [22]. (F) Jellyfish-inspired swimming robot [23]. (G) Cheetah-inspired ultrafast electromagnetic soft robot [24]. (H) Magnetic cilia capable of pumping liquid [25]. (I) Millipede-inspired soft robot with magnetic actuation [26].

explored a broader range of actuation strategies, including magnetic actuation [27], chemically responsive systems [28], [29], and smart materials such as shape memory alloys (SMA) [30], dielectric elastomers (DE) [31], and photoresponsive polymers [32]. These emerging approaches have significantly expanded the functional versatility and application scope of soft robotic systems. Among them, magnetic soft materials have demonstrated notable progress in both design and fabrication, enabling the development of magnetically actuated soft robots with distinct advantages [33]. Magnetic actuation offers wireless, remote control by applying external mag-

netic fields, making it particularly well-suited for applications that require precise manipulation in constrained or delicate environments [34]. This capability is especially advantageous in miniaturized systems, where traditional actuation methods are impractical [35]. The ability to deliver both force and torque control without direct physical connections positions magnetic actuation as a highly promising technique for the next generation of medical and biomedical robots [36]. Magnetism has already established a strong presence in engineering and continues to prove effective in enabling compact, responsive, and controllable robotic systems [37].

1.1.2 Soft Matter: Enhancing Flexibility and Biocompatibility

Flexible and biocompatible materials used in the fabrication of magnetic soft robots can be broadly classified into two categories: elastomers and gels, each offering distinct mechanical characteristics and functional advantages tailored to specific application requirements [12]. Among elastomers, silicone-based thermosetting materials are the most widely employed host matrices for magnetic composites, owing to their ease of processing, tunable stiffness, and chemical stability. Commercially available products such as Sylgard 184 (Dow Chemical), the Ecoflex series (Smooth-On), and Elastosil formulations (Wacker Chemie) provide a diverse range of mechanical properties and are compatible with standard fabrication techniques. These addition-curing silicones can be uniformly mixed with magnetic particles using planetary centrifugal mixers prior to catalyst addition, and cured at either room temperature or elevated temperatures, offering considerable flexibility in composite preparation [38]. Examples such as sheet-shaped robot [27], millipede-inspired robots [39], and jellyfish-inspired swimmers [23] have demonstrated the ability to navigate diverse environments, including liquid and terrestrial terrains.

Gels, particularly cross-linked hydrogels and organogels, represent a softer and more compliant alternative due to their high liquid content and low polymer concentration [40]. Hydrogels based on naturally derived polysaccharides (e.g., alginate, carrageenan) or synthetic polymers (e.g., polyacrylamide, poly(N-isopropylacrylamide)) are frequently employed in biomedical applications, such as drug delivery, due to their biocompatibility and biodegradability [41]. Notably, thermoresponsive hydrogels such

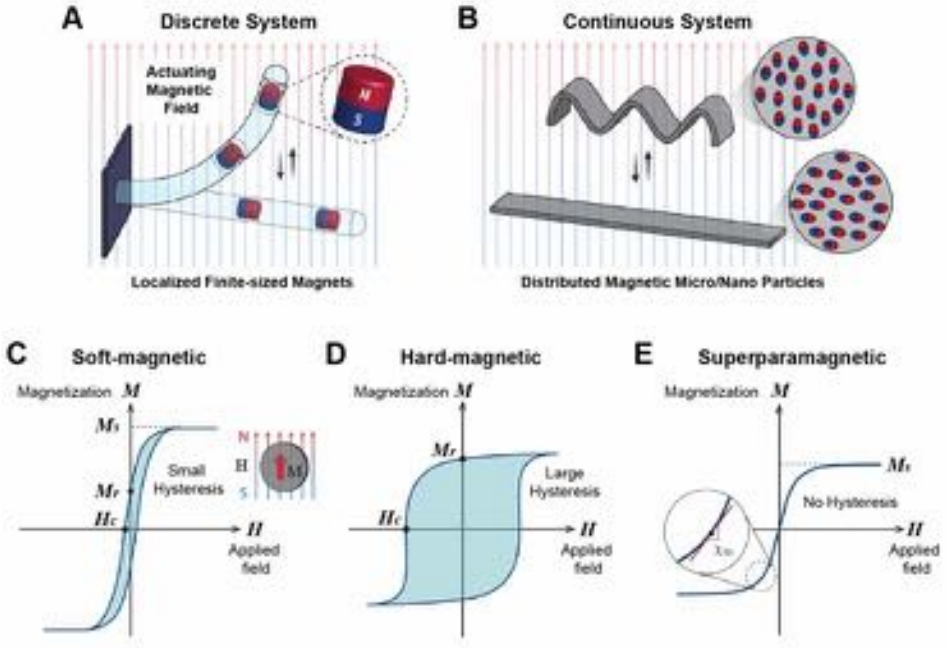

Figure 1.4: Classification and composition of magnetic soft materials. Magnetic soft materials are classified as either (A) discrete systems, with finite-sized magnets embedded in a flexible matrix, or (B) continuous systems, with micro- or nanoparticles dispersed in a soft polymer. Based on magnetic behavior, components are categorized as (C) soft-magnetic (high saturation magnetization, low coercivity, narrow hysteresis), (D) hard-magnetic (high coercivity and remanence, wide hysteresis), or (E) superparamagnetic (no hysteresis, rapid saturation under low fields) [12].

as PNIPAm enable dual-mode actuation when combined with magnetic fillers [42]. Poly(N-isopropylacrylamide) has been utilized to design thermoresponsive magnetic soft robots capable of dual actuation—magnetic and photothermal—enabling multimodal locomotion [43], or combining thermal actuation with magnetic guidance and navigation [44]. However, their mechanical weakness remains a major limitation [45], [46]. To address this, more robust hydrogel systems—such as double-network hydrogels (e.g., polyacrylamide–alginate) and nanoclay-reinforced poly(N,N-dimethylacrylamide) gels—have been developed to enhance mechanical toughness and extensibility without sacrificing softness, making them promising candidates for next-generation magnetic soft actuators [47], [48].

1.1.3 Magnetically-actuated Soft Robots

Magnetically responsive soft materials, often referred to as magnetorheological, magnetoactive, magnetosensitive elastomers or gels, and ferrogels, are composites that integrate soft polymer matrices with magnetic components to achieve both mechanical compliance and strong magnetic responsiveness [49], [50]. In this context, they are collectively termed *magnetic soft materials*, characterized by the inclusion of ferromagnetic or ferrimagnetic fillers that exhibit spontaneous magnetization. These materials can be categorized as either discrete systems (Figure 1.4A), with localized magnetic elements embedded in or attached to the soft matrix, or continuous systems(Figure 1.4B), in which micro- or nanoscale magnetic particles are dispersed throughout the matrix [51]–[53]. Continuous systems are further classified as isotropic when the particles are randomly oriented [54], or anisotropic when they are aligned by applying an external magnetic field during curing [55]. Depending on their magnetization behavior, magnetic materials are typically divided into soft-magnetic (Figure 1.4C), hard-magnetic (Figure 1.4D), and superparamagnetic (Figure 1.4E) types. Key magnetic parameters include remanent magnetization (M_r), coercivity (H_c), magnetic susceptibility ($\chi_m = \partial M/\partial H$), and saturation magnetization (M_s). These properties determine how the material responds to external magnetic fields and are essential for designing programmable actuation in magnetic soft robotics.

Fabrication of magnetic soft robots are commonly using molding, casting, and additive manufacturing techniques to achieve complex geometries and programmable magnetic profiles. Molding and casting remain widely used due to their simplicity and broad material compatibility, allowing incorporation of functional additives and post-curing magnetization for shape programming [56]. Extrusion-based 3D printing, such as direct ink writing, enables filament-level control of magnetization by aligning particles during deposition, requiring thixotropic inks tailored with rheological modifiers [57]. Light-based methods like DLP and CLIP offer higher spatial resolution and 3D magnetization control, though limited by optical penetration depth in particle-loaded resins [58]. At microscale, techniques such as photolithography and two-photon polymerization enable high-resolution structuring but face challenges in scalability and full 3D actuation [59]. Together, these approaches provide a versatile toolbox for developing mag-

netic soft robots with increasingly sophisticated and responsive functionalities.

1.1.4 Towards Clinical Applications

The potential of magnetic soft robots for biomedical applications has been demonstrated through a series of remarkable examples. Self-folding origami robots, for instance, have been reported to crawl through the gastrointestinal tract, patch internal wounds, and dislodge ingested foreign objects [51]. Similarly, soft capsule-like robots have been developed that can roll along the inner surface of the stomach to perform biopsies and deliver medication [60]. Magnetically steerable robotic catheters have shown promise for minimally invasive therapeutic and diagnostic procedures within the heart and pulmonary airways [61]. Moreover, ultra-thin, thread-like magnetic robots have been engineered to navigate the intricate and narrow vasculature of the brain for the treatment of intracranial aneurysms and stroke [62]. With dimensions ranging from hundreds of micrometers to a few centimeters, these soft and flexible robots are inherently less likely to damage surrounding tissues.

1.1.4.1 Minimally Invasive Treatment

Magnetic soft robots have demonstrated considerable promise for minimally invasive treatments, including localized therapeutic delivery, targeted embolization, mechanical or thermal ablation, tissue repair, controlled hemostasis, localized radiotherapy enhancement, and immunomodulation. Among these, drug delivery remains the most extensively explored application, with robots serving as carriers for drugs, cells, or genetic material [71]. At the microscale, swarm-based strategies are often employed to overcome the limited loading capacity of individual robots [72], while millimeter-scale systems exploit shape programmability for targeted transport and controlled release (Figure 1.5B) [64], [73], [74]. Beyond cargo delivery, magnetic soft robots have also been explored for other therapeutic modalities, including thermal ablation, embolization thrombectomy and endovascular stenting. For instance, a pangolin-inspired bilayer soft robot has been developed that achieves rapid, remote-controlled localized heating, enabling functionalities such as hyperthermia, bleeding mitigation, and *in situ* demagnetization on tissue phantoms and *ex vivo* samples

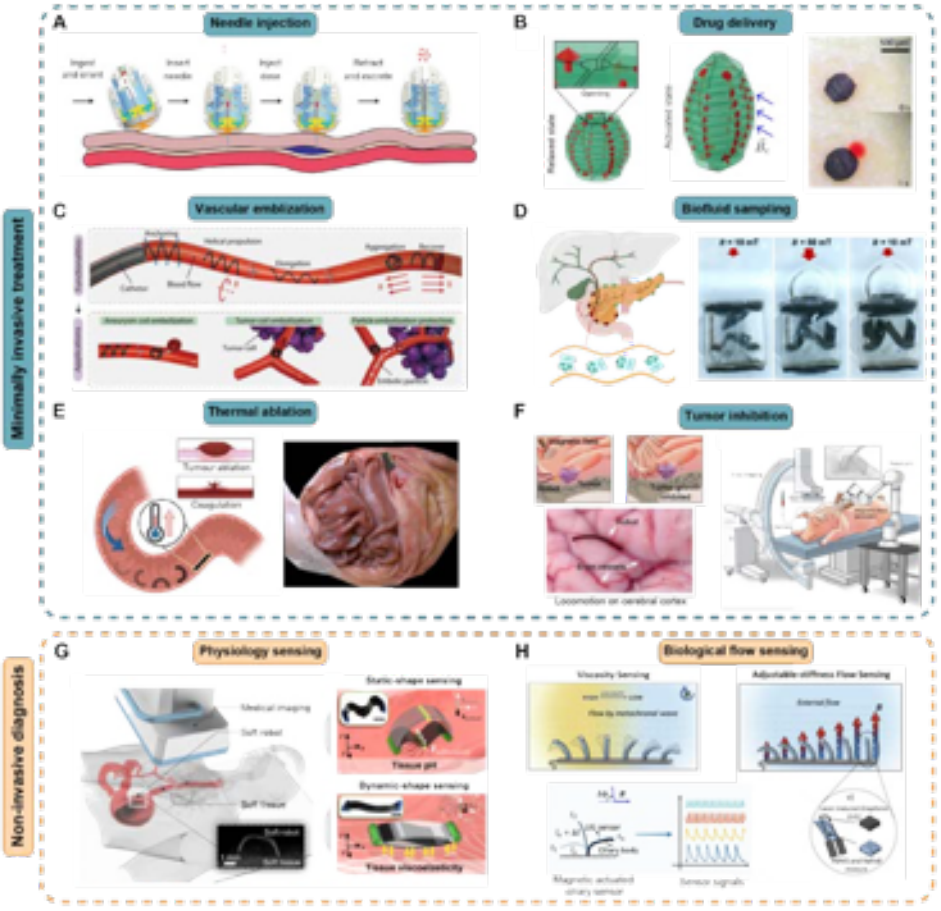

Figure 1.5: Applications of magnetic soft robots for minimally invasive intervention and non-invasive diagnosis. (A) An ingestible self-orienting system for oral delivery of macromolecules [63]. (B) A voxelated magnetic soft robotic capsule for target drug delivery [64]. (C) Magnetic soft microfibers for robotics embolization [65]. (D) Magnetically-actuated millimeter-scale soft capsule for sampling liquids in fluid-filled confined spaces [66]. (E) Pangolin-inspired magnetic soft robot for on-demand heating therapy [67]. (F) Magnetically driven biohybrid blood hydrogel fibres for personalized intracranial tumour therapy under fluoroscopic tracking [68]. (G) In situ sensing physiological properties of biological tissues using wireless miniature soft robots [69]. (H) Actuation-enhanced multifunctional sensing and information recognition by magnetic artificial cilia arrays [70].

(Figure 1.5E) [67]. In addition, magnetic soft microfiberbots with high steerability and shape reconfigurability have demonstrated the ability to perform robotic embolization in submillimeter neurovascular networks, offering a promising alternative to conventional catheter-based interventions (Figure 1.5C) [65]. Collectively, these advances underscore the versatility of magnetic soft robots and their growing potential in precision and minimally invasive medicine.

1.1.4.2 Non-invasive Diagnosis

For diagnostic purposes, magnetic soft robots must achieve a high degree of functional integration, encompassing precise locomotion, on-demand sampling, and *in situ* sensing. Recent studies have demonstrated the feasibility of using magnetically actuated soft capsule robots for tasks such as liquid sampling (Figure 1.5D) [66], tissue biopsy (Figure 1.5A) [63], and microbiome collection [75]. To transform these robots into intelligent diagnostic tools, the integration of environmental sensing capabilities is essential. Strategies for sensorizing magnetic soft robots generally fall into two main categories: direct and indirect approaches. Direct sensing involves embedding microelectronic components directly into the soft robotic system [76], [77], enabling real-time monitoring of physical or biochemical parameters. However, this approach faces significant challenges related to the mechanical mismatch between soft and rigid components, as well as potential electromagnetic interference. In contrast, indirect sensing leverages the robot's mechanical deformation—enabled by multimaterial designs—to infer environmental interactions(Figure 1.5G and H) [69], [70], [78]–[80]. This method is often complemented by external medical imaging modalities such as ultrasound (US), X-ray, or computed tomography (CT) [81], [82]. While indirect strategies offer greater compliance and compatibility with soft systems, they require continued innovation in responsive materials, signal transduction, and wireless communication techniques to fully realize their potential in clinical diagnostics.

1.2 Research Contributions

Magnetic soft robots have shown great potential for clinical applications. The current challenges in this field can be broadly categorized into four key

aspects: design and fabrication improving miniaturization and biocompatibility; locomotion within complex and uncertain biological environments; functionalization balancing general-purpose versatility versus application-specific optimization; and sensorization for creating fully integrated smart devices. This dissertation outlines the following research contributions (**RCs**) across these key areas.

Organisms in nature exhibit a variety of locomotion strategies, often characterized by their adaptability, coordination, and efficiency. Inspired by these biological systems, much of modern robotic locomotion research is grounded in biomimetics—replicating motion patterns observed in nature to enhance robotic adaptability to diverse environments. Bioinspired robots have been developed to emulate multi-legged walking inspired by arthropods, undulatory swimming modeled after fish and eels, flapping-wing flight seen in hummingbirds and insects, and wall-climbing mechanisms derived from geckos. This design philosophy is particularly impactful in the realm of milli- and microscale robotics, where space and material constraints demand solutions that offer both functional efficiency and environmental versatility.

RC.1

Bioinspired and untethered magnetic soft robots are developed, enabling locomotion within anatomically realistic environments.

In **RC.1**, we demonstrate how to design magnetic soft robots capable of navigating in anatomically realistic environments, such as the gastrointestinal (GI) tract. The GI tract presents a variety of physical challenges, including confined lumen structures (e.g., intestines), open cavities (e.g., stomach), transitions between dry and fluid-filled regions, variable diameters, and highly irregular, deformable surfaces. These heterogeneous conditions demand a high degree of adaptability in robot locomotion, morphology, and scalability. To address these challenges, our design strategy focuses on the following aspects:

(1) Fin-wave-inspired amphibious locomotion mechanism that allows for effective navigation in both dry and wet environments, and across narrow lumens and wide cavities;

(2) Multi-segmented architectures that enable snake-like movement through

tortuous lumens while maintaining agility and reconfigurability in open spaces;

(3) Thermoresponsive hydrogel-based mechanisms that enable dynamic size modulation in response to temperature changes, facilitating adaptive navigation through confined lumens and efficient expansion in larger anatomical spaces.

The amphibious locomotion mechanism draws inspiration from aquatic animals such as stingrays and squids, which utilize fin-like undulations or jet propulsion for movement in complex fluidic environments. This bioinspired approach offers smooth, continuous locomotion and enhanced surface adaptability. The multi-segmented robot design takes cues from serpentine locomotion in snakes, enabling enhanced maneuverability and body deformation to conform to complex internal geometries. Notably, both designs are actuated by a rotating magnetic field with tunable frequency and amplitude, allowing for wireless control of locomotion speed, direction, and shape deformation. This simple yet effective actuation method eliminates the need for onboard power or control components, facilitating miniaturization and safe deployment in clinical contexts. Our experimental results demonstrate that such magnetic soft robots exhibit robust and versatile locomotion across physiologically relevant terrains, making them promising candidates for future diagnostic and therapeutic interventions within the human body.

Building on bioinspired designs, enhancing the locomotion performance of magnetic soft microrobots is pivotal for enabling targeted navigation within complex internal environments. For clinical translation, these robots must demonstrate reliable and controllable movement inside the human body, where they are required to traverse inclined, vertical, or inverted surfaces within confined anatomical spaces. Such movement must be achieved against gravity, buoyancy, and friction, all while interacting with dynamic and heterogeneous biological tissues. Notably, many internal organ surfaces—such as those in the oral cavity, gastrointestinal tract, and stomach—are coated with a viscoelastic mucus layer. While this layer serves to protect epithelial tissues, it also presents significant tribological and adhesion challenges for robotic locomotion. Therefore, optimizing the robot–mucus interface is essential for improving traction, adhesion, and propulsion efficiency. Approaches such as biomimetic surface textures,

adaptive locomotion strategies, and materials engineering are critical to mitigate slippage and energy loss in mucosal environments. These advances are fundamental to ensuring that soft robots can navigate robustly and precisely toward clinical targets, ultimately enhancing their functionality in real-world biomedical applications.

RC.2

Biocompatible and bioadhesive coating is developed to improve the locomotion ability for navigation biological environments.

In **RC.2**, we investigate the impact of the mucus layer—ubiquitous on many internal organ surfaces—on the locomotion performance of magnetic soft robots. Given that mucus presents both a lubricating and viscoelastic barrier, it significantly influences friction, adhesion, and thus mobility. To address this, we first analyzed the biochemical composition of mucus and systematically characterized its interfacial adhesion behavior with commonly used soft robotic materials. Building upon these insights, we developed a biocompatible adhesive material that enhances interfacial adhesion between the robot and mucus-coated biological tissues. This adhesive is applied as a thin film coating on the surface of a ring-shaped robot capable of both rolling and compressive deformation. Critically, the adhesion strength can be modulated by adjusting contact time and contact area, enabling a balance between strong anchoring and dynamic mobility. The incorporation of this adaptive adhesive layer effectively mitigates slippage and improves traction, facilitating efficient and controllable locomotion across inclined and irregularly shaped surfaces. We demonstrate the robot's reliable maneuverability under various tilt angles and surface curvatures, highlighting the versatility of this approach. Notably, this strategy offers a generalizable solution and holds promise for integration into a broad range of soft robotic platforms intended for mucosal navigation.

Owing to their efficient locomotion and high environmental adaptability, soft robots are emerging as promising platforms for microrobotic systems in biomedical applications. A complete medical soft robotic system typically integrates three essential components: locomotion, functionalization, and sensorization. Among these, functionalization has attracted increasing research interest, serving as the critical intermediary step that bridges motion capability with therapeutic or diagnostic utility. Com-

mon clinical application scenarios include targeted drug delivery, tissue biopsy, and biomarker sampling. To enable these functionalities without compromising locomotion performance, ongoing research efforts focus on the development of biodegradable and biocompatible materials, as well as minimally invasive mechanisms for controlled payload release and *in situ* sampling. The integration of such functionalities not only enhances the therapeutic relevance of soft robots but also moves them closer to clinical translation as multifunctional, untethered devices for precision medicine.

RC.3

Magnetic soft robots are endowed with application-specific functionalities for therapeutic and diagnostic tasks.

In **RC.3**, we examine strategies for imparting specific biomedical functionalities to magnetic soft robots through the integration of responsive materials and application-oriented structural designs. Functionalization is critical for transitioning soft robotic platforms from simple mobile agents to multifunctional systems capable of performing clinical tasks such as therapeutic delivery, tissue manipulation, and fluid sampling. We investigate four representative approaches:

(1) A gelatin-based soft robot, engineered to encapsulate therapeutic agents and release them through environmentally triggered biodegradation;

(2) A thermoresponsive hydrogel-based soft robot that leverages temperature dependent volumetric changes to achieve controlled release of encapsulated cargo, enabling site-specific, stimulus-responsive therapeutic delivery;

(3) A ring-shaped magnetic soft robot capable of reversible deformation through magnetic actuation, designed for mechanical gripping and release of objects—demonstrating potential for tasks such as targeted material deposition, retrieval, or tissue manipulation;

(4) A shape memory polymer (SMP)-based actuator functioning as a soft pump, capable of performing localized liquid sampling in confined or otherwise inaccessible regions of biological environments through temperature-programmed actuation cycles.

These function-specific implementations highlight the synergistic use of smart materials and magnetic soft actuation to address diverse clinical needs. By tailoring material properties—such as degradability, thermal responsiveness, and shape memory behavior—alongside geometric adaptability and external magnetic control, we demonstrate that soft robots can be effectively customized for precise, on-demand biomedical interventions. This research paves the way for a new generation of intelligent, multifunctional soft robotic systems engineered for application-specific clinical tasks in minimally invasive and targeted therapeutic settings.

Equipping magnetic soft robots with sensing capabilities is essential for transforming them from passive actuators into intelligent, responsive systems capable of autonomous operation in complex biomedical environments. This integration, however, faces significant challenges due to constraints on size, biocompatibility, compliance, and wireless control. True intelligence in such robots requires not only actuation and functional tasks like drug delivery, but also real-time perception of physiological or environmental cues. Developing miniaturized, biocompatible, and reliable sensing strategies is thus critical for enabling closed-loop control, improving safety, and expanding their application in diagnostics, therapy, and surgical intervention.

RC.4

Non-invasive diagnostics using embedded sensors in magnetic soft robots is demonstrated *in vivo*.

To address this challenge, we propose a hydrogel-based sensor capable of wireless pH measurement in gastric juice, demonstrating a practical application for sensorizing soft robots. This hydrogel sensor combines biocompatibility with intrinsic responsiveness to chemical stimuli, thereby overcoming the limitations of conventional electronic sensors related to miniaturization, power supply, and compatibility within biological environments. We conducted *in vivo* experiments in animal models that illustrate the ability of SeroTab to non-invasively detect pH shifts and metabolic alterations induced by omeprazole administration. Our approach exemplifies a viable pathway toward fully integrated, soft robotic systems that can perform real-time environmental monitoring, enhancing functionality and enabling adaptive, closed-loop operation in biomedical contexts.

1.3 Outline of the Thesis

This doctoral thesis is organized into seven chapters to address the research questions. **Chapters 2-6** consist of research studies published in international peer-reviewed journals.

Chapter 2 links to **RC.1** by presenting a fin-wave-inspired magnetic soft robot capable of adaptive amphibious locomotion under a rotating magnetic field. The robot is composed of multiple soft rod-shaped legs with distinct magnetization profiles, enabling the generation of undulatory waves for effective movement across both solid (dry) and liquid (wet) environments. The design and spatial arrangement of the legs are guided by simulations based on Cosserat rod theory. The robot demonstrates robust maneuverability, including steering, surface transitioning (dry-to-wet), and buoyancy control (sinking/floating) within hybrid environments. Its ability to traverse fluid-filled pipes of varying diameters, both with and against the flow, highlights its potential for wireless navigation in confined clinical settings such as vascular interventions.

Chapter 3 links to **RC.1** and **RC.3** by introducing a snake-inspired, multi-segmented soft robot fabricated from biodegradable materials. The design enables the robot to navigate complex terrains—over solid ground, underwater, and even on oil-coated surfaces—while maintaining structural integrity. The robot also possesses drug-loading and release capabilities through material dissolution. This work illustrates how combining segmented bioinspired architecture with biocompatible, dissolvable materials can result in functional robots suited for targeted therapeutic applications.

Chapter 4 links to **RC.1** and **RC.2** by developing a ring-shaped magnetic soft robot coated with a biopolymeric film designed for locomotion on mucus-coated tissue surfaces. Leveraging mucoadhesive interactions, the robot exhibits controlled motion and adhesion, enabling clinical procedures in environments such as the gastrointestinal tract. Material characterization confirms that mucoadhesion is positively correlated with contact duration and preload force. The ring-shaped geometry and magnetization profile enable the decoupling of locomotion and functional modules. Demonstrated capabilities include pick-and-place, cargo transport, and controlled release of liquid capsules, showcasing the robot's multifunctionality and maneuverability on biologically relevant surfaces.

Chapter 5 links to **RC.1** and **RC.3** through the development of a

dual-responsive soft robot that integrates magnetic shape programming with thermally induced morphological transformation. The robot is capable of executing complex tasks such as object manipulation, locomotion, and controlled release through orthogonal stimuli—magnetic fields for actuation and temperature changes for structural transitions. For instance, magnetic actuation enables gripping, while thermal input induces a reversible shape shift from swollen to collapsed states. This dual-trigger strategy allows full, decoupled control over movement and function, offering a straightforward pathway to achieving multi-functionality in soft robotic systems.

Chapter 6 links to **RC.1**, **RC.3**, and **RC.4** by introducing *SeroTab*, a sensorized, ingestible soft robotic minitablet designed for real-time pH sensing and on-demand gastric juice sampling *in vivo*. Inspired by the streamlined motion of penguins, SeroTab utilizes magnetic actuation and a curvature-adaptive structure to autonomously navigate to the stomach. A shape-memory polymer (SMP) actuator, triggered by RF heating, enables the absorption of gastric fluid (up to 35 μL) into an internal chamber. Inside, a pH-responsive hydrogel with embedded biocompatible metal disks enables ultrasound-based, wireless pH readout in the range of 2–7. *In vivo* animal experiments confirm SeroTab's ability to detect pH changes and metabolic alterations following omeprazole administration. This platform demonstrates potential for early-stage, non-invasive diagnostics and out-of-hospital monitoring, facilitating faster triage and improved clinical decision-making.

Finally, we showcase the key findings of the doctoral research, with a specific emphasis on application-oriented design strategies in magnetic soft robotics. A comprehensive summary of the contributions made throughout the research is presented in **Chapter 7**, which also outlines valuable insights and future directions, highlighting the transformative potential of magnetic soft robots in advancing precision medicine and minimally invasive interventions.

1.4 Research Framework Funding

All the research studies that constitute this doctoral thesis have been supported by funds from the European Research Council (ERC) under the European Union's Horizon 2020 Research and Innovation programme un-

der grant 866494 project-MAESTRO, and financial support from the China Scholarship Council. All the studies presented in this thesis have been performed with the experimental setups at the Surgical Robotics Laboratory (SRL), in the Department of Biomaterials and Biomedical Technology (formerly known as the Department of Biomedical Engineering) of the University of Groningen and University Medical Center Groningen, Groningen, the Netherlands.

1.5 Scientific Output

The studies presented in this doctoral thesis have been a part of the following articles that have been published in the following journals:

1.5.1 Peer-Reviewed Journal Articles

1. **C. Wang**, V. P. Puranam, V., S. Misra, and V. K. Venkiteswaran, *"A snake-inspired multi-segmented magnetic soft robot towards medical applications,"* IEEE Robotics and Automation Letters, 7(2): 5795-5802, April 2022.

2. **C. Wang**, A. Mzyk, R. Schirhagl, S. Misra, and V. K. Venkiteswaran, *"Biocompatible film-coating of magnetic soft robots for mucoadhesive locomotion,"* Advanced Materials Technologies, 8(12): 2201813, June 2023.

3. C. Siebenmorgen, **C. Wang** (co-first author), L. B. Navarro, D. Parisi, S. Misra, V. K. Venkiteswaran, and P. van Rijn, *"Minimally designed thermo-magnetic dual responsive soft robots for complex applications,"* Journal of Materials Chemistry B, 12(22):5339–5349, June 2024.

4. **C. Wang**, R. Shi, A. Abalymov, H. Bao, T. K. LAM, Z. Wang, Y. Mei, Z. Cai, X. Chen, S. Misra, V. K. Venkiteswaran, *"Electronics-free soft robotic minitablet for on-demand gastric molecular sensing and diagnostics in vivo,"* Science Advances, Under review.

1.5.2 International Conference Proceedings (peer reviewed)

1. **C. Wang**, V. P. Puranam, S. Misra, and V. K. Venkiteswaran, *"A snake-inspired multi-segmented magnetic soft robot towards medical applications,"* in Proceedings of the IEEE International Conference on Soft Robotics (RoboSoft), pages 707–714, Edinburgh, UK, April 2022. **(Poster presentation)**

2. **C. Wang**, S. Misra, and V. K. Venkiteswaran, *"Fin-wave-inspired wireless small-scale soft robot for adaptive amphibious locomotion under single-mode magnetic field,"* in Proceedings of the Annual International Conference on Manipulation, Automation, and Robotics at Small Scales (MARSS), pages 1-7, IEEE, Delft, The Netherlands, July 2024. **(Oral presentation)**

1.5.3 Patents

1. **C. Wang**, X. Chen, S. Misra, and V. K. Venkiteswaran, *"Sensorized wireless soft robotic minitablet and method of sensorizing magnetic soft robotic medical device,"* US patent, 2025, (in process).

1.5.4 Awards

1. **Best Student Paper Award** (Highest ranking), **C. Wang**, S. Misra, and V. K. Venkiteswaran, *"Fin-wave-inspired wireless small-scale soft robot for adaptive amphibious locomotion under single-mode magnetic field,"* in Proceedings of the Annual International Conference on Manipulation, Automation, and Robotics at Small Scales (MARSS), pages 1-7, IEEE, Delft, The Netherlands, July 2024.

1.5.5 Journal Cover Images

1. **C. Wang**, A. Mzyk, R. Schirhagl, S. Misra, and V. K. Venkiteswaran, *"Biocompatible film-coating of magnetic soft robots for mucoadhesive locomotion,"* Advanced Materials Technologies, 8(12): 2201813, June 2023.

2. C. Siebenmorgen, **C. Wang** (co-first author), L. B. Navarro, D. Parisi, S. Misra, V. K. Venkiteswaran, and P. van Rijn, *"Minimally designed thermo-magnetic dual responsive soft robots for complex applications,"* Journal of Materials Chemistry B, 12(22):5339–5349, June 2024.

2

Fin-wave-inspired Wireless Soft Robot for Adaptive Amphibious Locomotion under Single-mode Magnetic Field

Note: *This chapter is adapted from the article "Fin-wave-inspired wireless small-scale soft robot for adaptive amphibious locomotion under single-mode magnetic field" by* ***C. Wang****, S. Misra, and V. K. Venkiteswaran, published in "Proceedings of the Annual International Conference on Manipulation, Automation, and Robotics at Small Scales (MARSS)", pages 1-7, February 2024.*

Abstract

Magnetic soft robots are capable of generating programmable deformation based on variable magnetization profiles, with the added potential advantages of easy fabrication and miniaturization. However, achieving efficient locomotion and maneuverability in complex and variable environments often requires intricate modulation of external magnetic field which limits their applications. Inspired by the undulating fin-wave often seen in aquatic organisms, this paper demonstrates a small-scale soft robot capable of adaptive amphibious locomotion under a rotating magnetic field, allowing the robot to efficiently move on the solid surface (dry) and in liquids (wet). The robot comprises a combination of multiple soft rod-shaped legs (6×1×1 mm) with different magnetization directions capable of generating undulating waves. Simulation of the undulating wave is conducted based

on Cosserat rod theory to aid in the design and arrangement of the legs. The maneuverability and capability of steering and transitioning from dry to wet surfaces as well as sinking and floating in hybrid environments are demonstrated. The robot's ability to move with and against the flow of liquid in pipes of variable diameter is studied and characterized. The results demonstrate the potential to use as a small-sized wireless robot in applications, such as navigating within human blood vessels for clinical interventions.

2.1 Introduction

Magnetically-actuated soft robots are foreseen to have a profound impact on medical applications, especially in minimally invasive surgery (MIS) [83]–[85]. As medical robots, their soft, untethered, miniaturized bodies offer greater capability for reaching confined and enclosed spaces within the human body in comparison to their tethered and rigid counterparts [86]–[91]. However, unstructured environments and a combination of liquid and solid interfaces are common in the areas of interest where robots need to operate, such as within the human body. Existing magnetic soft robots typically perform a single mode of locomotion either in liquid or on solid substrates under a simple external magnetic field [92]–[95]. Despite numerous studies highlighting the multi-modal locomotion capabilities of their robots, controlling and switching motion modes still necessitates complex external magnetic fields [96], [97]. The potential applications could greatly benefit from simplified actuation magnetic field requirements while maintaining motion efficiency.

Unlike terrestrial robots (e.g. quadruped [94], [98], [99], millipede [100]–[103]) and swimming robots (e.g. sperm bots [104], [105], the helical swimmers [90], [106]) that primarily specialize in either ground or water-based locomotion, robots with amphibious locomotion capabilities excel in both aquatic and terrestrial environments. This versatility grants them access to a wider range of settings, enhancing their overall adaptability [107]. Generally, amphibious robot designs can be classified into three categories based on their propulsion mechanisms and structural features: wheeled, legged, and undulating [108], [109]. Notably, legged robots lacking palmate feet usually struggle to swim [110], [111], while those with palmate feet can swim but face challenges related to complex controller design and limited

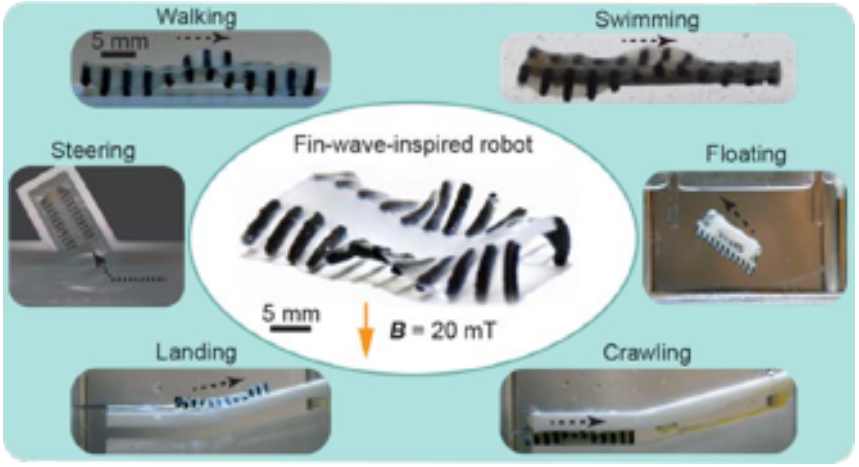

Figure 2.1: The fin-wave-inspired soft robot and examples of the robot's amphibious locomotion abilities in different media (e.g. water, oil, dry PLA surfaces) and environments (e.g. on dry and wet surfaces, underwater, narrow channel) under the actuation of rotating magnetic field ($\boldsymbol{B}$). The dashed arrows indicate the directions of the robot motion.

efficiency in terrestrial movement [112]. Prior research on sheet-shaped magnetic robots has showcased their ability to perform diverse forms of locomotion, including swimming in liquids, rolling, walking, and crawling on solid surfaces in response to changes in the direction of a rotating magnetic field [88], [113]. An origami-inspired robot has also demonstrated the ability to roll and flip on the ground and swim in water [96]. However, they do rely on a high degree of control over the applied magnetic field to adjust the locomotion mode based on the environment. This places significant constraints on the actuation system and causes difficulties when scaling to application requirements.

The undulating wave propulsion mechanism has undergone extensive research and finds widespread application in the design of macro-sized amphibious robots [114]–[117]. Inspired by stingrays and squids, Festo introduced the 'BionicFinWave' in 2018, an amphibious robot with the capability to swim and land [118]. Liu *et al.* conducted experiments to investigate swimming performance, focusing on factors such as undulating frequency and fin wavelength [119]. In the meanwhile, Zhang *et al.* calculated optimal thrust and efficiency for undulating fin waves with varying geometrical pa-

rameters, utilizing computational fluid dynamics [120]. Building on these studies, the use of magnetic actuation to produce fin-wave propulsion will allow translating these concepts to small-scale wirelessly-driven amphibious soft robots.

This paper introduces a fin-wave-inspired small-scale magnetic soft robot capable of locomotion in liquids and on solid surfaces. The key feature of this robot is its adaptive amphibious locomotion under a single mode of actuation magnetic field, facilitating ease of actuation and control. This capability enables seamless transitions between aquatic and terrestrial environments. Additionally, the robot can achieve both sinking and floating on command with a phase-changing capsule embedded in its body. We employ Cosserat rod theory to analyze the motion of magnetic elements, aiding in the miniaturized robot design. Through experimental demonstrations, we showcase the robot motion capabilities and adaptability, highlighting its potential applications in clinical settings, such as within blood vessels. In comparison to existing magnetic soft robots, our presented robot offers several advantages, including amphibious locomotion ability, ease of control, high frequency actuation, maneuverability, and the potential to carry payloads.

2.2 Materials and Methods

Inspired by swimming mechanisms in nature creatures like stingrays and squids, we use rhythmic magnetization changes to generate undulating waves. Two rows of magnetic rod-shaped legs are embedded along the sides of an unmagnetized soft body. These legs exhibit distinct deformations when exposed to a magnetic field, forming an undulating wave. On solid ground, the robot walks using these magnetic rod-shaped legs, while in aquatic environments, a thin soft film connecting the legs transforms them into a fin-wave, enabling swimming.

2.2.1 Design

The design and dimensions of the fin-wave-inspired amphibious magnetic soft robot are depicted in the left image of Figure 2.2(a). Symmetrically assembled on both sides of the robot body are two rows of legs shaped as rectangular rods, each measuring $6 \times 1 \times 1$mm. A thin 0.5 mm film connects

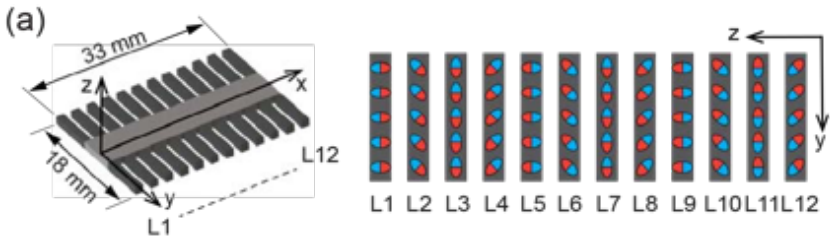

Figure 2.2: Design, modeling and fabrication of the soft robot. (a) Design of the robot and the magnetization directions within the legs (labeled ($L1$-$L12$))

these legs, facilitating swimming capabilities. The legs are labeled from $L1$ to $L12$ along the long x-axis under the coordinate system, as illustrated in Figure 2.2(a). The magnetization directions undergo continuous 45° changes between adjacent/successive legs, as depicted on the right side of Figure 2.2(a). Notably, these alterations in the magnetic dipoles of the legs occur within the yz plane while the actuation magnetic field rotates within the xz plane about the y-axis.

2.2.2 Materials

The robot's legs are constructed from a magnetic polymer composite (MPC) that responds to external magnetic fields, whereas the body and fin film are composed of silicone rubber without magnetic particles. The MPC comprises a silicone rubber matrix (Ecoflex-0010, Smooth-On Inc., USA) and a ferromagnetic powder of praseodymium-iron-boron (PrFeB) with a mean particle size of 5μm (MQFP-16-7-11277, Magnequench GmbH, Germany). In this study, a 1:1 mass ratio of magnetic microparticles to silicone rubber is employed. The MPC exhibits a relatively low elastic modulus of 2 MPa and 300% elongation at break, conferring a soft and flexible internal structure to the robot.

2.2.3 Modeling

To elucidate the arrangement of the robot legs and delve into the dynamics of its waveform, we employ a model grounded in Cosserat-rod theory. In this model, an individual leg of the robot is conceptualized as a flexible rod, firmly attached at its proximal end to a rigid base and free to move at

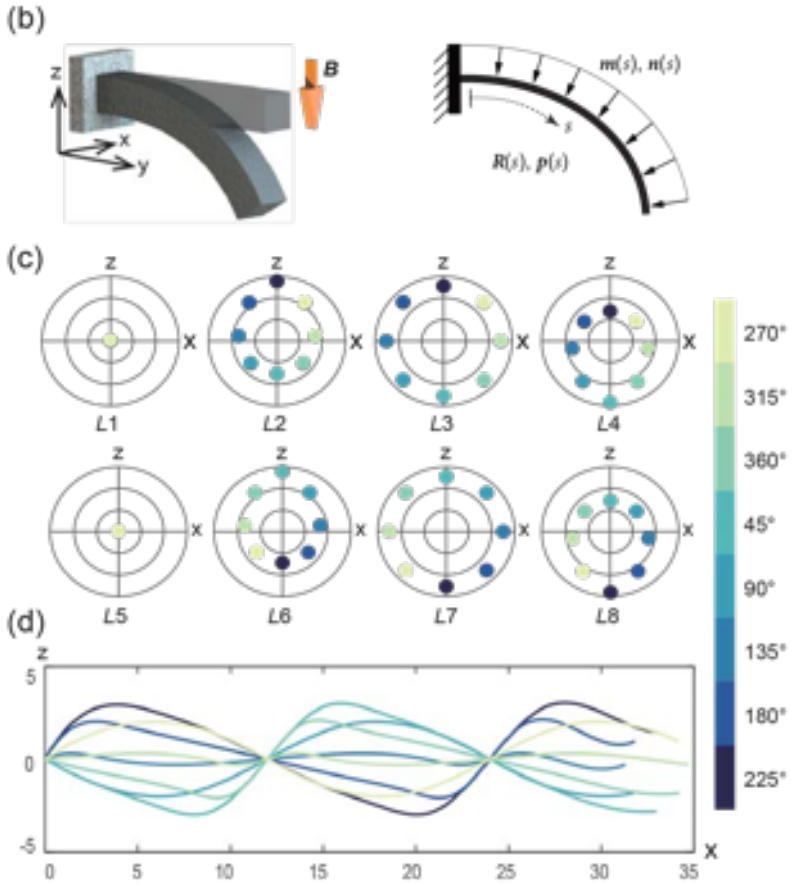

Figure 2.3: (b) Each individual leg is conceptualized as an elongated rod, anchored at one end to the robot body, and its actuation response modeled using Cosserat rod theory. $\boldsymbol{R}(s)$, $\boldsymbol{p}(s)$, $\boldsymbol{n}(s)$ and $\boldsymbol{m}(s)$ are material states vectors at the position $s \in [0, l]$ along the rod. (c) The positions of the distal tips of legs 1-8 (labeled as ($L1$-$L8$)), with a color bar indicating orientation of magnetic field to the x-axis. (d) Fin waves obtained by connecting the tips of all 12 legs under varying magnetic field directions.

its distal tip. Figure 2.3(b) provides a schematic illustration of how the leg bends under the influence of the magnetic field. This Cosserat-rod model is coupled with magnetization profiles and magnetic fields, enabling us to simulate the deformation of the legs. Here, each rod is characterized by

its centerline curve in three-dimensional space, denoted by $s \in [0, l]$, where $l \in \mathbb{R}^3$ represents the length of the leg. The discretized cross-section along s can be succinctly expressed by a material state vector:

$$\boldsymbol{y}(s) = [\boldsymbol{R}(s)\ \boldsymbol{p}(s)\ \boldsymbol{n}(s)\ \boldsymbol{m}(s)], \tag{2.1}$$

where $\boldsymbol{R}$ is rotation matrix of material orientation, $\boldsymbol{p}$ represents global position in Cartesian coordinates, $\boldsymbol{n}$ is internal force in the global frame, $\boldsymbol{m}$ represents internal moment in the global frame.

The actuation magnetic field is generated using 3D electromagnetic coils designed to produce a uniform magnetic field within the workspace, and therefore the contribution of the magnetic field gradient is assumed to be negligible [121]. Consequently, the applied force distribution per unit of s is denoted as $\boldsymbol{f}(\mathrm{s}) = 0$. Additionally, for the purposes of this study, gravity is disregarded. Therefore, the applied torque distribution per unit length of s can be represented as ($\boldsymbol{q} \in \mathbb{R}^3$), and is given by

$$\boldsymbol{q}(s) = \mu \times \boldsymbol{B}\ , \tag{2.2}$$

where $\mu \in \mathbb{R}^3$ is the magnetic dipole moment per unit, $\boldsymbol{B} \in \mathbb{R}^3$ is the magnetic field. Thus the equilibrium differential equations are expressed as:

$$\dot{\boldsymbol{n}}(s) + \boldsymbol{f}(s) = 0\ , \tag{2.3}$$

$$\dot{\boldsymbol{m}}(s) + \dot{\boldsymbol{p}}(s) \times \boldsymbol{n}(s) + \boldsymbol{q}(s) = 0\ , \tag{2.4}$$

where the dot denotes a derivative with respect to s.

The boundary value problem of Cosserat rod is solved using the fourth-order Runge-Kutta method, implemented using Matlab (2021a, Mathworks, USA). The detailed modeling and solution approach closely adhere to the methodologies outlined in [122], [123], and implementation details can be found in our previous work [124].

To set the robot in motion, a magnetic field is provided in the xz plane, rotating about y-axis. In the model, eight different orientation of the magnetic field are considered within one actuation cycle (0°-360°) with a spacing of 45°. Due to variations in magnetization, each leg undergoes distinct deformations. The 12 legs on one side of the robot are defined as $L1$-$L12$. The positions of the distal tips of $L1$ to $L8$ on the xz plane under different

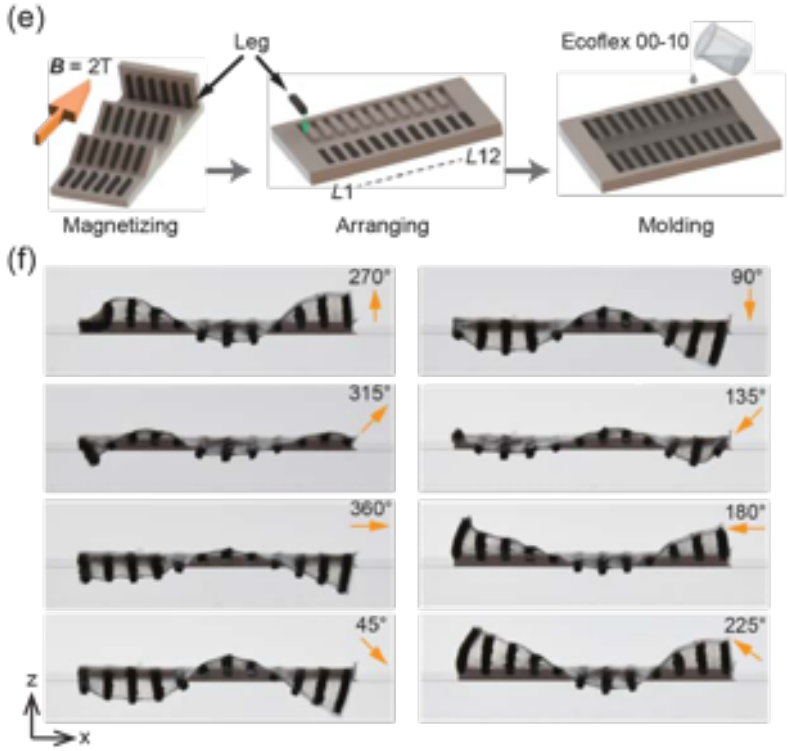

Figure 2.4: (e) The fabrication procedure goes from magnetization of individual legs to arrangement in a mold for the forming of robot body and fin. (f) Experimental results at 30 mT showing the fin wave on one side of the robot. The yellow arrows indicate the directions of the magnetic field.

magnetic field directions are presented in Figure 2.3(c). Notably, $L2$-$L4$ and $L6$-$L8$ move in circular patterns, with varying amplitudes and phase shifts. By contrast, $L1$ and $L5$ predominantly experience twisting, resulting in fixed tip positions on the xz plane. By connecting the tips of $L1$ to $L12$, an fin-like dynamic waveform emerges, as depicted in Figure 2.3(d). The simulation results showing undulating fin-like waves with magnitude changing and phase shift that theoretically can generate thrust in liquid environment as verified in [119], [120]. Also, the circular motion path of $L2$-$L4$ and $L6$-$L8$ have potential to generate movement on solid ground as demonstrated in [94]. Experimental results showcasing the generation

of this fin-wave under a rotating magnetic field at 30 mT are featured in Figure 2.4(f). It is worth noting that variations in the movement of individual legs in the experiment compared to simulation results may arise from factors such as the influence of gravity on the legs themselves and the presence of the thin film connecting the legs.

2.2.4 Fabrication

The fabrication procedure is detailed in Figure 2.4(e). Initially, 3D printed PLA molds are employed to shape the robot's legs. Subsequently, the magnetic polymer composite (MPC) undergoes a degassing process and is allowed to cure naturally at room temperature (24°C) for four hours. Once cured, the MPC legs are arranged within a specialized fixture and exposed to a 2 T magnetic field, achieved using an impulse magnetizer (ASC Model IM-10-30, ASC Scientific, USA), to obtain the desired magnetization profile. These magnetized legs are then transferred to another mold, where they are systematically repositioned according to the order derived from simulation results. Finally, silicone rubber is cast into these molds, resulting in the formation of the robot body and the interconnecting fin.

2.3 Experiments and Results

To demonstrate the capability and maneuverability of robot locomotion, experiments are carried out in different environments shown in the following sections.

2.3.1 Amphibious Locomotion

The robot's amphibious locomotion capabilities are demonstrated across various media: on solid ground (3D printed PLA surface), on the surface of water, underwater, and at the oil-water interface (as shown in Figure 2.5(a)-(d), **please refer to supplementary video**). Figure 2.5 (I) displays the robot postures from both top and side views at different time points in these environments.Accordingly, the motion velocities in these four media were measured under varying magnitudes and frequencies of the rotating magnetic field as shown in Figure 2.5 (II). Each experiment

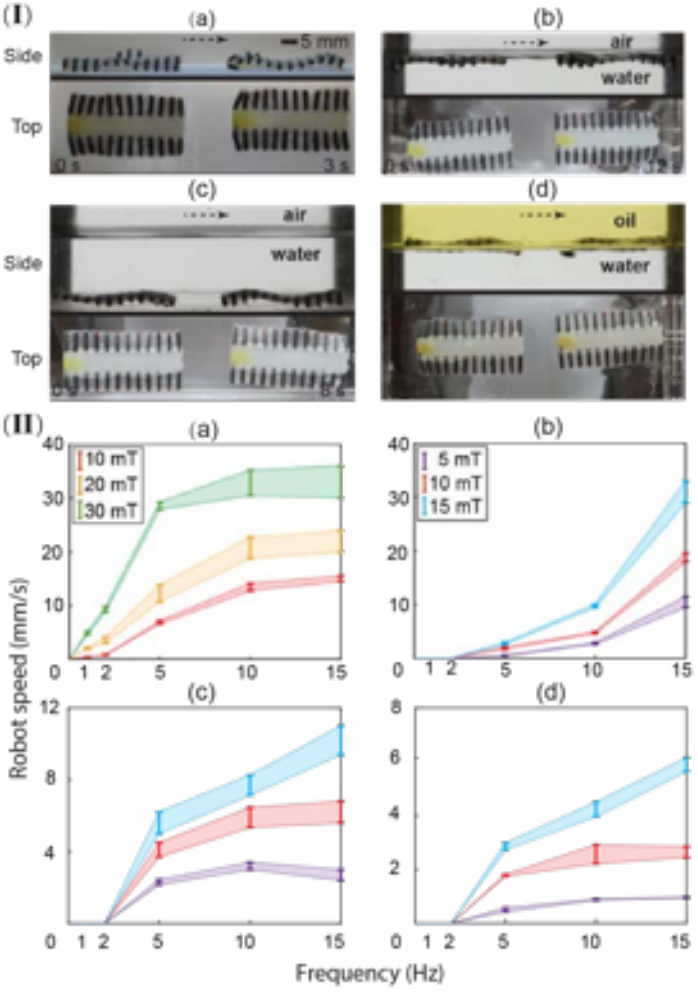

Figure 2.5: Demonstration and characterization of the locomotion and speed in different media: (I): Demonstration of basic locomotion abilities of the robot. (a) Walking on solid surface (PLA). (b) Swimming on the surface of water. (c) Motion on underwater ground. (d) Swimming between the interface of water and oil. A magnetic field of 10mT rotating at 15 Hz is used in the demonstrations. The dashed arrows indicate the directions of the robot motion. (II): Characterization of robot locomotion speed in the abovementioned four media under different magnitude and frequency of rotating magnetic field. (**please refer to supplementary video**)

was repeated three times to obtain average data and assess errors. It can be observed that the velocity in all media increases with the increases of magnetic frequency and/or magnetic field strength. When comparing the red lines (magnetic field at 10 mT and 10 Hz) in Figure 2.5 (II), walking demonstrates higher efficiency than swimming. Swimming is most efficient on the water surface, while it is slower at the oil and water interface. Walking on solid ground requires magnetic fields between 10 mT and 30 mT, while swimming demands lower field strengths (5 mT) but no higher than 15 mT for stable movement. Lower magnetic frequencies (1 mT and 2 mT) support walking on solid ground but not swimming. Higher magnetic frequencies enhance swimming more than walking, whereas greater field magnitudes improve walking more than swimming. These trends serve as guidelines for subsequent experiments involving special maneuvers.

2.3.2 Maneuverability and Capability

In addition to its fundamental amphibious locomotion, the robot possesses the capability to execute specialized maneuvers, enabling it to navigate complex environments. Steering is achieved by adjusting the tilt angle between the plane of the rotating magnetic field and the xz plane (as defined in Figure 2.2(a)). Altering this tilt angle induces a phase difference between the fins on either side of the body, prompting the robot to align with the plane of rotation of the magnetic field, resulting in turning [100]. The direction of turning, whether left or right, can be changed by reversing the tilt angle. Experiments to demonstrate the robot maneuverability on both solid ground and water surfaces are conducted and depicted in Figure 2.6(a) and (b), respectively (**please refer to supplementary video**).

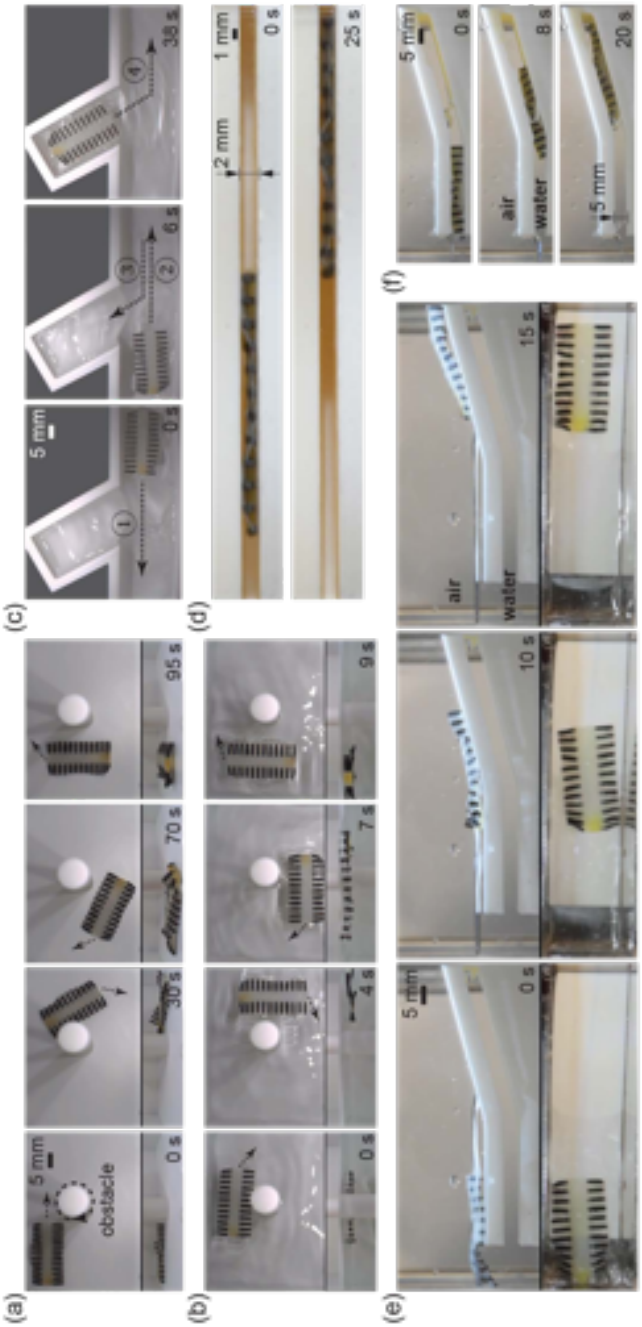

Figure 2.6: Demonstrations of robot maneuverability and capability: (a) The robot is steered to walk around a pillar/obstacle (Magnetic field: $|\boldsymbol{B}| = 10$ mT, frequency: $f = 1$ Hz). (b) The robot is steered to swim around a pillar on water surface ($|\boldsymbol{B}| = 10$ mT, $f = 10$ Hz). (c) The robot can be controlled to select the target path at a fork while swimming ($|\boldsymbol{B}| = 10$ mT, $f = 10$ Hz). (d) The robot is crawling in a 2 mm height narrow channel ($|\boldsymbol{B}| = 10$ mT, $f = 10$ Hz). (e) Demonstration of the robot transitioning from water to ground ($|\boldsymbol{B}| = 30$ mT, $f = 5$ Hz). (f) The robot switches between water and ground in a 5 mm height channel ($|\boldsymbol{B}| = 30$ mT, $f = 5$ Hz). The dashed arrows indicate the direction of the robot motion (**please refer to supplementary video**).

In Figure 2.6(c), the robot's navigational prowess within a tube with a two-way fork is highlighted. Initially, it travels straight from the right end to the left end and returns. Then, it turns at a 60° angle, entering the side channel. Figure 2.6(d) shows the robot's successful traversal of an extremely narrow 2 mm-high channel under a rotating magnetic field at 10 mT and 10 Hz. Capabilities of transition from swimming in deep water to landing on a dry slope are demonstrated in Figure 2.6(e) and Figure 2.6(f), both in open space and within a 5 mm-high narrow channel. Importantly, these transitions between water and solid ground are reversible (**please refer to supplementary video**).

Additionally, we also show that the robot can be altered to control its ballast for sinking or floating in liquid environments. A 2 mL acetone capsule is embedded onto the top surface of the robot body. This capsule is constructed from a rigid PE (Polyethylene) hollow pipe, with acetone injected into it using a syringe and sealed with thin silicone rubber films at both ends. Acetone has a low boiling point of 56°, and undergoes a phase change from liquid to gas when the temperature surpasses this critical value. Consequently, the capsule inflates upon heating, increasing the robot's volume and altering its buoyancy. The robot can float when the environmental temperature exceeds 56°C and sink when the temperature drops below this critical temperature. Figure 2.7 demonstrates the robot moving underwater with the embedded capsule (also acting as payload), followed by floating and motion on water surface, and subsequently sinking again (**please refer to supplementary video**). A pump is used to control the water temperature, facilitating heating and cooling, thus enabling repeated rounds of sinking and floating experiments to illustrate the repeatability of the acetone capsule (**please refer to supplementary video**).

2.3.3 Applications

Based on the robot's capabilities, a possible area of application is inside the human body, where such robots can potentially be used for surgical interventions by navigating blood vessels or other body conduits. To explore such potential clinical applications, experiments were conducted within fluid-filled circular pipes that mimic conditions found in blood vessels. Two pipes, one with a 22 mm diameter (Figure 2.8(a)) and another

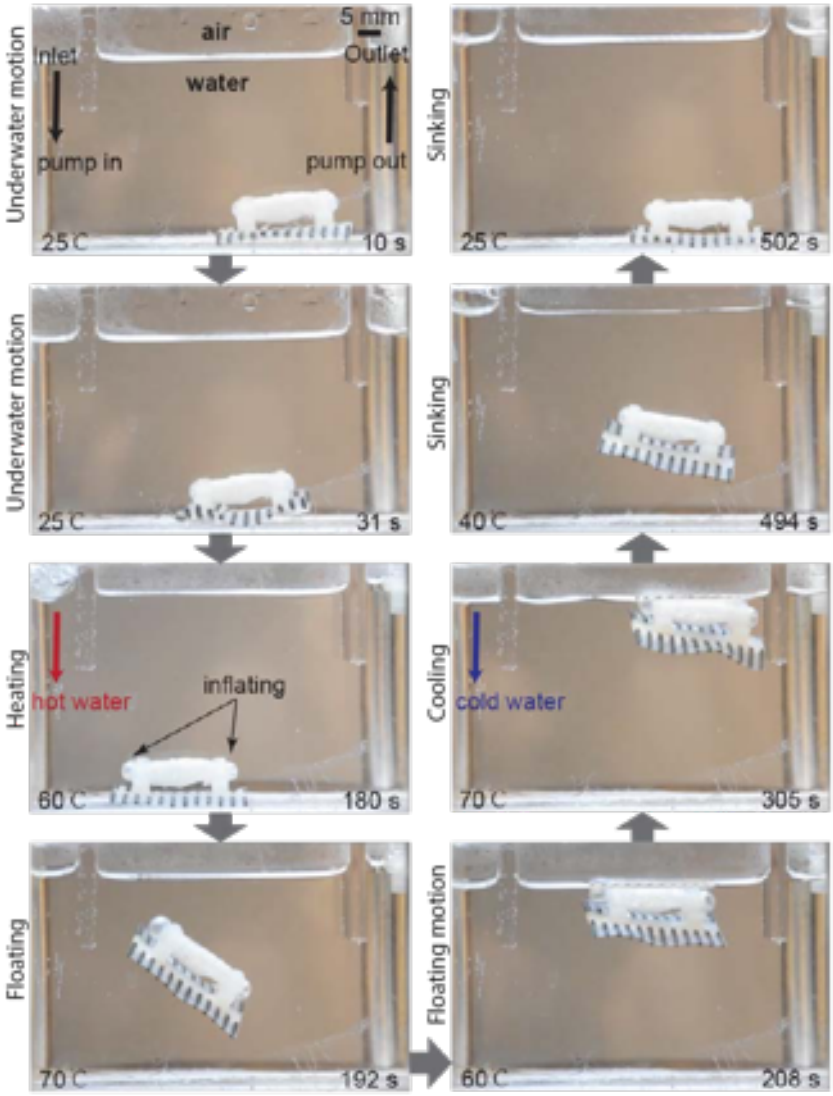

Figure 2.7: Demonstration of the robot sinking and floating in water (side view). The robot embedded with a buoyancy capsule is controlled to move underwater, float up to water surface, swim on water surface and sink again to reach the starting point. A pump is connected to the inlet on the left corner and and outlet on right corner of the tank setup, allowing injection of hot and cold water for the heating and cooling of the environment. (**please refer to supplementary video**)

with a 16 mm diameter (Figure 2.8(b)), are used to assess the robot's adaptability (with the robot width measuring 18 mm). Motion within the pipe was observed using cameras (top and side views) and ultrasound (US) imaging with a transducer ((SonixTouch Q+, BK Medical, Quickborn, Germany, shown in Figure 2.8(c) and (d)). Pulsatile flow was generated using a pump (HV-77 910-55, Masterflex, Illinois, USA), and the flow rate was adjustable, with actual flow rates visualized and measured using Doppler data from the US device (Figure 2.8(d)). Motion velocities of the robot, both with and against the flow, were measured in both the large and narrow pipes under different flow velocities, as depicted in Figure 2.8(e) and (f). Generally, the robot moves slower in the narrow pipe compared to the larger one. Additionally, it is observed that motion velocity along the flow direction increased with the flow velocity rise in the larger pipe, while motion against the flow direction decreased with increasing flow velocity. In the narrow pipe, the moving fluid assisted motion in the flow direction, but had minimal impact on motion speed when moving against the flow.

2.4 Discussion

The experimental results support the predicted undulating wave from simulations. By manipulating the directions of the magnetic field, we observed corresponding changes in the motion of the legs, resulting in undulating fin-waves with variations in magnitude and phase shifts. While the simulation and experimental fin-waves appear similar, it is worth noting that no quantitative comparisons were conducted in this study. The primary purpose of the simulations in this paper was to provide information regarding the leg arrangement required to achieve the desired undulating wave for amphibious locomotion. The optimization of motion efficiency, including aspects like robot body shape and the number of legs, has been explored in other research studies [119], [120], and is not considered this study.

The characterization of amphibious locomotion across various terrains, including solid ground, water surface, underwater, and at the oil-water interface, has been conducted. The actuation threshold for walking on solid ground ranged from 10 mT to 30 mT, while swimming in water required a lower magnetic field strength, starting from 5 mT and going up to 15 mT. The higher threshold for walking is attributed to the robot body

weight, necessitating greater actuation force compared to swimming, where buoyancy offsets gravity. The magnetic fields exceeding 30 mT during walking caused the robot to roll up, while fields higher than 15 mT during swimming on the water surface led to the robot flipping over. Additionally, it is important to note that the efficiency of forward and backward motion varies due to differences in the magnetization profiles of the robot legs, but this discrepancy does not impact the robot amphibious locomotion abilities. The motion velocities presented in Figure 2.5 II are characterized in the same direction of motion for consistency and clarity.

The use of an acetone capsule for adjusting the buoyancy of the robot is a cost-effective approach for the current experiments. However, it is essential to explore biocompatible materials for potential medical applications in the future. One promising candidate is Novec 7000 Engineered Fluid (3M, USA), which has a boiling point at 34°C, enabling phase changes at lower temperatures. In medical scenarios, it is impractical to heat the material by pumping hot water, so alternative methods need to be considered. One possibility is incorporating a phase-changing material mixed with mineral powder, allowing the temperature of the material to be remotely raised via RF heating [125]. Additionally, integrating the buoyancy capsule with the robot body can be considered for miniaturization, enhancing its suitability for clinical applications.

The motion ability of propulsion within pipes with flowing water indicates that the robot has potential to be utilized in blood vessels for clinical applications. The robot developed in this study can perhaps navigate some of the larger blood vessels within the human body, but needs to be miniaturized for more general use. This may be possible by using lithography to make the molds at a smaller scale [126]. If miniaturized, the robot can execute clinical tasks such as drug delivery and biosensing [127], [128]. Further research into navigation in complex conduit networks or a blood vessel phantom is needed. Additionally, closed loop control with tracking of the robot's position and orientation is essential for practical applications.

2.5 Conclusions and Future Work

This study demonstrates the unique amphibious locomotion capabilities and potential applications of a multi-legged small-scale magnetic soft robot inspired by fin-wave movement—a novel feature not previously shown in

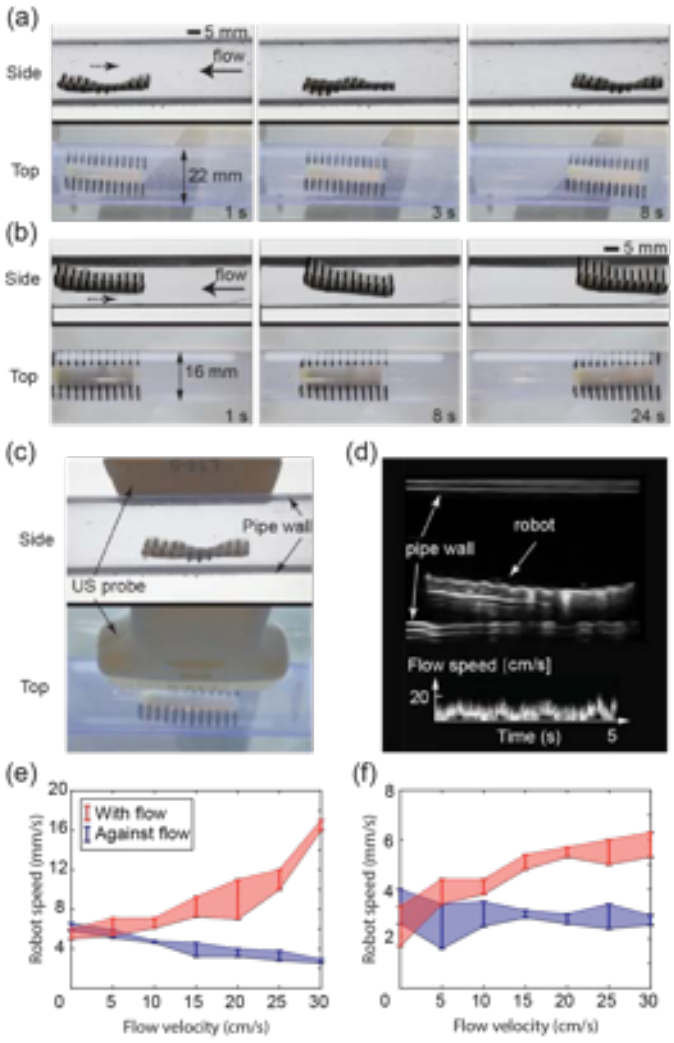

Figure 2.8: Demonstration and characterization of robot motion in pipes with flowing water. (a) The robot moving in a 22 mm and (b) 16 mm diameter pipe. (c) Robot motion is observed via both camera and ultrasound (US) probe. (d) US image when the robot is moving in the big pipe. The flow velocity is visualized and measured using Doppler mode. (e) Robot speed in the 22 mm and (f) 16 mm pipe under different flow velocities. Magnetic field for all the above experiments are 20 mT at a frequency of 10 Hz. The dashed arrows indicate the directions of the robot motion (**please refer to supplementary video**).

magnetic soft robots. The robot exhibits fin-wave locomotion on solid ground, water surface, underwater, and even at oil-water interfaces, showcasing its adaptability across diverse media. The robot is capable of locomotion in different media under a single-mode magnetic actuation, simplifying the control of motion. The design of the robot and arrangement of the magnetic legs are informed by simulation results. Experimental results highlight its abilities, including sinking and floating, landing, maneuvering through narrow channels, and navigating in pipes with flowing liquid. Notably, each individual leg on the robot is a simple rectangular rod, facilitating facile fabrication and offering the possibility of scaling down the overall size of the robot for potential miniaturization in clinical applications.

To facilitate future clinical applications, additional research efforts are essential to enhance the functionality of the robot. Exploring actuation and motion control using a rotating permanent magnet is essential for extending the operational range of the robot and expanding its potential applications. Building upon the current design and our prior research[121], it is feasible to integrate a magnetically-actuated capsule onto the robot, enabling functionalities like drug delivery and biopsy. Furthermore, the robot can serve as a hemostatic bandage by applying a chitosan coating to its body, forming robust bonds with mucosal surfaces, particularly in the gastrointestinal tract. Further miniaturization can be accomplished through technologies such as lithography and 3D printing, enabling the development of small-scale robot designs tailored to specific clinical tasks and applications.

2.6 Supplementary Video

Video: Fin-wave-inspired wireless small-scale soft robot for adaptive amphibious locomotion under single-mode magnetic field

Video link: https://www.youtube.com/watch?v=jrbq5dkS6Yc

3

A Snake-inspired Multi-segmented Magnetic Soft Robot Towards Medical Applications

Note: *This chapter is adapted from the article "A snake-inspired multi-segmented magnetic soft robot towards medical applications" by* ***C. Wang****, V. P. Puranam, V., S. Misra, and V. K. Venkiteswaran, published in "IEEE Robotics and Automation Letters", volume 7, issue no. 2, pages 5795-5802, April 2022.*

Abstract

Magnetically-actuated soft robots have potential for medical application but require further innovation on functionality and biocompatibility. In this study, a multi-segmented snake-inspired soft robot with dissolvable and biocompatible segments is designed. The actuation response under external magnetic field is investigated through simulations and experiments. A dissolve-controllable mixture of gelatin, glycerol and water (GGW) in a mass ratio of 1:5:6 is used to form the structure of the robot. The dissolution of GGW in water and mucus is tested. Magnetic cubes made of silicone rubber mixed with ferromagnetic particles are used to achieve snake-like motion under the influence of a rotating magnetic field. The motion of the robot is tested under different magnitudes and frequencies of the magnetic field. The ability of the robot to navigate obstacles, move over ground and under water as well as on the oil-coated surface, dissolve and release

a drug is demonstrated through experiments. The combination of multi-segmented design and biocompatible and dissolvable materials illustrates the potential of such robots for medical applications.

3.1 Introduction

Soft robots have strong potential for use in medical applications, particularly minimally invasive surgery (MIS), since their shape-programmable soft bodies are more flexible than their rigid counterparts in enclosed and confined spaces [84], [129]. Existing soft robots have been demonstrated to be maneuverable and controllable [130]. However, soft robots intended for MIS are required to be not only flexible, but also functional, bio-compatible and scalable to small sizes.

Multiple soft robots have been developed which were inspired by biological organisms such as caterpillar, worm, fish, and millipede [88], [94], [131], [132]. Within these, snake-inspired soft robots have the capability to navigate narrow spaces due to the style of locomotion [133], [134]. Snake locomotion is generated through the propagation of sinusoidal waves along the backbone of the snake in the ground and vertical planes, which creates lateral undulation and shifting contact points with the ground [135], [136]. By exploiting this motion pattern, it is possible to create small scale soft robots that can carry out functions in enclosed and confined spaces inside the human body such as gastrointestinal (GI) tract [84], [129], [137].

The flexibility and controllability of soft robots have been demonstrated through diverse actuation approaches. Electrical, pneumatic, acoustic, chemical and magnetic are currently the most widely used methods of actuation [130], [138]. In particular, magnetic actuation shows great promise for medical applications such as magnetic catheter ablation and electromagnetic navigation bronchoscopy, owing to its benefits including human-safe operation, wireless actuation and rapid response [139], [140]. Magnetic actuation eliminates the mechanical tether between robot and actuation unit. Untethered soft robots can navigate tortuous paths better than their tethered counterparts. Thus, magnetically-actuated soft robots can be used for MIS, targeted drug delivery and clinical diagnostics [84].

Many bio-inspired soft robots have been investigated within untethered magnetic devices. For instance, Joyee *et al.* analysed the motion mechanisms of the inchworm and designed a soft robot made of magnetic

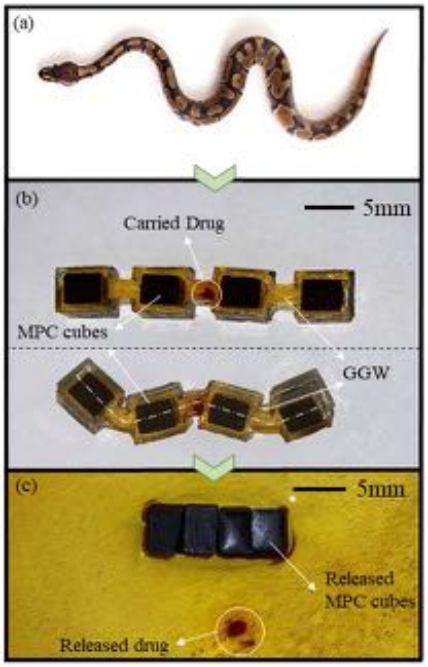

Figure 3.1: (a) An example of biological snake locomotion with "S" shape is shown on the top (©Getty Images, courtesy of Ian Mcdonnell). (b) The soft robot inspired by the snake is shown on the middle, the centerline along each segment forms an "S" shape when the robot moves under an external magnetic field. The robot is made of magnetic polymer composite (MPC) and a biodegradable mixture of gelatin, glycerol and water (GGW). A mock-drug is carried in the middle link of the robot. (c) In warm water (40°C), the GGW dissolves gradually, releasing the mock-drug and staining the water yellow. Once the GGW dissolves, the MPC cubes are attracted to each other and form a magnetic soft bar which can be moved using magnetic fields.

polymer composite (MPC) to mimic its motion [141]. Zheng *et al.* developed an ascidian-inspired soft robot that can crawl tumble, and pick and place objects [142]. Ren *et al.* demonstrated a sheet-shaped robot capable of multi-modal locomotion to adapt to confined spaces [97]. Although these robots demonstrate flexibility, application requirements including the functionality and biocompatibility should be investigated.

Various efforts have been made to endow soft robots with practical functions for use in specific applications. Previously, a helical microrobot with a transport claw for drug delivery actuated using external magnetic

field was proposed [143]. Venkiteswaran *et al.* showed legged robots with grippers, where motion and grasping can be controlled in tandem to grasp and release objects [100]. Additionally, origami-inspired magnetic soft materials such as magnetic responsive soft material (MRSM) film with reprogrammable magnetization patterns have been developed [144]. Moreover, chain-like soft devices have been studied as a promising approach for fabricating functional parts of soft robots with simple magnetic segments and soft links [145]. However, there are risks associated with losing track of the robots during operation and an inability to retrieve the robots after completing tasks when the robots are untethered, which poses problems for clinical applications if the robots are not biocompatible [146].

Biodegradable materials have been used to fabricate soft robots for safe operation inside the human body [147]. The functions of drug delivery and release of biodegradable materials have been demonstrated on microswimmers [148], [149]. There are several choices for biodegradable elastomers based on polyesters or hydrogels [150], [151]. A mixture of gelatin, glycerol and water (GGW) has been verified to be soft and biodissolvable, and the constituent components are commonly available [152].

In this paper, a snake-inspired magnetically-actuated soft robot with biocompatible and dissolvable components is designed, fabricated and tested (Fig. 3.1). The primary contribution of this study is the demonstration of multi-segment locomotion in combination with dissolvability and magnetic actuation, previously unseen in soft robots. The robot is able to move on ground, under water, on oil-coated surface and in a narrow tube. The motivation for this work is the improvement of functionality and biocompatibility for magnetic soft robots aimed at applications in the medical field. Multi-segmented soft robots have the potential to transport multiple components for group operation. Magnetic actuation enables untethered motion of the robot, while the use of biodegradable materials increases potential for medical application.

3.2 Design and Fabrication

In this section, the design of the multi-segmented magnetic soft robot is explained first. Then, the materials used for the robot are described. The dissolvability of the biodegradable mixture is tested. The fabrication process is also described in detail.

Table 3.1: Time for dissolution of biodegradable mixture.

Medium	Temperature	Ratio of Gelation : Glycerol : Water				
		1:1:6	1:3:6	1:5:6	1:7:6	1:9:6
Water	50℃	14.5s	16s	18s	19.5s	22s
	37℃	40s	58s	75s	95s	150s
Mucus	37℃	38s	59s	72s	100s	162s
Dry plate	37℃	96s	155s	>500s	>500s	>500s
	50℃	43s	67s	98s	125s	196s

3.2.1 Design

The design of the multi-segmented magnetic soft robot is shown in Figure 3.2(a). The robot body is made of four magnetic cubes joined through links made from the biodegradable mixture. The magnetic particles interact with an externally-generated magnetic field to produce magnetic torques which are used for motion actuation. The magnetic particles are mixed with silicone rubber which is biocompatible but undissolvable, thereby preventing the magnetic cubes from disintegrating. The biodegradable mixture is flexible, and the intermediate links twist and bend, enabling snake-like motion of the robot.

3.2.2 Materials

Two types of soft materials are used to fabricate the different parts of the robot. For magnetic actuation of the robot, a magnetic polymer composite (MPC) which comprises a silicone rubber matrix (Ecoflex-0010, Smooth-On Inc., USA) and a ferromagnetic powder of praseodymium-iron-boron (PrFeB) with a mean particle size of 5μm (MQFP-16-7-11277, Magnequench GmbH, Germany) is selected. The mass ratio of the magnetic microparticles to the silicone rubber is 1:1 in this study. The MPC has mechanical properties such as relatively low elastic modulus (2 MPa) and high elongation at break (300%), endowing the robot with a soft internal structure. The elastic modulus of MPC used in the simulations is 75 kPa. Detailed mechanical properties as well as the characterization of MPC can be found in our previous work [94].

For the biodegradable part of the robot, a mixture of gelatin, glycerol,

and water (GGW) with a mass ratio of 1:5:6 is used. This makes up the outer cover for the magnetic cubes and the links between the magnetic segments. The procedure of obtaining the biodegradable elastomer of GGW is as follows: gelatin is mixed with cold water first and allowed to bloom for 30 seconds. This is followed by adding glycerol and mixing them until the gelatin is thoroughly dispersed. The mixture is heated to 80°C, and mixing is continued until the gelatin is sufficiently dissolved and the liquid is transparent. This liquid is then used to create the body of the robot.

Changing the ratio of the mixture changes the dissolvability as well as the mechanical properties of GGW. By adding glycerol, the cross-linking property of gelatin is diminished which increases the solubility of the mixture. Based on this, an experiment is carried out to test the dissolvability of the GGW in order to control the dissolution time of the robot for potential use in different applications. Cubes ($5 \times 5 \times 5$mm) with various ratio of GGW are made and immersed in water at different temperature. Aside from the mixture ratio, the dissolution of GGW is also influenced by the environment temperature. An experiment is carried out to test the dissolvability of the GGW on an open hot dry plate. Additionally, in order to simulate environment conditions in digestive system, the GGW cubes are immersed in 3% mucus solutions (mucin from porcine stomach, Sigma-Aldrich, USA) at 37°C. The times for full dissolution of the cubes are listed in Table 3.1. There is no significant difference (max. 8s) between water and mucus with respect to the dissolution time, whereas the dissolution time of GGW on the open hot dry plate is much longer. This may be because the open hot plate did not provide even heating for the GGW cube. However the results still verify that the temperature dominates the dissolution of the GGW when the mixture ratio is constant. For applications which require relatively long time, the highest ratio of glycerol in the mixture can be an option. Also, the motion speed of the robot is adjustable. These can provide sufficient time for the robot to complete simple clinical tasks. Additionally, glycerol is a plasticizer, and therefore, a higher mass ratio of glycerol in the mixture leads to softer cured GGW. The ratio of 1:5:6 is selected for this study. The elastic modulus of GGW used in the simulations is 0.41 MPa [152]–[155].

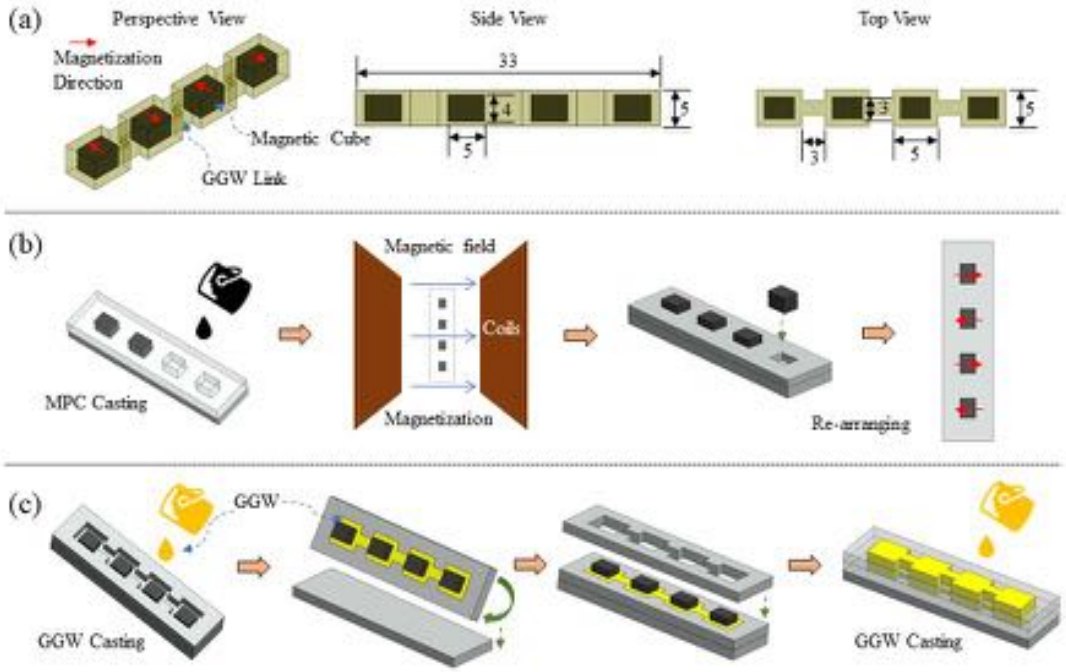

Figure 3.2: Design and fabrication procedure of the soft robot. (a) The robot consists of inner magnetic cubes and outer biodegradable segments. The red arrows depict magnetic dipole directions. Dimensions are in mm and shown in the side and top views. (b) The casting and curing of magnetic polymer composite (MPC) are carried out first. The cubes are magnetized and rearranged in the second mold for casting the mixture of gelatin, glycerol and water (GGW). (c) GGW is then added in two layers to fully encapsulate the magnetic cubes and form the structure of the robot.

3.2.3 Fabrication

The inner cubes are fabricated using MPC as shown in Figure 3.2(b). Molds are created using laser-cut acrylic (Poly-methyl methacrylate) to create the shape of the cubes. The MPC is set to cure at room temperature (24°C) for four hours, and the mixture is degassed before curing. Then the molds with cured MPC inside are subjected to a magnetic field of 1 T using a large electromagnet, to obtain the desired magnetization profile. The magnetized cubes are then transferred to another mold and rearranged with staggered magnetic dipole directions. The GGW is cured around the cubes in two layers, encapsulating one half of the cubes at a time as shown in Figure 3.2(c). The robot is cured in a refrigerator at 8°C. After this two-step process, the GGW encapsulates the cubes fully and also forms the links between them.

3.3 Motion Analysis

In this section, the magnetic actuation and motion of the robot are described. The actuation strategy for straight and turning motion and their dependence on the magnetization directions of the cubes are explained first. Based on a theoretical model, the magnetic moment as well as the deformation of the robot under different directions of the magnetic field are calculated. The postures of the robot under specific directions of magnetic field are shown and compared with the experimental results in next section.

The actuation magnetic field is generated using a set of electromagnetic coils. It can be assumed that the contribution of the magnetic field gradient is negligible. Therefore, the actuation of the robot is achieved by using the magnetic torque ($\mathbf{T} \in \mathbb{R}^3$) as given by

$$\mathbf{T} = \mu \times \mathbf{B} \ ,$$

where $\mu \in \mathbb{R}^3$ is the magnetic dipole moment, $\mathbf{B} \in \mathbb{R}^3$ is the magnetic field.

To actuate the robot, a magnetic field is provided in the YZ plane rotating about X axis as shown in Figure 3.3(a). The magnetic dipoles of the magnetized cubes tend to align with the direction of the magnetic field. Due to the opposite directions of the magnetic dipoles on adjacent cubes, the torques acting on the cubes tends to bend and twist the intermediate

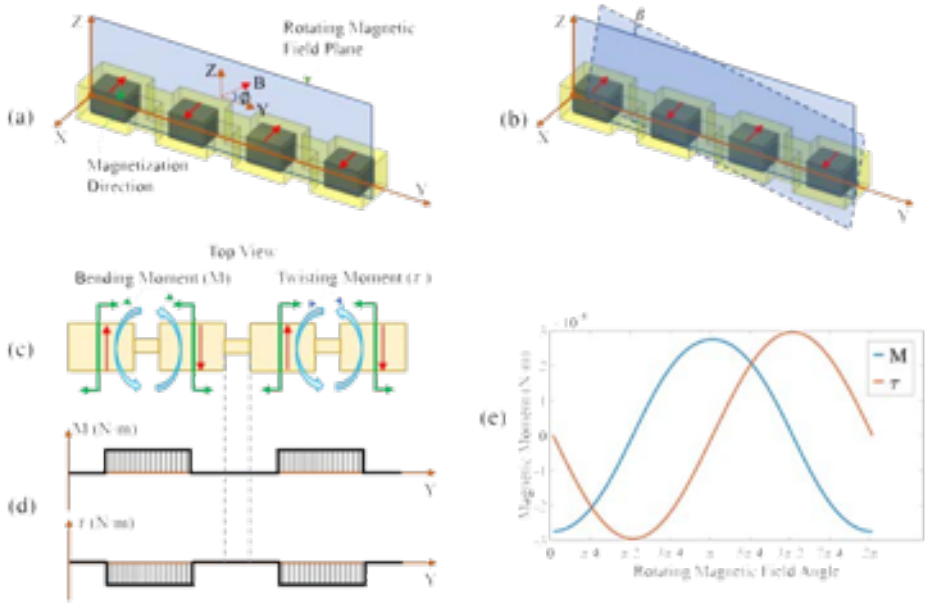

Figure 3.3: Description of actuation methods and force analysis for the robot. (a) The robot moves forward as the magnetic field (B) rotates in the YZ-plane about the X-axis in the range $\phi \in [0°, 360°]$. (b) To steer the robot by turning left and right, the plane of rotating field is titled by the angle (β) to the YZ plane. (c) Two couples of bending and twisting moments act on the segments respectively. (d) The diagrams of bending and twisting show that the middle link is unstressed. (e) The phase difference between bending and twisting enable the robot to move.

GGW links. This leads to the lift of one edge of a cube and anchoring of the opposite edge resulting in an "S" shape of the robot body in both the horizontal and vertical planes. At different orientations of the external magnetic field, the bending and twisting of the GGW links changes. The reaction force between the cube and the plate surface pushes the robot forward as the magnetic field rotates from 0° to 360° around the X-axis.

The steering of the robot is achieved using the following approach. Changing the tilt angle β between the plane of rotation of the magnetic field and YZ plane (shown in Figure 3.3(b)), changes the axis of the magnetic torque. If β is changed in small increments, the robot tends to align with the plane of rotation of the magnetic field. The direction of turning (left

or right) can be altered by reversing the direction of β.

In order to analyze the mechanism of motion, each link of the robot is modeled as a cantilever beam, and the cubes are considered rigid (shown in Figure 3.3(c)). Based on theoretical analysis under quasi-static condition, there are two couples of bending and twisting moment acting on the four cubes of the robot. The bending and twisting moment diagrams are shown in Figure 3.3(d). As shown in Figure 3.3(e), there is a phase difference (90°) between bending moment and twisting moment.

Assuming small linear deflections of the links, the bending angle (θ_b) and twisting angle (θ_t) for each segment are respectively calculated as:

$$\theta_b = \frac{Tl}{EI_b}\cos\phi \qquad \theta_t = \frac{Tl}{GI_t}\sin\phi,$$

where l is the length of the GGW link between the segments, ϕ is the magnetic field angle, E is elastic modulus of the link, G is the shear modulus, I_b is the area moment of inertia, and I_t is polar moment of inertia of cross section.

Considering the robot as a rigid body, the deformation of the robot can be calculated by the following kinematics equations:

$$\mathbf{P}_1 = \begin{bmatrix} \cos\theta_b & -\sin\theta_b & 0 \\ \sin\theta_b & \cos\theta_b & 0 \\ 0 & 0 & 1 \end{bmatrix} \begin{bmatrix} 1 & 0 & 0 \\ 0 & \cos\theta_t & -\sin\theta_t \\ 0 & \sin\theta_t & \cos\theta_t \end{bmatrix} \mathbf{P}_0,$$

where $\mathbf{P}_0$ represents the initial position of any selected point on the robot, $\mathbf{P}_1$ represents the new position of $\mathbf{P}_0$ after deformation. Based on the above equations, the simulations are carried out to describe the motion pattern of the robot using Matlab (2021a, Mathworks, USA). The vertices of each segment and link are selected and used to draw out the contour of the robot. The friction between the robot and surface and the gravity of the robot are neglected in the simulation. A comparison of the theoretical predictions versus experimental results for the postures of the robot under different directions of the magnetic field is shown in Figure 3.5.

3.4 Experiments and Results

In this section, the experiments for demonstrating the motion and function of the robot are described, the results are used for verifying the simulation

results as well. First, the experimental setup is introduced, followed by an experiment that shows the robot posture under changing orientation of the magnetic field. The motion speed under different cycle duration (frequency) and magnitudes of the magnetic field are tested. Experiments are carried out to demonstrate the maneuverability of the robot and the capability of moving on the low-friction oil-coated surface. In the final experiment, a robot carrying a mock-drug is controlled to move through a narrow opening, slither into a reservoir of water, dissolve and release the drug.

3.4.1 Experimental Setup

A setup consisting of six electromagnetic coils in a Helmholtz configuration with 12 × 12 × 12 cm workspace is used for magnetic actuation (see Figure 3.4(a)). The setup can generate a uniform magnetic field up to 50 mT in any given direction. The surface of the setup for testing is 3D-printed Polylactic acid (PLA). A 3D printed box of 10 × 8 × 4 cm with obstacles and a water reservoir is used as the testbed for testing functionalities of the robot. Two cameras are used for observing and recording the top and side views of the experiments.

3.4.2 Robot Locomotion

The postures of the robot from both top view and side view under different directions of the magnetic field are shown in Figure 3.5 (**see supplementary video**). Simulation results based on the analysis in Sec. 3.3 are shown in perspective view beside the experimental results. It is observed that pure bending occurs at 0° and 180°, pure twisting occurs at 90° and 270° respectively. In pure bending, the entire bottom face of the robot makes contact with the ground. In pure twisting and rest of the orientations, only one side edge of the first and last segment contacts with the ground. The two middle segments are always in face-to-face contact with the ground, serving to anchor the robot during motion.

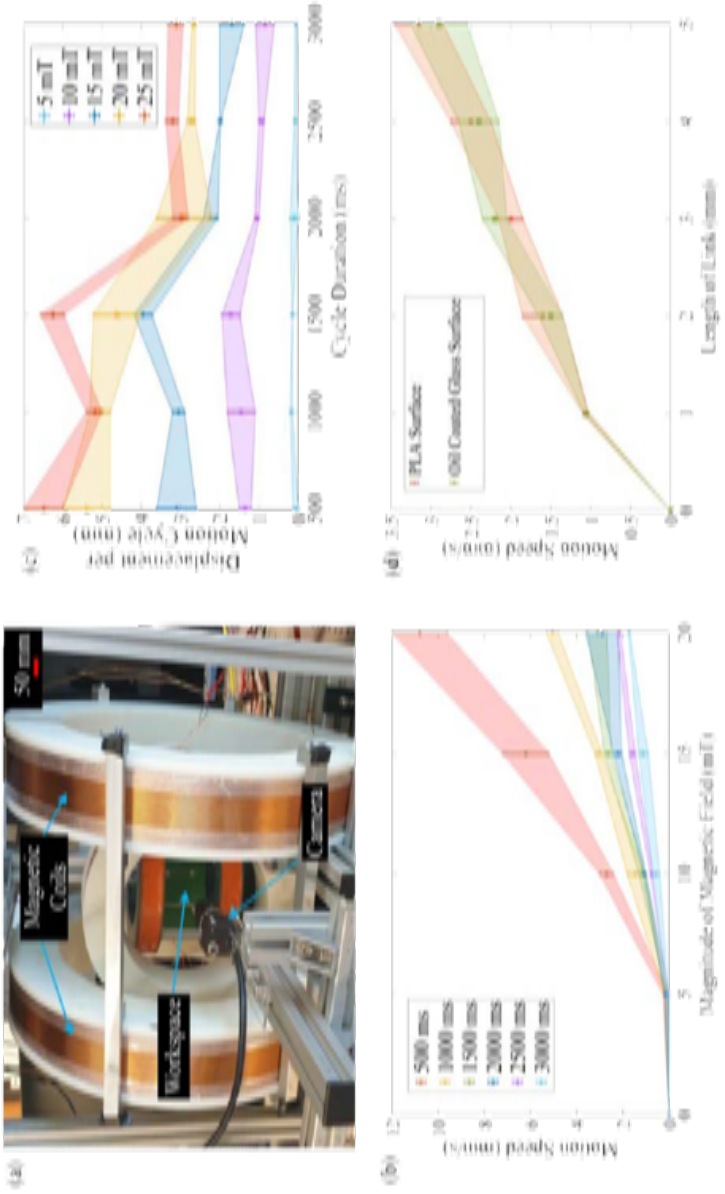

Figure 3.4: (a) The setup for magnetic actuation. (b) Motion speed of the robot under different magnitudes and cycle duration of the magnetic field. (c) Displacement per actuation cycle under different cycle duration.(d) Motion speed of the robot with different link lengths at 15mT magnitude and 1500ms cycle duration of magnetic field.

The motion speed on PLA surface is tested and the results are shown in Figure 3.4(b). The speed is influenced by both the time period of the actuation cycle and the strength of the magnetic field. Therefore, five groups of magnitude and six groups of cycle duration of the magnetic field are tested by controlling the variables. It is observed from the results that with a shorter cycle, the robot moves faster, and the robot moves slower when using a lower strength of magnetic field. The effect of actuation frequency on motion efficiency is tested by observing the relationship between cycle duration and displacement per motion cycle, shown in Figure 3.4(c). In order to observe the influence of the link size on the robot locomotion, five robots with different link length (1-5 mm) and three robots with different link width (1-3 mm) are fabricated. The motion speed of each size of robot is tested under 15mT and 1500ms cycle duration. It is observed that robot motion speed increases with link length. The robot with low width (1mm) on the link can be actuated under 5mT, while the robot with wider link (3mm) can be actuated under up to 50mT. The robot with wider link is more stable at higher fields, whereas the thin link leads to robot rolling over. Moreover, the robot motion on the oil coated surface (1mm thickness) coated surface is tested (**see supplementary video**). It can be seen from the results (Figure 3.4(d)) that low-friction surface has little influence on robot locomotion. To study the repeatability, three identical robots are tested, and the mean error across the specimens is shown in the graphs.

3.4.3 Maneuverability

The robot can be controlled by changing the tilt angle β. An experiment is carried out to demonstrate the maneuverability of the robot (**see supplementary video**). A tube with 9mm inner diameter and 12mm outer diameter is prepared to mimic narrow spaces inside the body such as the small intestine. As shown in Figure 3.6, the robot is controlled to turn by 90° and climb into the tube, and maneuver through the tube with bend of 90°.

3.4.4 Robot Functions

The functions of the robot demonstrated here are carrying a mock-drug, being steered to a target location in the workspace and drug release through dissolution (Figure 3.7). The maneuverability of the robot is demonstrated

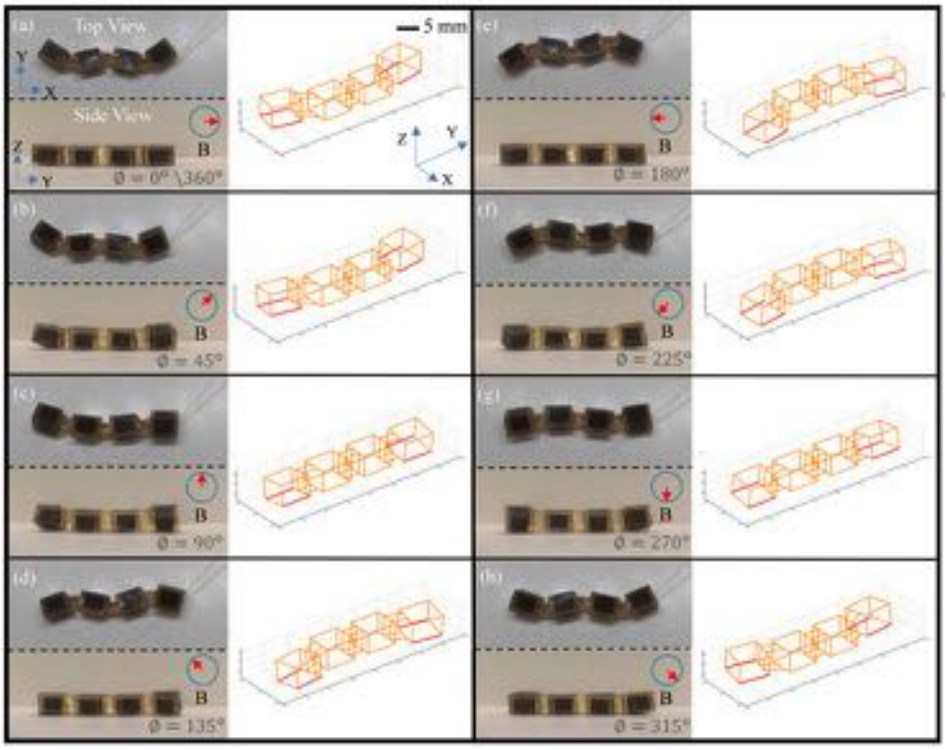

Figure 3.5: Experimental and simulation results of postures of the robot under specific directions of magnetic field. Experimental results are shown in both top view and side view on the left; simulation result is shown in perspective view on the right. The magnitude of magnetic field is 15 mT. The orientation of the magnetic field is described using the angle ϕ (**see supplementary video**).

by steering the robot to correct its heading and move through an obstacle (hole in the middle wall). After moving through the hole, the robot crawls down the slope into the reservoir of water. On the horizontal surface, a magnetic field of 10 mT is used, whereas on the slope a higher field of 15 mT is used.

In order to demonstrate the function of drug release, a small quantity of a mock-drug (Sudan Orange color dye, Merck, Germany) is integrated into the middle link. For higher contrast with the background, the robot is dyed orange by adding a small quantity of the dye to the GGW mixture. After the robot is steered through the obstacle, dissolution of the GGW outer links is achieved in warm water (40°C). The robot is controlled to

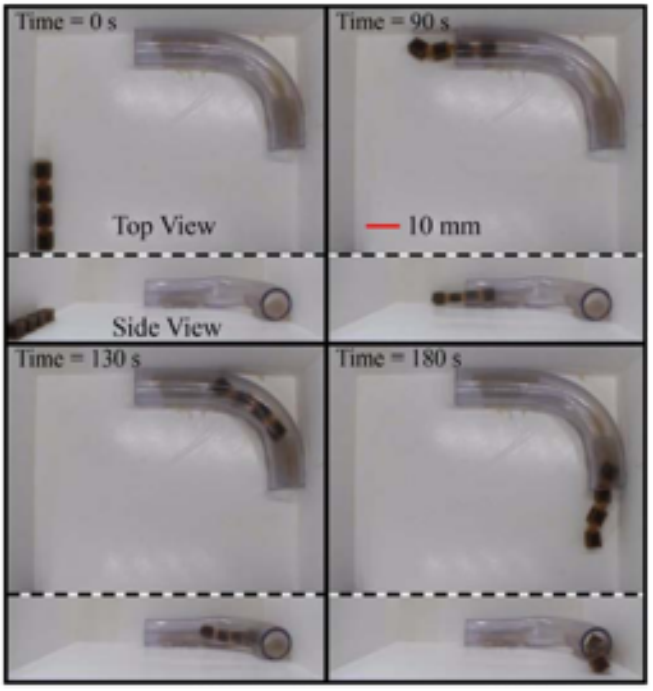

Figure 3.6: Maneuverability test: the robot is steered to change orientation, climb into a tube of 9mm inner diameter, maneuver through a 90° bend, and move out from the tube (**see supplementary video**).

continuously rotate in the water in order to speed up the dissolution. The mock drug is released when the middle GGW link is dissolved, staining the water with the dye. After complete dissolution of the GGW, the four magnetic cubes attract each other and form a rectangular bar. Finally, the bar-shaped cube group is guided to one side of the workspace (**See supplementary video**).

3.5 Discussion

The experimental results support the predicted motion from simulations. By varying the magnitude and frequency of the external rotating magnetic field, the velocity of the multi-segment soft robot can be controlled. While the postures from the simulation and experiment appear similar, no quantitative comparisons are made in this study due to challenges in extracting

3D pose information from experiment videos. Figure 3.4(b) shows increase in locomotion speed with the increase in magnetic field, which is expected since the magnetic torques increase, causing greater bending and twisting of the links. This holds up to 20 mT, above which the robot flips over due to high magnetic torque. From Figure 3.4(c), it appears that the motion is more efficient at intermediate cycle durations, which may be due to a combination of factors affecting the dynamics of robot motion such as inertia and friction. Additionally, the motion velocity is related not only to the magnitude and frequency of the magnetic field but also the magnetization of the MPC cubes. Nevertheless, these aspects are not investigated in this study which aims to illustrate the robot motion as a proof-of-concept and demonstrate its functionality and biocompatibility.

It should be noted that slight deformation in the middle link is observed in the experimental results, while simulations predict no deformation. This could due to fabrication errors leading to imbalance of torques along the robot body (and subsequently displacement), and also by the friction between the robot and the ground, which is ignored in the simulation. However, the deformation of the middle link is sufficiently small that it can be used as a stable location for other functions, such as carrying camera or other tools.

For the drug delivery function demonstrated in this paper, the mock drug is only carried in the middle link. In fact, the volume of drug (or other reagents) carried by the robot can be increased by mixing them into the all the GGW parts. Thus the multi-segmented robot can carry a relatively large volume of drug (520mm^3), compared to the single cube (90mm^3).

For medical application in the future, further studies are required to enhance the biocompatibility of the robot. The composition of the PrFeB microparticles and the silicone rubber makes the current robot only partially biocompatible. There are several options that can make the robot fully biocompatible. First, ferromagnetic FePt nanoparticles have been shown to be noncytotoxic and biocompatible [156], which could be a replacement of the PrFeB used in this work. Second, coating with a layer of biocompatible materials can also make the magnetic particles or robots fully biocompatible. Additionally, the robot can be removed from the body after operation [88], [157], [158].

The robot can be miniaturized with the current fabrication methods (**see supplementary video**). The link of the miniaturized robot is made

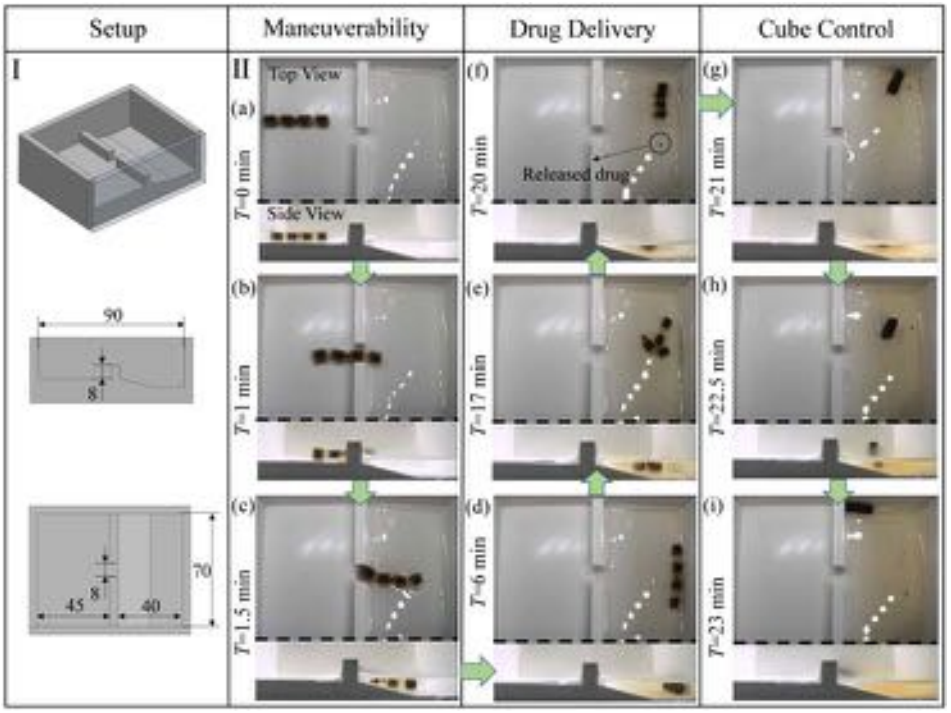

Figure 3.7: Experiment to demonstrate robot drug delivery function I. Workspace for the experiment. Perspective, top and side view are shown. Dimensions are in mm. The angle of the slope is 30°. II. Experimental results. The maneuverability of the robot is demonstrated by steering through a hole in the wall (a, b, c). The robot enters the water, and rotates until the GGW links dissolve, releasing the mock-drug (d, e, f). After dissolution, the magnetic cubes are moved to one side of the workspace. T represents the experiment time (**see supplementary video**).

of silicon rubber, which connects the MPC cubes without an outer biodegradable layer. For further miniaturization, new biodegradable materials which suits micro- or milli- scale fabrication should be considered. Additionally, other technologies such as 3D printing and lithography can help to realize small-scale robot design.

3.6 Conclusions

In this paper, the locomotion and drug delivery function of a multi-segmented magnetic soft robot are demonstrated. The snake-like locomotion of the

robot (previously not seen in magnetic soft robots) works on solid ground, in a narrow tube, on an oil-coated surface and also underwater. The drug delivery function is achieved by utilizing the GGW which is biodegradable. Although the MPC currently shows no toxicity, it can be made fully biocompatible. The mechanism of motion is analyzed through simulation and experiments. It has potential for optimization based on application requirements. Meanwhile, the dissolvability of the biodegradable GGW mixture in water suggests suitability for medical use. The combination of the snake-like locomotion and dissolvable materials endows the robot with the ability to transport multiple magnetic components and other payloads. Also, it is possible to control the magnetic components after dissolution, which is significant for robot retrieval.

This design has potential for further advancement, such as multi-modal locomotion of the robot including swimming in fluids. For use in the stomach or gastrointestinal tract, the stability of the locomotion should be investigated, since organs inside the body have uneven surfaces and are covered by body fluids such as mucus which provide lubrication. For further medical applications, miniaturization can be investigated. Also, sensor integration for tracking the robot inside the human body would be beneficial. The stable middle link of the robot provides a potential location for additional functions.

3.7 Supplementary Video

Video: A Snake-Inspired Multi-Segmented Magnetic Soft Robot towards Medical Applications

Video link: https://www.youtube.com/watch?v=OTTE9dzTnb8

4

Biocompatible Film-coating of Magnetic Soft Robots for Mucoadhesive Locomotion

Note: *This chapter is adapted from the article "Biocompatible film-coating of magnetic soft robots for mucoadhesive locomotion" by* ***C. Wang****, A. Mzyk, R. Schirhagl, S. Misra, and V. K. Venkiteswaran, published in "Advanced Materials Technologies", volume 8, issue no. 12, 2201813, June 2023.*

Abstract

Magnetically-actuated soft robots for medical applications are required to be functional, biocompatible as well as capable of robust motion inside organs within the human body in a myriad of environmental conditions. In this paper, a ring-shaped magnetic soft robot, with a flexible biopolymeric film coating, capable of motion on mucus-coated surfaces is designed and investigated. The biopolymeric film made from Chitosan-Glycerol (C-G) solution endows the robot with robust locomotion capabilities on surfaces of diverse geometrical shapes and orientations. By utilizing mucoadhesive locomotion, the robot has the potential to carry out clinical procedures on enclosed mucus-coated tissue surfaces. Three robot functions including pick-and-place, cargo transportation, and liquid capsule release are demonstrated on different surfaces to show the maneuverability, functionality, and potential of implementing clinical procedures through mucoadhesion.

Additionally, the C-G film-coated robot is tested to be biocompatible for a human colorectal adenocarcinoma cell line with epithelial morphology (HT29). The C-G film reduces the negative effects (superoxide generation) of ferromagnetic particles (FMP) released from the magnetic polymer composite (MPC). The mucoadhesion and mechanical properties of the C-G film are characterized through experiments. The results show that the mucoadhesion increases with the increase of contact times and/or preload forces. The softness of the C-G film can be adjusted by controlling the concentration of glycerol. The ring-shaped design and magnetization profile decouple the locomotion and functions of the robot. The C-G film-coated ring-shaped soft robot is demonstrated to be capable of stable mucoadhesion, perform clinically-applicable functions, and is biocompatible.

4.1 Introduction

Untethered small-scale soft robots have been recently demonstrated to have potential to carry out patient-oriented clinical treatments, such as targeted drug delivery and minimally invasive surgery which provide better prognosis for the patients [159]–[162]. Owing to the advantages of fast response and wireless actuation, magnetic actuation has gained popularity among other actuation methods for small-scale soft robots with respect to medical applications [163], [164]. Existing magnetic soft robots are capable of swimming, crawling, rolling and/or jumping motion patterns [159], [165]–[167]. Recent research has focused on improving robot capability through several aspects including multi-functionality, miniaturization, shape-programmability, multimodal locomotion, sensor integration and biocompatibility [168]–[177].

One of the key requirements for the translation of soft robot technologies into the clinic is for the robots to be robustly controlled inside the human body. This necessitates the robots to move reliably on the surfaces of internal organs (which may be inclined, vertical, or inverted surfaces in confined spaces), working against their own gravity, buoyancy, and friction. Several approaches for improving adhesion have been investigated targeting the abovementioned requirements. Inspired by organisms in nature, special structures and materials have been investigated and verified to have the capability of improving adhesion force on dry or wet condition surfaces [178]–[180]. For instance, directional mushroom-tipped micro

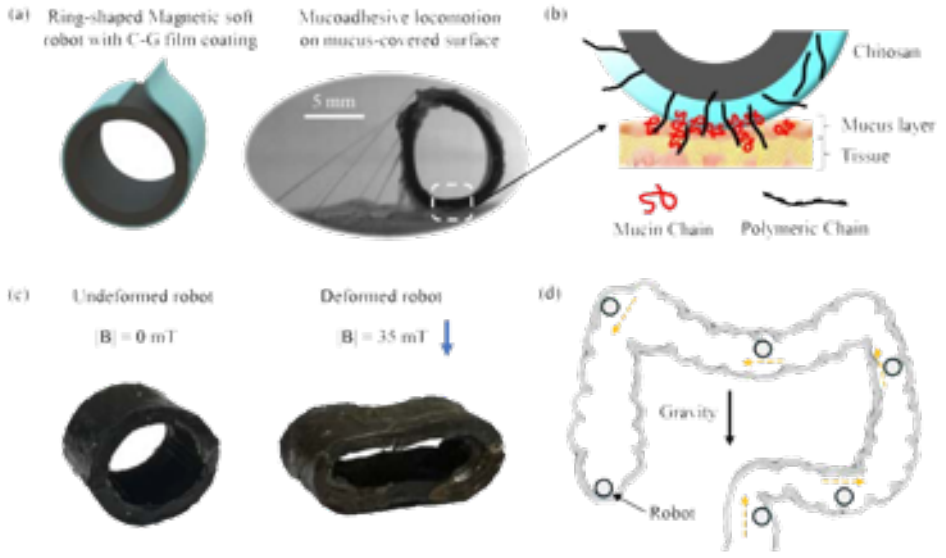

Figure 4.1: (a) Left: 3D model of the ring-shaped magnetic soft robot coated with chitosan-glycerol (C-G) film. Right: video snapshot of the robot rolling on a mucus-coated surface. (b) Illustration of polymeric chain in chitosan bonding with mucin chain in mucus. (c) The robot locomotion and compression are decoupled by using different magnitudes of the magnetic field. Left: robot maintains its circular shape without magnetic field. Right: the robot is compressed under 35 mT magnetic field. (d) Concept of mucoadhesive locomotion of the robot in an enclosed 3D surface (e.g. colon).

fibers inspired by gecko toes have been verified to have strong adhesion and friction on smooth and dry surface [181]. A spider-silk-inspired composite has been reported to have reliable adhesion on wet and cold substrates from 4 to -196°C [182]. In order to achieve controllable adhesion and detachment for soft robots, an octopus-inspired hydrogel adhesive has been proposed to enhance the stability of robots operation on *in vitro* biological tissues [183]. Additionally, forces generated by magnetic field gradients have been used to produce tethering forces for adhering soft robots [184].

The surfaces of many animal/human organs such as oral cavity, gastrointestinal tract and stomach are covered with mucus, where it is intended to provide lubrication and protection for epithelial cells of organ surfaces [185]. Mucus consists primarily of water (95%) making it a highly hydrated system. The remaining 5% is made up of mucin glycoproteins,

lipids and inorganic salts [186]. Mucin glycoproteins are the most important structural component of the mucus, resulting in its characteristic gel-like consistency, as well as cohesive and adhesive properties. The thickness and concentration of the mucus layer varies on different mucosal surfaces, from 50 μm to 450 μm and 3% to 5% in the stomach, to less than 1 μm and 1% in the oral cavity, respectively [187]. Due to its lubricating properties, mucus forms a slippery surface which can be difficult for small-scale soft robots to travel over.

Film coating on the robot surface can ameliorate interaction properties between the robot and mucus. Chitosan is a widely used polymer because it is able to establish various types of mucus interactions with hydrogen bonds and electrostatic interactions to promote adhesion [188]. This is attributed to the interaction of chitosan with sialic acid which is an anionic component present in the mucin. Chitosan presents characteristics including biocompatibility, biodegradability and low toxicity and is a versatile biomaterial used in textile, food industry and medical products. Chitosan has been widely used in drug delivery systems for long-term adhesion on the targeted tissue [189], [190]. Recent work has demonstrated the use of chitosan on a soft robot to provide adhesion to tissue surfaces, with the robot able to carry up to 20 times its own weight. The chitosan is applied to the ends of the robot in combination with microfabricated structures which allows for inchworm-like locomotion [191].

In this paper, the use of a flexible mucoadhesive film-coating on a small-scale soft robot that is actuated by magnetic fields is investigated (shown in Figure 4.1). The motivation of this work is to improve the capability and robustness of robot locomotion on mucus surfaces and demonstrate potential for mucoadhesion-based medical functions. The use of the C-G soft film coating addresses the challenge of efficient and controllable motion of soft robots while maintaining robust adhesion to mucus-coated surfaces. Compared to previous work, we extend the use of chitosan, using it in combination with glycerol to develop a composite film coating that is flexible and easily applied on soft robot bodies. The locomotion and maneuverability of the robot on surfaces at random tilt angles and of different shape profiles are demonstrated. The robot can also be compressed under an applied magnetic field, and the squeezing action is decoupled from its locomotion. Thus, the robot is also capable of pick-and-place tasks as well as transporting cargo and squeezing a liquid capsule, all under magnetic actu-

ation. The influence of C-G film on the mechanical properties of the robot is evaluated. The mucoadhesive properties of C-G film are characterized through adhesion tests and shear force tests. Additionally, the biocompatibility of C-G film, silicone rubber, magnetic polymer composite (MPC), ferromagnetic particles (FMP) and the C-G film-coated MPC is evaluated based on cell morphology, metabolic activity (MTT assay) and the level of intracellular oxidative stress (T1 relaxometry, DHE assay and DAF-FM assay). The primary contribution of this study is the demonstration of mucoadhesive locomotion in combination with functionality, biocompatibility, and magnetic actuation. Moreover, the development of the soft C-G composite film presented in this paper demonstrates a way to coat the entire external surface of the robot with a biopolymeric film, which may be extended to other soft robots.

4.2 Results and Discussion

4.2.1 Robot Design and Fabrication

The robot is designed for rolling and flipping locomotion under a rotating magnetic field. The robot can also be compressed by increasing the magnitude of the magnetic field in the direction of the initial magnetization. Due to its ring-shaped design and magnetization profile, the locomotion and compression can be decoupled (Figure 4.S1(a) and (b)). Through this decoupling, the robot can be navigated to targeted locations, and the compression (and release) can be used for functional tasks (e.g. controlled release of drugs). The design and dimensions of the ring robot are shown in Figure 4.2(a). The inner ring is made of magnetic polymer composite (MPC) which is responsive to the actuating magnetic field. The directions of magnetic dipoles in the robot body are shown with red arrows. The magnetic dipoles in the robot body are all in the same direction when the robot is compressed to a flat shape. This is achieved by magnetizing the robot in its compressed state.

To achieve mucoadhesive locomotion, the outer surface of the ring is coated in a layer of biopolymeric (Chitosan-Glycerol) film with mucoadhesive properties. The film is soft, smooth, and biocompatible (see Section 2.5 and 2.7). The thickness of the film varies from 100 μm to 500 μm, depending on the concentrations of the glycerol and the volume of the so-

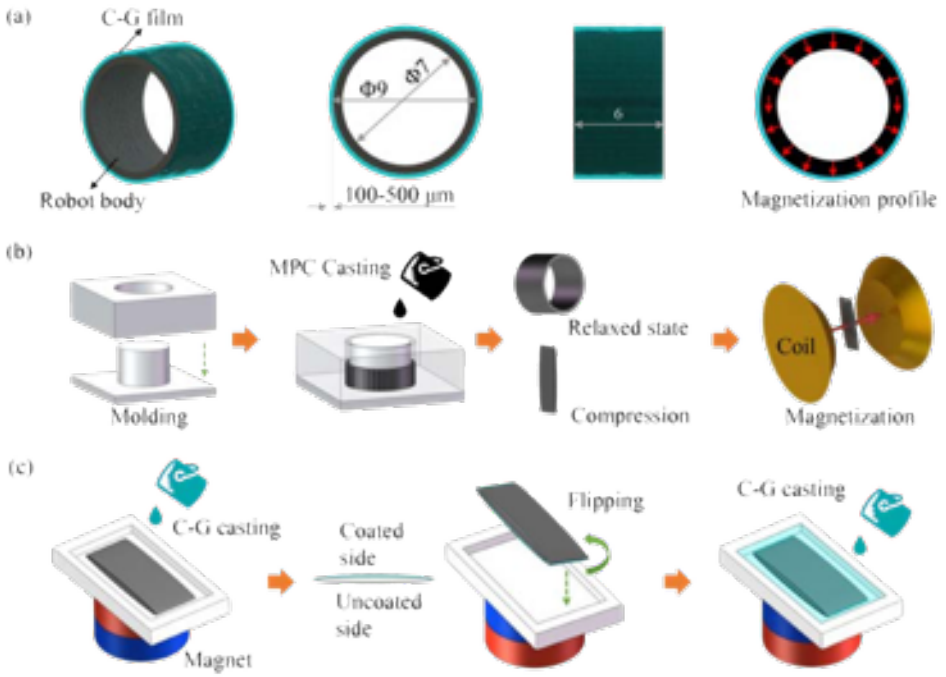

Figure 4.2: (a) Design and dimensions of the magnetic soft ring robot (black inner-ring) with chitosan-glycerol (C-G) coating (blue outer-ring). The magnetic dipoles in the robot are represented by the red arrows. Units not specified in this figure are mm. (b) Fabrication and magnetization procedure of the robot. The casting and curing of magnetic polymer composite in the shape of a ring (MPC) are carried out first. The ring is then compressed in a fixture and magnetized between a pair of electromagnetic coils. (c) The C-G solution is coated onto the robot in two steps to cover the entire outer surface.

lution before the formation of film. The polymeric chain in chitosan forms hydrogen bonds with the mucin chain in mucus (shown in Figure 4.1(b)), which provides adhesion force for the robot.

The robot body (inner ring) is fabricated using MPC as shown in Figure 4.2(b). Molds are created using laser-cut acrylic (Poly-methyl methacrylate) to create the shape of the robot ring. Then, the robot is taken out from the mold and compressed into a flat shape using a fixture. The compressed robot is subjected to a magnetic field of 2 T using an electromagnet to align the magnetic dipoles as shown in Figure 4.2(b). The magnetized ring is then transferred to another mold and kept flattened using an exter-

nal magnet. The chitosan-glycerol solution is slowly poured into the mold such that it covers the top surface of the robot. After the C-G solution cures, the process is repeated on the other side of the robot as shown in Figure 4.2(c). At the end of the fabrication process, the outer surface of the ring of the robot is fully coated with C-G film.

4.2.2 Robot Locomotion

To evaluate the mucoadhesive locomotion of C-G film coated robot, a series of setups with different terrains is designed and coated with mucus. A control experiment is carried out to show the capability and advantage of the coated robot compared to its uncoated counterpart when climbing a quarter circle slope against gravity (**Movie, Supporting Information**). As shown in Figure 4.3(a), the robot without coating slips and falls down half way up the slope, while the robot with C-G coating moves stably up to the top of the slope. Figure 4.3(b) and Figure 4.3(c) show the robot's ability to move on vertical and inverted horizontal surfaces, respectively. As a notable additional observation (Figure 4.3(a)), the coated robot takes less time than the uncoated one for the same displacement. To explore whether the C-G film coating increases the motion efficiency of the robot further, the displacement per motion cycle of uncoated and coated robot on surfaces with different tilt angles are measured under different cycle durations. Figure 4.3(e) and Figure 4.3(f) show the results of uncoated and coated robot, respectively. It can be observed that there is almost no motion on inclines at large angles for the uncoated robot, while the displacements per motion cycle of coated robot on all angles almost equal the no-slip displacement. The no-slip displacement is calculated theoretically according to the outer diameter of the robot. Additionally, motion speed of the coated robot on a horizontal surface under different magnitudes of magnetic field and different motion cycles are measured. The results shown in Figure 4.3(d) illustrate that the magnitudes of the magnetic field do not influence the motion speed of the robot under a certain rotation frequency. The above results indicate that the C-G film on the robot improves the motion efficiency on mucus-coated surface, and improves the capability of moving on surfaces irrespective of their inclinations from the direction of gravity.

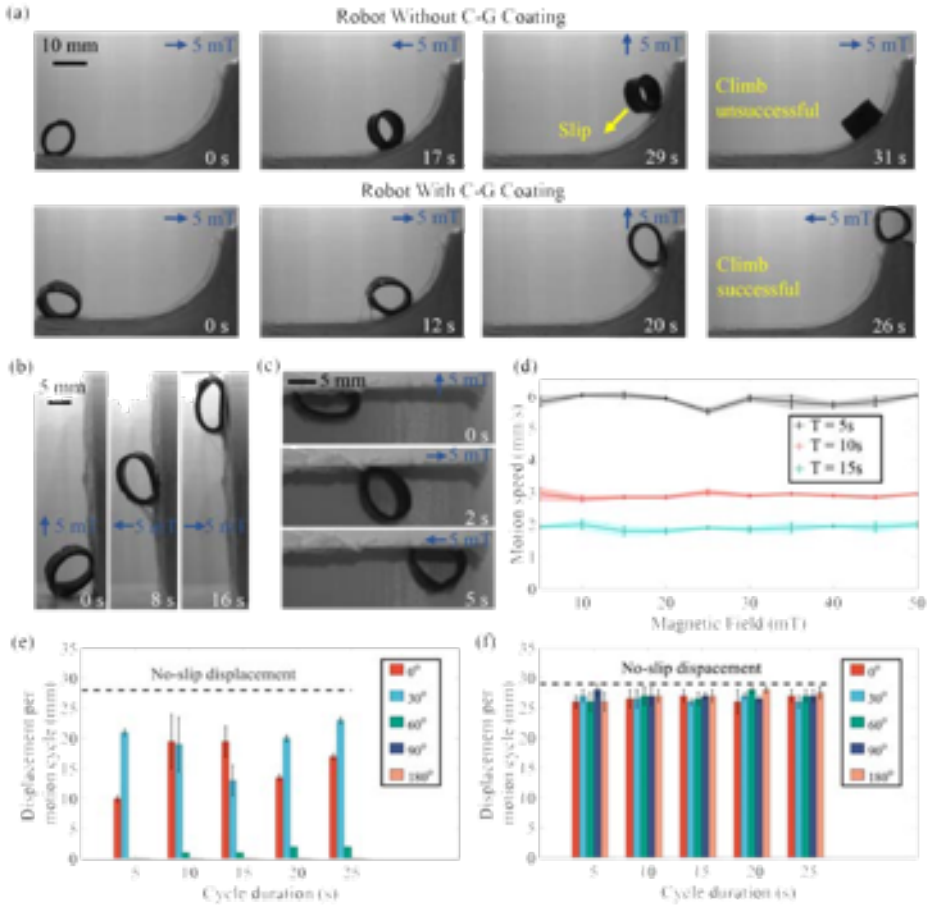

Figure 4.3: (a) Rolling locomotion is achieved by applying a 5 mT rotating magnetic field. The robot without C-G coating is unable to complete the climb up the slope, while the robot with CG coating completes the climb successfully. (b) The robot with C-G coating climbs a vertical (90°) surface. (c) The robot with C-G coating rolling on an inverted (180°) surface. (d) Robot motion speed under different magnitudes of rotating magnetic field with 5s, 10s, and 15s cycle duration on horizontal (0°) surface. (e) Displacement per motion cycle of the uncoated robot rolling on 0°, 30°, 60°, 90°, 180° surfaces. (f) Displacement per motion cycle of the coated robot rolling on 0°, 30°, 60°, 90°, 180° surfaces. The blue arrows represent the directions of the magnetic field. All motion experiments are performed on mucus-coated surfaces.

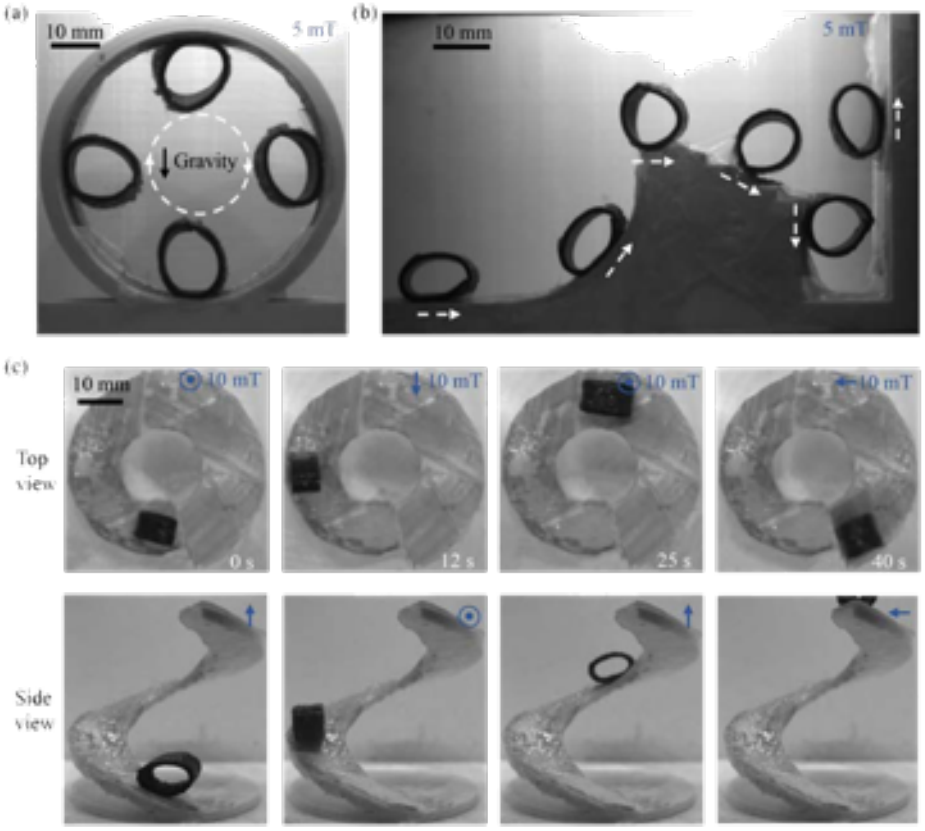

Figure 4.4: (a) Robot rolling on the inner surface of a full circle. (b) Robot rolling up a quarter circle slope, down steps, and climbing a vertical wall. (c) Robot moving on a spiral upward slope path. The blue arrows represent the directions of the magnetic field.

4.2.3 Robot Maneuverability

The robot has the ability to move on mucus-coated surfaces with different 3D shapes (Movie, Supporting Information). Figure 4.4(a) demonstrates the robot rolling in a full circle on the inner surface of a circle, against gravity, under a rotating magnetic field. The magnitude and cycle duration of the rotating magnetic filed are 5 mT and 10 s, respectively. The inner diameter of the setup is 35 mm which is around 4 times the robot outer diameter. Figure 4.4(b) shows that the robot rolls up a quarter circle slope,

an obstacle (2 mm in height), down steps (2 mm in height and 3 mm in width per step, the final step is 15 mm in height) and climbs a vertical wall in succession without slipping and falling. The magnitude and cycle duration of the rotating magnetic filed are 10 mT and 10 s, respectively. Also, the robot has the maneuverability to turn. By changing the tilt angle of the rotating magnetic field plane, the rolling directions of the robot can be changed (shown in Figure 4.S1(e)). To demonstrate the steering maneuverability, the robot is controlled to roll on an upward spiral path as shown in Figure 4.4(c). The path has an inner diameter of 20 mm and 15 mm width from the top view, and 60 mm height from the side view. The magnitude and cycle duration of the rotating magnetic filed are 5 mT and 5 s, respectively.

4.2.4 Robot Functions

Using the mucoadhesive locomotion, the robot has the ability to reach target locations and implement special functions that are difficult for the robot without coating (**Movie, Supporting Information**). In this paper, three functions, namely pick-and-place, cargo transportation, and liquid capsule release are demonstrated. The function of pick-and-place is demonstrated in the following experiment shown in Figure 4.5(a). The robot is first steered to a location where an object is present. The object is a 3D printed blue colored block (3×3×3 mm) made of PLA. The object location is 30 mm higher than the robot's original location. The robot is controlled to climb over the wall and steered to a location beside the object. Then, the robot is controlled to flip over and encircle the object by rotating the actuation magnetic field. By increasing the magnitude of the magnetic field, the robot is compressed to grasp the object. After being flipped back, the robot is navigated to roll to a target location through a downward step. Finally, the object is placed at the target location by decreasing the magnetic field to restore the robot original shape and flipping the robot.

The robot is also capable of moving through tubular structures and carrying and depositing soft cargo. This is demonstrated in a setup in the shape of an undulating tube with size similar to small intestine. The tube is 3D printed with an inner diameter of 15mm, and covered with a layer of mucus. The robot is actuated to move up the ascending part of the

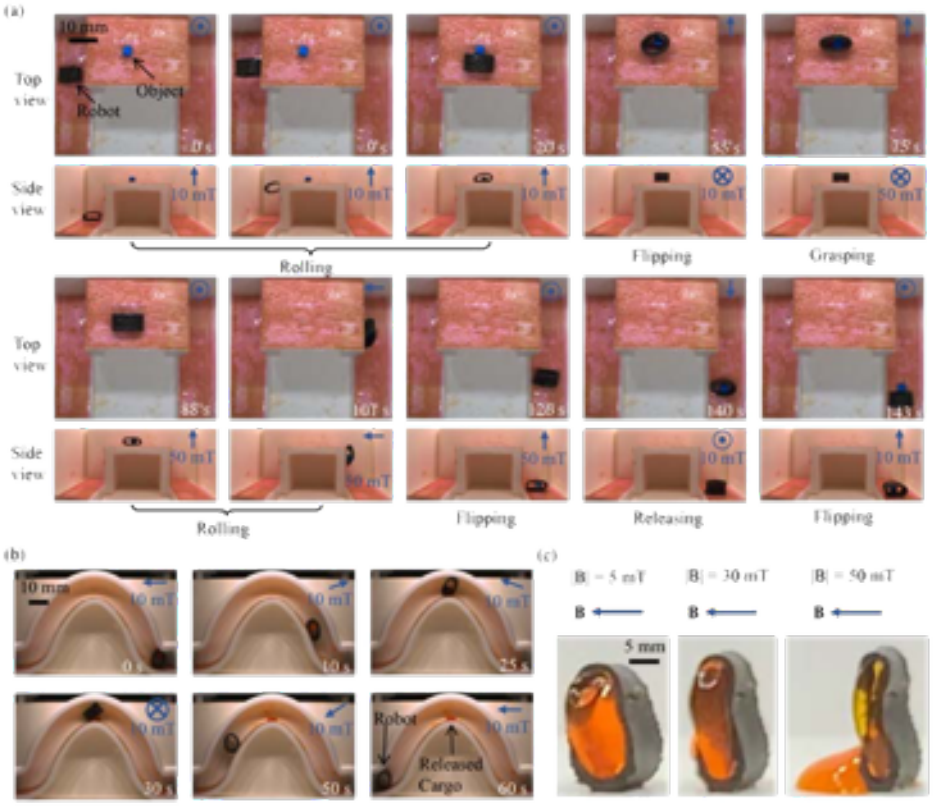

Figure 4.5: (a) Experiment to demonstrate the robot performing pick-and-place operation, where the robot moves a target object between two locations at different elevations. Both the top view and side view are shown. The blue arrows represent the directions of the magnetic filed at the given time instant. (b) Demonstration of cargo transportation function in a 3D-printed tubular structures. The robot carries a mock-drug up the undulating tube, releases it at the top and subsequently navigates to the bottom. (c) The robot demonstrating carrying of a liquid capsule and compression upon magnetic actuation to expel the liquid. The blue arrows represent the directions of the magnetic field.

tube with the soft cargo, tilt to deposit it at the top of the tube and roll down the descent (Figure 4.5(b)) (**Movie, Supporting Information**). The magnitude of the magnetic field used during the locomotion is 10 mT. After reaching the target location, the plane of rotating magnetic field changed to flip the robot to unload the cargo.

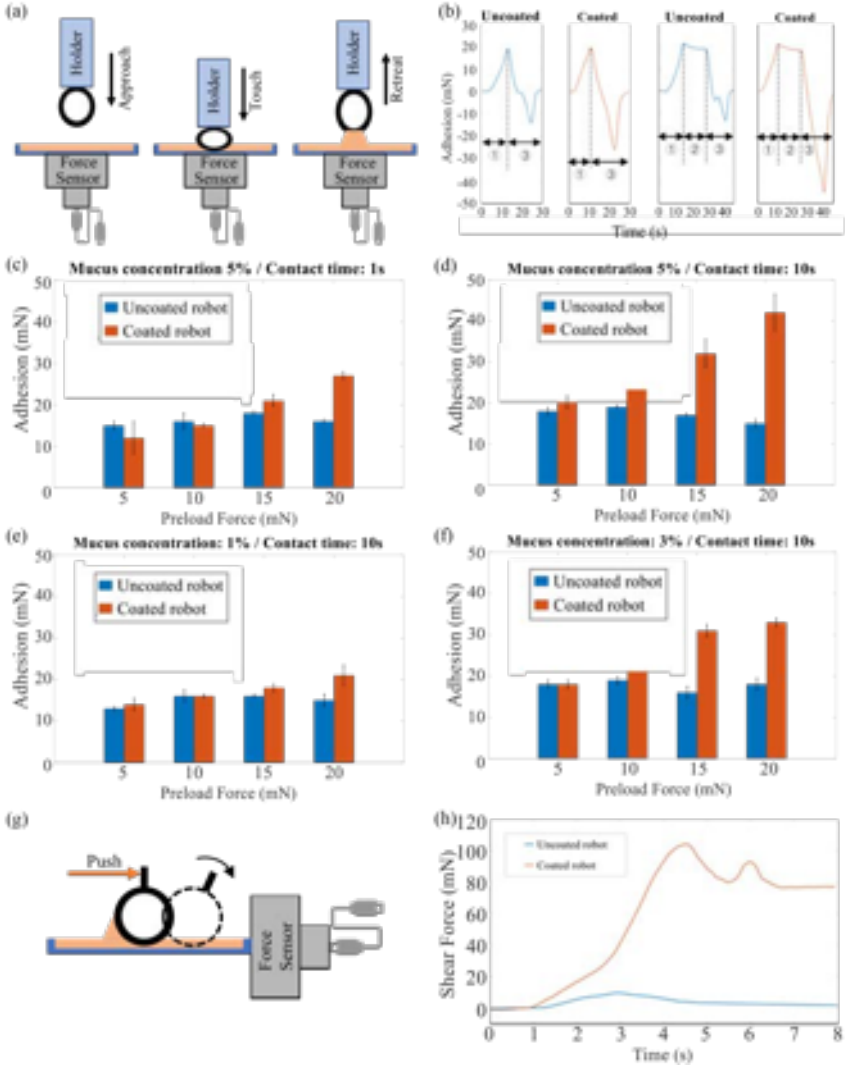

Figure 4.6: (a) Schematics of adhesion force testing. (b) Contact force signal for C-G film-coated and uncoated robots under different contact times, preload force, and contact areas. (c) Adhesion force testing on 5% concentration mucus surface under different contact forces with 1 s and (d) 10 s contact time. (e) Adhesion force testing on 1% and (f) 3% concentration mucus surface under different contact forces with 10 s contact time. (g) Method for shear force testing. (h) Force signal from shear force test over time.

The robot can also carry and squeeze soft capsules to release liquid contained within as shown in (Figure 4.5(c)) (**Movie, Supporting Information**). The robot can be compressed by increasing the magnitude of the magnetic field. When the magnetic field reaches 50 mT, the robot is fully compressed, leading to the liquid ball inside being crushed and the liquid in the liquid ball being squeezed out.

4.2.5 Characterization of Mucoadhesion Properties

To quantitatively analyze the adhesion properties between the C-G film-coated robot and mucus, experiments are designed and carried out to test the adhesion and shear force. The experiment concept and results are shown in Figure 4.6. For testing the adhesion, the robot is held in contact with the mucus plate for different contact times and contact forces (Figure 4.6(a)). The results of individual adhesion force tests are shown in Figure 4.6(b). Both coated and uncoated robots are tested. The positive peaks on the signal signify the maximum preload force act between the robot and mucus plate, the negative peaks indicate the maximum adhesion force generated by the C-G film and mucus. It can be seen from the results that the amplitude of the adhesion of coated robot changes when the contact time increases while there is no noticeable change for the uncoated robot. To explore the influence of preload force under different contact times, two groups of experiments are carried out and the results are shown in Figure 4.6(c) and (d) respectively. In Figure 4.6(c), the preload force increases from 5 mN to 20 mN and the contact time is 1 s. In Figure 4.6(d), the preload force increase from 5 mN to 20 mN and the contact time is 10 s. The results show that the adhesion force increases with the increase of preload force, and the adhesion force also increases with greater contact time.

In order to test the influence of the concentration of mucus on the adhesion force of robot, mucus-coated surfaces at three different concentrations are prepared. The adhesion forces are measured under different preload forces and 10 s contact time. Figure 4.6(e), (f) and (d) show the results of adhesion force measurement under 1%, 3% and 5% mucus-coated surfaces, respectively. The results show that the adhesion force of robot increases with the increase of the mucus concentration. It should be noted that the adhesion force of uncoated robot is equal or slightly higher than the coated

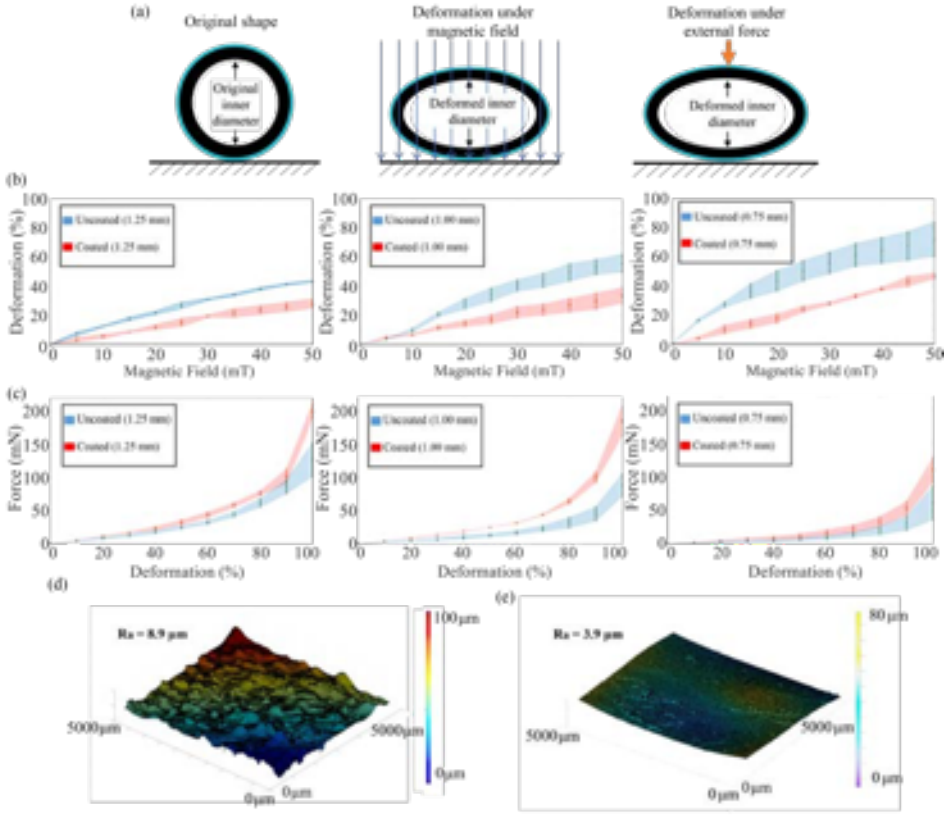

Figure 4.7: (a) Schematics showing deformation of the robot under magnetic field and external force. (b) Deformation percentage of the coated and uncoated robot under different magnitudes of the magnetic field. Three thicknesses of the robot are tested: 1.25 mm, 1 mm, and 0.75 mm. (c) Force applied on the coated and uncoated robot to achieve different deformations of the robot. Three thicknesses of the robot are tested. (d) Surface topography and roughness results of the C-G film by a laser-optical profilometer. (e) Surface topography and roughness of the MPC measured by a laser-optical profilometer.

robot in some cases when the contact time is short and the preload force is low. For the coated robot, the robot locomotion could be more stable by either increasing the contact time or the preload force to magnify the adhesion force. The purpose of this experiment is to explore the trend of adhesion force with the changes of the two factors (contact time and preload force), and compare the results of C-G film-coated robot with the

uncoated robot. The results reveal that there is no increasing trend for the uncoated robot while changing the contact time and preload force, whereas the adhesion force of the coated robot changes significantly with the change of the two factors. By using these two factors, the C-G coated robot has potential for controllable locomotion. The C-G film coated on the robot also affects the friction coefficient. An experiment is designed to measure the shear force during robot locomotion as shown in Figure 4.6(e). The coated and uncoated robot are placed on the mucus plate and pushed with a probe to rotate by 30°. The horizontal force (shear force) is measured by the force sensor. The results in Figure 4.6(f) depict that there is a significant increase in the shear force when the robot is coated with the C-G film. Also, the shear force of coated robot remains high after a motion cycle, whereas the shear force of uncoated robot decreases significantly after a motion cycle due to the lubricating action of mucus.

The results of characterization of mucoadhesive properties support the film coating concept. Two factors influence the adhesion and friction between the robot and mucus: contact time and preload force. The results suggest that the increase of the two factors lead to the increase of the adhesion and friction. Thus the adhesion and friction have potential to be controlled for different adhesion requirements. During locomotion, a suitable magnitude and frequency of the rotating magnetic field need to be selected to ensure the locomotion performance of the robot. In some cases, for instance, the concentrations of the mucus differ depending on locations inside the human body, such as the gastrointestinal tract and stomach. A higher magnetic torque and rolling speed can be used to overcome higher adhesion force, while a lower rolling speed and higher preload force are capable of increasing the adhesion force. Additionally, the adhesion and friction can be improved through microarchitectured structures on the surface of the robot [181], [191].

4.2.6 Characterization of C-G Films

Table 4.1: Effects of different concentrations of glycerol on mechanical properties of the C-G film.

Film Ingredients	Film Thickness	Tensile Modulus	Tensile Strength	Elongation at Break
Ecoflex 00-10	3 mm	55 kPa (100% Modulus)	826 kPa	800%
Chitosan	60 μm	566 MPa	31.38 kPa	3.9%
Chitosan + 5% Glycerol	90 μm	1.46 MPa	1.09 kPa	59.2%
Chitosan + 10% Glycerol	120 μm	800 kPa	0.65 kPa	77.1%
Chitosan + 20% Glycerol	90 μm	280 kPa	1.03 kPa	99.7%

The tensile modulus of pure chitosan film without glycerol is much higher than the tensile modulus of the robot. Without softening the film is too stiff to go on the robot, meaning that the film will break off when the robot deforms. The deformation of the robot shape is essential for motion and the demonstrated functions. To this end, glycerol is added as plasticizer to the chitosan film. The concentration of glycerol in the C-G film affects its mechanical properties. In order to study the changes in the mechanical properties of the film, different concentrations of glycerol are added to the chitosan solution. The mechanical properties of commercial product Ecoflex 00-10 are used as reference. It can be seen in **Table 4.1** that the softness and flexibility of the film are higher with increase in the concentration of glycerol. Adding glycerol will affect the concentration of the chitosan which is the main component responsible for mucoadhesion [189]. However, in this paper the changes in concentration of glycerol are minor compared to other studies [192]–[194] since the focus is on obtaining a suitable recipe that matches the mechanical properties of the film with that of the robot. Based on the results in Table 4.1, the plasticized chitosan film with 10% glycerol is used for coating the robot.

To explore the influence of C-G film coating on the robot mechanical properties, the deformations of coated and uncoated robot are measured under different magnitudes of magnetic field and external forces (Figure 4.7(a)). The deformation is measured as a percentage of change in inner diameter to the original inner diameter of the robot. It can be seen in Figure 4.7(b) that the deformation percentage increases with the increase of magnetic field, and the coated robot deforms less than the uncoated counterparts. The relationship between the deformation and external force is studied using a compression tester. The results in Figure 4.7(c) illustrate that more deformation requires more force on the robot. Naturally, the thinner robot deforms more than the thicker one, while the thicker robot has potential to provide more grasping force under greater magnetic field. Depending on the applications, the above results can be taken into account for designing the robot. In addition, the topography and roughness of the surface of the C-G film and MPC are measured using a laser-optical profilometer (Roughness Scantron 2000 Profilometer). The average surface roughness of the C-G film is 8.9 μm as shown in Figure 4.7(d) and the average surface roughness of the PMC is 3.9 μm as shown in Figure 4.7(e). Compared to the size of the robot, the C-G film does not significantly alter

the roughness of the surface.

4.2.7 Biocompatibility Tests

Biocompatibility assays are carried out with cells treated for 4 and 24 hours with extracts from the materials, since the mean duration of surgeries is 2 hours and procedures above 12 hours are rare [195]. Cell morphology results are shown in Figure 4.8(a) and (d) respectively (full results are shown in Figure 4.S3). The position of nucleus and distribution of F-actin cytoskeleton fibres within the cells is similar for all sample variants at both analyzed time points. Similarly, the qualitative evaluation of the cell shape and cell-cell interactions indicates lack of significant differences between the specimens. As the change of cell morphology may only in a very limited way reflect the cytotoxic effect of biomaterial, we tested metabolic activity of HT29 cells. The obtained results are shown in Figure 4.S2(a) and (b). Cells incubated with the suspension of the ferromagnetic particles (FMP) for 4 hours are characterized by a higher metabolic activity than the control group. This is only a temporary effect and the metabolic activity of HT29 returns to the level of the control after 24 hours. We have not found any significant changes in the metabolic activity of cells after incubation with the other types of extracts. Similarly, we have not found any changes in the intracellular nitric monoxide generation in response to the tested materials (Figure 4.S4(a) and (b)). However, the treatment of the HT29 cells with material extracts increased generation of intracellular superoxide. The results obtained in DHE assay are shown in Figure 4.8(b) and (e). It is notable that the concentration of superoxide after 4 hours increases with the increase of concentration of FMP, which indicates that the release of FMP from MPC may potentially affect the cells. After 24 hours, the concentration of superoxide returns to the level of the control. Similar results were obtained from the T1 relaxometry experiments. The T1 relaxometry allows local detection of the sum of free radicals, (including reactive oxygen and nitrogen species), within a few tens of nm from a nanodiamond probe. The good agreement of the outcomes of T1 relaxometry and DHE assay indicates clearly that presence of magnetic nanoparticles induces transient oxidative stress in HT29 cells. Rajnbary *et al.* have shown that magnetic nanoparticles trigger dose-dependent ROS generation in HT29 cells, which results in cell death [196]. We postulate that in

our study temporary oxidative stress did not lead to cell apoptosis due to switch on of antioxidant protective system and efficient repair processes. The results also show that coating of MPC with C-G film prevents this undesired cell response. Detailed procedures of discussed assays can be found in Section S2, Supporting Information.

4.3 Conclusion

In this study, we present a ring-shaped magnetic soft robot that is capable of stable and robust locomotion on mucus-coated surfaces through the use of a biopolymeric adhesive film coating. The efficiency and robustness of motion are improved through C-G film coating compared to the uncoated robot. Our design endows the robot with rolling, flipping and compression capabilities under the control of magnetic field. The robot can perform pick-and-place operations with cargo, as well as carry and squeeze liquid capsules. The C-G film does not lead to a detectable stress response in the form of free radical generation and improves the biocompatibility of the soft robot. The combination of the ring-shaped design, C-G film coating, and magnetic actuation has potential for implementing non-invasive clinical tasks inside the human body.

It is worth noting that the flexible C-G film is not limited to the ring-shaped soft robot presented in this paper. The film can be easily applied on other soft robots due to its flexibility and low surface roughness, for improving mucoadhesion or to reduce cytotoxicity. Moreover, the C-G film is biodegradable [197]. Thus, the film has the potential to load drugs such as brimonidine tartrate [198] and ibuprofen [199] for targeted mucosal drug delivery. The robots can be made fully biocompatible and partially dissolvable by utilizing the C-G film.

Clinical functionalities such as tissue biopsy are also possible, based on the compression and restore actions. However, the force of compression, grasping and restoration need improvement, taking into account the mechanical properties of human tissues [200], [201]. Besides increasing the magnitude of magnetic field, various materials such as shape memory polymer [202], [203] can be considered for optimizing the action forces. Other wireless actuation methods, such as chemical, temperature and light, can be introduced for actuating the robot to complement the minimalistic motion pattern and the reliable adhesion on the surface. Also, the mucuad-

hesive locomotion underwater can be investigated. *Ex vivo* experiments will help validate the efficacy of the film coating. For further development towards clinical applications, soft sensors need to be integrated into the robot for achieving precise location and operation. Other methods such as 3D printing and lithography can help to realize small-scale robot design. If miniaturized, the robots have the potential to broaden the application area to small and narrow spaces such as eyes and urethra inside the human body.

4.4 Experimental Section

4.4.1 Magnetic Polymer Composite Preparation

The robot is made of a magnetic polymer composite (MPC) which comprises a silicone rubber matrix (Ecoflex-0010, Smooth-On Inc., USA) and ferromagnetic microparticles (FMP) with a mean particle size of 5 μm (MQFP-16-7-11277, Magnequench GmbH, Germany). The mass ratio of the magnetic microparticles to the silicone rubber is 1:1. The MPC is degassed and then set to cure at room temperature (24 °C) for four hours. The mechanical properties of the MPC, such as tensile modulus, tensile strength and elongation at break are characterized and the results can be found in Section 2.7. Additionally, the mechanical properties of silicone rubber are similar to the mechanical properties of biological tissues such as gastrointestinal tract [200]. The robot therefore has potential to be safely used for medical applications *in vivo*.

4.4.2 Chitosan-Glycerol Film Preparation

Chitosan is selected as an intermediate medium to form hydrogen bonds with mucin glycoproteins. However, the stiffness of chitosan film is much higher than MPC (10^4 times according to the results from Table 4.1), which leads to the separation of the film from the soft robot body under deformation. To soften the chitosan film, glycerol is chosen as a plasticizer and a composite C-G film is prepared and used in this study. The procedure for preparing the Chitosan-Glycerol (C-G) film is as follows: First, chitosan solution (2%, w/v) is prepared by dissolving chitosan powder (medium molecular weight, Sigma-Aldrich, USA) into 1% (v/v) acetic acid solution

with a magnetic stirrer for 24 h until the solution is transparent. This is followed by adding glycerol into the chitosan solution and mixing for 1 h. Different concentrations of glycerol (5%, 10%, 20%, w/w) are added to the polymer solutions to observe the influence of glycerol on the mechanical properties of the chitosan film. The obtained solutions are then put into a centrifuge (6000 rpm) for 3min to remove air bubbles. Finally, the C-G film is obtained by casting C-G solutions on the robot body and drying for 48h at room temperature.

4.4.3 Mucus Preparation

The motion of the soft robots is to be demonstrated on mucus-coated surface. Pure human mucus is not selected for experiments in this paper as it cannot be stored for long periods of time and varies radically from person to person which decreases the reliability of experiments. Synthetic mucus has the same properties as natural mucus and has advantages such as easy availability and suitability for preparing experiment setups. In this paper, synthetic mucus is prepared and used to mimic the chemical composition of fresh mucus. The mucus is prepared by dissolving synthetic mucin (mucin from porcine stomach, Sigma-Aldrich, USA) into phosphate buffer solution (PBS, pH=7) at concentrations of 1-5% (w/v) and stirring on a magnetic stirrer for 1h at room temperature (22°C). The obtained mucus solution is then cast onto silicone rubber film and left to dry at room temperature for 6 h. The liquid thickness of mucus on the silicone rubber film is 1 mm. The dried mucus can be stored in a refrigerator at 8°C. Before experiments, the dried mucus needs to be sufficiently hydrated by deionized water [204], [205].

4.4.4 Experimental Setup

The liquid capsule (Section 2.4,Figure 4.5(c)) is prepared by dropping 2% sodium alginate solution into 1% calcium chloride solution for 5s. For higher contrast with the background, the mock drug is dyed orange by adding a small quantity of the dye (Sudan Orange color dye, Merck, Germany). The soft cargo used for demonstrating the cargo transportation function reference is made by the same process as the liquid capsule but with more reaction time (1 min) to produce a hydrogel. The setups for demonstrations in this paper are 3D-printed using Polylactic acid (PLA).

The surface of the setup is covered by a thin layer of silicone rubber which is coated with a layer of mucus. Experiments are carried out between 10-20 minutes after hydrating the mucus at room temperature (22°C).

4.4.5 Mechanical Performance Characterization of C-G film

Uniaxial tensile tests are carried out to characterize the tensile modulus, tensile strength, and elongation at break of the prepared C-G films with different concentrations of glycerol. The above mechanical properties are measured on a texture analyzer (CT3 Texture Analyzer, USA). The thickness of the films is measured using a custom-built low load compression tester (LLCT). The mechanical properties of the films are tested by following ASTM D882 and ASTM D412 standards respectively. All the values are average value from three times of test. The results can be found in Section 2.7.

4.4.6 Characterization of Mucoadhesion Properties

The adhesion and shear force are measured using a custom setup where a low range load cell is embedded (shown in Figure 4.6(a)). The load cell is able to measure force from 1 mN to 10 N. For measuring the adhesion, the robot and mucus plate are mounted on a movable holder and force sensor, respectively. The adhesion is measured by moving the robot to contact the mucus plate. The contact time can be controlled. For measuring the shear force, the sensor is mounted to measure force along the length of the mucus plate. The robot is placed on the mucus plate and pushed by a probe/stylus to rotate by 30°.

4.4.7 Biocompatibility Tests

Materials used in this study, including the C-G film, silicone rubber, magnetic polymer composite (MPC), C-G film-coated MPC and magnetic microparticles (2 mg/ml magnetic particles in medium), are tested for their biocompatibility. The MPC is prepared in two variants of mass ratio, 1:1 and 2:1 (silicone rubber : magnetic particles).

For testing biocompatibility of the materials used in fabricating the robots, a human colorectal adenocarcinoma cell line with epithelial mor-

phology (HT29) is used. Cells were cultured in the DMEM high glucose medium that contains 10% FBS and 1% antibiotics at 37°C with 5% CO_2/95% air until 90% confluence. An indirect method for evaluating cytotoxicity of materials is used in this study. Materials for tests are incubated in the cell culturing medium (medium-to-sample area ratio of 1.25 mL/cm2) for 24 hours at 37°C in a humidified atmosphere of 5% CO_2 in order to obtain extracts, which potentially contain cytotoxic components such as magnetic particles and derivatives of degraded polymers.

A DHE (Dihydroethidium) assay kit, containing a fluorescent probe, is utilized in order to inspect the generation of superoxide ($O_2^{\cdot -}$) in HT29 cells exposed to material extracts. DAF-FM Diacetate (4-Amino-5-Methylamino-2', 7'-Difluorofluorescein Diacetate), a fluorescent indicator developed to detect the intracellular nitric monoxide ($NO^{\cdot}$) is used in order to determine the impact of materials on free radicals generation in cells. T1 measurements allow local detection of the sum of all radicals within a few tens of nm from a nanodiamond particle with a mean hydrodynamic diameter of 70 nm and a flake-like structure (Adamas Nanotechnologies, NC, USA) as probes [206]–[210]. They are produced by HPHT synthesis and irradiated with 3MeV electrons at a fluence of 5×10^{19} e/cm^2 to produce nitrogen vacancy (NV) centers. As a result each particle contains around 500 NV centers. As a last step of fabrication these particles are treated in oxidising acids leading to oxygen termination [211].

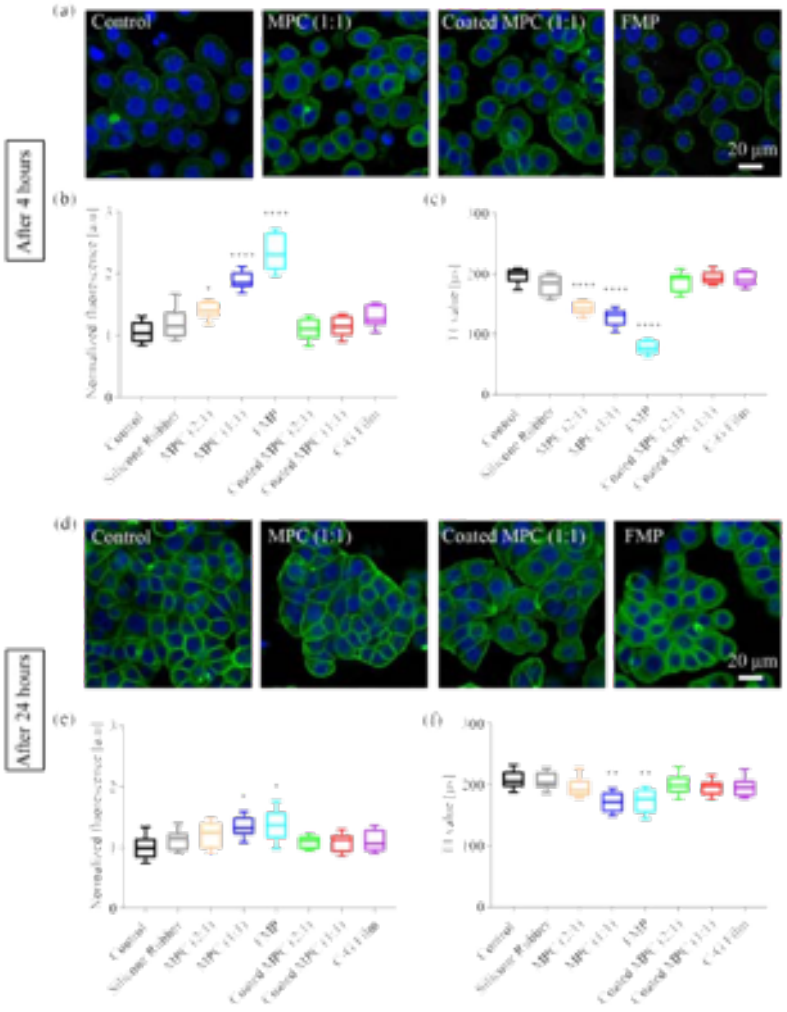

Figure 4.8: Results of biocompatibility tests. (a) Morphology of the human colorectal adenocarcinoma cell line with epithelial morphology (HT29) after treatment with various material extracts for 4 hours. (b) Results of Dihydroethidium (DHE) assay - detection of intracellular superoxide. (c) Results of T1 assay - detection of intracellular free radicals. (d) HT29 morphology after treatment with various material extracts for 24 hours. (e) Results of DHE assay - detection of intracellular superoxide. (f) Results of T1 assay - detection of intracellular free radicals. Positive control – untreated cells. The asterisk signs denote statistical significance (** $p < 0.01$, *** $p < 0.001$, **** $p < 0.0001$) to control groups.

4.5 Supporting Information

4.5.1 Mechanisms of Motion and Compression

After C-G coating and magnetization, the robot can be actuated to roll, flip or compress using an external magnetic field. The magnetization profiles in the robot body tend to align with the directions of the magnetic field (shown in Figure 4.S1(a)). By increasing the magnitude of the magnetic field, the compression in the direction of the magnetic field will increase accordingly (shown in Figure 4.S1(b)). The rolling motion is also implementable under the compression state. The robot can be flipped on its side by rotating the magnetic field perpendicular to the rolling direction. The adhesion force between chitosan and mucus is influenced by three factors: contact time, contact area and preload force.

The contact area changes with robot deformation under different magnitudes of magnetic field (Figure 4.S1(b)). The magnetic dipoles in the robot body tends to align with the magnetic field directions, which generates magnetic torque on the robot body. As the magnetic field increases, the robot changes shape into an ellipse of smaller minor diameter, increasing the contact area. The torque produced by the rotating magnetic field must overcome the adhesion force to achieve rolling motion.

The contact time of a given point on the robot is calculated assuming the thickness of the mucus layer is uniform/constant. As shown in Figure 4.S1(c), the contact time (T_{contact}) of any point on the robot can be calculated by the following expression:

$$T_{\text{contact}} = \frac{\arccos(\frac{r-d}{r})}{2\pi} \tag{4.1}$$

where r is the radius of the outer surface of the robot with C-G film coating, d is the thickness of the mucus layer.

The robot is able to roll on surfaces with a wide range of tilt angles from 0° to 180°. As shown in Figure 4.S1(d), the forces acting on the robot are adhesion ($\mathbf{F}_{\text{adhesion}}$), friction (shear force) ($\mathbf{F}_{\text{shear}}$), magnetic torque ($\mathbf{T}_{\text{magnetic}}$), contact reaction force ($\mathbf{F}_{\text{contact}}$) and gravity ($\mathbf{G}$). To maintain robust adhesion while rolling, the adhesion force must overcome the magnetic torque:

$$\mathbf{T}_{\text{magnetic}} > \mathbf{F}_{\text{shear}} \cdot r \tag{4.2}$$

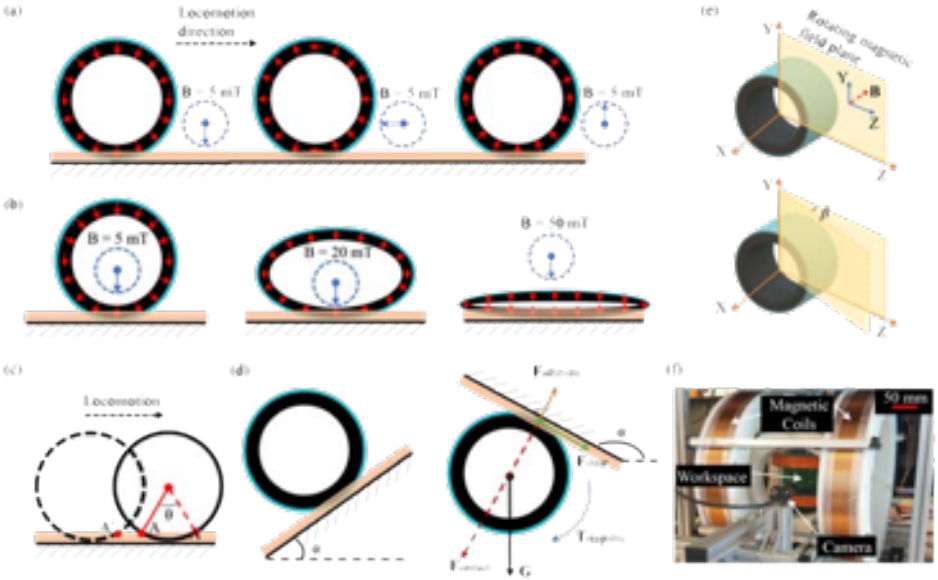

Figure 4.S1: (a) The robot rolls under a rotating magnetic field. (b) The deformation of the robot increases with the magnetic field. (c) The contact time between mucus and point A on the robot (film) depends on the thickness of the mucus layer and motion speed. (d) Schematics of mucoadhesive locomotion on varying tilt angle surfaces, showing the directions of gravity, contact force, adhesion force, shear force, and magnetic torque. (e) The robot turns by changing the tilt angle of the rotating magnetic field plane. (f) The electromagnetic coils setup for magnetic actuation.

where the magnetic torque is given by

$$\mathbf{T} = \mu \times \mathbf{B} \tag{4.3}$$

where μ is the magnetic dipole moment, $\mathbf{B}$ is the magnetic field.

Also, the components of adhesion force and shear force need to overcome the gravity:

$$\mathbf{F}_{\text{adhesion}} \cos(\pi - \alpha) + \mathbf{F}_{\text{shear}} \sin(\pi - \alpha) > \mathbf{G} \tag{4.4}$$

Compared to the uncoated robot, the friction coefficient and adhesion force of the C-G film-coated robot are higher. The adhesion force can be controlled by adjusting the motion speed, preload force, and deformation.

The steering of the robot is achieved using the following approach. Changing the tilt angle β between the plane of rotation of the magnetic field and YZ plane (shown in Figure 4.S1(e)), changes the axis of the magnetic torque. If β is changed in small increments, the robot tends to align with the plane of rotation of the magnetic field.

The actuation magnetic field is generated using a setup consisting of six electromagnetic coils (shown in Figure 4.S1(f)). It is assumed that the magnetic field is uniform and the contribution of the magnetic field gradient is negligible in the $12 \times 12 \times 12$ cm workspace. The setup can generate a magnetic field up to 50 mT in any given direction. Cameras are set on the top and side positions for recording the videos.

4.5.2 Biocompatibility Tests

4.5.2.1 MTT Assay

The cytotoxicity evaluation is performed with a standard MTT assay. The results are shown in Figure 4.S2. This assay measures metabolic activity and makes use of the ability of the tetrazolium dye MTT 3-(4,5-dimethylthiazol-2-yl)-2, 5-diphenyltetrazolium bromide which is reduced to insoluble, purple formazan. In doing so, cells were seeded in a 96-well plate at a density of 2.1×10^4 cells/mL and incubated for 24 hours at 37°C in 5% CO_2/95% air to allow attachment. Then, the remaining culture medium was replaced by material extracts and the cell culture was maintained for an additional 4 or 24 hours. The extracts were replaced with the MTT-containing culture medium (5 mg/mL) and incubated for an additional 3 hours. The cells cultured in the DMEM high glucose medium that contains 10% FBS and 1% antibiotics at 37°C with 5% CO_2/95% air until 90% confluence, without any additions were treated as the negative control. Subsequently, isopropanol was added to each well and the plate was gently shaken for 2 minutes. The spectrophotometrical absorbance was measured at 570 nm in a microplate reader (Biotek Instruments) and an average of at least six measurements was taken for each tested condition.

4.5.2.2 Cell Morphology

Cell morphology was determined upon 4 and 24 hours of incubation with material extracts. The results are shown in Figure 4.S3. Before imaging,

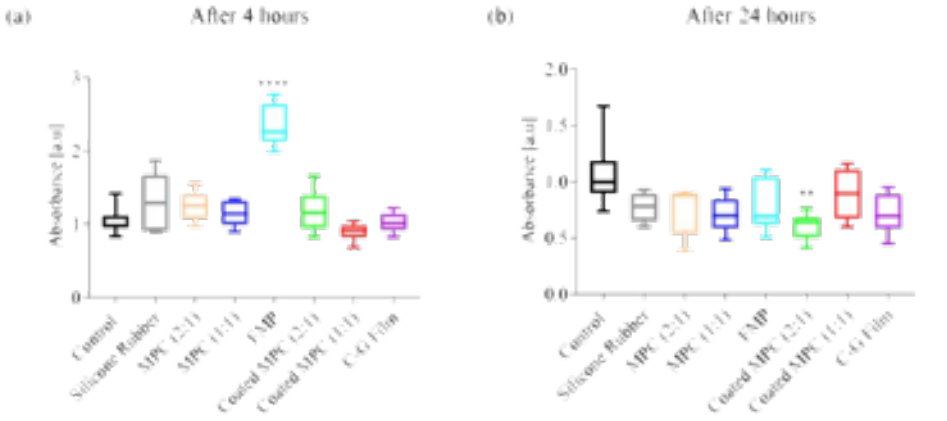

Figure 4.S2: Results of MTT assay - metabolic activity of HT29 cells. Normalized absorbance calculated for cells treated with various materials. (a) Results after treated for 4 hours. (b) Results after treated for 24 hours.

the cells were fixed with 4% paraformaldehyde solution for 10 minutes and permeabilized with 0.1% Triton X-100 (Sigma) for 7 minutes. Following washing with fresh PBS, cells were stained with FITC-phalloidin (Sigma) for 30 minutes and DAPI (Sigma) for 5 minutes so cell F-actin fibers of cytoskeleton and cell nuclei, respectively, could be observable. Images were acquired with a confocal laser scanning microscope (CLSM).

4.5.2.3 DHE Assay

A DHE (Dihydroethidium) Assay Kit, containing a fluorescent probe, was utilized in order to inspect the generation of superoxide (O_2^{-}) in HT29 cells exposed to material extracts. In general, a DHE indicator gets oxidized by either superoxide to form 2-hydroxyethidium ($2-OH^{-}E^{+}$) or by non-specific oxidation with other sources of ROS to form ethidium (E^{+}). Both reaction products bind to DNA to give off bright red fluorescence. Following 4- or 24-hour incubation with extracts at 37°C and 5% CO_2 the cells were treated with a DHE solution at a concentration of 2 μg/mL. Consequently, the cells were incubated for 10 minutes at 37°C and 5% CO_2 and rinsed with ice-cold culture medium before image acquisition. The fluorescence images were taken from at least 10 randomly selected cells per well using a CLSM Stellaris 8 Leica Microsystems. The excitation/emission

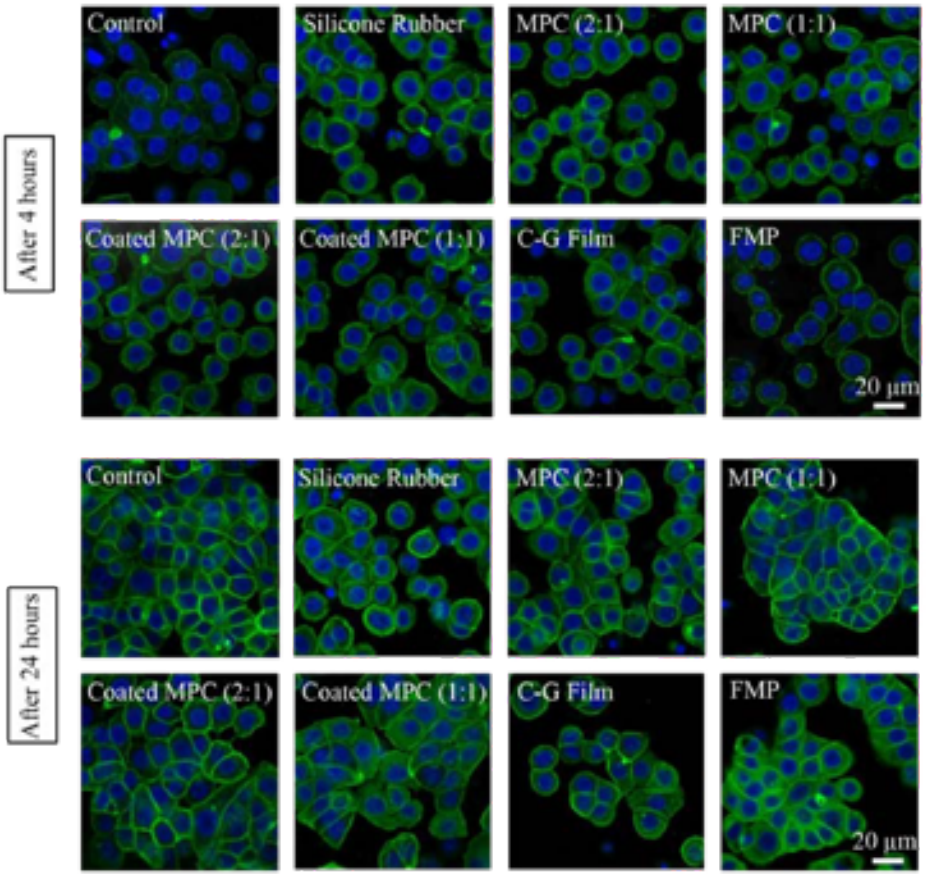

Figure 4.S3: HT29 cell morphology after treatment with various materials for 4 and 24 hours. The blue staining (DAPI) indicated nuclei and green (phalloidin Alexa Fluor 488) F-actin filaments of the cytoskeleton.

range was set to 514/580 nm. Finally, the mean fluorescence intensity, regarded as a function of the $O_2^{\cdot-}$ level generated by a cell, was determined by using the ImageJ open-source software.

4.5.2.4 DAF-FM Assay

DAF-FM Diacetate (4-Amino-5-Methylamino-2',7'-Difluorofluorescein Diacetate), a fluorescent indicator developed to detect the intracellular nitric

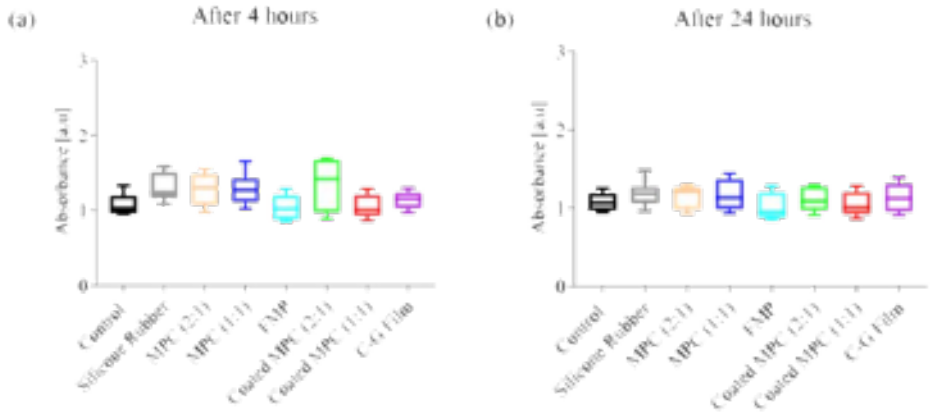

Figure 4.S4: Results of DAF-FM assay - detection of intracellular nitric monoxide. Normalized absorbance calculated for cells treated with various materials. (a) Results after treated for 4 hours. (b) Results after treated for 24 hours.

monoxide ($NO^{\cdot}$) was used in order to determine the impact of materials on free radicals generation in cells. The results are shown in Figure 4.S3. Upon 4- or 24-hour incubation of HT29 with extracts at 37°C and 5% CO_2, the cells were treated with the DMEM HG medium-containing DAF-FM solution at a concentration of 0.2 μg/mL. Subsequently, they were rinsed with fresh culture medium and incubated anew for 15 minutes to finalize the intracellular DAF-FM diacetate de-esterification. During the process, the non-permeable, nonfluorescent DAF-FM is formed and converted to the highly fluorescent benzotriazole form in the presence of $NO^{\cdot}$. Finally, the fluorescence images were captured from a set of 10 randomly selected cells per well using a CLSM. The excitation/emission range of 495/515 nm was chosen for imaging. The relative levels of intracellular $NO^{\cdot}$ were quantified from the mean fluorescence intensity of DAF-FM by employing the ImageJ open-source software.

4.5.2.5 T1 Relaxometry

T_1 measurements were performed using the fluorescent nanodiamond particles (FNDs) with a mean hydrodynamic diameter of 70 nm and a flake-like structure (Adamas Nanotechnologies, NC, USA) as probes. FNDs are obtained through high pressure and high temperature (HPHT) synthesis

and grinding. Then particles are irradiated and annealed at the temperature exceeding 700°C. As a result, they contain approximately 500 nitrogen vacancy (NV^-) centers per particle. The surface of FNDs is oxygen-terminated because in the last stage of their processing they are treated with oxidizing acids. Prior to T1 measurements, FNDs at a concentration of 2 μg/mL were internalized by cells during 4-hour incubation at 37°C and 5% CO_2. At the end of incubation, the cells were washed with fresh culture medium and exposed to material extracts for either 4 or 24 hours. A single confocal scan was performed in order to detect FNDs inside a particular HT29 cell. First, the NV^- centers were pumped to the bright ms=0 state of the ground state with a laser pulse. Afterwards, we probed if the NV^- centers were still there or had returned to the darker equilibrium state. This process gets shortened in presence of free radicals in the surrounding. Thus, the relaxation time (=T1) reveals the radical concentration. Each of T1 measurement takes on the order of millisecond. However, to obtain a sufficient signal to noise ratio the experiment is typically repeated 10000 times which takes around 10 min. The experiments were carried out by using a custom-build magnetometry setup.

4.6 Supplementary Video

Video: Biocompatible Film-coating of Magnetic Soft Robots for Mucoadhesive Locomotion

Video link: https://www.youtube.com/watch?v=Lsx18af0SEA

5

Minimally Designed Thermo-magnetic Dual Responsive Soft Robots for Complex Applications

Note: *This chapter is adapted from the article "Minimally designed thermo-magnetic dual responsive soft robots for complex applications" by C. Siebenmorgen,* ***C. Wang****, L. B. Navarro, D. Parisi, S. Misra, V. K. Venkiteswaran, and P. van Rijn, published in "Journal of Materials Chemistry B", volume 12, issue no. 22, pages 5339–5349, June 2024.*

Abstract

The fabrication of thermo-magnetic dual-responsive soft robots often requires intricate designs to implement complex locomotion patterns and utilize the implemented responsive behaviors. This work demonstrates a minimally designed soft robot based on poly-N-isopropylacrylamide (pNIPAM) and ferromagnetic particles, showcasing excellent control over both thermo- and magnetic responses. Free radical polymerization enables the magnetic particles to be entrapped homogeneously within the polymeric network. The integration of magnetic shape programming and temperature response allows the robot to perform various tasks including shaping, locomotion, pick-and-place, and release maneuvers of objects using independent triggers. The robot can be immobilized in a gripping state through magnetic actuation, and a subsequent increase in temperature transitions the robot from a swollen to a collapsed state. The temperature switch en-

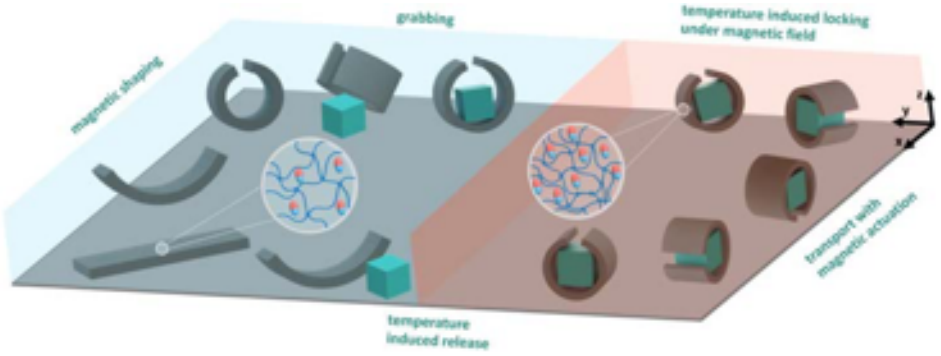

Figure 5.1: Schematic illustration depicting THANOS and its responsive behavior to thermal and magnetic stimuli, enabling pick-and-place maneuvers of objects. When heated, THANOS expels water and is shape locked. Upon cooling, THANOS absorbs water and becomes flexible for magnetic shaping.

ables the robot to maintain a secured configuration while executing other movements via magnetic actuation. This approach offers a straightforward yet effective solution for achieving full control over both stimuli in dual-responsive soft robotics.

5.1 Introduction

For many engineering inventions nature has served as a profound source of inspiration. In the field of robotics, insects have been an inspiration for the design of creating agile and adaptable robots, which can navigate through complex terrains [212], [213]. Marine organisms such as cephalopods have influenced the research progress in soft robotics, as they show complex locomotion such as crawling, and jet propulsion [214], [215]. Furthermore, cephalopods can undergo significant changes in body shape through muscular contractions to access confined spaces. This capability results from the soft properties and have led to biomimetic systems in the field of soft robotics.

Soft robots are made of flexible materials such as elastomers, gels, and polymers and contain domains that react to external stimuli, such as light, temperature, pH, acoustic waves, and electric and magnetic fields [216]–[222]. Among these stimuli, magnetic actuation stands out as a particularly promising method, offering various advantages, such as being non-invasive,

enables remote control, suitability for small-scale applications, and safety for medical use [223]–[225]. Using magnetic actuation in soft robotics is particularly useful in the context of biomedical applications, including the utilization of surgical robots [83], [85], [225]–[228]. Numerous examples of magnetically-activated robots have been reported previously, where the majority is based on polymeric materials, such as silicon elastomers, in which magnetic nanoparticles have been incorporated [94], [96], [97], [101], [229]–[234]. These robots show high flexibility, facile synthesis, and can be synthesized to be biocompatible. However, they rely solely on magnetic actuation where each soft robot is limited to actuation modes in a soft state, limiting their potential functionality. These robots cannot be altered or switched to different modes of actuation without modifications to their design or operating principles.

Creating dual-responsive soft robots, allows the incorporation of combined functionalities by integrating multiple responsive mechanisms. By employing temperature-responsive polymeric networks with incorporated magnetic particles, a dual responsive thermo-magnetic system can be realized. Poly(N-Isopropylacrylamide) (pNIPAM)-based hydrogels are a popular choice of material, as this polymer undergoes phase-transition close to body temperature, at around 32°C [235], [236]. It exhibits phase transition from a hydrophilic to a hydrophobic state when the temperature increases above its Volume Phase Transition Temperature (VPTT). Systems have been developed that enable either grabbing, transport, or different forms of locomotion. However, they require complex designs, and the use of several polymeric carrier systems to provide sufficient strength or induce the desired function. Particularly, the use of the magnetic field for different functions in one system remains challenging. Therefore, a design without any specific added complexity will potentially enhance its applicability as well as its down-scaling as the complexity will require small features for in vivo applications. Previously, pNIPAM-based thermo-responsive soft robots have been studied [237]. Breger et al. synthesized a double layer polymeric gripper, in which the first layer was based on pNIPAM-co-acrylic acid swelling hydrogel and the second layer consisted of non-swelling propylene furmarate polymers [238]. They further incorporated Fe_2O_4 nanoparticles for a dual thermo-magnetic response. Due to the phase transition of the thermo-responsive hydrogel, these soft robots demonstrated the capability of self-folding gripping motions when increasing the temperature

above the VPTT. However, a complex design of a star shaped double layer polymeric sheet is necessary, to achieve sufficient strength during gripping motion. Furthermore, variations in motion in response to temperature increase poses a challenge due to the intricate nature of the design. Du et al. used pNIPAM polymer-based millirobot with a magnetized head group by incorporating NdFeB particles, and a non-functionalized pNIPAM tail group [239]. This millirobot showed multimodal locomotion, such as crawling, helical propelling, and rolling. However, all locomotions can only be achieved when applying a magnetic field.

The work presented here takes a different approach towards dual responsive **th**ermo-ma**g**n**e**tic s**o**ft robotic**s** (THANOS) based on pNIPAM and ferromagnetic particles. The design offers a substantially simplified synthesis method achieved through a one-step temperature-induced free radical polymerization without the necessity of different polymer classes deposited with spatial control. The key novelty of THANOS lies in the combination of the simplicity in design along with the integration of magnetic shape programming and temperature response to ensure shape-locking (Figure 5.1). When exposed to a magnetic field, the robot can perform various complex locomotions, such as rolling, undulating, and inchworm-like motion. Simultaneously, the robot can be locked in the desired shape by increasing the temperature above the VPTT without the need for magnetic actuation. This capability empowers the robot to execute dual functions. Initially, the robot can be immobilized in a gripping (or any other) state by magnetic actuation. By raising the temperature and then deactivating the magnetic actuation, the robot can be fixed in the desired shape. Following this, the robot can execute secondary movements through magnetic actuation while remaining in the secured configuration. This control mechanism could be particularly valuable in application such as minimally invasive surgery, enabling the robot to perform dual tasks through independent stimuli that would otherwise be challenging.

5.2 Materials and Methods

5.2.1 Chemicals and Materials

N-Isopropylacrylamide (>98%, NIPAM) was purchased from Tokyo Chemical Industry (TCI), Belgium. N,N′-methylenebis(acrylamide) (99%, BIS),

potassium persulfate (99%, KPS), Poly(dimethylsiloxane) (PDMS) were purchased from Sigma-Aldrich, The Netherlands. N,N,N,N′-tetramethyleth ylenediamine (TEMED) was purchased from Bio-Rad Laboratories, United States of America. MQFP^{TM}-16-7-11277 5 μm sized PrFeB particles were obtained from Magnequench GmbH, Germany. All chemicals were used as received without any further purification. Ultra-pure water (18.2 $M\Omega$, arium 611 DI water purification system; Sartorius AG, Germany) was used for all experiments.

5.2.2 Preparation of Molds

The fabrication of PDMS molds for the preparation of pNIPAM sheets involves a two-step molding process. Initially, a negative mold featuring a 30×30×0.5 mm boss is created through laser cutting of acrylic (polymethyl methacrylate) (PMMA). Subsequently, PDMS is poured into the mold and subjected to curing at 70°C for a duration of 4 hours. Following the curing process, the PDMS molds, characterized by a 30×30×0.5 mm groove, are obtained by peeling off from the PMMA negative mold.

To achieve customized shapes in the maternal sheets, molds of the desired configurations are laser-cut and equipped with a thin wall serving the purpose of a cutting implement. This approach allows for precision in shaping the maternal sheets, ensuring the attainment of specific geometries to meet the unique requirements of the study.

5.2.3 Synthesis of pNIPAM Sheets

For the synthesis of THANOS sheets, 700 mg MQFP^{TM}-16-7-11277 particles were dispersed in 10 mL ultra-pure water in a 20 ml vial and were subsequently tip sonicated for 30 s using a Vibra cell (Sonic and Materials Inc., Danbury, Connectitcut, USA) with a duty cycle of 60% set at an output control of 5. To this suspension 566 mg NIPAM (0.5M) and 154 mg BIS (0.1M) were added and subsequently degassed with N_2 for 15 min. In a 2 ml vial 4 mg KPS was dissolved in 1 mL ultra-pure water and subsequently degassed with N_2 for 15 min. The solutions were transferred to a nitrogen atmosphere and were stored in an ice bath to extend the duration of the free radical polymerization reaction to approximately 5 seconds. Prior to crosslinking 700 μL of the monomer-particle suspension

was transferred to a 1.5 mL Eppendorf tube, in which 10 μL of KPS initiator was added. With continuous agitation, the mixture was then poured into the previously prepared molds and covered with a round PMMA cover slip with a diameter of 60mm. The soft robot was subsequently washed with ultra-pure water and stored in ultra-pure water at room temperature.

The preparation of pNIPAM@Control sheets followed the same procedure. However, MQFP^{TM}-16-7-11277 particles have not been added to the monomer solution and therefore it was not subjected to tip sonication. Furthermore, additional 10 μL of TEMED have been added simultaneously with 10 μL of KPS to the mixture to initiate the polymerization.

5.2.4 Magnetization

Following the synthesis process, the sheets undergo a transformation process facilitated by placement into a specialized non-magnetic fixture designed for shaping purposes. The sheet, in conjunction with the fixture, is subsequently subjected to a 2 T magnetic field. The magnetic field is generated utilizing an impulse magnetizer (ASC Model IM-10-30, ASC Scientific, USA) to achieve the targeted magnetization profile as per the experimental requirements.

5.2.5 Scanning Electron Microscopy Sample Preparation

To image the cross-section of the sheets, they were frozen with $N_{2(l)}$, broken in half and subsequently freeze dried for 24 h using a Labogene Scanvac Coolsafe freeze dryer at a condenser temperature of -110 °C. Double 90° angled Zeiss short pin stubs with a diameter of 25.4 mm were covered with carbon-based adhesive disks. The cross-section of the pNIPAM sheet was then placed on the double 90° short pin stubs and subsequently sputter coated with 5 nm Cr with a working distance of 50 mm, a stab height of 15 mm, and a tilt stage angle of -10°. The images were taken with an Atlas Zeiss Supra 55 STEM scanning electron microscope with a field emission gun running at 3 kV. MQFP^{TM}-16-7-11277 particles have been imaged using a stub with a diameter of 9 mm, covered with a carbon-based adhesive disk, and were subsequently sputter coated with 5 nm Cr with a working distance of 15 mm, and a stab height of 15 mm. The images were

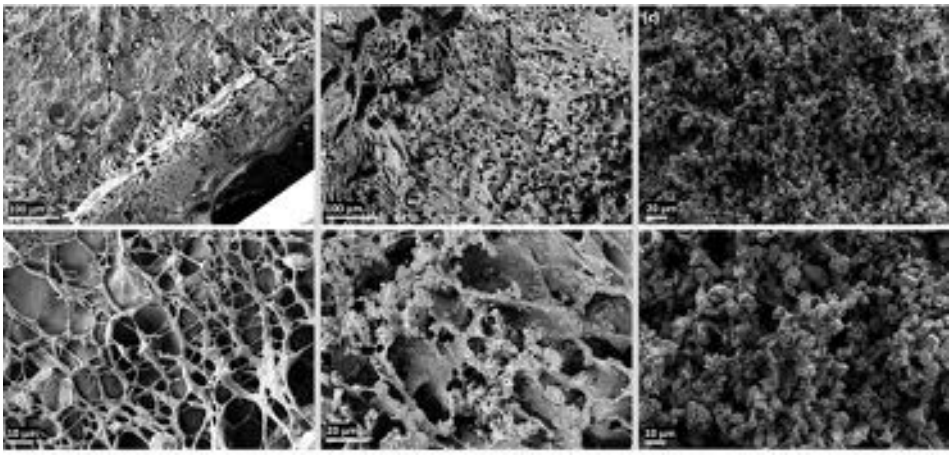

Figure 5.2: SEM images depict (a) the cross-section of the pNIPAM@Control sheet after freeze drying, (b) the cross-section of THANOS after freeze drying, showcasing a uniform dispersion of ferromagnetic particles within the hydrogel, and (c) ferromagnetic MQFP^{TM}-16-7-11277 particles observed as a powder without being incorporated in a polymeric matrix.

taken with the same scanning electron microscope, but due to charging of the sample, the field emission gun was running at 2 kV.

5.2.6 Volume Phase Transition Temperature

To test the temperature response of THANOS and pNIPAM@Control sheets, the degree of the surface area reduction of the sheets due to gradual temperature changes (1°C/min) was monitored. For this purpose, the sheets were placed on a mm grid inside a water bath on top of a heating plate with temperature control. The sheets were then imaged with a standard and infrared camera. The infrared camera allowed for a double control of the actual temperature of the sheets. Subsequently, the percentage of the surface area was plotted against the temperature.

5.2.7 Time Dependent Shrinking

To investigate the time dependant shrinking of THANOS and pNIPAM@Control, both sheets were transferred from a water bath at room temperature to a heated water bath at 50°C, while monitoring the reduction of the surface area. For this purpose, the sheets with a dimension of 15x5mm were

placed on a mm grid inside a water bath at 50°C on top of a heating plate with temperature control. The sheets were then imaged with a standard camera and the measurement was repeated for five times. The percentage of the surface area was subsequently plotted against the time.

5.2.8 Rheological Characterization

Rheological experiments were performed in a Discovery Hybrid Rheometer (HR-2) from TA Instruments (United States). 25 mm diameter parallel plates were used for all the rheological tests. The samples were loaded into the rheometer, and dynamic strain sweeps were executed at 100 rad/s to determine a strain within the linear viscoelastic (LVE) regime. Consequently, frequency sweeps were performed over a range of frequencies varying from 100 to 0.1 rad/s, and oscillatory strain amplitude between 1 and 10 %. All the measurements were carried out either at room temperature or at 50 °C. The temperature control system consisted of an electric element coupled with a convection oven, fed with nitrogen gas at a very low flow rate (¡ 1 l/min).

5.3 Results

5.3.1 Fabrication of pNIPAM-based Soft Robotic Material

pNIPAM@Control and THANOS sheets followed a similar free radical polymerization approach. In contrast, pNIPAM@Control required the addition of TEMED and KPS to initiate the polymerization, whereas THANOS robotic sheets could be initiated with solely KPS. KPS will readily homolytically cleave upon increasing the temperature, which can be already at room temperature, and induce free radical polymerization. However, before initiating the free radical polymerization of THANOS sheets, the aqueous suspension containing solely PrFeB particles was tip sonicated using low frequency ultrasonic waves. Subsequently, NIPAM and BIS were added to the suspension. Without this additional step, free radical polymerization did not occur.

Sonication of aqueous solutions leads to cavitation of present microbubbles, which ultimately results in so called 'hot spots'. These localized hot

spots give rise to extreme conditions, with temperatures above 5000 K and pressures exceeding 1000 atm [240]. There are two possible explanations for the initiation of the polymerization of THANOS robotic sheets without the addition of TEMED: (1) The conditions created by hot-spots could cause defects on the surface of the MQFP^{TM} particles, which could ultimately enhance the surface reactivity. (2) Ultrasonication of the suspension could lead to the generation of reactive species. These reactive species could act as initiation sites when in contact with KPS.

Sonochemical related induced radical formation of the monomer-particle suspension allowed a complete polymerization of the sheets within seconds, while the reaction of the control group took several minutes. The extremely short reaction time is crucial for the synthesis of THANOS robotic sheets since the MQFP^{TM} particles would otherwise sediment. Despite minimizing sedimentation by the reduced reaction time and suspending the reaction mixture before crosslinking, the upper section of the robot exhibited slight discoloration. This suggests that a slightly lower concentration of particles are residing within the top of the polymeric matrix. To obtain a better understanding of the macroscopic features of the polymeric sheets and the subsequent incorporation of magnetic particles within the THANOS robot, SEM images of the cross-section of both sheets have been taken. Figure 5.2 shows SEM images of (a) the cross section of the previously freeze-dried NIPAM@Control sheet, (b) the cross section of the previously freeze-dried THANOS sheet and (c) ferromagnetic particles MQFP^{TM}-16-7-11277, which are not incorporated inside a polymeric matrix. In Figure 5.2 (b), the successful and overall uniform integration of ferromagnetic particles into the polymer matrix of the pNIPAM sheets is demonstrated. As described previously, the reaction rate of the free radical polymerization of THANOS sheets is influencing the distribution of particles. An increase in the reaction rate is crucial, as high density MQFP^{TM} particles would otherwise sediment especially, when relying on a different initiation system.

5.3.2 Rheological Characterization of pNIPAM Sheets

Rheological experiments were performed to evaluate how the presence of magnetic particles and temperature variations affect the rheological properties of the polymeric sheets. Figure 5.S1 shows the complex viscosity and complex modulus of THANOS depending on the angular frequency at

25°C and 50°C, while Figure 5.S2 displays the rheological results of pNIPAM@Control. Increasing the temperature from 25°C to 50°C leads to an increase in complex viscosity and complex modulus in both cases, so for THANOS and for pNIPAM@Control. Furthermore, the incorporation of magnetic particles within the polymeric network leads to an increase in complex viscosity at 25°C at an angular frequency of 0.1 rad s^{-1} by a factor of 10, while the complex modulus increases by a factor of 1000. Increasing the temperature above the VPTT to 50°C increases the complex viscosity and complex modulus in both THANOS and pNIPAM@Control. THANOS shows increased values for the complex viscosity and the complex modulus at an angular frequency of 0.1 rad s^{-1} by a factor of 100 when compared to pNIPAM@Control at 50°C. There are two phenomena that can explain the difference in the complex modulus and complex viscosity of THANOS and pNIPAM@Control. Firstly, the integration of rigid ferromagnetic particles into the dual-responsive sheet can increase the overall modulus. The incorporation of magnetic particles within the polymeric sheet reduces the overall flexibility due to a higher resistance of deformation, ultimately leading to a stiffer material. The reinforcement effect of inorganic nanoparticles for hydrogels has been reported previously but offers here still enough flexibility to take on magnetically-induced shapes and various modes of induced locomotion [241]. Secondly, the reaction time, and thus, the kinetics, of the free radical polymerization of pNIPAM@Control compared to THANOS sheets differs significantly. This effect may alter the crosslinking density, which will ultimately influence the resulting rheological properties of the sheet.

5.3.3 Thermo-responsive Behaviour of pNIPAM Sheets

As described previously, pNIPAM networks are thermo-responsive, in which the VPTT refers to the temperature under which the polymeric network switches from a swollen to a collapsed state by absorbing or repelling water from the polymeric network [235]. Below the VPTT, pNIPAM shows hydrophillic characteristics and undergoes hydrogen bonding with water molecules via the amide groups of the polymer and is therefore in the swollen/hydrated state. Typically, the VPTT of pNIPAM hydrogels is around 32°C [242]. At this temperature the polymer undergoes conformational change and starts to collapse under which the hydrogen bonds to

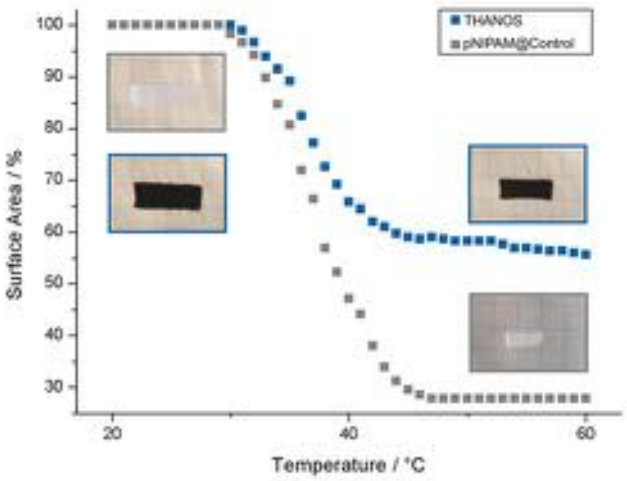

Figure 5.3: Characterization of the VPTT by plotting the percentage of the surface area based on the swollen state of pNIPAM@Control (grey) and THANOS (blue) against the temperature.

water weaken. The polymeric network becomes more hydrophobic. However, several factors, such as the crosslinking density, presence of salts and ionic species in the solution, and the polarity of copolymers influence the VPTT [243]–[248]. Typically, copolymerization with more hydrophobic comonomers will shift the VPTT towards higher temperatures, whereas increased hydrophilicity of comonomers decreases the VPTT.

To characterize the temperature responsive behavior of pNIPAM-based sheets, the surface area of each sheet has been plotted against the temperature. For a better visualization of the reduction in surface area upon elevating the temperature, sheets with a dimension of 30x10mm were used. The surface area is plotted against the temperature, in which 100% on the y-axis represents the surface area of the sheet in the swollen state at room temperature. Figure 5.3 displays the thermo-responsive characteristics of THANOS and pNIPAM@Control sheets at temperatures between 24°C-60°C by gradually increasing the temperature of the water bath in steps of 1°C/min. The VPTT of THANOS and pNIPAM@Control is at 37°C. As mentioned earlier, pNIPAM typically exhibits a VPTT at 32°C. The variance in the VPTT observed in both pNIPAM@Control and THANOS can be attributed to the overall chemical composition of the polymeric sheets.

Furthermore, THANOS has a maximum surface area shrinkage of 44%, while pNIPAM@Control shows a 72% reduction in surface area upon elevated temperatures. The significant reduction in the shrinkage capability of THANOS can be explained by the integration of rigid ferromagnetic particles, ultimately, limiting the flexibility of the polymeric chains.

Additionally, the time dependant shrinking capability of THANOS and pNIPAM@Control at 50°C was examined. At 50°C a fully collapsed state of both sheets is expected. For this purpose, each sheet was placed from a water bath at room temperature to a heated water bath at 50°C and the reduction of the surface area was subsequently plotted against the time (Figure 5.S1). The shrinking capability is fast and the maximum reduction in surface are after 45s for both pNIPAM@Control and the THANOS sheet. The overall reduction shows only a slight deviation in the maximum shrinking capability when compared to the results obtained by gradually increasing the surrounding temperature (Figure 5.3). Therefore, it can be concluded that an instantaneous increase in temperature leads to similar shrinking results.

5.3.4 Magnetic-responsive Behaviour of the Robot

The mechanical behaviour of the robot under an external magnetic field is studied using simulations and experiments. Three magnetic profiles are investigated: S, L and C. A setup consisting of six electromagnetic coils arranged in a Helmholtz configuration with a workspace of 12×12×12 cm is utilized for magnetic actuation (see Figure 5.S4). This setup can generate a uniform magnetic field of up to 50 mT in any given direction. Two cameras are employed for observing and recording the top and side views of the experiments.

Cosserat rod theory-based model is utilized to simulate the deformation of the robot. The detailed modelling method is described in **Section A, Supporting Information**. A comparison between experiments and simulation results on the deformation of the three magnetic profiles are shown in Figure 5.4(c-e). The results indicate that the deformation of the robot increases rapidly at lower magnetic fields and plateaus out around 10 mT. This phenomenon arises due to the decrease in magnetic torque acting on the robot body as the magnetic particles within the robot body align with the direction of the magnetic field. More simulation and experiment

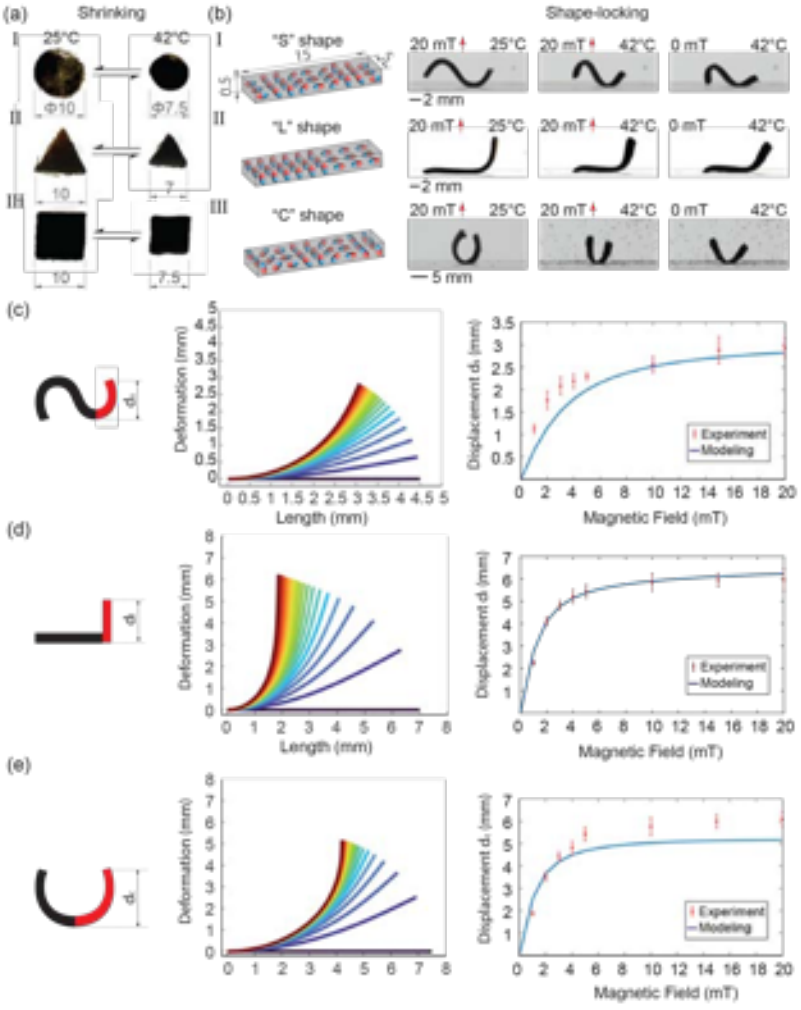

Figure 5.4: Thermal-shrinking and shape-locking features of the dual responsive sheets. (a) Reversible thermal shrinking of different shapes, namely circular (I), triangular (II) and rectangular (III). Dimensions are in mm. (b) Magnetic programming and shape-locking property of three typical geometry shapes are shown. The magnetization profile of each shape is indicated in the first column of figures. The red solid arrows indicate the direction of the applied magnetic field. Simulation results of deformation of the (c) "S", (d) "L" and (e) "C" shaped robot. The deformation of the right quarter of the robot under increased magnetic field strength from 0 mT to 20 mT is shown in the middle graph. Both experiment and simulation results of the displacement of the right tip are shown in the right graph.

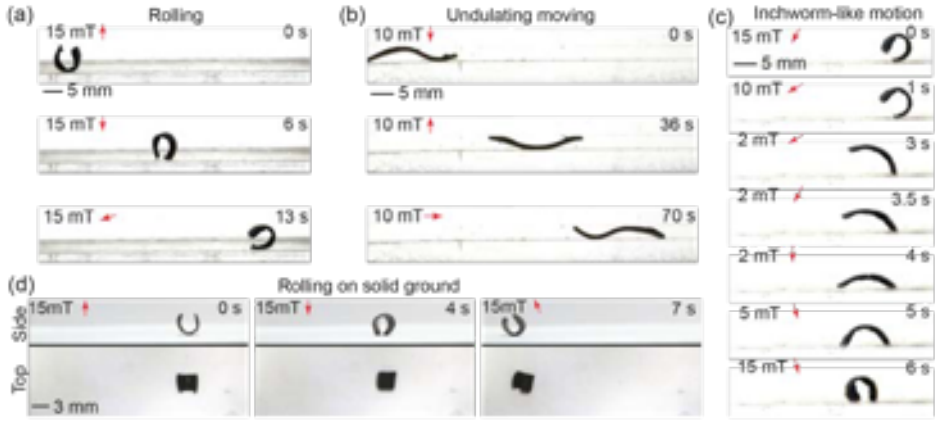

Figure 5.5: Demonstration of multimodal locomotion of the sheet-shaped robot. (a) The robot exhibits the ability to roll underwater using a rotating magnetic field at 15 mT and 0.2 Hz. (b) The robot executing undulating movements within a channel with a height of 3 mm, achieved under a rotating magnetic field at 10 mT and 0.2 Hz. (c) The robot's capacity to perform inchworm-like motion underwater by applying a specialized swing magnetic field as shown. (d) The robot, at a semi-dried status, showcases the capability to roll on solid ground outside water, propelled by a rotating magnetic field at 15 mT and 0.2 Hz.

results can be found in Figure 5.S5 - Figure 5.S9.

It is important to note that the shrinkage of the robot results in changes not only in its volume but also in the relative concentration of magnetic powder within the robot. As a result, the magnetic moment which actuates the robot also changes. Figure 5.S7 illustrates the impact of powder concentration on the deformation of the robot under magnetic field strengths ranging from 0 mT to 10 mT. It demonstrates that displacement increases rapidly at low powder concentrations and gradually at higher concentrations. Additionally, the shrinkage of the robot results in an increase in stiffness. The effect of robot stiffness on displacement under magnetic fields ranging from 0 mT to 20 mT is studied and depicted in Figure 5.S8. It is evident that higher stiffness leads to a reduction in robot deformation.

5.3.5 Thermo-magnetic Dual Responsive Properties

The pNIPAM sheet mixed with magnetic particles responds to both environment temperature and external magnetic field. The design flexibility of

the sheet enables the creation of various planar shapes through mold design. In order to demonstrate the isotropic shrinkage, three different shapes (circle, triangle, square) are tested as shown in Figure 5.4(a) (**please refer to supplementary video**). A setup is designed to control the temperature of the water in a tank. Temperature adjustments are achieved by utilizing a resistance heater for heating and pumping of cold water for cooling. In accordance with the VPTT results, the water temperature is calibrated to reach up to 50°C. The initial dimensions of the planar sheet are measured at room temperature (25°C), while the shrunken size is determined at the completion of the shrinking process (42°C). As illustrated in Figure 5.4(a), the sheets show isotropic shrinkage as they retain their original shapes in the collapsed state, which further demonstrates a homogeneous distribution of magnetic particles inside the polymeric matrix.

By programming the magnetization profiles, the sheet can undergo deformation into predefined shapes when subjected to an external magnetic field. Simultaneously, the stiffness of the sheet exhibits an upward trend with increasing temperature. Consequently, the shape induced by the external magnetic field can be locked in place upon reaching the completed shrinking point, subsequent to the removal of the magnetic field. Figure 5.4(b) (**please refer to supplementary video**) showcases the programmable magnetization and shape-locking characteristics of the sheet, featuring the letters "S", "L", and "C". Initially, a constant magnetic field is applied in a fixed direction, as indicated by the red arrows in the figure. The magnetic particles within the sheets align with the magnetic field direction, generating a magnetic torque on the sheet and inducing the intended deformations. During this process, the water is heated while maintaining the magnetic field to preserve the formed shape.

We determined the VPTT of THANOS and pNIPAM@Control to be 37°C, which is the state where the gel is between fully swollen and fully collapsed. The fully shrunken state is needed for the shape locking which is reached at 42°C (see Figure 5.3). Therefore, the ultimate shapes are conclusively locked at 42°C simultaneously with the deactivation of the magnetic field. While here external heating is used to induce the collapse of the network, it is known that hyperthermia approaches (heating by alternating magnetic fields) is also possible with pNIPAM [249].

5.3.6 Multimodal Locomotion of the Sheet-shaped Robot

The locomotion capabilities of the minimally designed (sheet structure) robot are demonstrated across various motion patterns and environmental settings (**please refer to supplementary video**). Specifically, the "C" shaped magnetized sheet is chosen for this study to showcase the robot's motion abilities. Under the influence of a rotating magnetic field, the robot adeptly executes underwater rolling, as depicted in Figure 5.5(a). The robot further demonstrates its capacity to move within a channel through undulating wave motions induced by a rotating magnetic field, as illustrated in Figure 5.5(b). Moreover, the robot exhibits the ability to navigate underwater in an inchworm-style gait by employing a swing magnetic field, as evidenced in Figure 5.5(c). Notably, the robot can also transition to terrestrial locomotion by rolling on solid ground outside an aqueous environment. This transition is achieved by eliminating water from the robot inner body to increase the magnetic particle concentration and removing residual water on the body surface to reduce the adhesion force on the solid ground, as depicted in Figure 5.5(d). The dehydration process is executed using a hot wind gun. The amphibious locomotion ability broadened the potential application area of the robot.

To compare the aforementioned motion patterns, the displacement per motion cycle is experimentally calculated for each motion pattern under magnetic fields ranging from 0 mT to 20 mT and magnetic frequencies ranging from 0.1 Hz to 1 Hz. The comparison results (shown in Figure 5.S9) reveal that rolling motion exhibits the highest displacement per actuation cycle, whereas undulating motion demonstrates the lowest. Notably, the speed of rolling on solid ground is lower than that underwater, primarily due to changes in the robot's dimensions caused by the absence of water within its body.

5.3.7 Multifunction of the Robot

Based on the properties of thermal shrinking, shape locking and magnetic actuation, the robot exhibits a unique capability to reach target locations and perform specialized functions that pose challenges for other magnetic soft robots. As shown in Figure 5.6(a) (**please refer to supplementary video**), the robot, after undergoing shrinking, successfully navigates

Figure 5.6: Demonstrations of robot maneuverability and functions. (a) and (b) The robot capability of transition from a spacious channel to a narrower channel by changing the size of the robot. (c) The robot can be controlled to navigate in a maze-like structure. (d) The robot is able to pick up, transport and release an object ($3 \times 3 \times 3$ mm cube) to a target place by the control of magnetic field and temperature.

through a narrow channel (4.5 mm in height), overcoming its original diameter of 6 mm at room temperature. Similarly, by elevating the water temperature, the robot adeptly maneuvers through a narrow channel (3 mm in width), which is narrower than its initial width of 5 mm, as illustrated in Figure 5.6(b) (**please refer to supplementary video**). The steering of the robot is accomplished by adjusting the tilt angle of the rotating magnetic field plane (for detailed control methodology, refer to our previous work) [93]. This maneuverability is demonstrated as the robot navigates a designed maze, as shown in Figure 5.6(c) (**please refer to supplementary video**). The pick-and-place function is exemplified in

the subsequent experiment depicted in Figure 5.6(d) (**please refer to supplementary video**). Initially, the robot rolls up and flips to cover an object, specifically a $3 \times 3 \times 3$ mm 3D printed PLA cube. Upon increasing the temperature to 45°C, while maintaining the magnetic field, the robot undergoes full shrinkage, successfully grasping the object. The shrunken robot, along with the object, is then flipped back and rolled to the target location under magnetic field control while maintaining the temperature at 45°C. Upon reaching the target location, the magnetic field is deactivated, and the water temperature is lowered by circulating cold water into the tank and removing the heated water from it. Subsequently, the robot reverts to its original size and soft state, leading to the release of the object at the target location.

5.4 Discussion

The experimental results support the characterization results. By increasing the temperature of the environment, we observed the changes on the size of the sheets. It is worth noting that THANOS robots undergo isotropic shrinkage, ultimately validating the homogeneous distribution of particles within the polymeric matrix as shown in Figure 5.4(a). Enhancing the molding process can result in improved precision and refinement of the edges and shapes of the sheets. Also, more complicated planar shapes can be made based on the fabrication method presented in this paper. Furthermore, exploring the potential of employing advanced manufacturing techniques such as photolithography or 3D printing is intriguing, as it could enable the downsizing of the robot, making it more accessible to confined and enclosed spaces for potential medical applications that are otherwise difficult to reach [238], [250]–[252]. However, validation is essential; for instance, rheological modifiers are sometimes necessary for 3D printing, which may ultimately impact the resulting mechanical properties of the robot but there are alternatives available that offer the same control and network formations as depicted in the THANOS system [253].

The locomotive capabilities of the robot in the swollen state are demonstrated through the actuation using magnetic field. This work presents various motion patterns, including rolling, undulating, and inchworm-like motion. The frequency of the rotating magnetic field utilized for rolling and undulating movements is set at 0.2 Hz, with the possibility of enhanc-

ing movement speed by adjusting the frequency in accordance with specific requirements.

Typically, hydrogel-based magnetic soft robots can only be actuated underwater due to the buoyancy provided, which overcomes body weight and compensates for the low actuation force/torque. It is noteworthy that in the collapsed state, the THANOS robot demonstrates the ability to move on solid ground outside water, a phenomenon not previously observed. This capability arises from the temperature responsive behavior of the hydrogel, in which an increase in temperature weakens hydrogen bonding of the amide groups of pNIPAM with water, ultimately resulting in an increase in hydrophobic interactions, and thus, leading to repulsion of water. This phenomenon increases the ratio of magnetic particles within the polymeric network [254]. Consequently, the magnetic torque acting on the robot body can surpass the body weight in the air. This unique feature holds significant implications for potential future applications, particularly in medical scenarios, such as the gastrointestinal tract, where both dry and wet conditions exist. The amphibious locomotion ability of the robot shows great potential to access challenging locations that may pose difficulties for other robotic systems. Future studies with a clear biomedical application to which THANOS can be tailored in terms of mechanical/(bio)chemical/responsive properties need to confirm the locomotive capabilities and function of THANOS in environments that are relevant for the respective targeted medical application.

Within the time frame of our experiments, we could not observe any alterations of the mechanical properties of THANOS. However, future studies have to determine its degradation rate and the demagnetization behaviour of THANOS. The latter depends on the properties of the ferromagnetic particles. According to the manufacturer's specification, MQFPTM-16-7-11277 particles have a demagnetization factor of 0.21. Therefore, the particles have a relatively low susceptibility to demagnetization. Nevertheless, future investigations must study this aspect before transferring to potential applications.

Furthermore, we expect that the ratio of ferromagnetic particles not only impacts the magnetic response of the corresponding soft robot but also influences the mechanical properties of the polymeric matrix. Additionally, the size and composition of these particles are expected to play a significant role in determining the resulting properties. In this study, we focused

on achieving complex locomotion of THANOS by using a straightforward synthesis method. Moving forward, further investigations into the optimal ratio, composition, and size of the ferromagnetic particles embedded in the polymeric matrix, as well as the monomer-to-crosslinker ratio, is necessary to obtain optimal properties for the desired application.

As mentioned in Section 5.3.3, the VPTT of pNIPAM-based polymeric matrices can be tuned by altering its chemical composition. The current THANOS robot has a transition temperature at 37°C. For use in biomedical applications, future studies should customize the VPTT to align with temperatures closely resembling physiological conditions. Furthermore, alternative heating methods must be incorporated since heating through adjustments in the surrounding temperature would not be feasible. Consequently, either infrared irradiation or hyperthermia approaches would be necessary [255].

Future studies need to verify the temperature response of THANOS using the above mentioned techniques. However, one can also envision the inclusion of other responses that can be more in line with biological environments such as stimulated bioadhesion [256], [257]. Besides tailoring the VPTT, future investigations should explore the integration of additional external stimuli, such as light or pH, within the polymeric matrix to ultimately broaden the applicability of these systems [258]. The locomotion capabilities of the robot can be enhanced for applications in real body environments, such as biological tissues covered by a layer of mucus. Such a coating could also potentially enhance the robot's biocompatibility and prevent leakage of magnetic particles [121].

5.5 Conclusions

This study introduces a dual-responsive thermo-magnetic soft robot, combining the advantages of temperature-responsive polymeric networks and magnetic actuation. The integration of ferromagnetic particles inside a pNIPAM matrix results in a versatile robot with programmable responses to both temperature changes and external magnetic fields. The synthesis method, employing a one-step temperature-induced free radical polymerization with controlled cooling, ensures a straightforward fabrication process. The extremely short reaction time results in a homogeneous distribution of magnetic particles inside the polymeric network.

The presented soft robot exhibits a range of complex locomotion patterns, including rolling, undulating, gripping, and inchworm-like motion achieved through magnetic actuation. The shrinkage ability at elevated temperatures enables the robot to perform dual locomotion tasks for pick-and-place maneuvers of objects. Firstly, the robot can be immobilized in a gripping state by magnetic actuation. Subsequently, the shape is locked under continuous magnetization by raising the temperature. Above the VPTT of pNIPAM, the polymer matrix goes from a swollen to a collapsed state. This enables the robot to grab an object and maintain the desired shape autonomously, eliminating the necessity for continuous magnetic control. Secondly, the dual responsive behaviour allows the robot to reach the target location by magnetic field control. Ultimately, the object is released by decreasing the temperature, in which the robot transitions back to the initial swollen state.

Overall, this dual-responsive thermo-magnetic soft robot presents a promising advancement in the field of soft robotics, offering a versatile platform with intriguing possibilities for applications in biomedical domains, such as surgical procedures, where controlled and programmable responses to environmental stimuli are crucial.

5.6 Supporting Information

5.6.1 Section A: Supporting Notes

To assess the mechanical behavior of the robot subjected to pre-designed magnetization profiles under an external magnetic field, we utilize a model based on Cosserat rod theory. Additionally, this model aids in the robot's design process. In this model, the robot is conceptualized as a flexible rod (along the long axis of the robot), firmly attached at its proximal end to a rigid base while being free to move at its distal tip.

This Cosserat rod model is coupled with magnetization profiles and magnetic fields, allowing us to simulate the deformation of the robots. Each rod is characterized by its centerline curve in three-dimensional space, denoted by $s \in [0, l]$, where $l \in \mathbb{R}^3$ represents the length of the robot. The discretized cross-section along s can be succinctly expressed by a material state vector:

$$\boldsymbol{y}(s) = [\mathbf{R}(s),\ \mathbf{p}(s),\ \mathbf{n}(s),\ \mathbf{q}(s)]\,, \tag{5.1}$$

where $\mathbf{R}(s)$ is the rotation matrix of the material orientation, $\mathbf{p}(s)$ represents the global position in Cartesian coordinates, $\mathbf{n}(s)$ is the internal force in the global frame, and $\mathbf{q}(s)$ is the internal moment in the global frame.

The actuation magnetic field is generated using 3D electromagnetic coils (shown in Figure 5.S4), designed to produce a uniform magnetic field within the workspace. Therefore, the contribution of the magnetic field gradient is assumed to be negligible, and the applied force distribution per unit of s is denoted as $\mathbf{f}(s) = 0$. Additionally, gravity is disregarded in this study. The applied torque distribution per unit length of s, $\boldsymbol{\tau}(s) \in \mathbb{R}^3$, is given by:

$$\boldsymbol{\tau}(s) = \mathbf{m}(s) \times \mathbf{B}, \tag{5.2}$$

where $\mathbf{B} \in \mathbb{R}^3$ is the magnetic flux density, and $\mathbf{m}(s) \in \mathbb{R}^3$ is the magnetic dipole moment per unit length, defined as:

$$\mathbf{m} = \frac{1}{\mu_0} B_r V_{\text{rob}} = \iiint_{V_{\text{rob}}} \mathbf{M}_{\text{rob}}\, dV, \tag{5.3}$$

where μ_0 is the vacuum permeability, B_r is the residual flux density, V_{rob} is the volume of the robot, and $\mathbf{M}_{\text{rob}}$ is the magnetization of the robot.

The equilibrium differential equations for the Cosserat rod are:

$$\dot{\mathbf{n}}(s) + \mathbf{f}(s) = 0, \tag{5.4}$$

$$\dot{\mathbf{m}}(s) + \dot{\mathbf{p}}(s) \times \mathbf{n}(s) + \boldsymbol{\tau}(s) = 0, \tag{5.5}$$

where the dot denotes the derivative with respect to s.

The boundary value problem defined by the Cosserat rod equations is solved using the fourth-order Runge-Kutta method, implemented in MATLAB (2021a, MathWorks, USA). The measured residual flux density and the density of the magnetic particles used in this study are 911 mT and 7.61 g/cm^3, respectively.

5.6.2 Section B: Supporting Figures

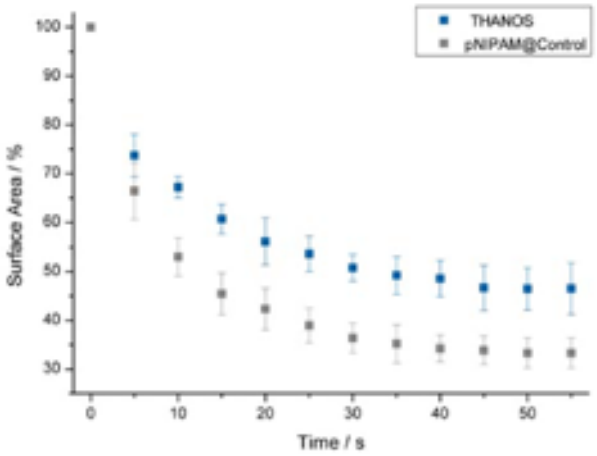

Figure 5.S1: Characterization of the time-dependent shrinking capability of **THANOS** (blue) and **pNIPAM@Control** (grey) at a temperature of 50°C.

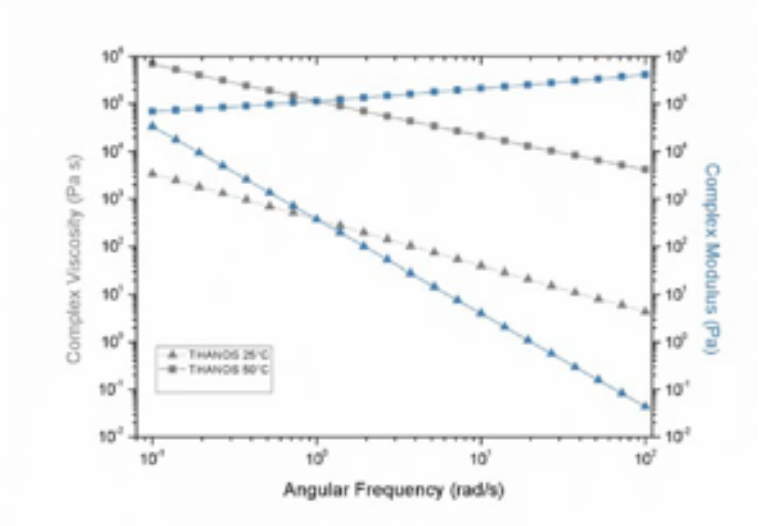

Figure 5.S2: Complex viscosity (grey) and complex modulus (blue) of **THANOS** as a function of angular frequency. Triangles indicate the values of **THANOS** at 25°C, while rectangles indicate the values at 50°C.

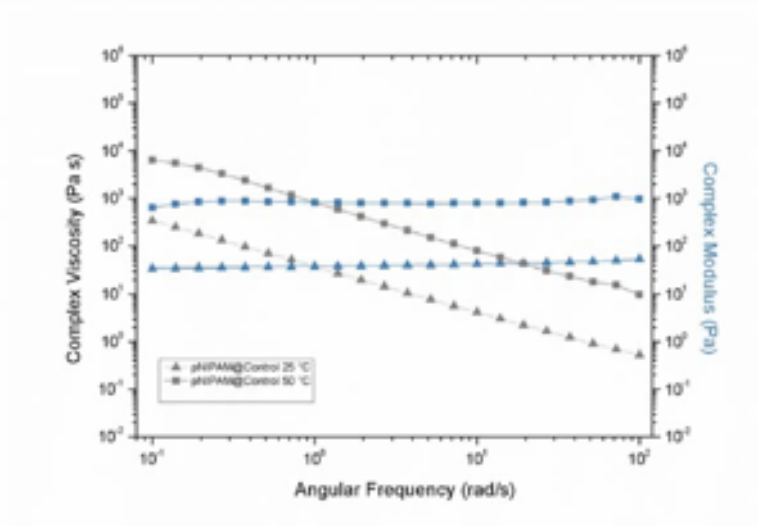

Figure 5.S3: Complex viscosity (grey) and complex modulus (blue) of **pNIPAM@Control** as a function of angular frequency. Triangles indicate the values of **pNIPAM@Control** at 25°C, while rectangles indicate the values at 50°C.

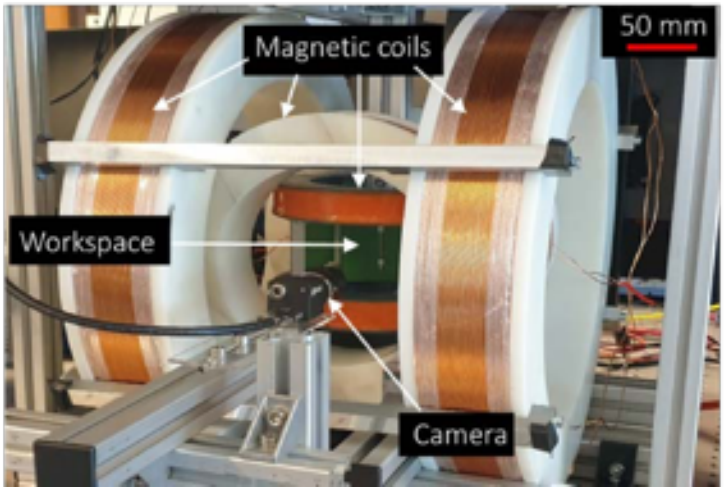

Figure 5.S4: Magnetic actuation setup.

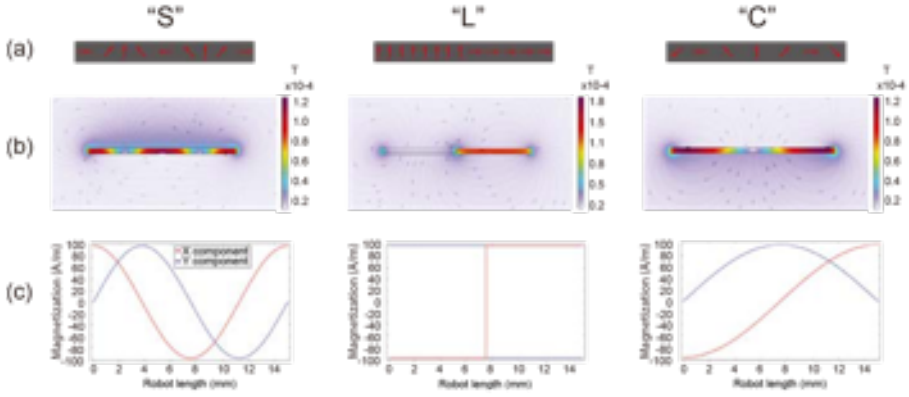

Figure 5.S5: (a) Designed magnetization profile (shown in red arrows), (b) the magnetic flux density, and (c) magnetization strength and direction (in X and Y components) of the "S", "L", and "C" shaped robots.

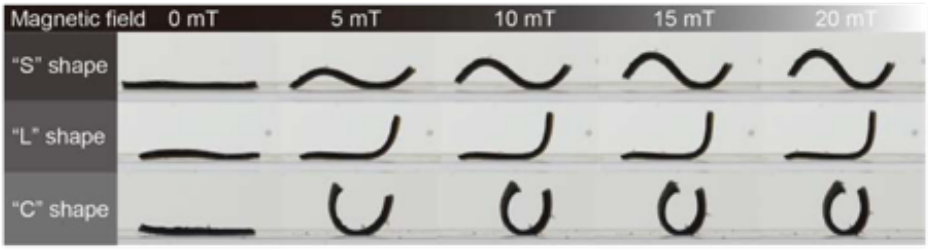

Figure 5.S6: Snapshots of experiments showing the deformation of the "S", "L", and "C" shaped robots as the magnetic field increases from 0 mT to 20 mT.

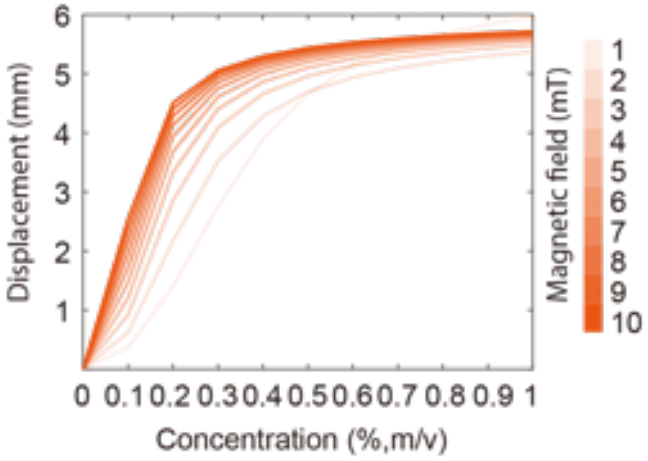

Figure 5.S7: Simulation results showing the influence of magnetic particle concentration on the displacement of the "L" shaped robot. The applied magnetic field is increased from 1 mT to 10 mT.

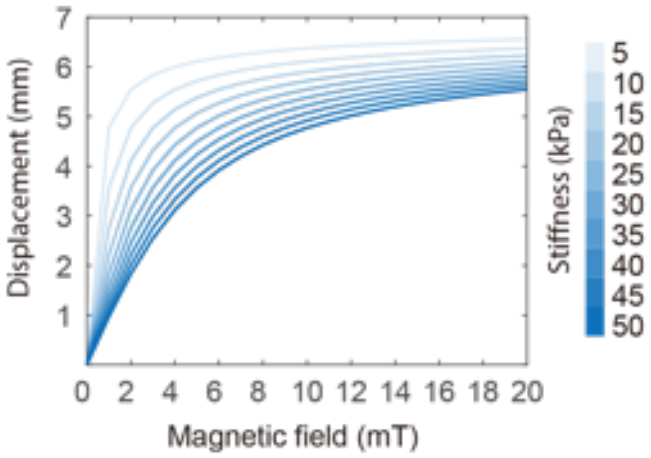

Figure 5.S8: Simulation results of the influence of robot stiffness on the displacement of the "L" shaped robot. The applied magnetic field is increased from 1 mT to 20 mT.

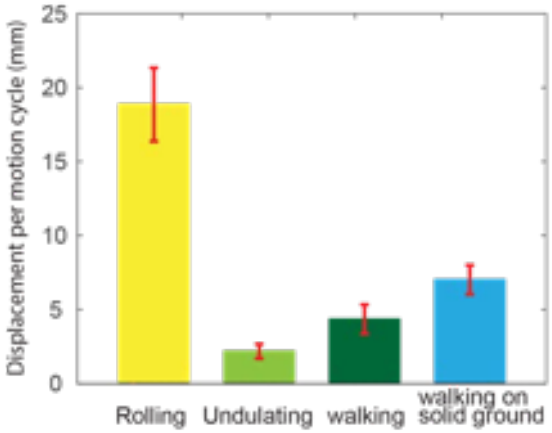

Figure 5.S9: Experimental results: comparison of the displacement per motion cycle of the four motion patterns. Displacements are measured under different magnetic field strength and frequency.

5.7 Supplementary Video

Video: Minimally designed thermo-magnetic dual responsive soft robots for complex applications

Video link: https://www.youtube.com/watch?v=elRkZP9ZNEI

6

Electronics-free Soft Robotic Minitablet for On-demand Gastric Molecular Sensing and Diagnostics *in vivo*

Note: *This chapter is adapted from the article "Electronics-free soft robotic minitablet for on-demand gastric molecular sensing and diagnostics in vivo" by* ***C. Wang****, R. Shi, A. Abalymov, H. Bao, T. K. LAM, Z. Wang, Y. Mei, Z. Cai, X. Chen, S. Misra, V. K. Venkiteswaran, Science Advances, Under review.*

Abstract

Monitoring gastric physicochemical parameters enables real-time assessment of gastrointestinal disorders, while *in situ* sampling of gastric fluid supports precise molecular diagnostics. Integrating both functions within a single device improves diagnostic efficiency and patient experience. Existing ingestible devices face challenges in sensorization, miniaturization, and biocompatibility due to the incompatibility between soft bodies and rigid electrical components. Here we introduce SeroTab, a sensorized ingestible soft robotic minitablet that enables real-time pH sensing and on-demand sampling of gastric juice *in vivo*. Drawing inspiration from the streamlined sliding motion of penguins, SeroTab combines magnetic actuation with a curvature-adaptive structure to autonomously traverse anatomical obstacles and reach the targeted gastric region. Gastric fluid is actively absorbed into an internal chamber (up to 35 μL) by a shape memory polymer actua-

tor triggered by external RF heating. A pH-responsive hydrogel inside the chamber absorbs the fluid for untargeted metabolomic analysis and enables ultrasound-based pH sensing via swelling of embedded biocompatible metal disks (pH 2–7). *In vivo* experiments in animal models illustrate the ability of SeroTab to non-invasively detect pH shifts and metabolic alterations induced by omeprazole administration. The results support SeroTab's potential to simplify early-stage screening and enable out-of-hospital diagnostics upon detecting physiological abnormalities, streamlining patient triage and decision-making in primary care.

6.1 Introduction

The global burden of gastrointestinal (GI) diseases remains substantial, with an estimated 7 billion incident cases and 8 million deaths annually, exacerbated by constrained medical resources and delayed patient access to care [259], [260]. Timely and effective GI disease diagnosis and patient triage at the primary care level can alleviate hospital burden and improve patient outcomes [261]. Many countries adopt tiered healthcare systems in which general practitioners (GPs) serve as gatekeepers, managing patient flow and easing hospital demand [262], [263]. However, GPs often face diagnostic uncertainty, partly due to limited access to advanced tools and the high cost of precision diagnostics, leading to diagnostic delays and further straining hospitals. Basic diagnostic tools available in primary care (e.g., pulse oximetry, basic auscultation devices and ultrasound imaging) are predominantly designed for initial screening and general physiological monitoring [264]. While these devices aid GPs in identifying deviations from baseline health, they typically fall short in sensitivity, specificity, or biomarker resolution necessary for definitive diagnosis of complex or organ-specific pathologies. Overcoming these challenges necessitates the development of innovative point-of-care diagnostic devices capable of delivering rapid, accurate assessments within primary care settings [261], [264].

GI disorders are common in primary health care, accounting for approximately 10% of consultations [265]. Among GI diagnostic targets, gastric acid serves as a crucial pathophysiological indicator correlated with a spectrum of GI dysfunctions, including gastroesophageal reflux disease (GERD), gastric ulcer, gastroenteritis, and gastric cancer [266]–[268]. Clinical assessment of gastric acid secretion requires both rapid and precise ex-

amination of gastric juice samples obtained from the lesion site, necessitating on-site detection of physicochemical parameters (e.g., pH, temperature, and pressure) for urgent medical care, alongside comprehensive laboratory analysis of biological omics profiles (e.g., proteomics, metabolomics, and the microbiome) to elucidate disease biomarkers and track disease progression [269], [270]. The traditional aspiration test for sampling the gastric juice [271] requires the placement of a nasogastric tube into the stomach, leading to patient discomfort and contraindications [272]. Recent advances in personalized medicine have brought forth orally administered, tetherless electronic capsules (e.g., Heidelberg^{TM} [273], PillCam^{TM} and VitalSense^{TM} capsules), offering non-invasive detection of gastric fluid parameters [274], [275]. However, the passive movement of these devices, driven solely by digestive tract peristalsis, limits their ability to conduct targeted sampling and precise sensing [276]. Additionally, these electronic sensing devices face challenges in miniaturization, power supply, and biocompatibility.

Emerging magnetic soft robots combine active control and biocompatibility, enabling precise navigation of small-scale agents within the human body for accurate diagnostics, localized treatment, and therapeutic interventions [277], [278]. By programming soft materials with specific magnetization profiles, robots are endowed with locomotion and deformation capabilities, allowing them to adapt to *in vivo* environments and access confined spaces under the control of external magnetic fields [279]–[282]. In combination with functional materials and external stimuli, the robots can be equipped for clinical treatment [276], [283], [284]. For instance, magnetically actuated robotic capsules/tablets/pills [285] have demonstrated potential in performing liquid sampling [66], [286], tissue biopsy [63], [287], drug delivery [288], and microbiome collection [75], [289], [290] at targeted sites. Robots have also been developed with integrated sensing capabilities for rapid diagnosis and real-time physiological monitoring. Methods for sensorizing magnetic soft robotic devices are generally classified into two categories: direct and indirect. Direct sensing entails the integration of microelectronic systems [76], [77], [288], [291], whereas indirect sensing leverages the mechanical deformation of the robot's structure in synergy with multimaterial configurations [69], [70], [78]–[80], [292], [293], assisted by external medical imaging systems (e.g., ultrasound (US), X-ray, and computed tomography (CT)) [81], [82]. The direct sensing approach encounters challenges related to the integration of soft and rigid materials as

well as electromagnetic interference, while the latter demands innovations in materials and communication strategies. Additionally, the use of entirely soft materials holds great promise for improving operational safety and biocompatibility [294], while also requiring further innovation in the integration of biocompatible sensing elements with compliant actuators.

Here, we introduce SeroTab, a sensorized ingestible soft robotic minitablet designed to enable simultaneous pH sensing and liquid sampling for pre-diagnostics and biomarkers collection at precise locations within the GI tract. SeroTab's sliding locomotion, inspired by the movement of penguins, is facilitated by the optimized interaction between an external magnetic field and the embedded ferromagnetic material within the device. The liquid sampling function, enabled by a shape memory polymer (SMP), is remotely activated using an external RF heater operating at a body-safe temperature. A pH sensitive hydrogel component, engineered with a tailored structure to create a pronounced acoustic impedance contrast, enhances its detectability via ultrasound imaging. Simultaneously, the hydrogel absorbs and retains gastric fluid, preserving the sample for biomarkers analysis after retrieving. We evaluate SeroTab's locomotion, sampling, and sensing capabilities in lab-designed setups and *ex vivo* swine organs. Real-time gastric pH data is successfully acquired in rabbit models *in vivo*. Biomarkers are extracted from the retrieved hydrogel after operation, and metabolomics analysis is conducted based on the mass spectrometry analysis. The results demonstrate SeroTab's ability to perform both rapid and precise non-invasive gastric diagnostics.

6.2 SeroTab Design, Functions, Operating Principle and Envisioned Medical Application

The SeroTab, featuring a soft, biocompatible, and wirelessly-actuated design, serves as an ingestible robotic platform for non-invasive access to gastric environments (Fig. 6.1A and 6.S1). The device is designed for comprehensive physiological assessment at targeted gastric sites, enabling early screening and accurate diagnosis of gastric disorders. The detection process is divided into two stages: on-site pH sensing of gastric juice for rapid pre-diagnosis, followed by on-demand gastric fluid sampling for precise mass spectrometry analysis after retrieval. Targeted locomotion is

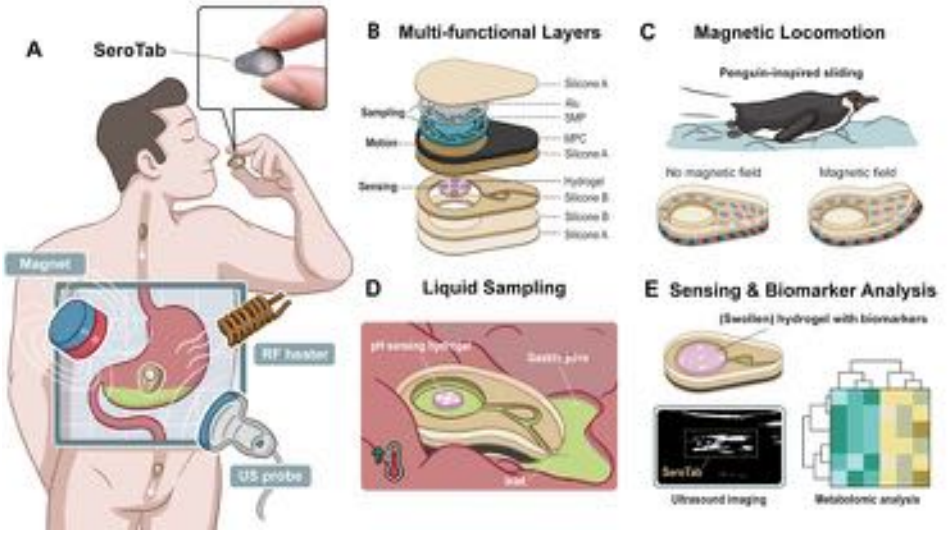

Figure 6.1: **Sensorized ingestible soft robotic minitablet (SeroTab) for on-demand pH detection and biomarker collection of gastric juice.** (**A**) Ingestion process and magnetic navigation of SeroTab to a targeted stomach site, followed by heat-triggered gastric juice sampling and ultrasound-assisted pH sensing. (**B**) Exploded-view schematic illustrating the device's multi-material composition, featuring an internal channel-cavity structure and three key functional components: (**C**) Magnetic-polymer composite (MPC) layer enabling penguin-inspired magnetically actuated locomotion. (**D**) Alu-SMP layer for heat activated liquid pumping. (**E**) Hydrogel-based ultrasound-readable structure designed for on-site pH sensing and post-analysis of biomarkers.

achieved through external magnetic navigation guided by ultrasound (US) imaging (Fig. 6.1A). Upon reaching the desired gastric site, an external RF heater induces localized heating within the device to initiate gastric fluid sampling (Fig. 6.1A). The pH-sensitive hydrogel embedded in the device swells upon contact with the sampled fluid, and its mechanical response is subsequently visualized via US imaging, enhanced by the inclusion of acoustic contrast agents within the hydrogel matrix (Fig. 6.1A). The hydrogel exhibits effective pH responsiveness across the range of 2 to 7, achieving a maximum swelling ratio of up to 62% within the SeroTab. Following the pH sensing phase, the SeroTab is retrieved from the body, and the hydrogel is extracted for mass spectrometry analysis to enable precise disease diagnosis.

Fig. 6.1B illustrates the structure of the SeroTab through an exploded view, highlighting its planar-stacked architecture that enables the integration of multifunctional components within a compact volume. At the core of the device lies a hollow cylindrical chamber (38.5 μL capacity) designed for fluid collection, which is accessed through a microfluidic channel incorporating a Tesla valve to promote unidirectional flow and minimize backflow or leakage (Fig. 6.S12). A hydrogel sensor that swells in response to pH is placed inside the chamber and embedded with metal discs to enhance acoustic visibility and enable real-time dimensional tracking via ultrasound. The chamber is sealed with thin silicone rubber membranes on both faces to prevent fluid escape. A cylindrical cavity on top hosts a shape memory polymer (SMP) actuator, functioning as a sampling pump, with a conformal aluminum layer adhered on top to enhance localized heating. Above the housing layer, a silicone rubber sheet embedded with magnetic particles facilitates external magnetic actuation. All layers are seamlessly integrated using a layered printing fabrication approach (Fig. 6.S2), ensuring robustness, biocompatibility, and watertight sealing suitable for gastric deployment.

The navigation of SeroTab within the body, after being swallowed, is facilitated by an external magnet. Its sliding locomotion—bioinspired by the streamlined gliding motion of penguins (left, Fig. 6.1C)—is enabled through magnetic actuation, allowing controlled movement along tissue surfaces in a wireless and untethered manner. To enable this, the device undergoes magnetization by being fixed onto a custom fixture and exposed to a pulsed high-intensity magnetic field, resulting in a programmed magnetization profile within the magnetically responsive MPC (magnetic particle composite) layer. In the absence of an external magnetic field, the SeroTab remains in a relaxed, planar state. Upon exposure to a magnetic field generated by a permanent magnet (50-250 mT), the device aligns with the field and bends due to the magnetic torque acting on the MPC layer (right, Fig. 6.1C). By introducing a magnetic force with a moving magnet, translational sliding motion can be generated, allowing for controlled locomotion in a wireless and untethered manner.

Before oral administration, the SeroTab must undergo a training process to precondition the shape memory polymer (SMP) and enable its fluidic sampling function. This involves placing the device on a heating plate and applying mechanical pressure to the SMP surface once it has

been heated above its thermal transition temperature (40 °C) (Fig. 6.1D and Fig. 6.3A). The pressure is maintained as the SMP cools to room temperature (20 °C), thereby fixing it in a compressed, temporary shape and sealing the internal chamber. Upon subsequent exposure to radiofrequency (RF) heating within the gastrointestinal tract, the SMP recovers its original configuration, resulting in a rapid volume expansion (up to 38.5 μL within 1 minute, depending on the applied temperature) and a corresponding drop in internal chamber pressure. The resulting pressure differential passively draws gastrointestinal fluid into the chamber through the microfluidic inlet, initiating the sampling process.

Upon contact with the sampled gastric fluid, the pH-responsive hydrogel sensor undergoes a reversible volumetric swelling transition, while simultaneously absorbing the surrounding liquid (Fig. 6.1E (i)). The hydrogel is embedded with an array of biocompatible metal disks to maximize acoustic impedance mismatch with the surrounding media, thereby enhancing contrast in ultrasound imaging; their interspatial displacement, modulated by the swelling ratio, is captured in real time using an external ultrasound imaging system. This enables non-invasive, quantitative assessment of local pH variations within the gastrointestinal environment (Fig. 6.1E (ii)). After the sensing phase, SeroTab is retrieved from the body with gastric fluid retained in the hydrogel matrix. The collected sample is then subjected to high-resolution mass spectrometry, enabling comprehensive molecular profiling for biomarker identification and diagnostic evaluation (Fig. 6.1E (iii)).

6.3 Demonstration and Characterization of Magnetically Actuated Locomotion from 3D-printed Models to *ex vivo* and *in vivo* Assessments

The gastrointestinal (GI) tract exhibits a highly dynamic and anatomically complex structure, characterized by distinct mucosal folds, peristaltic motion, and a mucus layer that can either facilitate lubrication and induce adhesion (Fig. 6.S7). These factors present significant physical challenges for the locomotion and functionality of ingestible soft robotic devices. To overcome friction and mucus-related resistance during locomotion, effective control requires sufficient flexibility and actuation force, with reduced

contact area serving to minimize drag. In this section, we demonstrate the advantages of SeroTab's penguin-inspired sliding motion pattern in terms of maneuverability, transitioning from lab-designed models to *ex vivo* and *in vivo* experiments.

The wireless actuation of SeroTab relies on the interaction between the magnetic powder embedded in its body and an external permanent magnet. To quantitatively evaluate the magnetic force and torque acting on SeroTab, we develop a force-sensing platform with two embedded force transducers to measure forces in the pulling (x) and lifting (z) directions (Fig. 6.2A). A cylindrical permanent magnet (N35, 30 × Φ 45 mm) is mounted underneath allowing for the adjustment in the horizontal (d) and vertical (h) directions. The relative distance between the magnet and SeroTab determines the magnetic force and torque acting on SeroTab. Centered on the midpoint of SeroTab (fixed on the platform), we move the magnet from left to right over a 200 mm distance while varying the vertical distance from 15 mm to 40 mm (Scan area shown in Fig. 6.S5A). Force data are recorded at intervals of 10 mm and 5 mm per step, respectively.

We also conduct simulations using COMSOL Multiphysics (Version 6.3, COMSOL AB, Sweden) to analyze the SeroTab-magnet interaction. The magnetic torque ($\mathbf{M}$) induces bending of SeroTab's body (6.2), while the magnetic force ($\mathbf{F}$) consists of a pulling component (F_x) which overcomes surface friction (f), and a lifting component (F_z) which counteracts gravity (g) (6.1) (Fig. 6.2B). Magnetic field distribution maps (Fig. 6.S5A) are generated to visualize the scanned area used for calculating the magnetic field (Fig. 6.2B and Fig. 6.S5B) and magnetic force (Fig. 6.2C and Fig. 6.S5C) at varying horizontal and vertical distances. The magnetic actuation generates a maximum pulling force of 22 mN and a peak lifting force of 17 mN, offering application-dependent versatility in force direction. Higher pulling force facilitates sliding locomotion by overcoming friction and adhesion, whereas greater lifting force counteracts gravity and enables flipping of the SeroTab. In addition, magnetic torque induces bending of the SeroTab body, contributing to reduce contact area. Alternative configurations using multiple magnets to enhance locomotion are presented in Fig. 6.S5 and Fig. 6.S4.

The bending of SeroTab's body results in the elevation of its head from the ground. Depending on the magnet's distance, the head can be lifted by up to 1.75 mm (Fig. 6.2D and Movie S1). To demonstrate smooth slid-

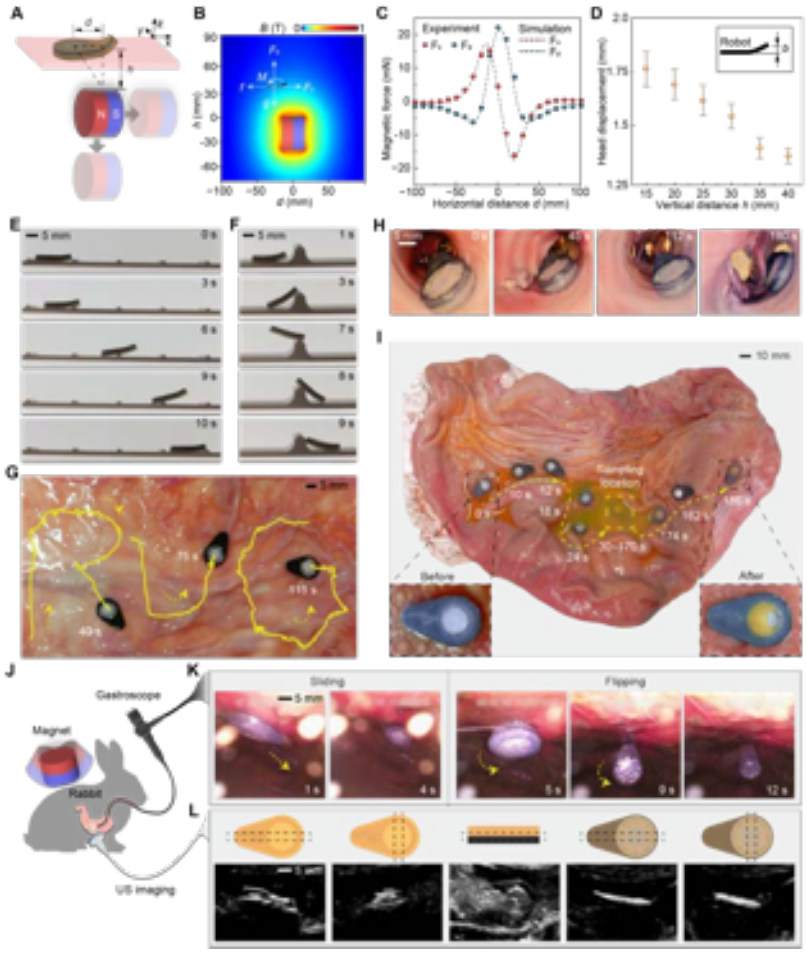

Figure 6.2: **Magnetically-actuated locomotion for targeted liquid sampling.** (**A**) Schematic illustration of the magnetic actuation mechanism and locomotion principle. (**B**) Simulated magnetic field distribution map and magnetic force analysis. (**C**) Comparison of measured and simulated pulling force (F_x) and lifting force (F_z) at 15 mm vertical distance. (**D**) Assessment of SeroTab's head-lifting displacement. (**E**) Demonstration of SeroTab' ability to overcome small obstacles and (**F**) big obstacles. (**G**) Maneuverability tests of sliding motion on tissue surface and (**H**) a tubular organ *ex vivo*. (**I**) Targeted motion and liquid sampling on an opened porcine stomach. (**J**) Schematic representation of *in vivo* testing setups. (**K**) Endoscopic observation of SeroTab's movement to assist with (**L**) visualization using an ultrasound imaging system (For comparative purposes, endoscopy was employed exclusively in this phase of the experiment alongside ultrasound imaging).

ing motion facilitated by body bending, a 3D-printed setup with 0.5 mm high obstacles is created (Fig. 6.2E and Movie S2). SeroTab overcomes the surface undulations using only the linear movement of the magnet without requiring orientation adjustments, enhancing operational practicality for clinical applications. For navigating over larger obstacles, we rotate the magnet while moving it to generate higher torque, enabling SeroTab to lift or even flip (Fig. 6.2F and Movie S2). *Ex vivo* experiments on tissue surfaces (Fig. 6.2G and Movie S3) and within tubular organs (Fig. 6.2H and Movie S4) taken from a pig demonstrate the controllability of the penguin-inspired sliding motion. A full procedure is also tested in a dissected porcine stomach containing residual gastric juice in a central pit. Starting with an empty chamber, SeroTab flips and slides into the pit, overcomes obstacles, samples the gastric juice via an RF heater, and then flips out, stopping at the target site with the chamber filled (Fig. 6.2I and Movie S5).

In vivo validation of magnetically controlled locomotion is performed in the stomach of a live rabbit (Fig. 6.2J). SeroTab is administered under light anesthesia by injecting it into the esophagus with saline, enabling voluntary swallowing prior to deep sedation. A handheld external permanent magnet, positioned above the skin near the stomach, is used to guide and anchor SeroTab at the desired location. We also use an endoscope to visualize and confirm its correct positioning, observing both sliding and flipping motions (Fig. 6.2K). Following endoscopic verification, we use an ultrasound (US) imaging system (EPIQ7c, Philips, Netherlands) to monitor SeroTab's movement and status within the stomach. It should be noted that endoscopy was used only during this phase of the experiment for comparative assessment. It is not required in other stages, as the capsule can be visualized and tracked using ultrasound alone. A reference table of US images corresponding to different orientations of SeroTab is created to assist users in identifying its posture (Fig. 6.2L). The table includes US images of the long-axis and short-axis views of Face A, the long-side edge, and the long-axis and short-axis views of Face B, arranged from left to right.

6.4 Design and Characterization of RF Heating Triggered Liquid Sampling Actuator

After reaching the targeted locations within the stomach through magnetic navigation, SeroTab initiates the sampling process in response to an external radio frequency (RF) heater (SH-2/350, UltraFlex, USA) with a rated power of 3.4 kVA and an operating frequency of 125 kHz. The embedded aluminum element heats up in response to the external RF heater applied at a distance. The generated heat is transferred to the shape memory polymer (SMP) positioned beneath the aluminum element. The SMP, designed with a specific planar structure to facilitate axial deformation, is positioned at the top of the SeroTab chamber and functions as a pump to absorb liquid through a microchannel. Once the SMP reaches its transition temperature, it begins recovering from its trained/compressed state (Fig. 6.3A). The recovery of the SMP induces a volume change in SeroTab's chamber, resulting in a decrease in air pressure inside. When SeroTab is placed in liquid, the pressure difference drives the liquid to flow into the chamber through a microchannel that connects it to the external environment.

To visualize the liquid sampling process, we position the inlet of SeroTab in a tank filled with green liquid (a green chemiluminescent solution composed of hydrogen peroxide, oxalate ester, and fluorescent dye). The RF heater, placed 10 mm behind SeroTab, continuously heats the aluminum heating receiver, triggering the recovery of the SMP. As the SMP restores its shape, the glowing liquid is drawn into the chamber (Fig. 6.3B and Movie S6). We simulate the pressure-induced sampling system based on characterized data (Fig. 6.S10, Fig. 6.S15, and Fig. 6.S16) considering capillary effect (Fig. 6.S14) and the Tesla valve (Fig. 6.S12) in COMSOL Multiphysics (Version 6.3, COMSOL AB, Sweden). The simulation results closely match the experimental data (Fig. 6.3C), validating the accuracy of our theoretical model (6.6). To ensure active sampling at the desired location and minimize contamination, the capillary effect is studied and mitigated through the design and materials of the microchannel (Fig. 6.S14). In addition, a optimized Tesla valve is incorporated in the middle of the microchannel to enhance the diodicity of the fluid flow, preventing the sampled liquid from unintentionally leaking out of the chamber during operation (e.g., due to impact load from an accidental fall). The op-

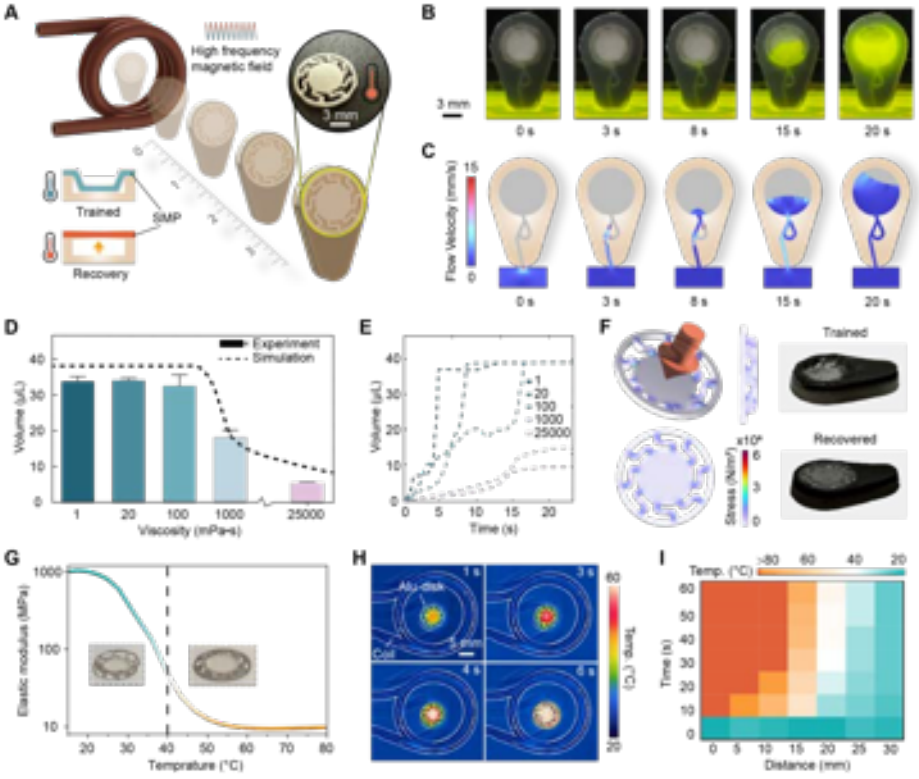

Figure 6.3: **Heat-triggered liquid sampling function.** (**A**) Schematic illustration of SeroTab being heated at various distances from the radio frequency (RF) heater. The built-in SMP actuator begins to recover upon reaching its transition temperature. (**B**) Experimental and (**C**) simulated results from sampling the fluorescent liquid. (**D**) Experimental and simulated maximum sampling volume at varying liquid viscosities. (**E**) Simulated sampling rate at different liquid viscosities. (**F**) Stress distribution of the trained SMP actuator and experimental images of SeroTab during shape training and recovery. (**G**) Temperature-dependent elastic modulus of the SMP actuator, with a transition temperature of 40 °C. (**H**) Infrared thermal images of the aluminum heating element positioned 10 mm above the RF heater coil, illustrating heat transfer and distribution. (**I**) Spatiotemporal characteristics of the temperature rise in the heating element with a 0.45 kW RF heater.

timized diodicity improves as the Reynolds number of the liquid increases (Fig. 6.S12).

We further evaluate the liquid sampling capability across different viscosities. Sodium alginate solutions with varying viscosities are prepared by adjusting the weight ratio of sodium alginate to water. SeroTab successfully absorbs up to 35 μL of liquid, with a maximum viscosity capacity of 100 mPa·s (Fig. 6.3D). Note that the designed chamber volume of SeroTab is 38.5 μL, and the viscosity of human gastric juice ranges from 1 to 10 mPa·s. The sampling efficiency declines when the liquid viscosity exceeds this threshold. The ability to sample viscous liquids depends on the recovery performance of the SMP, which can be adjusted for specific sampling scenarios (e.g., mucus) [295]. Additionally, we simulate the time-dependent sampling process for liquids of different viscosities (Fig. 6.3E) based on the measured SMP recovery rate (Fig. 6.S10) at a given temperature.

The lattice structures connecting the outer ring and inner disk of the SMP enable deformation along its axial direction, transforming it from its original planar shape. The training of the SMP is performed by heating it above its transition temperature, followed by applying and maintaining a distributed force on the inner disk. We analyze the structure mechanics of the procedure shown in Fig. 6.3F. Images of SeroTab in both its trained and recovered states are also captured. In our study, the transition temperature of the SMP is set to 40 °C by controlling the ambient temperature during the curing process. The temperature-dependent elastic modulus is experimentally characterized for a range of temperatures using a Dynamic Mechanical Analyzer (Viscoanalyser VA2000, Metravib) through tensile testing (Fig. 6.3G).

Remote heating using alternating magnetic fields offers advantages in controllability, targeting, and non-invasiveness compared to other remote heating methods such as thermochemical, photothermal, and acoustic heating [296]. To achieve an efficient heating process, we employ the Joule heating mechanism, where a high-frequency magnetic field induces eddy currents within the material. A 10 μm aluminum membrane, cut into the same shape as the SMP, is attached to it to generate and transfer heat to the SMP's wavy structures. Heat is primarily generated at the center of the membrane and then transferred to the edges through the lattice structures (Fig. 6.3H). To enhance heating efficiency while maintaining structural flexibility, an additional aluminum circular disk can be placed at the cen-

tral top of the shaped aluminum membrane. We investigate the heating performance as influenced by key variables, including the RF heater's output power, material dimensions, operating distance, and heating duration (Fig. 6.S8). Our results indicate that sufficient heating (40 °C) can be achieved within 1 minute at distances of up to 2 cm, which is considered adequate for applications in the rabbit stomach in this study (Fig. 6.3I). Lager heating distance can be readily achieved by increasing output power, or using a thicker aluminum disk, thereby extending potential applications to deeper organs or within the human body as discussed in Supplementary Materials.

6.5 Characterization and Calibration of Acoustic pH Sensor

We integrated a pH responsive sensor into the chamber of SeroTab to enable real-time chemical monitoring upon command. The sensor consists of a pH-sensitive hydrogel that undergoes swelling in response to the surrounding fluid (Fig. 6.4A), producing a mechanical expansion that can be quantified by ultrasound imaging through the integrated high ultrasound contrast metal disks (Fig. 6.4B). To achieve this functionality, we adapted a hydrogel formulation previously developed for implantable ultrasound-readable sensing applications [78] and incorporated it into our magnetically actuated robotic platform. The sensor integrated into the chamber of SeroTab consists of a pH-sensitive hydrogel that exhibits a mechanical response to surrounding liquids. This response manifests as swelling, which is driven by the chemical composition of the hydrogel. The hydrogel is synthesized using p(DMAEMA-DPAEMA) (poly[2-(dimethylamino)ethyl methacrylate-co-2-(diisopropylamino)ethyl methacrylate]), with polyethylene glycol diacrylate (PEGDA; number-average molecular weight M_n = 700) as a crosslinker. DMAEMA and DPAEMA contain tertiary amine moieties that undergo protonation with decreasing pH, leading to subsequent changes in osmotic pressure. To balance the need for both rapid response time and compact dimensions, the hydrogel is cut into circular disks with a diameter of 4 mm and thickness of 200 μm. To enable ultrasound visualization of hydrogel expansion, five circular Zn disks (1 mm in diameter and 50 μm in thickness) are embedded within the hydrogel to cre-

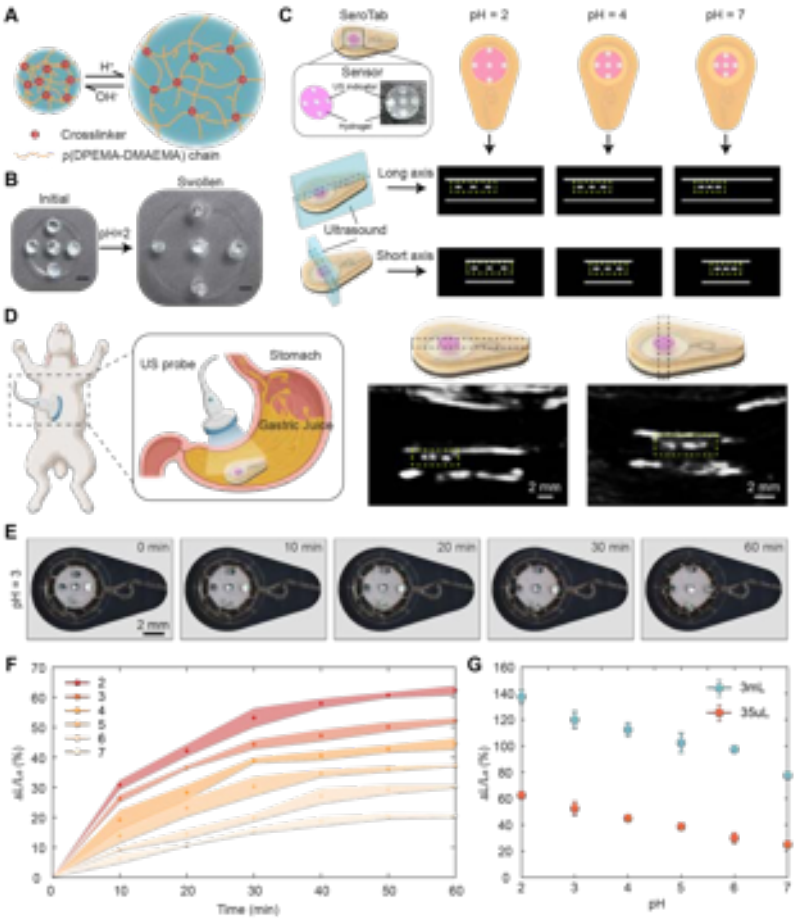

Figure 6.4: **Hydrogel-based pH sensor for ultrasonic detection.** (**A**) Schematic illustration and (**B**) experimental demonstration of the pH-responsive hydrogel swelling mechanism. The scale bar represents 1 mm. (**C**) Integration of the pH sensor within the SeroTab chamber. The distributed zinc disk inside the hydrogel enhances ultrasonic contrast, enabling detection of hydrogel size changes in response to different pH solutions. (**D**) *In vivo* verification of ultrasonic detection of SeroTab and the pH sensor in a live rabbit stomach. Ultrasound images of the long axis (left) and short axis (right) are captured. (**E**) Time-dependent response of a SeroTab when immersed in simulated gastric juice at pH 3. (**F**) Calibration of time-dependent responses of the pH sensor in a 35 μL chamber with solutions of different pH values. $\Delta L/\Delta L_0$ (%) denotes the swelling ratio. (**G**) Saturated swelling ratio of the pH sensor after immersion in 35 μL and 3 mL of gastric juice at different pH values for 12 hrs.

ate a high acoustic impedance mismatch. The design of the hydrogel and the distribution of the Zn disks are illustrated in (Fig. 6.S3F). Fig. 6.4B presents experimental observations of the sensor dimension before and after swelling in a simulated gastric juice at pH 2.

Ultrasound B-mode imaging is employed to quantitatively evaluate the pH-dependent geometry of the hydrogel sensor while simultaneously tracking and observing the entire SeroTab, where the sensor is embedded. The acoustic impedance mismatch between the Zn disks and surrounding materials—including the hydrogel matrix, gastric juice, tissue, and silicone rubber—enhances their visibility in B-mode images. During an ultrasound scan, acoustic waves generated by the transducer penetrate tissues and reflect off the SeroTab and Zn disks, forming cross-sectional images that reveal their spatial relationships. In the specific hydrogel sensor design presented here, a Zn disk is positioned at the center of the hydrogel piece, with additional Zn disks symmetrically placed on either side. The cross-sectional positioning of these disks enables ultrasonic measurement of the sensor's diameter. Their symmetric and circular distribution allows for orientation-independent ultrasonic visualization. Fig. 6.4C illustrates the concept of ultrasound imaging along the long and short axes of SeroTab from the view of its face A, demonstrating how the distances between Zn disks change with varying pH levels. In the ultrasound images, the three bright dots represent the cross-sectional views of the Zn disks, while the bright lines correspond to the upper and lower surfaces of SeroTab.

We evaluate the feasibility of ultrasonic detection for pH sensing in a live rabbit model. The ultrasound (US) scan began after gastric juice was sampled into SeroTab's chamber, where the sensor is located. The position and orientation of SeroTab within the stomach can be identified from US images acquired from different scanning directions as shown in Fig. 6.2L. A magnet was used to adjust and fix the orientation of SeroTab, ensuring that Face A was aligned with the US probe so that the Zn markers embedded in the hydrogel sensor became visible. Successful measurements are indicated by the appearance of three bright spots at equal distance (Fig. 6.S17A), whereas fewer than three visible spots indicate an invalid measurement (Fig. 6.S17B), requiring further adjustment via magnetic control and US probe re-orientation. By adjusting the ultrasound system's output parameters (e.g., dynamic range, gain, frequency, and focus), we enhance the acoustic visibility of the Zn disks while minimizing noise. The SeroTab and

Zn disks are successfully visualized across the sensor's diameter, and ultrasound images along both the long and short axes are captured (Fig. 6.4D).

To calibrate the relationship between the mechanical response of the hydrogel sensor and the pH level of the surrounding solution, we use simulated gastric fluid (SGF) with pH values ranging from 2 to 7. Fig. 6.4E and Movie S7 represent experimental measurements for the time-resolved swelling behavior of the sensor in the cavity of the SeroTab filled with 35 μL SGF solution at pH 3. Upon direct exposure to SGF at low pH (e.g., pH = 2), the sensor swells by 30% in less than 10 min and reaches more than 60% in 60 min. As shown in Fig. 6.4F, the swelling ratio ($\Delta L/\Delta L_0$%) exhibits a continuous increase over 60 minutes, whereas it decreases with rising pH. In a larger volume of SGF (3 mL), the sensor reaches its saturated swelling state (up to 135% at pH=2) after 12 hours, indicating its capacity for prolonged exposure and potential to sample and sense larger volumes of gastric fluid.

6.6 *In vivo* Study

We perform *in vivo* live rabbit experiments in which we comprehensively test SeroTab's feasibility and operability on oral delivery, magnetic control, sampling, pH sensing and biomarker analysis. The schematic and experimental setups are presented in Fig. 6.5A and B, respectively. SeroTab is positioned at the oropharynx and swallowed into the rabbit's stomach with the aid of a 5 mL physiological saline flush. Ultrasound scans were used to confirm gastric entry, following which magnetic navigation was employed to guide and position SeroTab in the middle part of the stomach (Movie S9). Remote heating was then applied via the RF heater to initiate sampling of the surrounding gastric fluid. The heating distance was maintained at approximately 2 cm, with an activation duration of 30 s to achieve a transition temperature of 40 °C (Fig. 6.S8). The ultrasound probe was fixed in place throughout the swelling procedure to visualize a consistent cross-section of the sensor, where three bright dots (corresponding to embedded Zn markers) were observed. Ultrasound images were recorded, and the distances between the markers were measured at defined time points (0, 10, 30, and 60 min; Movie S10).

In this study, we explore a potential application of the SeroTab function as part of clinical diagnostics for gastric physiology. We use omeprazole,

which is a proton pump inhibitor (PPI) primarily used to treat conditions caused by excessive gastric acid secretion, such as gastric ulcer and gastroesophageal reflux disease (GERD). Its administration leads to an elevation of gastric pH by inhibiting the $H^+/K^+ - ATPase$ in parietal cells, thereby reducing acid secretion. We injected omeprazole subcutaneously (20 mg/kg) three hours before anesthesia to regulate gastric acid secretion in live rabbit models (n=3 animals, experimental). To confirm model establishment and enable comparison, gastric juice samples were collected via gastric tube, and their pH values were measured externally before the operation. SeroTab is delivered post-anesthesia to sample gastric juice from the stomach. Ultrasound images of the hydrogel sensor inside the SeroTab are obtained at 0, 10, 30, and 60 minutes (Fig. 6.5C), and the swelling ratio of the sensors are measured (Fig. 6.5E). The corresponding pH values are inferred from the measured time-resolved swelling ratios by referencing the calibration curve shown in Fig. 6.4F. For comparison, the same procedure was repeated using saline as a substitute for omeprazole (Fig. 6.5D). Following the pH sensing procedure, the SeroTab is retrieved from the rabbit stomach. To assess its biocompatibility and safety, tissue samples from the gastric operation site were collected, processed for hematoxylin and eosin (H&E) staining, and subjected to histological analysis under microscopy (Fig. 6.5F and Fig. 6.S21). The results showed no evidence of epithelial disruption, inflammatory infiltration, or necrotic damage in the gastric mucosa, indicating good tissue compatibility and thermal safety of the SeroTab during operation.

In the current test protocol in the live rabbits, the complete SeroTab operation, including SeroTab ingestion, locomotion, sampling, and sensing, requires approximately 70 minutes. The hydrogel swelling (until saturation) accounts for the majority of this duration (about 60 minutes), although distinct volumetric changes sufficient for reliable pH determination can be observed within the first 10 minutes. Accordingly, the estimated operational duration of a clinically optimized version is expected to be under 20 minutes, which is comparable to standard gastrointestinal endoscopy examinations [297]. Further reduction of operation duration through optimization of hydrogel response (as described in the Supplementary Materials) and operation automation can improve patient outcomes.

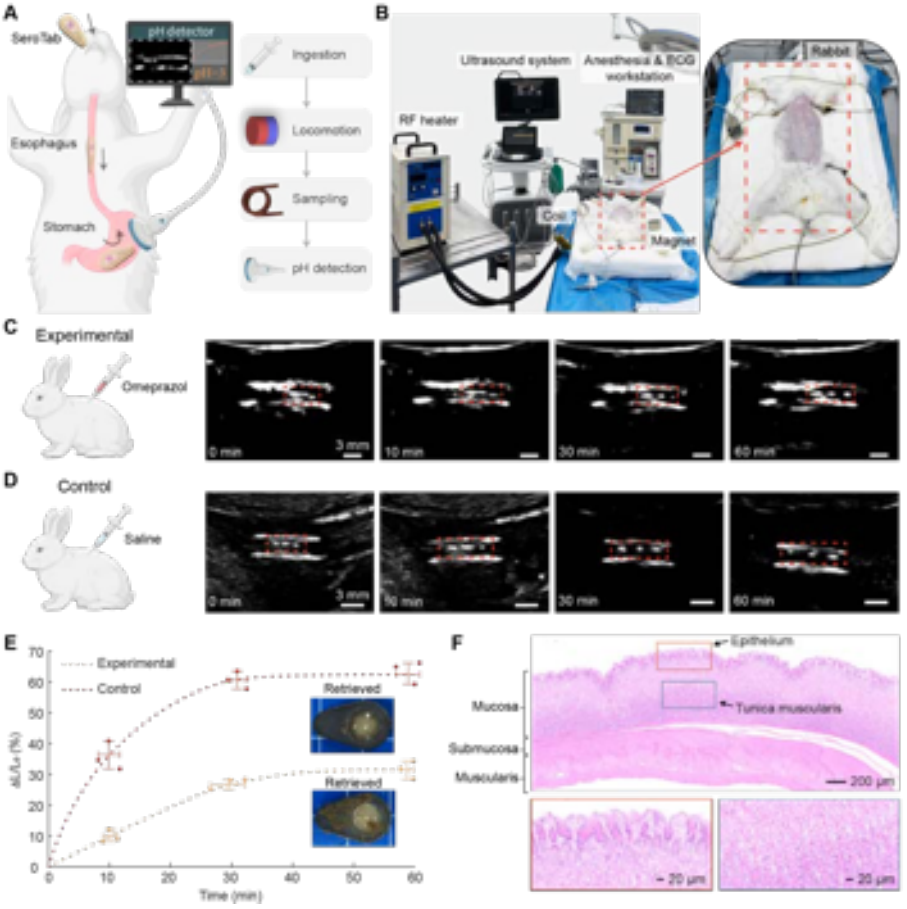

Figure 6.5: ***In vivo* study: *In situ* pH detection and post-sampling biomarker analysis of rabbit gastric juice.** (**A**) Schematic illustration and (**B**) Experimental setups of the oral administration, targeted sampling and sensing procedure for a SeroTab in the rabbit stomach. (**C**) Ultrasound images (right) of the SeroTab and sensor in the rabbit stomach from the experimental group and (**D**) control group, highlighting the expansion of the pH sensor. (**E**) Summary data showing the swelling ratio of the SeroTab in both experimental and control groups (n = 3 independent samples per group). (**F**) Hematoxylin and eosin (H&E) staining of gastric cross-sections post-operation demonstrates the biocompatibility of SeroTab.

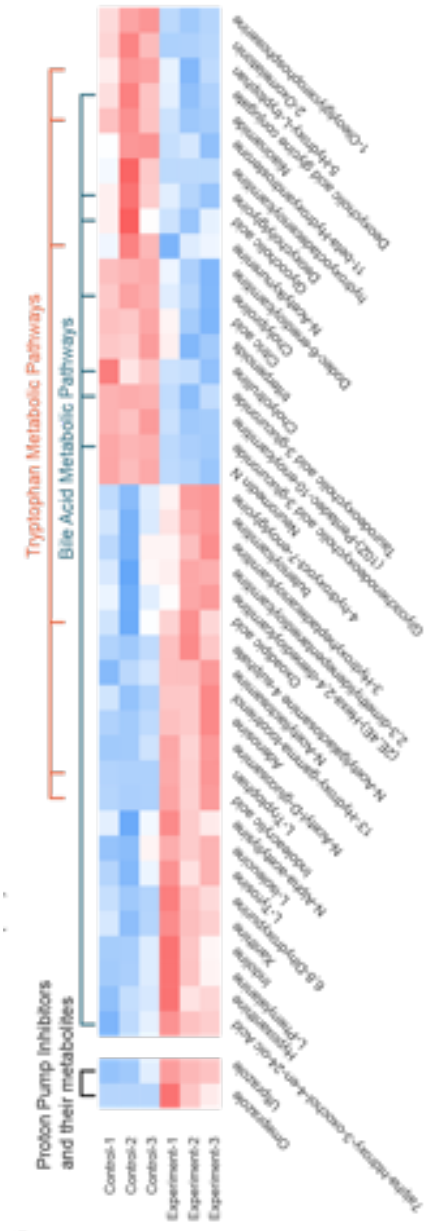

Figure 6.5: ***In vivo* study: In situ pH detection and post-sampling biomarker analysis of rabbit gastric juice.** (**G**) Results of mass spectrometry and metabolomic analysis.

To evaluate the molecular diagnostic potential of SeroTab, we conducted high-resolution mass spectrometry-based non-targeted metabolomics analysis on the hydrogel matrix retrieved from the device following *in vivo* gastric fluid sampling. The analysis identified 43 metabolites with significant changes (p-value < 0.05) and a fold change exceeding ± 1.5 between experimental groups, as determined by MS^2 spectra. Among these, the omeprazole component and 42 associated metabolites were detected, including 12 amino acids and 8 bile acid-related compounds. These findings underscore the hydrogel's ability to efficiently sequester and preserve gastric biomolecules, enabling robust downstream profiling (Fig. 6.5G). Further pathway analysis revealed that omeprazole administration induced notable alterations in bile acid metabolism and tryptophan metabolism pathways—two key metabolic axes intimately associated with gastric acid regulation and gut microbiota dynamics. These results are consistent with omeprazole's pharmacodynamic mechanism, wherein inhibition of the H^+/K^+-ATPase in parietal cells elevates gastric pH, consequently disrupting the intestinal microbial environment and suggesting a significant impact on host-microbiome interactions. Moreover, the detected metabolite clusters can serve as potential biomarkers for detecting drug-associated adverse effects, monitoring therapeutic outcomes, and guiding personalized treatment strategies in patients receiving PPI therapy.

These findings not only demonstrate the biochemical fidelity of the SeroTab's hydrogel-based sampling system but also highlight its value as a non-invasive platform for in situ diagnostics within the gastrointestinal tract. Given that changes in gastric fluid composition have been implicated in various gastrointestinal diseases, this approach holds promise for enabling both rapid pre-diagnosis and precise molecular analysis for various gastric diseases. In particular, disease states such as gastric cancer are known to induce distinct shifts in gastric secretions and metabolite concentrations, highlighting the potential of this method for early-stage, non-invasive disease screening and personalized therapeutic monitoring.

6.7 Discussion

This study demonstrates the utility of SeroTab in enabling both rapid and precise examination of gastric physiology by integrating a soft robotic capsule with a built-in pH-sensitive hydrogel, supported by conventional

ultrasound imaging and mass spectrometry analysis. Both *ex vivo* and *in vivo* tests demonstrate consistency with traditional aspiration methods by gastric tube, while our device offers advantages in flexibility, miniaturization and wireless operation, showing great potential for accessing challenging anatomical regions—such as small or confined spaces—with reduced patient discomfort. To our knowledge, this is the first demonstration of using a flexible, biocompatible hydrogel to enable sensing in a soft robotic tablet/capsule. Beyond sensing, the hydrogel also facilitates liquid sampling and improves sample retention through its inherent absorbent properties. This addresses the incompatibility between rigid components and soft robotic systems, enhancing both biocompatibility and flexibility. Future studies in swine and human models should aim to reduce contamination and enhance device controllability during the expelling process. Proper sealing of the device after sampling minimizes contamination and prevents sample leakage, while an accelerated expelling process enhances operational efficiency.

The integration of *in-situ* pH sensing and on-demand gastric fluid sampling provides a complementary diagnostic approach. Because fluctuations in gastric pH are closely associated with multiple gastrointestinal disorders such as gastric ulcer, gastritis, and infection, real-time in-situ sensing can help determine whether subsequent molecular analysis is necessary. Post-analysis of the retrieved hydrogel offers detailed biochemical and molecular information for definitive diagnosis (Fig. 6.S23). This combined strategy establishes a balanced diagnostic workflow that supports both rapid screening and precise follow-up analysis, potentially improving clinical efficiency and reducing unnecessary procedures. Future studies toward potential clinical translation should focus on improving biosafety and controllability, minimizing the risk of sample contamination and enhancing magnetic control to accelerate transit within and egestion from the complex intestinal environment.

In contrast to conventional cylindrical ingestible robotic devices such as capsule endoscopes, the SeroTab features a planar-stacked architecture that enables a space-efficient design. This configuration accommodates multiple functional layers within a compact volume, while potentially reducing swallowing difficulty and lowering the risk of gastrointestinal obstruction [298], [299]. The layered-printing fabrication method enables the precise construction of complex structures, such as the microfluidic

channels with a Tesla valve, and the integration of multiple materials to support multifunctional capabilities. Also, it offers foundational fabrication techniques for more customized designs that produce specific motion patterns, such as swimming or crawling, to adapt to various regions and environments within the human body, including the vascular and intestinal systems. However, further miniaturization of the device is necessary to enable navigation through highly confined anatomical regions, such as neural networks and urinary tracts. In such cases, ultrasound-based detection of the miniaturized hydrogel structures may become challenging due to resolution limitations. Alternative high-resolution imaging modalities, such as X-ray (Fig. 6.S19B) or computed tomography, should be considered for effective visualization.

Sampling high-viscosity biological fluids expands SeroTab's applications. For example, mucus (20-1000 cP) from the gastrointestinal tract contains critical biological data, including bacteria, immune cells, and metabolites, enabling diagnostic insights into gastrointestinal diseases and microbial imbalances. This requires tuning the mechanical properties of the SMP-based pumping actuator to enhance its recovery ability. Notably, the pumping mechanism can be adapted to design a drug delivery system by reversibly training the SMP. In addition, developing hydrogels capable of sensing a broader range of pH values [78], or other physiological parameters such as temperature and pressure, will further expand the utility of the device across various organs and environmental conditions. Although the hydrogel used in this study is designed for single-use, short-term sensing within the gastric environment, long-term stability and potential signal drift should be systematically evaluated. In addition, further exploration of its reversible swelling and deswelling [300] behavior could enable future applications in continuous monitoring.

In the event of unexpected exposure or rupture in the acidic gastric environment, the magnetic composite used in the device is inherently stable, and its biocompatibility can be further improved by incorporating biocompatible and acid-resistant polymer coatings on the magnetic particles [301]. Future designs may incorporate alternative materials such as tungsten (W) or molybdenum (Mo) as ultrasound markers in place of Zn, as they are chemically stable in gastric conditions while maintaining high ultrasound contrast [302] to mitigate potential risks in the event of unexpected exposure or rupture in the acidic gastric environment. In addition,

ferromagnetic SmFeN particles have demonstrated superior cytocompatibility compared with PrFeB particles (Fig. S22), making them a promising candidate for future developments. Collectively, these considerations highlight opportunities to integrate more biocompatible and chemically robust materials to further improve device safety and long-term clinical applicability.

In this study, magnetic control is utilized to guide and anchor SeroTab in the middle portion of the stomach, minimizing inter-animal variation, and allowing for consistent and reproducible gastric juice sampling and sensing. Passive locomotion, primarily driven by intestinal peristalsis, has been widely adopted in capsule devices for biomarker-triggered sampling, general diagnostics, and screening [75], [76], [276], [303]. However, magnetic actuation provides superior site-specific control, allowing localized, on-demand sampling at the target region and enabling long-term monitoring at the lesion site once detected. Other wireless actuation methods, such as optical, acoustic, or chemically actuated systems, represent potential alternatives but require careful evaluation of actuation power, biocompatibility, and response time.

The RF-triggered actuator in SeroTab enables active sampling that is decoupled from magnetic control and independent of the local biochemical environment, in contrast to osmotic sampling capsules that rely on passive diffusion or specific biochemical triggers to initiate collection [286], [290], while also delivering high suction pressure, rapid response, and the capability to sample highly viscous fluids (up to 1000 mPa·s) [66]. Future designs aiming for diagnostic specificity could incorporate smart, disease-responsive actuators that autonomously trigger upon specific biomarkers (e.g., abnormal pH, enzymatic activity, or pathogenic presence) [75], [303], thereby eliminating the need for external heating devices and improving system portability and clinical accessibility. However, these should account for disease-induced physiological variations (such as pH fluctuations caused by GERD) and should ensure that actuation is not triggered prematurely.

From a translational standpoint, the current prototype requires coordinated operation of magnetic actuation, RF heating, and ultrasound imaging modules for experimental validation, which may complicate clinical workflow in its present form. In future developments, these modules could be integrated into a single platform, potentially in combination with a robotic positioning system for automated operation. With computer-aided

control, standardized pre-programmed operation modes, and AI-assisted image recognition, clinicians would be able to perform capsule localization, activation, and decision-making through an intuitive, simplified workflow (Fig. 6.S23). In addition, the integration of emerging wearable ultrasound technologies, such as flexible ultrasound patches [81], offers wireless, continuous, and high-resolution imaging for real-time localization and monitoring, with superior portability and user-friendliness compared to conventional ultrasound systems. Collectively, these advances would accelerate the clinical translation of soft robotic diagnostic platforms toward integrated, non-invasive, and patient-tailored healthcare solutions capable of supporting early diagnostics and real-time decision-making in primary care settings.

6.8 Materials and Methods

6.8.1 Materials and Fabrication of the SeroTab Enclosure

The fabrication of the SeroTab enclosure follows a layered-printing strategy that enables strong interfacial bonding between multiple functional materials (Fig. 6.S2). Laser-cut self-adhesive polyethylene terephthalate (PET) films (100 μm thick) are prepared in four mold types, each with a rectangular contour for precise alignment (Fig. 6.S2 A). Mold-1 (0.5 mm thick) is placed on a flat PMMA base, followed by casting and blade-printing of silicone B (Dragon skin 30, Smooth-On Inc., USA) (Fig. 6.S2 B), which is cured at 50 °C for 2 hours. Mold-2 and mold-3 (each 0.5 mm thick) are then sequentially applied, with repeated casting and curing to form internal structures. Removal of the central portions in these layers creates a sampling chamber and a microfluidic channel integrated with a Tesla valve to enhance directional flow and prevent backflow (Fig. 6.S2 C and D). A pre-fabricated hydrogel-based pH sensor is positioned within the chamber (Fig. 6.S2 E), followed by gelatin filling for temporary structural support (Fig. 6.S2 F). After cooling and curing at room temperatur (10 min), mold-1 (0.2 mm thick) is placed on top and sealed using silicone A (Ecoflex 00-10, Smooth-On Inc., USA) casted and cured to seal the chamber and channel (Fig. 6.S2 G). Mold-4 (0.6 mm thick) is then aligned and adhered on top, followed by casting and curing of a magnetic polymer composite (MPC),

which consists of a silicone matrix (Ecoflex 00-10, Smooth-On Inc., USA) embedded with ferromagnetic praseodymium-iron-boron (PrFeB) powder (mean particle size: 5 μm; MQFP-16-7-11277, Magnequench GmbH, Germany) (Fig. 6.S2 H). The mass ratio of the magnetic microparticles to the silicone rubber is 2:1 in this study. The central section of mold-4 is removed to form a cavity housing a shape memory polymer (SMP, NOA63, Norland Products Inc., USA) and a matched aluminum heating receiver (Fig. 6.S2 I). A final sealing layer (mold-1, 0.2 mm thick) is added and cured to complete the structure (Fig. 6.S2 J).
After curing process, the SeroTab is extracted from the mold. The assembled SeroTab is then subjected to magnetization by applying a 2 T impulse magnetic field using an impulse magnetizer (ASC Model IM-10-30, ASC Scientific, USA), thereby establishing its internal magnetic profile necessary for navigation (Fig. 6.S2 K). To prepare the SeroTab for use, the gelatin filling must first be discharged through the microfluidic channel by applying heat and pressure. The device is heated to 60 °C, after which a cylindrical punch (6 mm diameter) is used to compress the shape memory polymer (SMP). The training process is completed by maintaining the compression until the SMP cools down to 30 °C, allowing it to fix into the deformed configuration.

6.8.2 Design and Fabrication of the SMP Actuator

The shape memory polymer (SMP) functions as a pumping actuator, consisting of an outer ring and a central disk connected by multiple S-shaped pillars. The design and dimensions of the SMP actuator are illustrated in Fig. 6.S3 E. When the inner disk is pressed while the outer ring is fixed—above the polymer's transition temperature—a spatial displacement occurs between the two components. To accommodate the limited ductility of the SMP, the S-shaped pillars are employed to provide mechanical compliance. These structures allow for relative displacement through controlled bending and twisting, while maintaining overall structural integrity.

The fabrication of the SMP actuator is a two-step replica molding process. First, a positive master mold is 3D printed to define the desired geometry. This master is then used to fabricate a negative mold by casting polydimethylsiloxane (PDMS, 10:1 monomer to crosslinker ratio

by weight), followed by curing at 50 °C for 6 hours to form an inverse template. Subsequently, shape memory polymer (SMP, NOA63, Norland Products Inc., USA) is cast into the PDMS negative mold, degassed for 5 minutes at 100 mbar to eliminate trapped air and ensure complete mold filling. The SMP is then preheated at 40 °C, or 5 minutes, followed by UV-A light exposure for 30 minutes at 40 °C. After curing and cooling, the fully formed SMP actuator is carefully demolded.

To establish the programmed actuation profile, each SMP actuator first underwent a standard thermomechanical training procedure consisting of heating above the transition temperature, manual deformation into the target configuration, cooling to fix the temporary shape, and reheating to recover the original geometry. To evaluate the reproducibility of this training process, we performed repeated programming–fixation–recovery trials on multiple samples. Three SMP actuators were subjected to 20 consecutive training cycles, and the deformation after fixation (Δh) and after recovery (ε_m) was recorded for each cycle to calculate the shape fixity ($\frac{\Delta h}{\varepsilon_d} \times 100\%$) and shape recovery ratios ($(1 - \frac{\varepsilon_m}{\Delta h}) \times 100\%$) by comparing to the designed deformation (ε_d). As shown in Fig. 6.S11, both ratios remained consistently near 100% across all cycles for all three samples, with negligible variation either within individual samples or between different samples. The results demonstrate that the SMP actuator exhibits highly stable and repeatable thermomechanical behavior, indicating that the programmed shape-memory response can be reliably maintained over extended operation.

6.8.3 Synthesis and Fabrication of the Hydrogel-based Sensor

The pH-responsive hydrogel was synthesized via a copolymerization strategy utilizing 2-(dimethylamino)ethyl methacrylate (DMAEMA) and 2-(diisopropylamino)ethyl methacrylate (DPAEMA), both purchased from Sigma-Aldrich. The monomers were mixed in a 7:3 weight ratio (DMAEMA:DPAEMA). In the first polymerization stage, 2 wt% of the photoinitiator 2-hydroxy-2-methylpropiophenone (Darocur 1173, Sigma-Aldrich) was added to the mixture, which was then exposed to ultraviolet (UV) light (365 nm, 500 mW/cm^2) for 1 minute to initiate the formation of oligomeric chains. Subsequently, poly(ethylene glycol) diacrylate (PEGDA,

$M_n \approx 700$, Sigma-Aldrich) was added at a concentration of 1.9 wt% relative to the total monomer content to enable network formation. To facilitate the final crosslinking step, 0.1 wt% of a secondary photoinitiator, 2,2-dimethoxy-2-phenylacetophenone (DMPA, Sigma-Aldrich), was incorporated. The resulting prepolymer solution was transferred into a glass syringe for subsequent sensor molding and polymerization.

The sensor fabrication procedure follows a sandwich-like assembly method, in which two hydrogel layers are formed sequentially with a Zn disk embedded at the interface. Two hydrophobic, soft, and transparent plastic film were assembled with a 75 μm gap between them, created using a double-sided adhesive tape to form a microchannel. Each film was affixed to a glass slide to ensure a flat and uniform surface. The prepolymer solution was carefully dispensed at the entrance of the channel, and capillary action enabled the solution to spontaneously fill the gap. The assembly was then exposed to UV light for a second curing process lasting 7 minutes, resulting in the formation of a chemically crosslinked hydrogel matrix responsive to environmental pH changes. After curing, one membrane was peeled off, and Zn disks were positioned according to the designed layout. A new film was then placed on top, maintaining a 125 μm inter-film spacing. The capillary-driven filling and subsequent UV polymerization steps were repeated to fabricate the second hydrogel layer, encapsulating the Zn disk at the interface between the two layers. Finally, individual hydrogel sensors were extracted using a 4 mm precision biopsy punch. Prior to use, the sensors were conditioned by immersion in phosphate-buffered saline (PBS, pH 7.4; Sigma Aldrich) for 12 hours, followed by drying under ambient conditions.

Note that the swelling process of the hydrogel sensor until full saturation can take more than one hour. However, detectable change in swelling ratio occurs within the first 10 minutes, allowing reliable pH determination during this period (Fig. 6.4F). The response time can be further accelerated by reducing the hydrogel's thickness or by tuning the copolymer composition between DMAEMA and DPAEMA. A higher proportion of DMAEMA increases the swelling ratio and decreases the response time, whereas a higher proportion of DPAEMA enhances the Young's modulus and elongation at break. Additionally, adjusting the crosslinking density (PEGDA content) can modulate the hydrogel's response time, swelling ratio, and mechanical properties [300], [304]. Other strategies, such as in-

corporating fixed fiducial markers on the non-deformable part of the device in future designs, could provide a stable reference baseline for hydrogel deformation measurements. This configuration would reduce the number of Zn markers required within the hydrogel layer (≤ 3), thereby simplifying the sensor structure and fabrication process. Furthermore, minimizing the hydrogel volume could accelerate the swelling response and facilitate overall device miniaturization, ultimately improving both sensing performance and integration potential.

6.8.4 *Ex vivo* Experiments

Porcine gastrointestinal anatomy and tissue properties closely resemble those of humans, making it a suitable *ex vivo* model for preliminary evaluation. Fresh porcine organs were obtained from a local slaughterhouse and used within 12 hours postmortem. Mucosal surfaces and residual fluids (e.g., mucus, gastric juice) were preserved to mimic *in vivo* conditions. For locomotion experiments, the stomach, small intestine, and trachea were used. All organs were used as received, without any additional cleaning procedures. Gastric juice was collected for sampling experiments (Fig. 6.2 I), contact angle measurements (Fig. 6.S16), and surface tension measurements (Fig. 6.S15). Only a portion of the organs was cleaned to remove mucus for friction measurements, which were then compared with mucus-covered surfaces (Fig. 6.S7).

6.8.5 *In vivo* Experiments

Studies involving animals were conducted at Shanghai Xinova Medical Research Co., Ltd. on six healthy New Zealand White rabbits (∼3.0 kg, sex not limited), obtained from a certified supplier [Animal License No. SYXK (Hu) 2021-0019, Approval No. XNM-YX-20241219-01]. All animal procedures were reviewed and approved by the Institutional Animal Care and Use Committee of Xinova, and performed in accordance with international ethics guidelines and the national institutes of health guide for the care and use of laboratory animals.

Rabbits were fasted for 48 hours prior to the procedure, with free access to water. Anesthesia was induced using Su-Tai (2–5 mg/kg, i.v. or i.m.) and maintained via 1–2% isoflurane inhalation through a veterinary anesthesia machine (WATO EX-20 Vet, Mindray, China). Animals were

placed in the supine position, intubated, and continuously monitored using a multiparameter monitor (MX550, Philips, Netherlands). Intraoperative fluid administration was provided as needed, and physiological parameters were recorded every 15 minutes.

Gastroscopy was performed 3 hours after omeprazole or saline injection to assess gastric conditions and collect 0.5 mL of native gastric fluid for baseline pH measurement. SeroTab was then orally administered using a small volume of physiological saline to facilitate swallowing and navigated to the targeted gastric site by an external permanent magnet. Upon reaching the site, an external RF heater was applied to activate the device's sampling mechanism. Ultrasound imaging (EPIQ7c, Philips, Netherlands) was subsequently used to visualize the device in situ and monitor pH-responsive deformation through the displacement of embedded metal markers. In a preliminary animal study, endoscopic (Fig. 6.2 K) and X-ray (Fig. 6.S19) imaging were performed to confirm the positioning and immersion of the device within the stomach. Endoscopic and X-ray imaging were used only during early trials for positional confirmation; later experiments relied solely on ultrasound guidance.

At the end of the *in vivo* experiment, all rabbits were humanely euthanized under deep anesthesia via intravenous injection of 10% potassium chloride (1 mL/kg), following the institutional SOP for euthanasia at Shanghai Xinova Medical Research Co., Ltd. Upon confirmation of death, a full abdominal dissection was performed. The stomach was carefully excised and opened to retrieve the SeroTab device, which was gently extracted using tweezers, avoiding contact with the central sensing region. The device was rinsed, sealed in a sterile cryotube, and stored at –80 °C for further analysis. Gastric tissue in contact with the device was inspected macroscopically for signs of damage (e.g., bleeding, edema, necrosis), photographed, and fixed in 10% neutral-buffered formalin (at a volume ratio of $\geq$10:1) for histological analysis. Tissue sections were later processed for hematoxylin and eosin (H&E) staining and microscopic evaluation. All sample collection and preservation procedures followed standardized protocols to ensure consistency and traceability.

6.8.6 Metabolomic Analysis

For the metabolomic profiling of gastric fluid absorbed by the hydrogel, each sample retrieved from the SeroTab was homogenized in 1 mL of ice-cold methanol/water (4:1, v/v) using a bullet blender. After centrifugation at 15,000 g for 10 minutes at 4 °C, the supernatant was collected and subjected to vacuum drying at 4 °C. The resulting residues were reconstituted in 50% methanol (methanol/water, 50:50, v/v) and analyzed using an untargeted metabolomics approach. Data acquisition was performed on a Thermo Scientific Vanquish™ UHPLC system coupled with an Orbitrap Exploris 120 high-resolution mass spectrometer (Thermo Scientific), following previously established protocols [305]–[307]. Metabolite separation was carried out on an ACQUITY UPLC HSS T3 column (2.1 mm × 100 mm, 1.8 μm; Waters Corporation, Milford, MA, USA), with a mobile phase consisting of 0.1% formic acid in water (A) and 0.1% formic acid in acetonitrile (B). To capture a broader range of metabolomic features, data were acquired in both positive and negative ionization modes. Raw mass spectrometry data were processed using Progenesis QI software (Nonlinear Dynamics, Newcastle, UK) for peak alignment, detection, deconvolution, normalization, and metabolite identification. Differential metabolite analysis was conducted by calculating the fold changes (FC) between groups, with statistical significance determined based on a threshold of FC >1.5 and p-value <0.05. Statistical significance was determined using Student's t-test. The METLIN Database (http://metlin.scripps.edu/) and Human Metabolome Database (http://www.hmdb.ca/) were used for identification and alignment of metabolites. The KEGG (Kyoto Encyclopedia of Genes and Genomes) database was utilized for metabolic pathway enrichment analysis further to investigate the biological relevance of the altered metabolites.

6.8.7 Analysis of the Magnetic Actuation Force

To evaluate the mechanical response of the SeroTab under predefined magnetization profiles, we performed finite element analysis using COMSOL Multiphysics to compute the magnetic field distribution of the permanent magnets and the resulting magnetic forces acting on the device. The locomotion of the SeroTab is driven primarily by magnetic pulling forces generated by the spatial gradient of the field, which directs movement from

regions of lower to higher magnetic flux density. To exploit this effect, we utilized the edge region of a cylindrical permanent magnet, where the field is both strong and highly non-uniform. Additionally, the programmed magnetization profile of the SeroTab allows for controllable orientation under external magnetic fields, enabling both directional alignment and bending deformation. We divide the magnetic force ($\mathbf{F}$) acting on the SeroTab into three components: the magnetic pulling force (F_x), which drives forward sliding locomotion; the magnetic rotating force (F_y), which rotates the SeroTab; and the magnetic lifting force (F_z), which counteracts gravity and facilitates flipping. The Magnetic force ($\mathbf{F}$) and magnetic torque ($\mathbf{M}$) acting on the SeroTab are defined by the following equations:

$$\mathbf{F} = \nabla((\iiint_{V_{Mag}} \mathbf{m} dV_{Mag}) \cdot \mathbf{B}) \tag{6.1}$$

$$\mathbf{M} = \iiint_{V_{\mathrm{Mag}}} \mathbf{m} \times \mathbf{B}\, dV \tag{6.2}$$

where $\mathbf{B} = (B_x, B_y, B_z)$ is the magnetic flux density generated by the permanent magnet at point (x, y, z), $\mathbf{m} = (m_x, m_y, m_z)$ is the magnetization of the SeroTab (see (Fig. 6.S6)), V_{Mag} represents the volume of MPC within the SeroTab.

We investigated the magnetic actuation performance of single-, dual-, and four-magnet configurations to optimize the applied magnetic forces (Fig. 6.S4). Magnetic forces were calculated by sweeping three key parameters: the magnet's rotation angle (θ), the horizontal distance (d), and the vertical distance (h) between the magnet and the SeroTab. In the single-magnet setup, the magnetic pulling force peaked when the magnet was rotated to 90°. Introducing a second magnet on the opposite side significantly enhanced the pulling force while reducing the lifting component, compared to placing both magnets on the same side. The four-magnet configuration yielded the highest overall pulling force; however, the increase was not linear and did not result in a doubling of force. In summary, the single-magnet configuration offers ease of operation and greater flexibility in orientation, while the dual-magnet (opposing) setup effectively strengthens the pulling force and minimizes the undesired lifting force.

Based on the theoretical results, we constructed both single- and dual-magnet systems to experimentally validate the magnetic actuation of the

SeroTab. The magnetic field was measured using a Gaussmeter, and the magnetic force was quantified using a custom-designed two-axis force sensing platform (Fig. 6.S5). The experimental data showed strong agreement with the simulation results, confirming the accuracy of the model. Additionally, the measurements revealed the optimal spatial relationship between the SeroTab and the magnet for maximizing the pulling force.

6.8.8 Analysis of Ultrasonic pH Sensing

The ultrasound images were acquired using a medical ultrasound system (EPIQ7c, Philips, Netherlands) equipped with a C1-5 broad-spectrum convex array transducer (Philips). To ensure image clarity, ultrasound gel was applied at the probe-skin interface, and imaging parameters including gain, dynamic range, frequency, and focal depth were manually adjusted to align with the location of the SeroTab. High-quality B-mode images were obtained, in which the embedded Zn disks appeared as distinct bright segments. The measurement tool within the ultrasound system was used to determine the distance between the left and right Zn markers, enabling quantification of pH-responsive deformation.

Selection of metal (Zn) as ultrasonic indicators takes into consideration their biocompatibility and acoustic mismatch with the surrounding hydrogel, silicone, and soft tissues [78], [302]. To enhance the ultrasound visibility of the embedded Zn markers in the SeroTab, their dimensions were optimized based on acoustic impedance mismatch theory. The acoustic impedance of a material is defined as:

$$Z = \rho c \tag{6.3}$$

where Z is the acoustic impedance, ρ is the material density, and c is the speed of sound in the medium.

At the interface between two materials, the reflection of ultrasound waves is governed by the reflection coefficient R, calculated as:

$$R = \left| \frac{Z_2 - Z_1}{Z_2 + Z_1} \right|^2 \tag{6.4}$$

where Z_1 and Z_2 are the acoustic impedances of the two interfacing media. A greater mismatch leads to a higher reflection coefficient and thus stronger echogenic signals in B-mode ultrasound imaging.

Zinc (Zn) exhibits a high acoustic impedance of approximately 26.7 MRayl, which contrasts strongly with surrounding materials such as hydrogel (∼1.5 MRayl), gastric fluid (∼1.6 MRayl), and silicone rubber (∼1.0 MRayl). This results in a reflection coefficient $R > 0.85$, sufficient for generating bright and distinct echoes in ultrasound images.

To determine the appropriate thickness of the Zn disk, we considered the ultrasound wavelength λ in the surrounding medium:

$$\lambda = \frac{c}{f} \tag{6.5}$$

where f is the operating frequency of the transducer. Given an ultrasound frequency of 5 MHz and average sound speed in tissue ($c \approx 1500$ m/s), the corresponding wavelength is $\lambda \approx 300$ μm. The Zn disk thickness was chosen as 50 μm, corresponding to approximately $\lambda/6$, which is sufficient to generate detectable reflection while minimizing acoustic shadowing or harmonic distortion.

Zn markers were fabricated with a diameter of 1 mm and thickness of 50 μm. This size provided a localized, high-contrast signal without excessive interference with surrounding structures. Marker spacing and alignment were optimized to remain within the axial and lateral resolution limits of the ultrasound system, ensuring consistent visibility during in vivo imaging [78].

6.8.9 Analysis of Liquid Sampling Procedure

Liquid absorption relies on the pressure differential between the internal chamber and the external environment, which is generated by the elastic recovery of the shape memory polymer (SMP) actuator. Upon thermal activation, the SMP recovers its original shape, leading to an increase in the chamber volume and a corresponding decrease in internal pressure. This pressure difference between the surrounding environment and the chamber drives the intake of fluid through the microchannel, analogous to the working principle of an eyedropper. Based on this mechanism, we conducted a simulation of the fluid sampling process using COMSOL Multiphysics to evaluate the dynamic pressure response and fluid inflow behavior.

Assuming isothermal conditions and negligible gas exchange with the environment, the internal pressure $P(t)$ of the chamber at time t can be described using a simplified inverse relationship:

$$P(t) = P_0 - \frac{1}{k}V(t) \tag{6.6}$$

where P_0 is the atmospheric pressure, $V(t)$ is the chamber volume at time t (Fig. 6.S10), k is a system-dependent constant that incorporates chamber geometry and gas properties.

As the volume $V(t)$ increases due to SMP deformation, the internal pressure $P(t)$ decreases, generating a pressure gradient $\Delta P = P_0 - P(t)$ across the microchannel. This gradient induces liquid inflow without the need for external pumps. The absorbed fluid volume is governed by the magnitude of the pressure difference (ΔP), the viscosity and surface tension of the surrounding fluid, as well as the contact angle between the fluid and the microchannel surface. In addition, the effect of capillarity was analyzed to minimize unintended passive fluid ingress and optimize the reliability of controlled sampling [308], [309]. According to the Lucas–Washburn (LW) equation [310], which describes capillary-driven flow as:

$$\frac{dh}{dt} = \frac{(P_A + P_h + P_c)(r^2 + 4\varepsilon r)}{8\mu h} \tag{6.7}$$

where h is the liquid column height, r is the channel radius, μ is the liquid viscosity, ε is the slip coefficient, P_A is the unbalanced atmospheric pressure, P_h is the hydrostatic pressure, and P_c is the capillary pressure. The capillary pressure is defined as:

$$P_c = \frac{2\sigma \cos\theta}{r} \tag{6.8}$$

where σ is the liquid surface tension and θ is the contact angle at the channel wall.

According to the model, capillary-driven flow is strongly influenced by the channel radius, surface tension, contact angle, and fluid viscosity. To accurately simulate the fluid behavior within the SeroTab, we experimentally measured the surface tension and contact angle of gastric juice extracted from porcine stomachs (Fig.6.S15 and Fig.6.S16). Based on these measured properties, we conducted time-dependent capillary flow simulations in COMSOL Multiphysics (Fig. 6.S14B). The simulation results indicated that the capillary effect within the SeroTab's microchannel is

minimal under the tested conditions, primarily due to the inherent properties of the native materials and the specialized design of the microchannel structure.

6.8.10 Design and Optimization of the Tesla Valve

To enhance flow rectification and minimize unintended liquid leakage during operation, a Tesla-type (T45-R) microvalve was integrated into the SeroTab's microfluidic channel (Fig.6.S12A). The design aimed to maximize the diodicity (D_i), defined as the ratio of the pressure drop in the reverse flow direction ($\Delta p_{\leftarrow}$) to that in the forward flow direction ($\Delta p_{\rightarrow}$) [311], [312]:

$$D_i = \frac{\Delta p_{\leftarrow}}{\Delta p_{\rightarrow}} \tag{6.9}$$

A higher diodicity value reflects stronger resistance to reverse flow, ensuring robust directional fluid transport during the sampling process.

The Tesla valve geometry was parameterized by key structural variables, including the curvature radius (R), turning angles (α, β), and segment lengths (L_1, L_2, L_3, L_4), as illustrated in Fig. 6.S12A. The segment lengths L_1 and L_2 were calculated based on geometric relationships as:

$$L_1 = R\sin\beta + R\cos\left(\frac{\pi}{2} - \theta\right) + \frac{R\cos\beta + R\sin\left(\frac{\pi}{2} - \theta\right)}{\tan\theta} \tag{6.10}$$

$$L_2 = \sqrt{\left(R\sin\left(\frac{\pi}{2} - \theta\right) + R\cos\beta\right)^2 + \left(\frac{R\cos\beta + R\sin\left(\frac{\pi}{2} - \theta\right)}{\tan\theta}\right)^2} \tag{6.11}$$

where θ is the turning angle within the Tesla structure.

Considering the inertial-dominated regime where Tesla valves operate effectively (typically at moderate Reynolds numbers, $Re \sim 10$–1000), finite element simulations were conducted in COMSOL Multiphysics to optimize the geometric parameters. The final design achieved optimal performance with $R = 1.1$ mm, $\alpha = 41°$, and $\beta = 45°$ (Fig. 6.S12A).

Flow field simulations (Fig. 6.S12B) showed significant asymmetry between forward and reverse directions, and the flow diodicity increases markedly with increasing Reynolds number (Fig. 6.S12C). This optimized Tesla

microvalve structure effectively restricts backflow, stabilizes fluid sampling, and minimizes unintended liquid leakage within the SeroTab system.

To evaluate the functional contribution of the Tesla valve in SeroTab, we performed comparative impact-induced leakage tests using devices with and without the Tesla valve. A control device was fabricated by replacing the Tesla valve with a straight microchannel of identical cross-section and material, and using the same fabrication process (Fig. 6.S13A). Each device was pre-filled with a fixed volume of dyed buffer and subjected to different mechanical disturbances, including a 1 m free fall and the release of 10 g and 50 g weights from a 20 cm height. Leakage was quantified gravimetrically, and representative visual evidence is shown in Fig. 6.S13B and Movie S11. Each impact condition was repeated five times to ensure statistical reliability. Across all impact conditions, the Tesla-valve device exhibited effective leakage prevention, whereas the straight-channel control showed substantially greater leakage. The results confirm that, although the Tesla valve does not function as a complete check valve under static or low-flow conditions, it effectively suppresses reverse flow during transient mechanical shocks, thereby minimizing unintended loss of the collected gastric fluid.

From a broader perspective, the Tesla valve in its current passive form provides a lightweight and fabrication-compatible strategy to suppress impact induced backflow. However, integrating more sophisticated microscale check-valve architectures in future designs may further enhance post-sampling contamination prevention and enable complete blockage of reverse flow even under static pressure conditions. Achieving this will require continued innovation in microfabrication techniques and the incorporation of smart or responsive materials capable of active sealing.

6.8.11 Analysis of Inductive Heating Procedure

Remote heating can be achieved using alternating magnetic fields or radio-frequency (RF) fields through two primary mechanisms: Joule heating and hysteresis losses. While magnetic hysteresis is widely used for remote heating due to its compatibility with multifunctional nanoparticles, Joule heating offers higher efficiency and greater controllability, making it a more effective approach for precise thermal management [296]. The selection and design of the heating element were based on the fundamental principles

of electromagnetic induction and transient thermal energy balance. The heating power generated within the material under an alternating magnetic field primarily results from eddy currents, and the volumetric heating power density P is given by:

$$P = \frac{J^2}{\sigma} \tag{6.12}$$

where J is the induced current density and σ is the electrical conductivity of the material. To maximize heating efficiency, a material with high electrical conductivity and low magnetic susceptibility was preferred. Aluminum was selected over other candidates such as iron and copper due to its high conductivity ($\sigma_{\text{Al}} \sim 3.5 \times 10^7$ S/m), low density (2.7 g/cm^3), biocompatibility, and the absence of magnetic hysteresis losses which would otherwise complicate heating control.

The geometry of the aluminum film was optimized to enhance heating performance while maintaining flexibility and minimizing energy requirements. The characteristic skin depth δ, which defines the penetration depth of the induced currents, is given by:

$$\delta = \sqrt{\frac{2}{\omega \mu \sigma}} \tag{6.13}$$

where $\omega = 2\pi f$ is the angular frequency, μ is the magnetic permeability, and σ is the electrical conductivity.

We use a 10 μm-thick aluminum film which is cut into the same shape as SMP to transfer the heating and ensure flexibility. To further enhance localized heating without sacrificing the global flexibility of the structure, an additional 100 μm-thick aluminum circular disk was laminated at the center of the thin film. This layered configuration increases local thermal energy generation where needed, while keeping the overall thermal mass low.

The heat generated within the aluminum sheet follows the transient energy conservation equation:

$$P_{\text{in}} = \rho V c_p \frac{\partial T}{\partial t} + H_L \tag{6.14}$$

where ρ is the density, V is the volume of the aluminum, c_p is the specific heat capacity, $\partial T/\partial t$ is the temporal temperature rise rate, and H_L represents the heat loss to the surroundings.

Heat losses occur through convection and radiation, which are modeled as:

$$H_L = hA(T_s - T_{\text{ambient}}) + \sigma\epsilon A(T_s^4 - T_{\text{ambient}}^4) \tag{6.15}$$

where h is the convective heat transfer coefficient, A is the exposed surface area, ϵ is the surface emissivity, and σ is the Stefan–Boltzmann constant. Minimizing H_L is essential to achieve rapid heating; therefore, the device was designed with compact geometry and encapsulated with low-conductivity materials to reduce convective and radiative losses.

Furthermore, the placement of the external RF coil relative to the SeroTab significantly influences the induced magnetic flux density B, which decreases with distance approximately as:

$$B(r) \propto \frac{1}{r^3} \tag{6.16}$$

where r is the separation distance. A coil-to-device distance of 10–20 mm was selected to balance strong magnetic coupling with safe operation within biological tissues.

We conducted multivariate experiments to investigate the heating efficiency influenced by various factors, including the power of the RF heater, heating time, operating distance, and material thickness. The results, presented in Fig. 6.S8, suggest that heating efficiency can be improved by using a higher power heater and a thicker aluminum disk, which together enhance the ability to heat over larger distances, making them suitable for larger animal experiments. In conclusion, careful selection of aluminum, optimization of thickness and layered structure, precise control of external coil positioning, and reduction of thermal losses collectively contribute to efficient, rapid, and localized heating of the actuator, achieving the required transition temperature (40°C) within approximately 60 seconds under *in vivo* conditions.

To evaluate the heating robustness of the SMP actuation system, we performed a controlled benchtop experiment in which the aluminum disk was subjected to fixed RF heating parameters (60 s heating duration, 450 W RF power, a 2 cm heating distance, and a 100 μm aluminum disk thickness). During the test, the aluminum disk was incrementally rotated relative to the RF coil in 2° steps, and the surface temperature was recorded every 10 s over a 60 s activation period. The results show that the SMP

reached its activation threshold of 40 °C within 30 s for angular offsets up to 6°, indicating that minor orientation variations do not meaningfully compromise heating efficiency (Fig. 6.S9). Furthermore, as shown in Fig. 6.S8, heating performance can be additionally compensated by adjusting operational parameters such as heating duration, RF power, distance, and aluminum thickness. Collectively, these findings demonstrate that the system maintains reliable and flexible thermal performance under physiologically relevant orientation variations in the dynamic gastrointestinal environment.

6.8.12 Ultrasound measurement and resolution

The quality of ultrasound imaging is primarily determined by the lateral resolution and the signal-to-noise ratio (SNR), which together set the minimum detectable pH-induced dimensional change in the Zn disks. The lateral resolution is governed by the beamwidth, which depends on the wavelength, aperture size, and focal depth, as expressed in Eq. (S17). Higher transmit frequencies and stronger focusing result in narrower beams and improved resolution, whereas deeper focal positions broaden the beam and degrade spatial precision. The SNR is influenced by frequency-dependent acoustic attenuation, focusing conditions, and aperture size, with the highest SNR observed near the focal region and progressively reduced at greater imaging depths due to tissue scattering and attenuation.

$$\Delta x_{\text{lat}} \propto \frac{\lambda F}{D} \tag{6.17}$$

where λ is the ultrasound wavelength, F is the focal depth, and D is the aperture length of the transducer.
To analytically estimate the minimum detectable change in lateral spacing between two point-like scatterers, we model the lateral point spread function (PSF) of the ultrasound imaging system as a Gaussian function, a widely used approximation for phased arrays and convex probes in the focal region:

$$g(x) = A \exp\left(-\frac{x^2}{2\sigma^2}\right) \tag{6.18}$$

where A is the peak amplitude and σ is the standard deviation of the

Gaussian. The full width at half maximum (FWHM), corresponding to the lateral resolution of the system, is related to σ by:

$$\mathrm{FWHM} = 2\sqrt{2\ln 2}\,\sigma \approx 2.355\sigma \tag{6.19}$$

For two point-like targets separated by distance d, the valley intensity between them is:

$$I_v(d) = 2A\exp\left(-\frac{d^2}{8\sigma^2}\right) \tag{6.20}$$

A small change in spacing Δd produces a corresponding change in valley intensity, approximated using a first-order Taylor expansion:

$$|\Delta I_v| \approx \left|\frac{\partial I_v}{\partial d}\right| \Delta d = \frac{Ad}{2\sigma^2}\exp\left(-\frac{d^2}{8\sigma^2}\right)\Delta d \tag{6.21}$$

To be detectable against background noise with standard deviation σ_n, this intensity change must exceed a threshold $k\sigma_n$ ($k \approx 1{-}3$):

$$|\Delta I_v| \gtrsim k\sigma_n \tag{6.22}$$

Solving for the smallest detectable spacing change yields:

$$\Delta d_{\min} \approx \frac{2\sigma^2}{d}\exp\left(\frac{d^2}{8\sigma^2}\right)\frac{k}{\mathrm{SNR}} \tag{6.23}$$

where the image-domain signal-to-noise ratio is defined as:

$$\mathrm{SNR} = \frac{A}{\sigma_n} \tag{6.24}$$

We performed numerical simulations to quantify how ultrasound parameters and target geometry influence the accuracy of lateral distance measurements. Using a baseline configuration of 5 MHz center frequency, 2 cm imaging depth, and Zn disks of 1 mm diameter and 50 μm thickness, we evaluat the relative distance error $\Delta d/d_0$. Increasing ultrasound frequency improves lateral resolution and reduces measurement error (Fig. 6.S18A), whereas increasing imaging depth broadens the PSF and decreases SNR, leading to a monotonic increase in $\Delta d/d_0$ (Fig. 6.S18B). Simulations incorporating variations in Zn disk diameter and thickness further show that larger or thicker reflectors yield higher echo amplitudes and improved

noise robustness (Fig. 6.S18C-D), thereby reducing measurement variability. These results collectively demonstrate how imaging settings and target geometry govern the minimum resolvable displacement in ultrasound-based localization.

Under the same conditions as the *in vivo* experiments (5 MHz, 2 cm depth, 1 mm × 50 μm Zn disks), the inter-disk spacing (which reflects the local pH value) was extracted from ultrasound images by analyzing the lateral intensity profile across the Zn-induced bright spots. As shown in Fig. 6.S18E, a straight line passing through the three Zn disks is manually defined, and a one-dimensional gray-scale profile along this line is extracted using bilinear interpolation. The location of each Zn disk is determined by identifying the point of maximum intensity gradient within the rising edge of its corresponding bright spot, corresponding to the onset of the acoustic reflection from the disk. The inter-disk spacing is then calculated as the pixel distance between these edge positions multiplied by the calibrated pixel-to-millimeter conversion factor obtained from the depth scale on the ultrasound image. Measurements from *in vivo* ultrasound frames (at 0 min and 60 min) consistently produced $\Delta d/d_0 < 0.1$, indicating that dimensional changes as small as 10% can be reliably detected under the experimental imaging conditions.

6.8.13 *In vitro* Tests of Cytocompatibility

To assess the biocompatibility of SeroTab, in vitro cytotoxicity tests were conducted using a human colorectal adenocarcinoma cell line (HT29) with epithelial morphology. HT29 cells were cultured in high-glucose Dulbecco's modified Eagle's medium (DMEM; Gibco) that contains 10% fetal bovine serum (FBS; Gibco) and 1000 U mL^{-1} penicillin-streptomycin (Gibco) at 37 °C in in 95% air and 5% CO2 gas mixture. SeroTabs were incubated in the cell culture medium at a medium-to-sample area ratio of 1.25 mL cm^{-2} for 24 hours at 37 °C in a humidified 5% CO_2 atmosphere in order to obtain extracts, which potentially contain cytotoxic components such as magnetic particles or degradation byproducts of the polymer matrix. These extracts were subsequently collected and used for cytotoxicity evaluation. The viability of HT29 cells were measured by the CellTiter-Glo (CTG) assays (Promega, Madison, WI). Briefly, HT29 cells were harvested and seeded in 96-well plates at a density of 9000 cells per well and pre-incubated for 24

hours. Then the culture medium was replaced with the prepared extracts of SeroTabs and cultured for an additional 24, 48, and 72 hours. Following the incubation period, cell viability was measured using the standard CTG assay according to the manufacturer's instructions.

To compare the cytocompatibility of PrFeB and SmFeN magnetic particles, NHDF cells were cultured in Dulbecco's Modified Eagle Medium (Gibco, Cat. No. 11965092), supplemented with 10% fetal bovine serum (Gibco, Cat. No. 10270106) and 1% penicillin–streptomycin (Gibco; Cat. No. 15140122). Cells were maintained at 37 °C in a humidified 5% CO_2 incubator and passaged every 2–3 days using 0.05% trypsin-EDTA (Gibco; Cat. No. 25300062). Cell viability was evaluated using the CCK-8 assay. NHDF cells were seeded in 96-well plates (Corning, Cat. No. 3596) at 1×10^4 cells/well in 100 μL of complete culture medium and allowed to attach for 24 h. After attachment, the medium was replaced with 100 μL of fresh medium containing MNPs at final concentrations of 0.1–10 mg/mL (corresponding to 0.01–1 mg per well). Cells were incubated with the particles for 24 h (Day 1) and 72 h (Day 3) at 37 °C and 5% CO_2. At each time point, the exposure medium was removed and replaced with 100 μL of culture medium containing 10% CCK-8 reagent (Abcam, Cat. No. ab228554) followed by 1 h of incubation. Absorbance was measured at 450/650 nm using an Infinite F200 PRO microplate reader (Tecan).

We performed a dose–response viability assay using concentrations ranging from 0.01 to 1 mg/well and assessed metabolic activity on days 1 and 3 (Fig. 6.S22). PrFeB particles exhibit a clear, dose-dependent reduction in viability, remaining above 90% only at concentrations ≤ 0.05 mg/well. At 0.1 mg/well, viability decrease to ∼80%, indicating the onset of cytotoxic effects, whereas at higher doses (0.5–1 mg/well) metabolic activity drop sharply to 38–47%, demonstrating marked toxicity at elevated concentrations. In contrast, SmFeN particles show substantially higher cytocompatibility, maintaining $> 100\%$ viability at low doses (0.01–0.05 mg/well) and remaining non-toxic up to 0.5 mg/well. Even at 1 mg/well, SmFeN preserve $> 80\%$ viability, indicating that only the highest concentrations approach cytotoxic levels, while lower doses remain safe. Collectively, these findings demonstrate that both particle types are biocompatible within their low-dose working ranges, but SmFeN exhibits a significantly broader safety window and becomes cytotoxic only at the uppermost concentrations tested.

6.8.14 Evaluation of Biocompatibility

For histological analysis, the esophagus and stomach tissues from each rabbit group were collected after surgery and immersed in 4% formaldehyde for hematoxylin and eosin (H&E) staining. Tissue was aseptically dissected and fixed overnight at 4 °C in 10% formalin. Subsequently, the samples were dehydrated through a graded ethanol series from 70-100%, cleared with xylene to remove the ethanol and infiltrated with paraffin. The processed tissue was embedded in paraffin, sectioned into 5-μm-thick slices, placed on microscope slides and stained with hematoxylin/eosin for histological examination. Images of stained tissue sections were acquired using a light microscope with a slide scanner (Pannoramic 250/MIDI, 3D HISTECH Ltd., Hungary).

6.9 Supplementary Figures

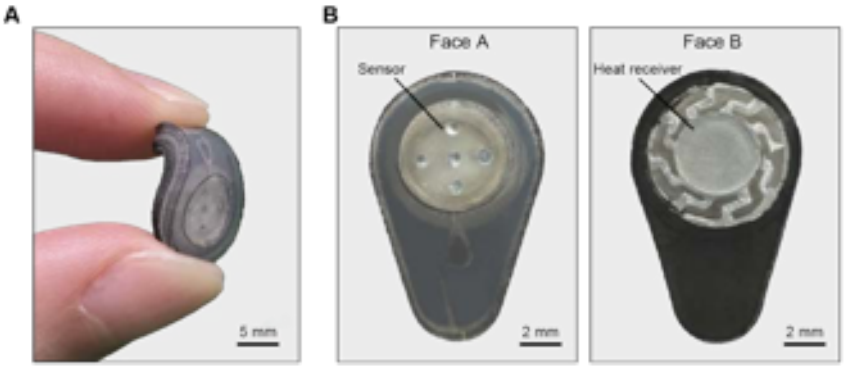

Figure 6.S1: **Images of SeroTab that highlight the visual characteristics and soft features.** (**A**) being compressed and bent between fingers, demonstrating its flexibility. (**B**) Views of both faces of the SeroTab, each highlighting different components.

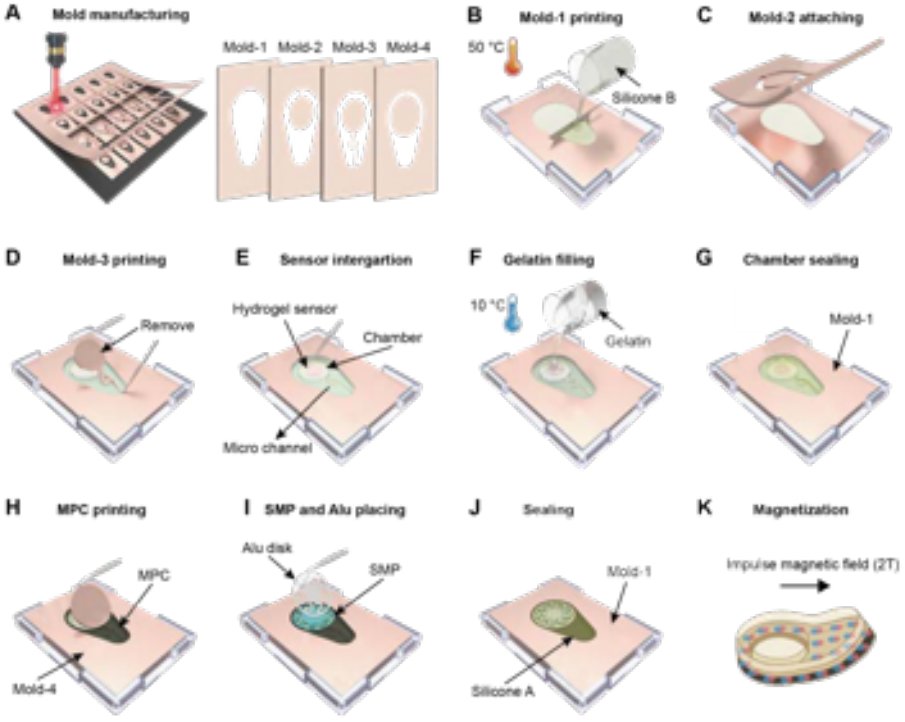

Figure 6.S2: **Fabrication procedure of the SeroTab.**

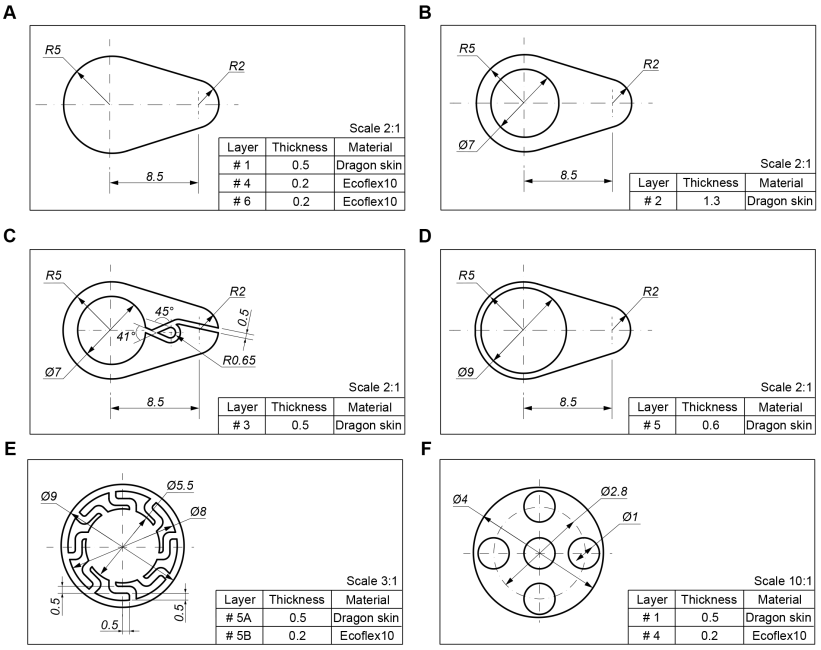

Figure 6.S3: **Design and dimensions of different layers of the SeroTab.** (**A**) Dimension and materials of layer 1, layer 4, layer 5, (**B**) layer 2, (**C**) layer 3, (**D**) layer 5, (**E**) SMP (layer 5A), aluminum heating element (layer 5B) and (**F**) pH sensor.

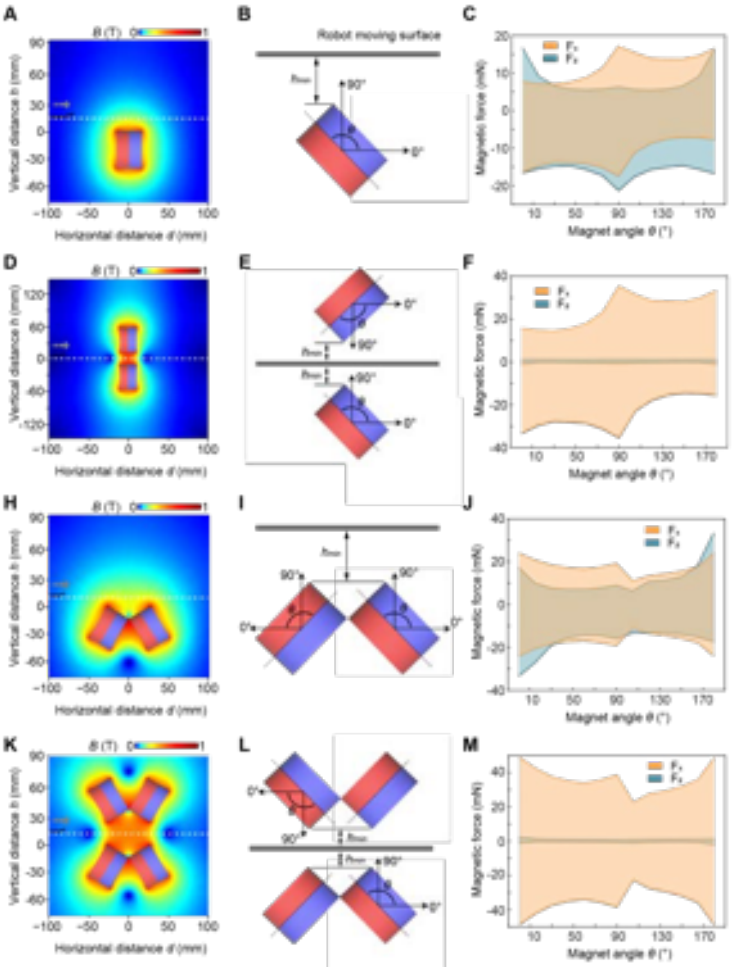

Figure 6.S4: **Comparison and enhancement of applied magnetic force on SeroTab with different magnet configurations.** (**A**) Simulated magnetic field distribution map with a single magnet. (**B**) Schematic illustration of controllable variables influencing magnetic force. (**C**) Simulated results of pulling force (F_x) and lifting force (F_z) act on SeroTab. (**D**), (**E**) and (**F**) demonstrate the use of two magnets on opposite sides to enhance pulling force and reduce lifting force. (**H**), (**I**) and (**J**) show the effects of using two magnets on one side. (**K**), (**L**) and (**M**) illustrate the strategy of using four magnets to further optimize pulling force and minimize lifting force.

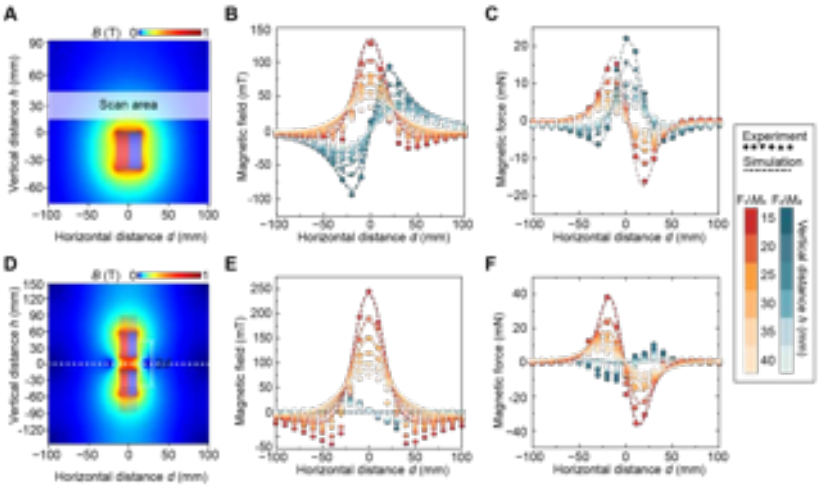

Figure 6.S5: **Comparison of measured and simulated pulling force (F_x) and lifting force (F_z).** (**A**) Simulated magnetic field distribution map with a single magnet, showing the vertical and horizontal distance between SeroTab and the magnet. (**B**) Comparison of measured and simulated magnetic fields as a function of horizontal and vertical distance. (**C**) Comparison of measured and simulated magnetic forces influenced by horizontal and vertical distance. (**D**), (**E**) and (**F**) demonstrate the use of two magnets on opposite sides to enhance the pulling force and reduce lifting force.

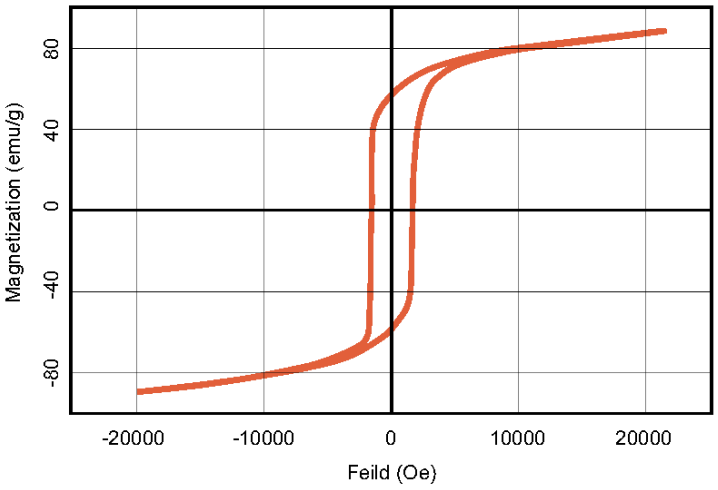

Figure 6.S6: **Magnetization properties (B-H curve) of the magnetic polymer composite (MPC) in the SeroTab.** The magnetization behavior of MPC is measured using a vibrating-sample magnetometer (VSM).

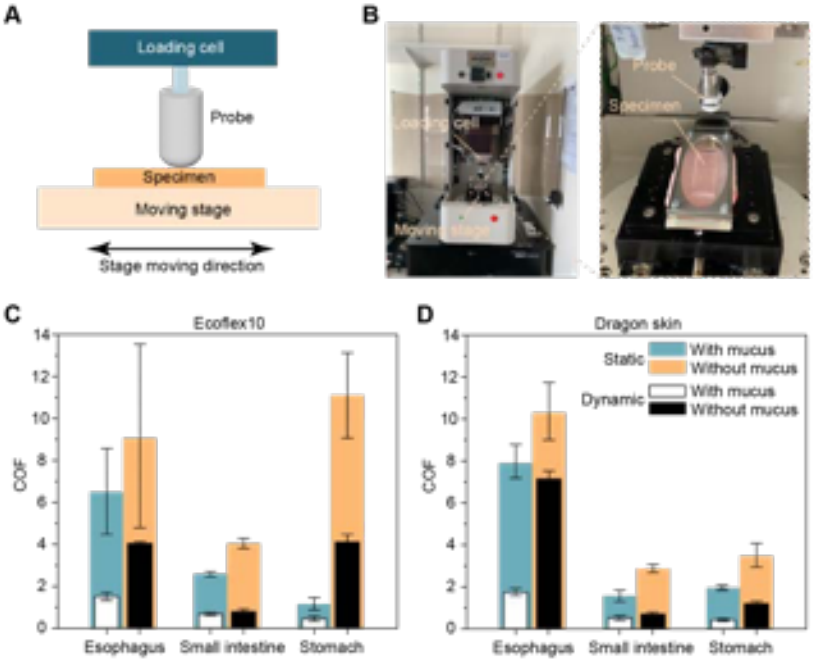

Figure 6.S7: **Measurement of the coefficient of friction (COF) between SeroTab's materials and organ tissues.** (**A**) Schematic illustration of the COF measurement mechanism, where a piece of SeroTab's material is attached to the probe. (**B**) Experimental setup. (**C**) COF values for Ecoflex 10 and (**D**) Dragon skin in contact with tissues from the esophagus, small intestine, and stomach.

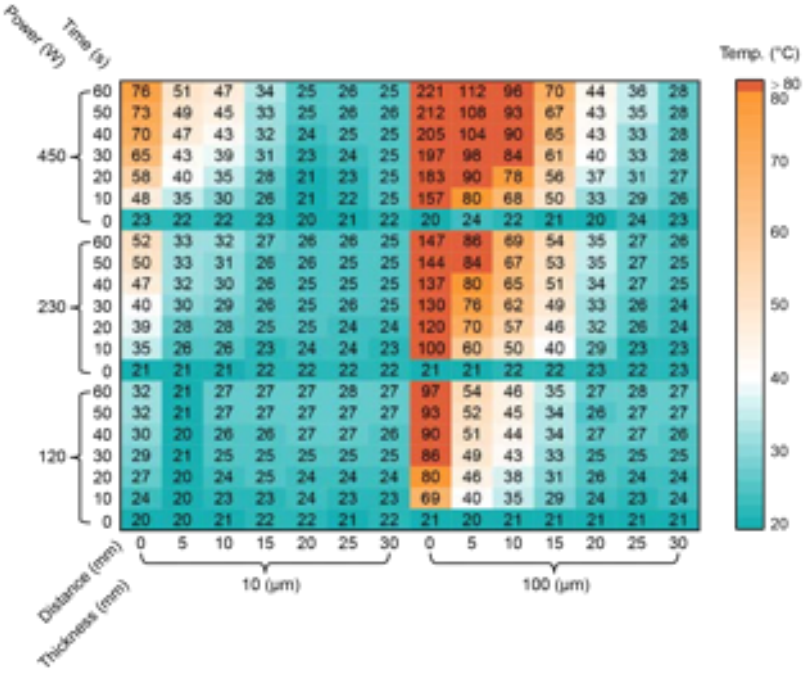

Figure 6.S8: **Heating efficiency of the aluminum heating element.** A comprehensive data summary analyzing the effects of heating time, RF heater power, heating distance, and aluminum thickness on temperature.

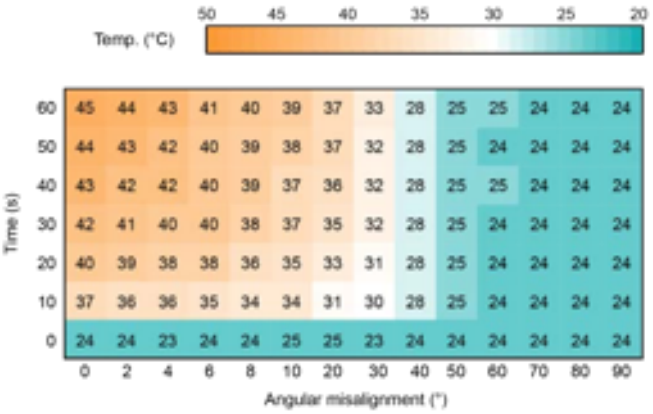

Figure 6.S9: **Orientation effects on heating efficiency.** The heating time, RF heater power, heating distance, and aluminum thickness are set to be 60 s, 450 W, 2 cm, and 100 μm, respectively.

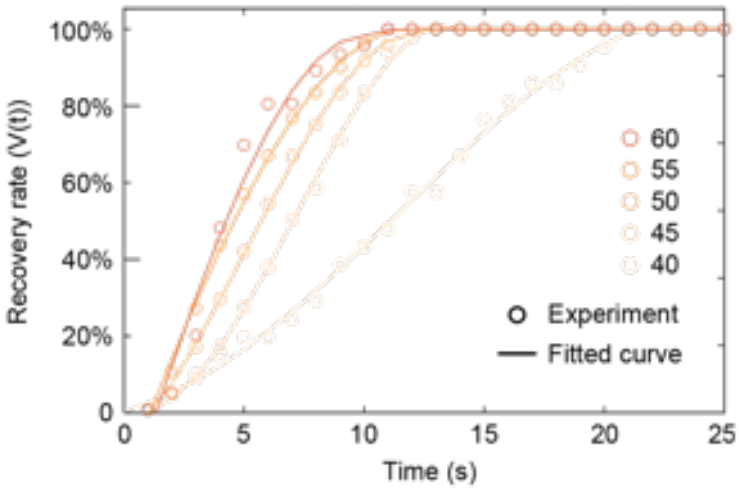

Figure 6.S10: **Recovery rate of the SMP actuator at different temperatures.**

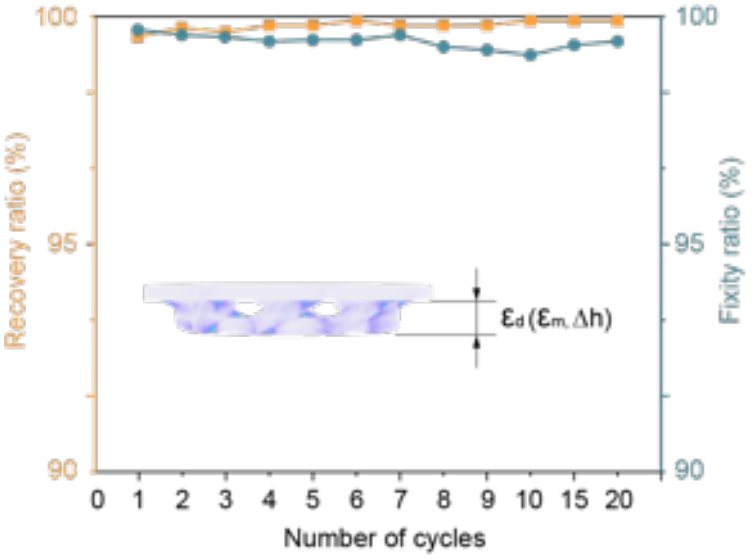

Figure 6.S11: **Shape recovery ratio and fixity ratio of the SMP over repeated training cycles.**

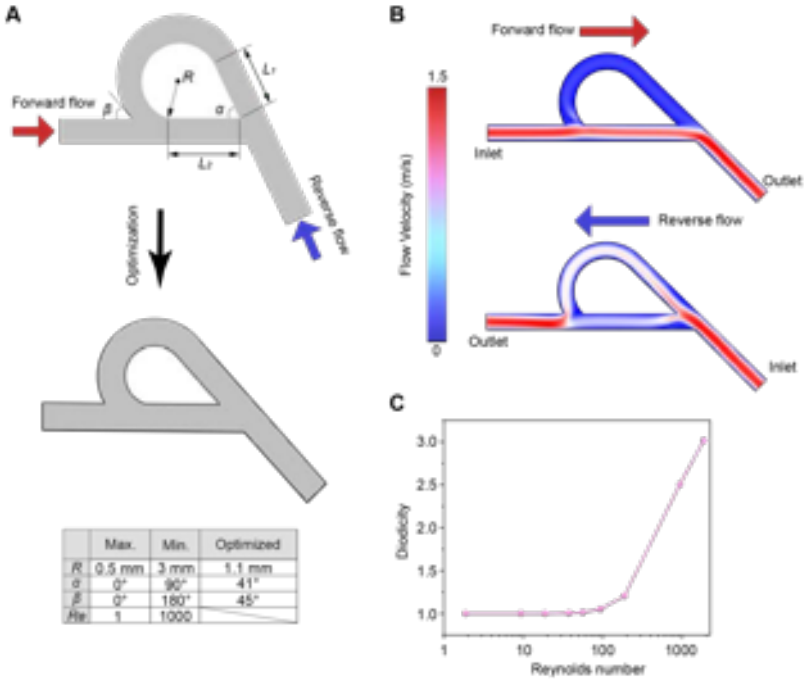

Figure 6.S12: **Parameter optimization of the Tesla valve in the SeroTab** (**A**) Schematic illustration and table of optimized variables in the Tesla valve. (**B**) Simulated flow velocity of the Tesla valve in the forward direction (top) and reverse direction (bottom). (**C**) Simulated diodicity at different Reynolds numbers of the optimized Tesla valve.

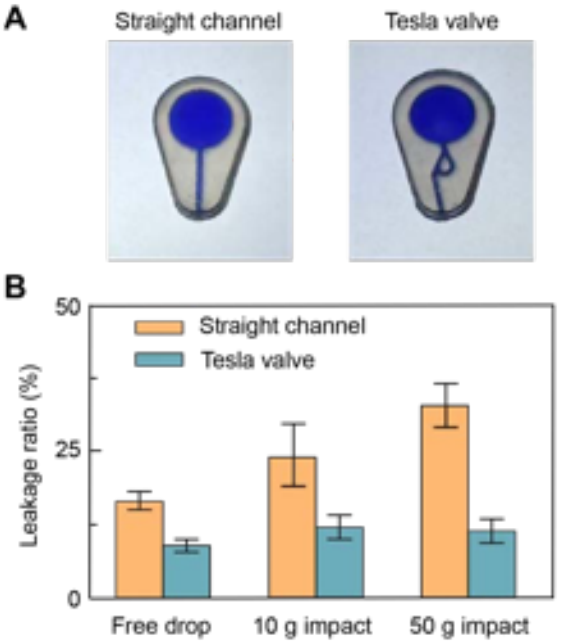

Figure 6.S13: **Comparative evaluation of straight channels and Tesla valves for leakage minimization under impact loading.** (**A**) Images of the chamber–channel part with a straight channel and a Tesla valve, respectively. (**B**) Experimental results of leakage ratios under different impact conditions: free drop from 1 m, 10 g impact from 20 cm, and 50 g impact from 20 cm. Each impact condition is repeated five times to ensure statistical reliability

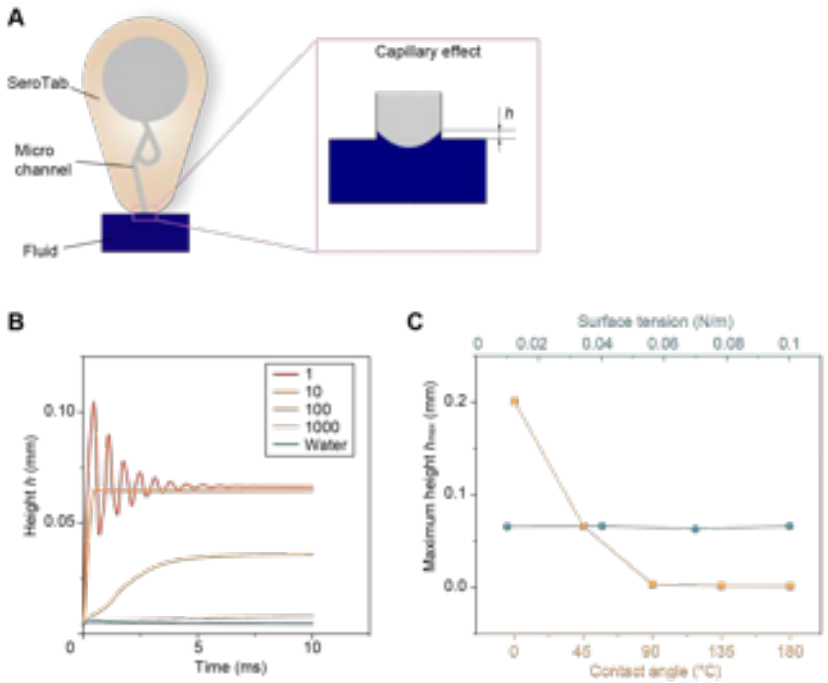

Figure 6.S14: **Capillary effect in the microchannel of SeroTab.** (**A**) Simulated liquid level of the capillary effect using COMSOL Multiphysics 6.3. (**B**) Time-dependent liquid level height for liquids with different viscosities. (**C**) Simulation results illustrating the influence of liquid properties on the maximum liquid level height.

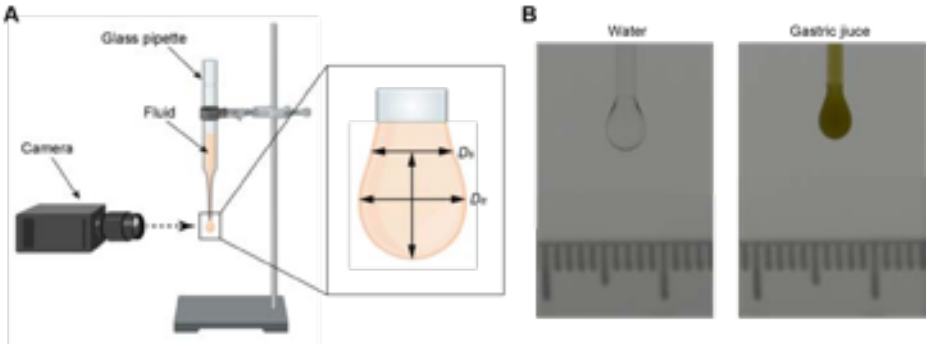

Figure 6.S15: **Measurement of liquid surface tension** (**A**) Schematic illustration of the mechanism for measuring surface tension. (**B**) Images of water and gastric juice droplets captured for the measurement of surface tension.

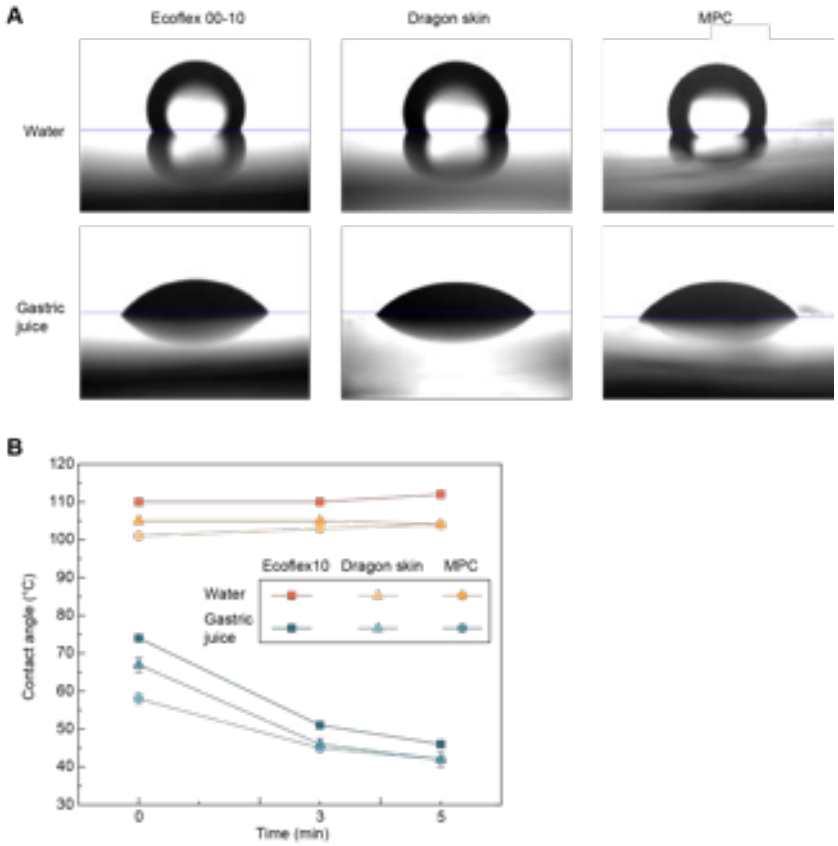

Figure 6.S16: **Measurement of contact angle.** (**A**) Images and (**B**) comparison of contact angle between different materials and liquids.

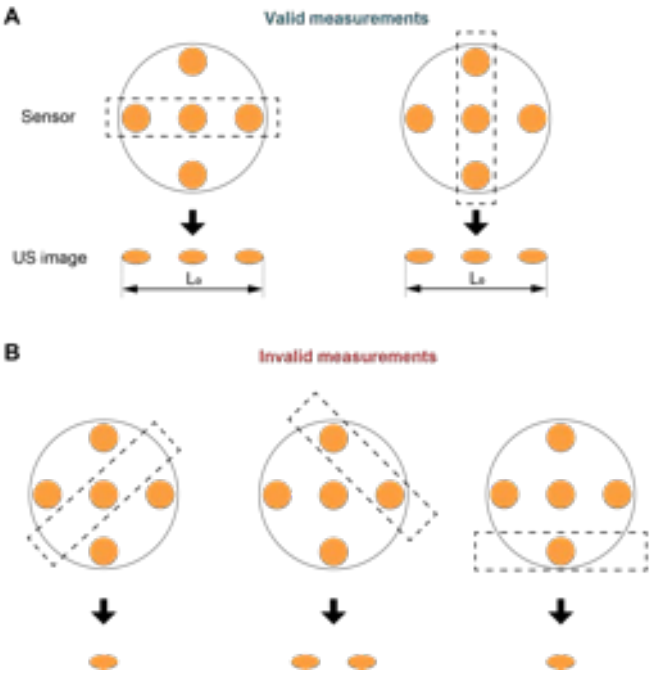

Figure 6.S17: **Schematic illustration of the ultrasound measurement strategy for the hydrogel-based sensors.** (**A**) Valid measurements are indicated by the appearance of three high–ultrasound-contrast spots at equal distances. (**B**) Fewer than three visible spots indicates an invalid measurement.

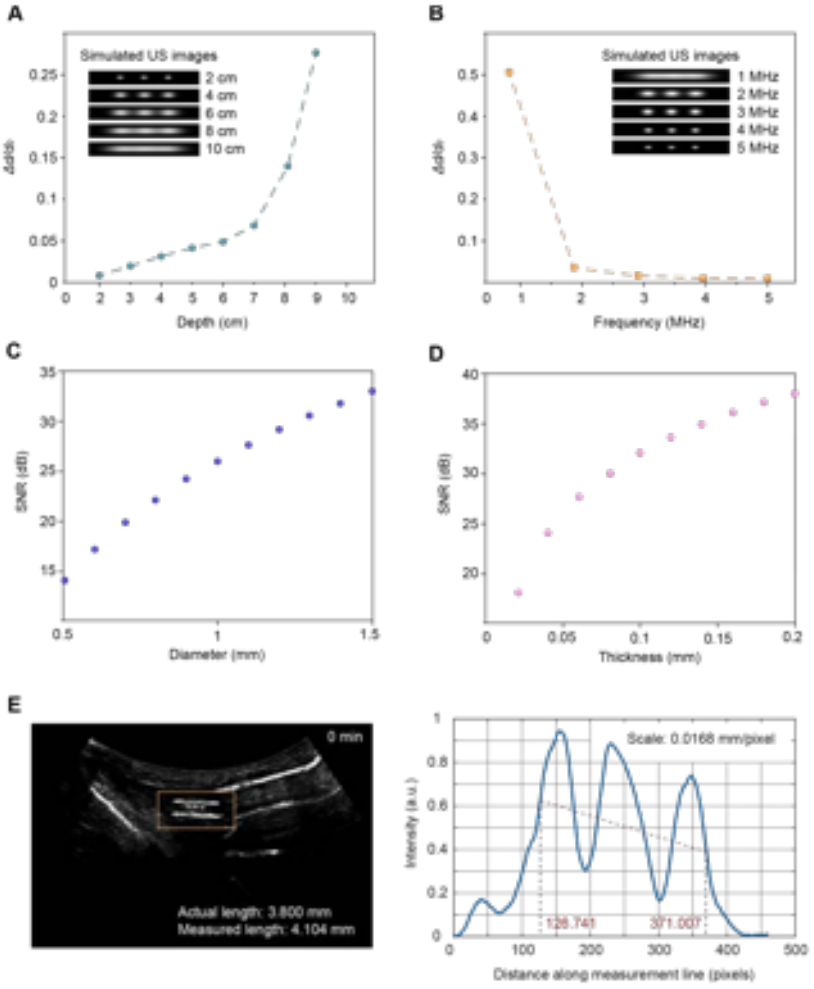

Figure 6.S18: **Quantitative evaluation of ultrasound detection resolution.** (**A**) Numerical simulation results for the measurement accuracy at different focal depth and (**B**) ultrasound frequencies. $\Delta d/d_0$ is the deviation of measured length divided by the actual length. (**C**) Numerical simulation results for the effects of diameter and (**D**) thickness of Zn disks on the signal-to-noise (SNR) at 2 cm depth and a frequency of 5 MHz. (**E**) Examples of length measurements by MATLAB coding using the ultrasound image from SeroTab at 0 min in a rabbit model.

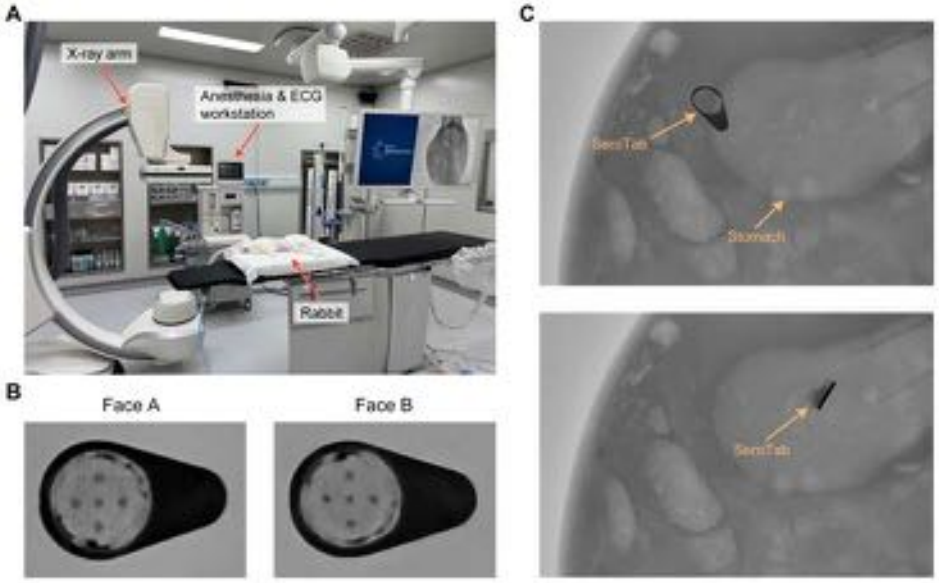

Figure 6.S19: **X-ray imaging of SeroTab in a live rabbit stomach.** (**A**) Experimental setup. (**B**) X-ray images of the SeroTab from its two faces. (**C**) X-ray confirmation of SeroTab's position and orientation in the stomach.

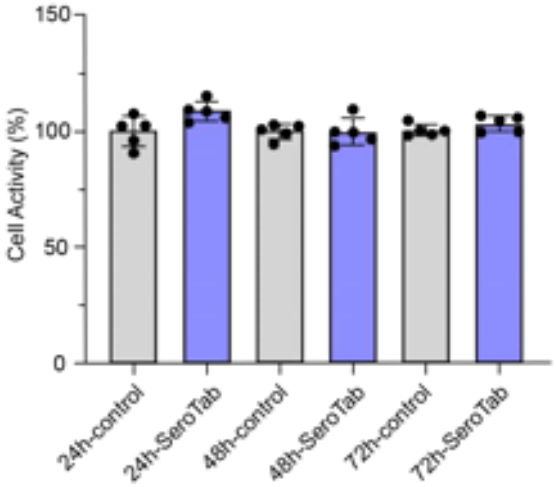

Figure 6.S20: **Cytotoxicity evaluation of HT29 cells after 24, 48, and 72 hours of incubation with extracts from SeroTab.**

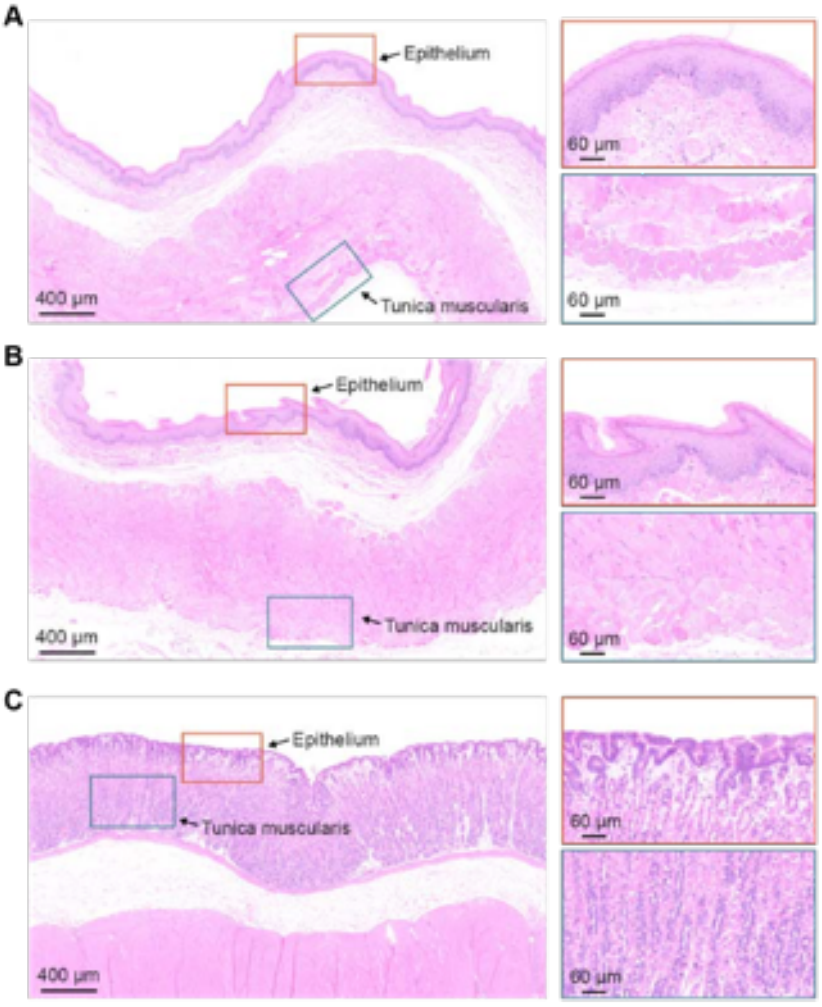

Figure 6.S21: **Hematoxylin and eosin staining of cross sections of the esophagus and stomach after operation to assess biocompatibility.** (**A**) Control group of esophagus sample. (**B**) Experimental group of esophagus sample. (**C**) Control group of stomach sample.

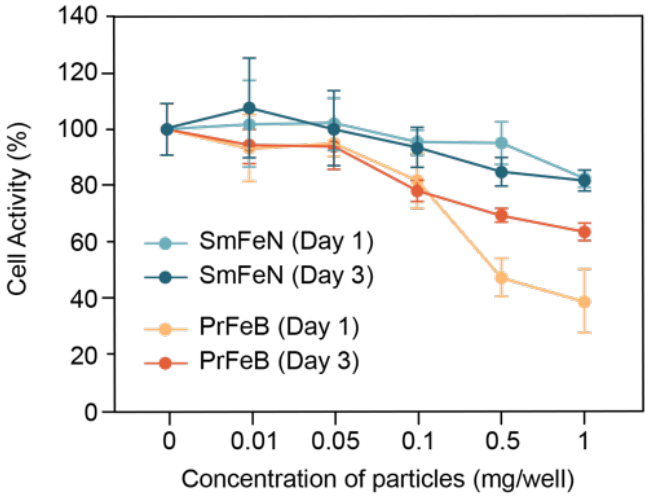

Figure 6.S22: **Cytocompatibility of PrFeB and SmFeN toward NHDF cells.**

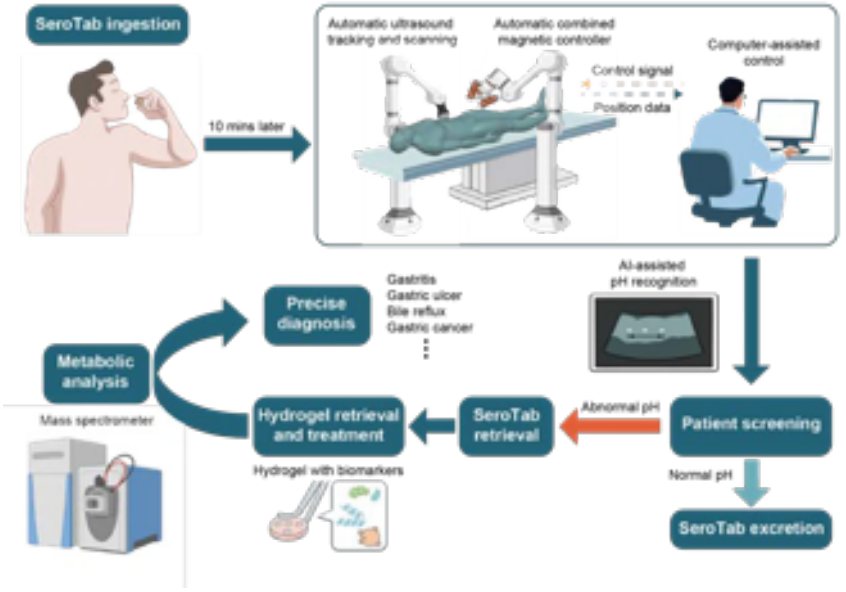

Figure 6.S23: **Illustration of the envisioned clinical workflow for SeroTab**

6.10 Supplementary Movies

Caption for Movie S1. Penguin-inspired motion pattern: posture, sliding, and orientation. Phase 1: SeroTab's body bends in response to an approaching magnet. Phase 2: SeroTab is magnetically pulled along a surface by an external moving magnet. Phase 3: SeroTab's orientation aligns with the rotation of the external magnet.

Caption for Movie S2. Penguin-inspired locomotion overcoming obstacles. Phase 1: SeroTab slides smoothly over small surface irregularities, maintaining stable motion. Phase 2: SeroTab adapts its posture to overcome larger obstacles.

Caption for Movie S3. SeroTab's motion path control on tissue surfaces *ex vivo*. SeroTab follows a pre-defined path spelling "RuG" on porcine tissue (small intestine) under external magnetic actuation.

Caption for Movie S4. SeroTab's magnetic navigation in tubular organ model *ex vivo*. SeroTab is guided through a porcine trachea via external magnetic actuation, with its motion monitored in real time using an endoscope.

Caption for Movie S5. Demonstration of locomotion and liquid sampling in porcine stomach *ex vivo*. SeroTab is magnetically guided to a target site containing gastric juice in an open porcine stomach. Upon arrival, an external radiofrequency (RF) heater is applied to activate the sampling mechanism. After fluid collection, the device is re-navigated to a second target location.

Caption for Movie S6. Demonstration of liquid sampling procedure. SeroTab is positioned with its inlet immersed in a luminous liquid. An external RF heater placed 10 mm behind the device activates the internal SMP actuator for fluid intake.

Caption for Movie S7. Swelling behavior of the hydrogel-based pH sensor in simulated gastric juice. The pH-sensitive hydrogel, em-

bedded with Zn disks, begins to swell upon contact with simulated gastric juice (pH = 3) inside the sampling chamber of SeroTab.

Caption for Movie S8. Demonstration of SeroTab's motion in live rabbit stomach *in vivo*. Phase 1: SeroTab performs sliding motion toward the target site under magnetic guidance. Phase 2: A flipping motion enables it to overcome anatomical obstacles. Phase 3: SeroTab reorients to align its inlet with the gastric juice. Phase 4: The external magnet is removed, allowing SeroTab to be released into the gastric fluid for sampling.

Caption for Movie S9. Ultrasound imaging for SeroTab localization and observation in live rabbit stomach *in vivo*. Phase 1: Ultrasound imaging captures SeroTab flipping over within the stomach. Phase 2: SeroTab swings under the control of an external magnet, as visualized via ultrasound. Phase 3: SeroTab adjusts its posture to enhance ultrasound visibility.

Caption for Movie S10. Ultrasound imaging for pH sensor detection in live rabbit stomach *in vivo*. Phase 1: Ultrasound imaging reveals the long-axis cross section and the position of Zn disks embedded within the hydrogel pH sensor. Phase 2: Ultrasound imaging reveals the short-axis cross section and the position of Zn disks within the hydrogel pH sensor.

Caption for Movie S11. Comparative study of Tesla valve-enabled leakage prevention under impact. A 500 g weight is released onto the devices to mimic accidental mechanical shocks. The device incorporating a Tesla valve shows improved resistance to leakage compared with the straight-channel configuration.

The supplementary videos are available upon request from the author.

7

Conclusions

This dissertation presents a comprehensive investigation of magnetic soft robots, focusing on their design, fabrication, actuation, and biomedical applications. Through a series of targeted experimental studies, this work addresses fundamental challenges in enabling magnetic soft robots to operate effectively in complex and dynamic physiological environments. Beginning with locomotion strategies, we developed robots capable of amphibious movement, biodegradable navigation through tortuous lumens, and stable locomotion on mucus-lined surfaces. These designs underscore the critical role of environment-specific mechanics and functional materials in enhancing performance within biological contexts. Building on this, we introduced reconfigurable and responsive systems that enable controlled manipulation and targeted therapeutic functions. Most notably, we integrated sensory capabilities into a magnetic soft robot, culminating in the creation of SeroTab—a fully ingestible, sensorized soft robot validated through *in vivo* animal studies. The successful demonstration of autonomous movement, environmental adaptability, drug delivery, cargo transportation, sampling, and real-time physiological sensing highlights the growing maturity of magnetic soft robots as potential clinical tools. By bridging bioinspired design principles with responsive materials and soft robotics technique, this research contributes new pathways for smart, multifunctional medical robots. This chapter summarizes the key contributions of this thesis and outlines directions for future research. The author also offers a personal perspective on the future development of medical devices.

7.1 Bioinspired Design for Robotic Locomotion

Bioinspired strategies have been a cornerstone in the development of magnetic soft robots throughout this dissertation, offering adaptable and efficient locomotion modes for operation in complex biomedical environments. In **Chapter 2**, inspiration from aquatic organisms (e.g., stingray, squid) led to the development of a fin-wave-driven robot capable of amphibious locomotion, achieving seamless transitions between dry and wet terrains under magnetic actuation. **Chapter 3** builds upon locomotion strategies observed in snakes, enabling a biodegradable, multi-segmented robot to perform peristaltic crawling through tortuous anatomical pathways while delivering payloads, demonstrating potential drug delivery. **Chapter 4** explores rolling motion in 3D spaces, facilitating controlled manipulation and transport on mucus-covered surfaces. Additionally, **Chapter 5** demonstrates the multimodal locomotion capabilities of a sheet-shaped magnetic soft robot, enabling adaptive performance across diverse environmental conditions. **Chapter 6** draws inspiration from the sliding motion of penguins to develop SeroTab capable of navigating the gastric environment and overcoming anatomical obstacles. These nature-inspired locomotion strategies not only enhance the environmental adaptability of magnetic soft robots but also provide a functional foundation for future clinical tools capable of navigating the body with precision, safety, and autonomy.

7.2 Biomaterials for Improved Locomotion

The environment within the human body features complex anatomical structures and is covered with various biological fluids. Achieving reliable locomotion across three-dimensional structures within the organs is essential for efficient and precise targeting, as well as for maintaining operational stability at the interventional site. **Chapter 4** addresses this challenge by introducing a ring-shaped magnetic soft robot equipped with a mucoadhesive coating. This bioinspired surface treatment significantly enhances the robot's ability to anchor and maneuver on mucus-covered tissues, enabling stable manipulation and transport tasks within the gastrointestinal environment. The integration of functional biomaterials with magnetic actuation illustrates a promising strategy for improving both the performance and biocompatibility of soft robots in clinically relevant sce-

narios.

7.3 Multi-stimuli Materials for Functionalization

The integration of stimuli-responsive materials has played a pivotal role in enhancing the functionality of magnetic soft robots throughout this dissertation. These materials impart the ability to adapt mechanical behaviors and morphologies in response to external stimuli, thereby enabling on-demand actuation within biological environments. In **Chapter 3**, biodegradable material (gelatin) is utilized to ensure safe degradation within the body while enabling targeted releasing during locomotion. **Chapter 5** introduces a dual-responsive system that combines magnetically programmable structures with temperature-sensitive hydrogels (pNIPAM), allowing for controlled gripping, release, and reconfiguration—demonstrating potential for targeted drug delivery and minimally invasive intervention. **Chapter 6** further illustrates the functional integration of smart materials through the development of SeroTab, an ingestible soft robot equipped with a shape memory polymer (SMP) actuator and an aluminum-based heat generator, which can be remotely activated via an external RF heater. This configuration enables on-demand sampling of gastric fluid within physiological environments, demonstrating robust and responsive *in vivo* performance. Collectively, these efforts highlight the critical role of smart materials in enabling multifunctional magnetic soft robots for intelligent diagnostics and targeted therapeutic applications within the human body.

7.4 Responsive Hydrogels for Sensorization

Timely and accurate physiological information from deep organs is critical for disease diagnosis and real-time health monitoring. However, conventional electronic sensors face challenges in terms of power supply, miniaturization, and biocompatibility, which limit their applicability in implantable or ingestible systems. **Chapter 6** addresses this challenge by introducing an indirect sensing strategy that leverages medical ultrasound imaging to monitor the mechanical deformation of a pH-responsive hydrogel, validated through *in vivo* experiments in live rabbits. This hydrogel exhibits volumetric changes in response to variations in local acidity, which can be non-

invasively visualized and quantified via ultrasound. This approach offers a biocompatible and energy-efficient solution for *in vivo* sensing, providing a promising direction for the development of soft robotic systems capable of physiological monitoring without relying on embedded electronics.

7.5 Outlook

This doctoral thesis presents a comprehensive investigation into the design, fabrication, actuation, and biomedical application of magnetic soft robots. By leveraging principles of bioinspired design, functional soft materials, and integration with ultrasound imaging, the work systematically addresses core challenges spanning adaptive locomotion, functional enhancement, and embedded sensing. Despite the progress demonstrated in this thesis, the clinical translation of magnetic soft robots remains contingent upon overcoming several critical challenges. Figure 7.1 illustrates the concept of robotic surgery performed by a soft robot, which requires innovation not only in the soft robotic surgical tools themselves, but also in the actuation system, control system, medical imaging system, and human–machine interface.

7.5.1 Functionalization and Sensorization

This thesis demonstrates the preliminary realization of several clinically relevant functionalities and introduces a sensorization strategy specifically tailored for magnetic soft robots. While these results underscore the feasibility of integrating functional complexity within soft, untethered systems, further research is needed to systematically develop task-specific capabilities aligned with real clinical needs. To advance toward true medical utility, magnetic soft robots must be endowed with specific functions such as targeted drug delivery, on-demand tissue operation, *in situ* sampling, and real-time physiological sensing. Achieving such goals necessitates the integration of stimuli-responsive actuation mechanisms—activated by thermal, chemical, or pH cues—with multimodal sensing platforms capable of detecting critical biological parameters such as temperature, pressure, and hormones.

Recent advances in soft electronics [313], bioresponsive hydrogels [78], and flexible microfluidics [11] provide promising avenues for embedding

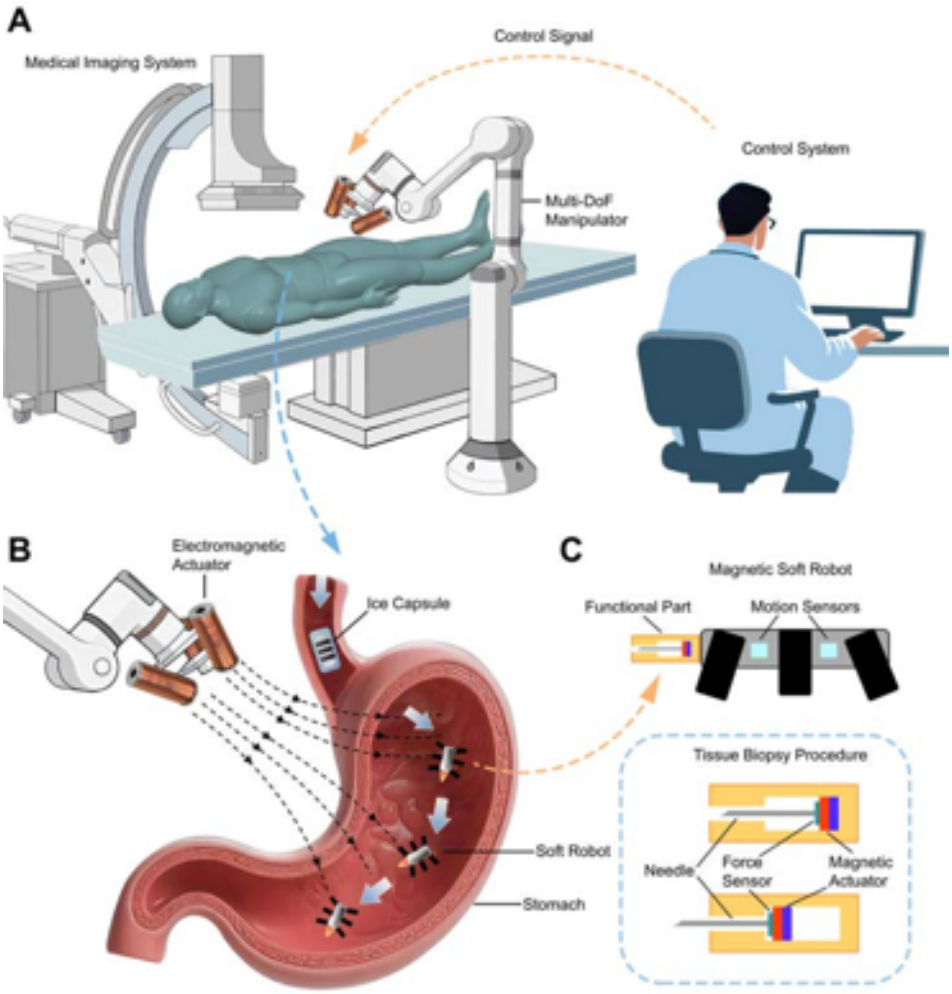

Figure 7.1: **Concept of magnetic soft robots for clinical applications.** (**A**) Overview of the actuation system, control strategy, and operational workspace. (**B**) The soft robot is capable of navigating within the human body to perform targeted tasks, guided by an externally applied magnetic field. (**C**) The robot is embedded with functional units and sensors for localization, as well as for performing specific therapeutic and diagnostic tasks.

these capabilities without sacrificing mechanical compliance or miniaturization, while offering design principles for functional actuators and soft sensors. However, realizing these complex functions at miniature scales

introduces challenges in force generation, energy efficiency, and material adaptability [314]. Future systems will require ultra-compact actuators capable of delivering high force-to-weight ratios to execute mechanically demanding interventions such as tissue penetration, lesion ablation, or micro-stent deployment. Addressing these challenges will likely hinge on breakthroughs in metamaterials and structure design—including magnetically reconfigurable lattices, anisotropic composites, and thermomechanically active hydrogels—capable of rapid, reversible, and large-scale deformations under controlled stimuli.

7.5.2 Modeling, Localization and Control

Accurate modeling of magnetic soft robots remains a central challenge due to the intrinsic nonlinearities of soft materials and the complex magneto-mechanical interactions during actuation. Soft robots often experience large deformations, nonholonomic constraints, and continuously changing contact conditions with biological substrates, making classical rigid-body modeling approaches insufficient. Furthermore, the integration of magnetic fields introduces additional coupling between spatially varying fields and the robot's compliant body, requiring multi-physics simulations that encompass elasticity, fluid–structure interaction, and magnetic forces [12]. To overcome these challenges, future research should focus on developing high-fidelity, yet computationally efficient modeling frameworks that can capture soft continuum dynamics under magnetic actuation. Promising directions include the use of reduced-order finite element methods [315], real-time physics engines calibrated by experimental data [316], machine learning and digital twin simulations [317] that bridge analytical and data-driven modeling.

Precise localization is critical for enabling closed-loop control and safe interaction of magnetic soft robots within deep anatomical environments. While traditional medical imaging modalities such as X-ray, interventional MRI, CT or ultrasound can provide positional feedback, they are often limited by cost, accessibility, temporal resolution, or compatibility with magnetic actuation [318]. Therefore, there is a growing need for miniaturized, low-cost, and real-time localization solutions and devices specifically tailored for soft robots. Emerging methods such as magnetic localization using external sensor arrays, wearable ultrasound patches [81], and hybrid op-

tical–magnetic tracking systems offer promising alternatives [220]. Future systems should aim to integrate such localization techniques into robotic platforms, while balancing spatial resolution, power efficiency, and clinical usability.

In addition to single-agent control, swarm-based strategies for magnetic soft robots are gaining attention for their potential to enhance task efficiency, robustness, and functional versatility [72]. Coordinated control of robot collectives could improve drug delivery throughput, expand sensing coverage, and enable complex procedures such as cooperative manipulation or localized diagnostics. However, implementing reliable swarm control requires scalable methods for global magnetic actuation, real-time individual localization, and decentralized decision-making. Emerging approaches, including magnetic field multiplexing [319], and AI-assisted swarm intelligence [320], are paving the way for intelligent collective behaviors. Ultimately, the fusion of closed-loop, AI-driven control with swarm dynamics represents a promising frontier in the development of next-generation soft robotic systems for minimally invasive medical applications.

7.5.3 Miniaturization and Biocompatibility

The clinical translation of magnetic soft robotic systems critically depends on their ability to navigate deep-seated, confined, and highly sensitive anatomical environments with minimal invasiveness. This necessitates continued advancements in the miniaturization of robotic architectures, magnetic actuation modules, and control subsystems—without compromising mechanical compliance or magnetic responsiveness. Recent developments in high-resolution microfabrication techniques, including two-photon lithography [321], Femtosecond laser programming [322], and soft lithographic patterning [323], offer viable pathways toward constructing sub-millimeter-scale magnetic devices. These technologies enable applications in highly constrained biomedical domains, such as intravascular intervention, endoluminal inspection, and wireless biosensing.

Equally pivotal to translational feasibility is the deployment of materials with verified biocompatibility and, where appropriate, biodegradability. Biocompatible substrates such as medical-grade silicones, gelatin-based hydrogels, and bioresorbable polymers (e.g., PLGA, PCL) have been widely adopted to minimize immunogenicity and ensure functional integration

with host tissue [324]. The use of magnetic nanoparticles with optimized surface chemistries, including PEGylation or zwitterionic coatings, can significantly mitigate biofouling and inflammatory responses [157], [325]. Furthermore, transient magnetic systems leveraging fully degradable architectures hold promise for eliminating the need for surgical retrieval post-deployment. Recent investigations have demonstrated the functional viability of such systems in *in vivo* models spanning gastrointestinal, cardiovascular, and cerebrovascular applications [12], [326]. To ensure safe and regulatory-compliant deployment in clinical settings, rigorous biocompatibility profiling—including standardized *in vitro* cytotoxicity and hemocompatibility assays, as well as comprehensive *in vivo* performance and degradation studies—must accompany device development in alignment with ISO 10993 and FDA guidelines.

7.6 Author's Perspective

Engineers stand at the intersection of clinical practice and patient need.

After more than four years of dedicated work in the development of medical devices, the author of this thesis has formed a personal perspective on translational medical engineering. The design of medical devices must account not only for the patients' needs—such as minimizing pain and ensuring safety—but also for the clinicians' requirements, including usability, workflow integration, and procedural efficiency.

Future medical device development should begin with a deep understanding of clinical needs, grounded in continuous dialogue with healthcare professionals. These needs vary significantly depending on the level of the healthcare setting. In primary care environments, such as general practitioners' offices, devices should focus on enhancing diagnostic capabilities while remaining compact, affordable, and easy to operate. Given the limited availability of high-end diagnostic infrastructure in such settings, a single multifunctional platform-as a kind of 'lab-on-robot' system-could provide versatile diagnostic support, reduce unnecessary referrals, and alleviate the burden on tertiary hospitals.

In contrast, devices designed for use in tertiary or advanced-care hospitals should prioritize precision, real-time responsiveness, and integration with complex treatment protocols. These systems should leverage cutting-edge technologies to improve procedural accuracy, assist in minimally inva-

sive interventions, and enable exploration of novel therapeutic approaches.

Ultimately, truly impactful medical technologies emerge when engineers embed themselves within clinical contexts and co-create solutions tailored to both the clinician's workflow and the patient's well-being.

Bibliography

[1] D. Rus and M. T. Tolley, "Design, fabrication and control of soft robots," *Nature*, vol. 521, no. 7553, pp. 467–475, 2015.

[2] C. Majidi, "Soft robotics: a perspective—current trends and prospects for the future," *Soft Robotics*, vol. 1, no. 1, pp. 5–11, 2014.

[3] D. Trivedi, C. Rahn, W. Kier, and I. Walker, "Soft robotics: Biological inspiration, state of the art, and future research," *Applied Bionics and Biomechanics*, vol. 5, no. 3, pp. 99–117, 2008.

[4] M. H. Dickinson, C. T. Farley, R. J. Full, M. A. R. Koehl, R. Kram, and S. Lehman, "How animals move: an integrative view," *Science*, vol. 288, no. 5463, pp. 100–106, 2000.

[5] D. Trivedi, C. D. Rahn, W. M. Kier, and I. D. Walker, "Soft robotics: Biological inspiration, state of the art, and future research," *Applied Bionics and Biomechanics*, vol. 5, no. 3, pp. 99–117, 2008.

[6] S. Kim, C. Laschi, and B. Trimmer, "Soft robotics: a bioinspired evolution in robotics," *Trends in Biotechnology*, vol. 31, no. 5, pp. 287–294, 2013.

[7] F. Ilievski, A. D. Mazzeo, R. F. Shepherd, X. Chen, and G. Whitesides, "Soft robotics for chemists," *Bioinspiration Biomimetics*, 2011.

[8] B. Mazzolai, L. Margheri, M. Cianchetti, P. Dario, and C. Laschi, "Soft-robotic arm inspired by the octopus: Ii. from artificial requirements to innovative technological solutions," *Bioinspiration Biomimetics*, vol. 7, no. 2, pp. 025005, 2012.

[9] H.-T. Lin, G. G. Leisk, and B. Trimmer, "Goqbot: a caterpillar-inspired soft-bodied rolling robot," *Bioinspiration Biomimetics*, vol. 6, no. 2, pp. 0260075, 2011.

[10] R. F. Shepherd, F. Ilievski, W. Choi, S. A. Morin, A. A. Stokes, A. D. Mazzeo, X. Chen, M. Wang, and G. M. Whitesides, "An integrated design and fabrication strategy for entirely soft, autonomous robots," *Nature*, vol. 536, no. 7617, pp. 451–455, 2016.

[11] M. Wehner, R. L. Truby, D. J. Fitzgerald, B. Mosadegh, G. M. Whitesides, J. A. Lewis, and R. J. Wood, "An integrated design and fabrication strategy for entirely soft, autonomous robots," *Nature*, vol. 536, no. 7617, pp. 451–455, 2016.

[12] Y. Kim and X. Zhao, "Magnetic soft materials and robots," *Chemical Reviews*, vol. 122, no. 5, pp. 5317–5364, 2022.

[13] M. Cianchetti, C. Laschi, A. Menciassi, and P. Dario, "Biomedicalapplications of soft robotics," *Nature Reviews Materials*, vol. 3, no. 6, pp. 143153, 2018.

[14] M. T. Tolley, R. F. Shepherd, B. Mosadegh, K. C. Galloway, M. Wehner, M. Karpelson, R. J. Wood, and G. M. A. R. Whitesides, "Untethered soft robot," *Soft Robotics*, vol. 1, no. 7, pp. 213223, 2014.

[15] S. I. Rich, R. J. Wood, and C. Majidi, "Untethered soft robotics," *Nature Electronics*, vol. 1, no. 2, pp. 102112, 2018.

[16] M. Cianchetti, C. Laschi, A. Menciassi, and P. Dario, "Soft robotics:technologies and systems pushing the boundaries of robot abilities," *Soft Robotics*, vol. 1, no. 1, pp. eaah3690, 2016.

[17] P. Polygerinos, N. Correll, S. A. Morin, B. Mosadegh, C. Onal, K. Petersen, M. Cianchetti, M. T. Tolley, and R. F. Shepherd, "Softrobotics: Review of fluid-driven intrinsically soft devices; manufacturing, sensing, control, and applications in human-robotinteraction," *Advanced Engineering Materials*, vol. 19, no. 12, pp. 1700016, 2017.

[18] T. Ranzani, S. Russo, N. W. Bartlett, M. Wehner, and R. J. Wood, "Increasing the dimensionality of soft microstructures through injection-induced self-folding," *Advanced Materials*, vol. 30, no. 38, pp. 1802739, 2018.

[19] R. F. Shepherd, F. Ilievski, W. Choi, S. A. Morin, A. A. Stokes, A. D. Mazzeo, X. Chen, M. Wang, and G. M. Whitesides, "Multigait soft robot," *Proceedings of the National Academy of Sciences*, vol. 108, no. 51, pp. 20 400–20 403, 2011.

[20] Z. Wang, N. Freris, and X. Wei, "Spirobs: Logarithmic spiral-shaped robots for versatile grasping across scales," *Device*, vol. 3, no. 4, 2025.

[21] A. Comoretto, H. Schomaker, and J. Overvelde, "Physical synchronization of soft self-oscillating limbs for fast and autonomous locomotion," *Science*, vol. 388, no. 6747, pp. 610–615, 2025.

[22] V. Venkiteswaran, D. Tan, and S. Misra, "Tandem actuation of legged locomotion and grasping manipulation in soft robots using magnetic fields," *Extreme Mechanics Letters*, vol. 41, pp. 101023, 2020.

[23] Z. Ren, W. Hu, X. Dong, and M. Sitti, "Multi-functional soft-bodied jellyfish-like swimming," *Nature Communications*, vol. 10, no. 1, pp. 1–12, 2019.

[24] G. Mao, D. Schiller, D. Danninger, B. Hailegnaw, F. Hartmann, T. Stockinger, M. Drack, N. Arnold, and M. Kaltenbrunner, "Ultrafast small-scale soft electromagnetic robots," *Nature Communications*, vol. 13, no. 1, pp. 4456, 2022.

[25] X. Dong, G. Lum, W. Hu, R. Zhang, Z. Ren, P. Onck, and M. Sitti, "Bioinspired cilia arrays with programmable nonreciprocal motion and metachronal coordination," *Science advances*, vol. 6, no. 45, pp. eabc9323, 2020.

[26] H. Lu, M. Zhang, Y. Yang, Q. Huang, T. Fukuda, Z. Wang, and Y. Shen, "A bioinspired multilegged soft millirobot that functions in both dry and wet conditions," *Nature communications*, vol. 9, no. 1, pp. 3944, 2018.

[27] W. Hu, G. Z. Lum, M. Mastrangeli, and M. Sitti, "Small-scale soft-bodied robot with multimodal locomotion," *Nature*, vol. 554, no. 7690, pp. 81–85, 2018.

[28] R. Yoshida, "Self-oscillating gels driven by the belousov–zhabotinsky reaction as novel smart materials," *Advanced Materials*, vol. 22, no. 31, pp. 3463–3483, 2010.

[29] G. Fusi, D. D. Giudice, O. Skarsetz, S. D. Stefano, and A. Walther, "Autonomous soft robots empowered by chemical reaction networks," *Advanced Materials*, vol. 35, no. 7, pp. 2209870, 2023.

[30] H. Rodrigue, W. Wang, M.-W. Han, T. J. Kim, and S.-H. Ahn, "An overview of shape memory alloy-coupled actuators and robots," *Soft Robotics*, vol. 4, no. 1, pp. 3–15, 2017.

[31] G.-Y. Gu, J. Zhu, L.-M. Zhu, and X. Zhu, "A survey on dielectric elastomer actuators for soft robots," *Soft Robotics*, vol. 12, no. 1, pp. 011003, 2017.

[32] W. Jiang, D. Niu, H. Liu, C. Wang, T. Zhao, L. Yin, Y. Shi, B. Chen, Y. Ding, and B. Lu, "Photoresponsive soft-robotic platform: biomimetic fabrication and remote actuation," *Biomimetic Fabrication and Remote Actuation*, vol. 24, no. 48, pp. 7598–7604, 2014.

[33] N. Bira, P. Dhagat, and J. R. Davidson, "A review of magneticelastomers and their role in soft robotics," *Frontiers in Robotics and AI*, vol. 7, pp. 588391, 2020.

[34] H.-J. Chung, A. M. Parsons, and L. Zheng, "Magnetically controlled-soft robotics utilizing elastomers and gels in actuation: A review," *Advanced Intelligent Systems*, vol. 3, no. 3, pp. 2000186, 2021.

[35] B. J. Nelson, I. K. Kaliakatsos, and J. J. Abbott, "Microrobots forminimally invasive medicine," *Annual Review of Biomedical Engineering*, vol. 12, no. 1, pp. 55–85, 2010.

[36] B. J. Nelson, I. K. Kaliakatsos, and J. J. Abbott, "Actuating soft matter with magnetic torque," *Advanced Functional Materials*, vol. 26, no. 22, pp. 3859–3880, 2016.

[37] X. Zhao and Y. Kim, "Soft microbots programmed by nanomagnets," *Nature*, vol. 575, pp. 58–59, 2019.

[38] X. Zhao and Y. Kim, "Ferromagnetic soft continuum robots," *Science Robotics*, vol. 4, pp. eaax7329, 2019.

[39] V. K. Venkiteswaran, L. F. P. Samaniego, J. Sikorski, and S. Misra, "Bio-inspired terrestrial motion of magnetic soft millirobots," *IEEE Robotics and automation letters*, vol. 2, no. 4, pp. 1753–1759, 2019.

[40] H. An, B. Sun, S. Picken, and E. Mendes, "Long time response of soft magnetorheological gels," *The Journal of Physical Chemistry B*, vol. 116, no. 15, pp. 4702–4711, 2019.

[41] R. Weeber, M. Hermes, A. Schmidt, and C. Holm, "Polymer architecture of magnetic gels: A review," *Journal of Physics: Condensed Matter*, vol. 30, no. 6, pp. 063002, 2018.

[42] C. Siebenmorgen, C. Wang, L. Navarro, D. Parisi, and S. Misra, "Minimally designed thermo-magnetic dual responsive soft robots for complex applications," *Journal of Materials Chemistry B*, vol. 12, no. 22, pp. 5339–5349, 2024.

[43] X. Du, H. Cui, T. Xu, C. Huang, Y. Wang, Q. Zhao, Y. Xu, and X. Wu, "Reconfiguration, camouflage, and color-shifting for bioinspired adaptive hydrogel-based millirobots," *Advanced Functional Materials*, vol. 30, no. 10, pp. 1909202, 2020.

[44] J. Breger, C. Yoon, R. Xiao, H. Kwag, M. Wang, J. Fisher, T. Nguyen, and D. Gracias, "Self-folding thermo-magnetically responsive soft microgrippers," *ACS applied materials interfaces*, vol. 7, no. 5, pp. 3398–3405, 2015.

[45] X. Liu, J. Liu, S. Lin, and X. Zhao, "Hydrogel machines," *Materials Today*, vol. 36, pp. 102–124, 2020.

[46] X. Zhao, X. Chen, H. Yuk, S. Lin, X. Liu, and G. Parada, "Soft materials by design: unconventional polymer networks give extreme properties," *Chemical Reviews*, vol. 121, no. 8, pp. 4309–4372, 2021.

[47] J. Lee, W. Han, H. Jang, and H. Choi, "Highly tough, biocompatible, and magneto-responsive fe3o4/laponite/pdmaam nanocomposite hydrogels," *Scientific reports*, vol. 9, no. 1, pp. 15024, 2019.

[48] H. Haider, C. Yang, W. Zheng, J. Yang, M. Wang, S. Yang, M. Zrínyi, Y. Osada, Z. Suo, Q. Zhang, and J. Zhou, "Exceptionally tough and notch-insensitive magnetic hydrogels," *Soft Matter*, vol. 11, no. 42, pp. 8253–8261, 2015.

[49] J. Ginder, S. Clark, W. Schlotter, and M. Nichols, "Magnetostrictive phenomena in magnetorheological elastomers," *International Journal of Modern Physics B*, vol. 16, no. 17n18, pp. 2412–2418, 2002.

[50] M. Schümann and S. Odenbach, "In-situ observation of the particle microstructure of magnetorheological elastomers in presence of mechanical strain and magnetic fields," *Journal of Magnetism and Magnetic Materials*, vol. 441, pp. 88–92, 2017.

[51] S. Miyashita, S. Guitron, K. Yoshida, S. Li, D. Damian, and . M. Rus, D., "Ingestible, controllable, and degradable origami robot for patching stomach wounds," in *Proceedings of the IEEE International Conference on Robotics and Automation (ICRA)*. IEEE, 2016, pp. 909–916.

[52] S. Yim, E. Gultepe, D. Gracias, and M. Sitti, "Biopsy using a magnetic capsule endoscope carrying, releasing, and retrieving untethered microgrippers," *IEEE Transactions on Biomedical Engineering*, vol. 61, no. 2, pp. 513–521, 2013.

[53] D. Filgueiras-Rama, A. Estrada, J. Shachar, S. Castrejón, D. Doiny, M. Ortega, E. Gang, and J. Merino, "Remote magnetic navigation for accurate, real-time catheter positioning and ablation in cardiac electrophysiology procedures," *Journal of visualized experiments: JoVE*, pp. 3658, 2013.

[54] J. Martin, R. Anderson, D. Read, and G. Gulley, "Magnetostriction of field-structured magnetoelastomers," *Physical Review E—Statistical, Nonlinear, and Soft Matter Physics*, vol. 74, no. 5, pp. 051507, 2006.

[55] R. Bustamante, "Transversely isotropic nonlinear magneto-active elastomers," *Acta mechanica*, vol. 210, pp. 183–214, 2010.

[56] Z. Ren and M. Sitti, "Design and build of small-scale magnetic soft-bodied robots with multimodal locomotion," *Nature protocols*, vol. 19, no. 2, pp. 441–486, 2024.

[57] Y. Kim, H. Yuk, R. Zhao, S. Chester, and X. Zhao, "Printing ferromagnetic domains for untethered fast-transforming soft materials," *Nature*, vol. 558, no. 7709, pp. 274–279, 2018.

[58] J. Tumbleston, D. Shirvanyants, N. Ermoshkin, R. Janusziewicz, A. Johnson, D. Kelly, K. Chen, R. Pinschmidt, J. Rolland, A. Ermoshkin, and E. Samulski, "Continuous liquid interface production of 3d objects," *Science*, vol. 347, no. 6228, pp. 1349–1352, 2015.

[59] J. Kim, S. Chung, S.E.and Choi, H. Lee, J. Kim, and S. Kwon, "Programming magnetic anisotropy in polymeric microactuators," *Nature materials*, vol. 10, no. 10, pp. 747–752, 2011.

[60] Y. Sun, W. Zhang, J. Gu, L. Xia, Y. Cao, X. Zhu, H. Wen, S. Ouyang, R. Liu, J. Li, and Z. Jiang, "Magnetically driven capsules with multimodal response and multifunctionality for biomedical applications," *Nature Communications*, vol. 15, no. 1, pp. 1839, 2024.

[61] C. Heunis, J. Sikorski, and S. Misra, "Flexible instruments for endovascular interventions: Improved magnetic steering, actuation, and image-guided surgical instruments," *IEEE robotics automation magazine*, vol. 25, no. 3, pp. 71–82, 2018.

[62] Y. Kim, E. Genevriere, P. Harker, J. Choe, M. Balicki, R. Regenhardt, J. Vranic, A. Dmytriw, A. Patel, and X. Zhao, "Telerobotic neurovascular interventions with magnetic manipulation," *Science Robotics*, vol. 7, no. 65, pp. eabg9907, 2022.

[63] A. Abramson and et al., "Oral delivery of systemic monoclonal antibodies, peptides and small molecules using gastric auto-injectors," *Nature biotechnology*, vol. 40(1), pp. 103–109, 2022.

[64] J. Zhang, Z. Ren, W. Hu, R. Soon, I. Yasa, Z. Liu, and M. Sitti, "Voxelated three-dimensional miniature magnetic soft machines via multimaterial heterogeneous assembly," *Science robotics*, vol. 6, no. 53, pp. eabf0112, 2021.

[65] X. Liu, L. Wang, Y. Xiang, F. Liao, N. Li, J. Li, J. Wang, Q. Wu, C. Zhou, Y. Yang, and Y. Kou, "Magnetic soft microfiberbots for robotic embolization," *Science Robotics*, vol. 9, pp. 87, eadh2479.

[66] X. Dong and et al., "Millimeter-scale soft capsules for sampling liquids in fluid-filled confined spaces," *Science Advances*, vol. 10(35), pp. eadp2758, 2024.

[67] R. Soon, Z. Yin, M. Dogan, N. Dogan, M. Tiryaki, A. Karacakol, A. Aydin, P. Esmaeili-Dokht, and M. Sitti, "Pangolin-inspired untethered magnetic robot for on-demand biomedical heating applications," *Nature Communications*, vol. 14, pp. 1, 2023.

[68] B. Wang, J. Shen, C. Huang, Z. Ye, J. He, X. Wu, Z. Guo, L. Zhang, and T. Xu, "Magnetically driven biohybrid blood hydrogel fibres for personalized intracranial tumour therapy under fluoroscopic tracking," *Nature Biomedical Engineering*, pp. 1–15, 2025.

[69] C. Wang and et al., "In situ sensing physiological properties of biological tissues using wireless miniature soft robots," *Science advances*, vol. 9(23), pp. eadg3988, 2023.

[70] J. Han and et al., "Actuation-enhanced multifunctional sensing and information recognition by magnetic artificial cilia arrays," *Proceedings of the National Academy of Sciences*, vol. 120(42), pp. e2308301120, 2023.

[71] S. Tottori, L. Zhang, F. Qiu, K. Krawczyk, A. Franco-Obregón, and B. Nelson, "Magnetic helical micromachines: fabrication, controlled swimming, and cargo transport," *Advanced materials*, vol. 24, no. 6, pp. 811–816, 2012.

[72] J. Yu, D. Jin, K. Chan, Q. Wang, K. Yuan, and L. Zhang, "Active generation and magnetic actuation of microrobotic swarms in bio-fluids," *Advanced materials*, vol. 10, no. 1, pp. 5631, 2019.

[73] X. Zhao, J. Kim, C. Cezar, N. Huebsch, K. Lee, K. Bouhadir, and D. Mooney, "Active scaffolds for on-demand drug and cell delivery," *Proceedings of the National Academy of Sciences*, vol. 108, no. 1, pp. 67–72, 2011.

[74] X. Liu, Y. Yang, M. Inda, S. Lin, J. Wu, Y. Kim, X. Chen, D. Ma, T. Lu, and X. Zhao, "Magnetic living hydrogels for intestinal localization, retention, and diagnosis," *Advanced Functional Materials*, vol. 31, no. 27, pp. 2010918, 2021.

[75] R. Del-Rio-Ruiz and et al., "Soft autonomous ingestible device for sampling the small-intestinal microbiome," *Device*, pp. 100406, 2024.

[76] S. R. Madhvapathy and et al., "Miniaturized implantable temperature sensors for the long-term monitoring of chronic intestinal inflammation," *Nature Biomedical Engineering*, pp. 1–13, 2024.

[77] J. Rivnay and et al., "Are implantable, living pharmacies within reach?" *Science*, vol. 386(6719), pp. 271–273, 2024.

[78] J. Liu and et al., "Bioresorbable shape-adaptive structures for ultrasonic monitoring of deep-tissue homeostasis," *Science*, vol. 383(6687), pp. 1096–1103, 2024.

[79] H. Tang and et al., "Injectable ultrasonic sensor for wireless monitoring of intracranial signals," *Nature*, vol. 630(8015), pp. 84–90, 2024.

[80] Q. Wang and et al., "Untethered micro/nanorobots for remote sensing: Toward intelligent platform," *Nano-Micro Letters*, vol. 16(1), pp. 40, 2024.

[81] C. Wang and et al., "Bioadhesive ultrasound for long-term continuous imaging of diverse organs," *Science*, vol. 377(6605), pp. 517–523, 2022.

[82] H. Hu and et al., "A wearable cardiac ultrasound imager," *Nature*, vol. 613(7945), 2022.

[83] C. Laschi, B. Mazzolai, and M. Cianchetti, "Soft robotics: Technologies and systems pushing the boundaries of robot abilities," *Science Robotics*, vol. 1, no. 1, pp. eaah3690, 2016.

[84] M. Tonutti, D. S. Elson, G. Z. Yang, A. W. Darzi, and M. H. Sodergren, "The role of technology in minimally invasive surgery: state of the art, recent developments and future directions," *Postgraduate Medical Journal*, vol. 93, no. 1097, pp. 159–167, 2017.

[85] C. Wang, V. Puranam, S. Misra, and V. Venkiteswaran, "Micro-robots for minimally invasive medicine," *Annual Review of Biomedical Engineering*, vol. 12, pp. 55–85, 2010.

[86] J. Burgner-Kahrs, D. Rucker, and H. Choset, "Continuum robots for medical applications: A survey," *IEEE Transactions on Robotics*, vol. 31, no. 6, pp. 1261–1280, 2015.

[87] Z. Li and E. Diller, "Multi-material fabrication for magnetically driven miniature soft robots using stereolithography," *Proceedings of the IEEE International Conference on Manipulation, Automation and Robotics at Small Scales (MARSS)*, pp. 1–6, 2022.

[88] W. Hu, G. Z. Lum, M. Mastrangeli, and M. Sitti, "Small-scale soft-bodied robot with multimodal locomotion," *Nature*, vol. 554, no. 7690, pp. 81–85, 2018.

[89] Y. Kim, G. Parada, S. Liu, and X. Zhao, "Ferromagnetic soft continuum robots," *Science Robotics*, vol. 4, no. 33, pp. eaax7329, 2019.

[90] S. Tottori, L. Zhang, F. Qiu, A. Krawczyk, K.K.and Franco-Obregón, and B. Nelson, "Magnetic helical micromachines: fabrication, controlled swimming, and cargo transport," *Advanced materials*, vol. 24, no. 6, pp. 811–816, 2012.

[91] J. Tian, X. Zhao, X. Gu, and S. Chen, "Designing ferromagnetic soft robots (ferrosoro) with level-set-based multiphysics topology optimization," *Proceedings of the IEEE International Conference on Robotics and Automation (ICRA)*, pp. 10 067–10 074, 2020.

[92] S. Tottori, L. Zhang, F. Qiu, K. Krawczyk, A. Franco-Obregón, and B. Nelson, "Magnetic helical micromachines: fabrication, controlled swimming, and cargo transport," *Advanced materials*, vol. 24, no. 6, pp. 811–6, 2012.

[93] C. Wang, V. Puranam, S. Misra, and V. Venkiteswaran, "A snake-inspired multi-segmented magnetic soft robot towards medical applications," *IEEE Robotics and Automation Letters*, vol. 7, no. 2, pp. 5795–5802, 2023.

[94] V. K. Venkiteswaran, L. F. P. Samaniego, J. Sikorski, and S. Misra, "Bio-inspired terrestrial motion of magnetic soft millirobots," *IEEE Robotics and Automation Letters*, vol. 4, no. 2, pp. 1753–1759, 2019.

[95] A. Bhattacharjee, L. Rogowski, X. Zhang, and M. Kim, "Untethered soft millirobot with magnetic actuation," *Proceedings of the IEEE International Conference on Robotics and Automation (ICRA)*, pp. 3792–3798, 2020.

[96] Q. Ze, S. Wu, J. Dai, S. Leanza, G. Ikeda, P. Yang, G. Iaccarino, and R. Zhao, "Spinning-enabled wireless amphibious origami millirobot," *Nature Communications*, vol. 13, no. 1, pp. 3118, 2022.

[97] Z. Ren, R. Zhang, R. H. Soon, Z. Liu, W. Hu, P. R. Onck, and M. Sitti, "Soft-bodied adaptive multimodal locomotion strategies in fluid-filled confined spaces," *Advanced Science*, vol. 7, no. 27, pp. eabh2022, 2021.

[98] D. Rus and M. Tolley, "Design, fabrication and control of soft robots," *Nature*, vol. 521, no. 7553, pp. 467–475, 2015.

[99] R. Shepherd, F. Ilievski, W. Choi, S. Morin, A. Stokes, A. Mazzeo, X. Chen, M. Wang, and G. Whitesides, "Multigait soft robot," *Proceedings of the National Academy of Sciences of the United States of America*, vol. 108, no. 51, pp. 20 400–20 403, 2011.

[100] V. K. Venkiteswaran, D. K. Tan, and S. Misra, "Tandem actuation of legged locomotion and grasping manipulation in soft robots using magnetic fields," *Extreme Mech. Lett.*, vol. 41, no. 2, pp. 11 010–1023, 2020.

[101] Z. Cui, Y. Wang, S. Zhang, T. Wang, and J. den Toonder, "Miniaturized metachronal magnetic artificial cilia," *Proceedings of the National Academy of Sciences of the United States of America*, vol. 120, no. 35, pp. e2304519120, 2023.

[102] T. Islam, Y. Bellouard, and J. den Toonder, "Highly motile nanoscale magnetic artificial cilia," *Proceedings of the National Academy of Sciences of the United States of America*, vol. 118, no. 35, pp. e2104930118, 2021.

[103] H. Gu, Q. Boehler, H. Cui, E. Secchi, G. Savorana, C. De Marco, S. Gervasoni, Q. Peyron, T. Huang, S. Pane, and A. Hirt, "Magnetic cilia carpets with programmable metachronal waves," *Nature Communications*, vol. 11, no. 1, pp. 2637, 2020.

[104] Z. Wang, A. Klingner, V. Magdanz, S. Misra, and I. Khalil, "Soft biomicrorobots: Toward biomedical applications," *Advanced Intelligent Systems*, vol. 6, no. 2, pp. 2300093, 2023.

[105] K. Zhang, A. Klingner, Y. Le Gars, S. Misra, V. Magdanz, and I. Khalil, "Locomotion of bovine spermatozoa during the transition from individual cells to bundles," *Proceedings of the National Academy of Sciences of the United States of America*, vol. 120, no. 3, pp. e2211911120, 2023.

[106] C. Li, S. Misra, and I. Khalil, "Closed-loop control characterization of untethered small-scale helical device in physiological fluid with dynamic flow rates," *Advanced Intelligent Systems*, vol. 5, no. 5, pp. 2200322, 2023.

[107] Z. Cheng, W. Feng, Y. Zhang, L. Sun, Y. Liu, L. Chen, and C. Wang, "A highly robust amphibious soft robot with imperceptibility based on a water-stable and self-healing ionic conductor," *Advanced materials*, vol. 35, no. 28, pp. 2301005, 2023.

[108] R. Baines, F. Fish, and R. Kramer-Bottiglio, *Amphibious robotic propulsive mechanisms: Current technologies and open challenges.* Bioinspired sensing, actuation, and control in underwater soft robotic systems, 2021.

[109] K. Ren and J. Yu, "Research status of bionic amphibious robots: A review," *Ocean Engineering*, vol. 227, pp. 108862, 2021.

[110] S. Yoo, B. Jun, H. Shim, and P. Lee, "Design and analysis of carbon fiber reinforced plastic body frame for multi-legged subsea walking robot," *Ocean Engineering*, vol. 102, pp. 78–86, 2015.

[111] H. Lu, M. Zhang, Y. Yang, Q. Huang, T. Fukuda, Z. Wang, and Y. Shen, "A bioinspired multilegged soft millirobot that functions in both dry and wet conditions," *Nature Communications*, vol. 9, no. 1, pp. 3944, 2018.

[112] G. Wang, X. Chen, S. Yang, P. Jia, X. Yan, and J. Xie, "Subsea crab bounding gait of leg-paddle hybrid driven shoal crablike robot," *Mechatronics*, vol. 48, pp. 1–11, 2017.

[113] Z. Ren, W. Hu, X. Dong, and M. Sitti, "Multi-functional soft-bodied jellyfish-like swimming," *Nature Communications*, vol. 10, no. 1, pp. 2703, 2019.

[114] A. Ijspeert, A. Crespi, D. Ryczko, and J. Cabelguen, "From swimming to walking with a salamander robot driven by a spinal cord model," *Science*, vol. 315, no. 5817, pp. 1416–1420, 2007.

[115] K. Low, "Modelling and parametric study of modular undulating fin rays for fish robots," *Mechanism And Machine Theory*, vol. 44, no. 3, pp. 615–632, 2009.

[116] W. Chu, K. Lee, S. Song, M. Han, J. Lee, H. Kim, M. Kim, Y. Park, K. Cho, and S. Ahn, "Review of biomimetic underwater robots using smart actuators," *International Journal of Precision Engineering*, vol. 12, pp. 1281–1292, 2012.

[117] A. McKee, I. MacDonald, S. Farina, and A. Summers, "Undulation frequency affects burial performance in living and model flatfishes," *Zoology*, vol. 119, no. 2, pp. 75–80, 2016.

[118] Festo. Bionicfinwave: Underwater robot with unique fin drive concept. [Online]. Available: https://www.festo.com/PDF_Flip/corp/Festo_BionicFinWave/en/index.html

[119] H. Liu and O. Curet, "Swimming performance of a bio-inspired robotic vessel with undulating fin propulsion," *Bioinspiration Biomimetics*, vol. 13, no. 5, pp. 056006, 2018.

[120] Z. Yong-hua, Z. Shi-wu, Y. Jie, and K. Low, "Morphologic optimal design of bionic undulating fin based on computational fluid dynamics," *Proceedings of the IEEE International Conference on Robotics and Automation (ICRA)*, pp. 491–496, 2007.

[121] C. Wang, A. Mzyk, R. Schirhagl, S. Misra, and V. Venkiteswaran, "Biocompatible film-coating of magnetic soft robots for mucoadhe-

sive locomotion," *Advanced Materials Technologies*, vol. 8, no. 12, pp. 2201813, 2023.

[122] J. Till, V. Aloi, and C. Rucker, "Real-time dynamics of soft and continuum robots based on cosserat rod models," *International Journal Of Robotics Research*, vol. 38, no. 6, pp. 723–746, 2019.

[123] D. Rucker and R. Webster III, "Statics and dynamics of continuum robots with general tendon routing and external loading," *IEEE Transactions on Robotics*, vol. 27, no. 6, pp. 1033–1044, 2011.

[124] M. Richter, V. Venkiteswaran, and S. Misra, "Multi-point orientation control of discretely-magnetized continuum manipulators," *IEEE Robotics and Automation Letters*, vol. 6, no. 2, pp. 3607–3614, 2021.

[125] Y. Tang, M. Li, T. Wang, X. Dong, W. Hu, and M. Sitti, "Wireless miniature magnetic phase-change soft actuators," *Advanced materials*, vol. 34, no. 40, pp. 2204185, 2022.

[126] Z. Cui, Y. Wang, S. Zhang, T. Wang, and J. den Toonder, "Miniaturized metachronal magnetic artificial cilia," *Proceedings of the National Academy of Sciences of the United States of America*, vol. 120, no. 35, pp. e2304519120, 2023.

[127] S. Wu and X. Zhao, "Tissue adhesive semiconductors," *Science*, vol. 381, no. 6658, pp. 608–609, 2023.

[128] C. Wang, Y. Wu, X. Dong, M. Armacki, and M. Sitti, "In situ sensing physiological properties of biological tissues using wireless miniature soft robots," *Science Advances*, vol. 9, no. 23, pp. eadg3988, 2023.

[129] M. Eshaghi, M. Ghasemi, and K. Khorshidi, "Design, manufacturing and applications of small-scale magnetic soft robots," *Extreme Mech. Lett.*, pp. 101268, 2021.

[130] D. Rus and M. T. Tolley, "Design, fabrication and control of soft robots," *Nature*, vol. 521, no. 7553, pp. 467–475, 2015.

[131] S. Kim, C. Laschi, and B. Trimmer, "Soft robotics: a bioinspired evolution in robotics," *Trends Biotechnol.*, vol. 31, no. 5, pp. 287–294, 2013.

[132] A. D. Marchese, C. D. onal, and D. Rus, "Autonomous soft robotic fish capable of escape maneuvers using fluidic elastomer actuators," *Soft Robot.*, vol. 1, no. 1, pp. 75–87, 2014.

[133] C. Branyan, C. Fleming, J. Remaley, A. Kothari, K. Tumer, R. L. Hatton, and Y. Mengüç, "Soft snake robots: Mechanical design and geometric gait implementation," *in Proc. IEEE/RSJ Int. Conf. Robot. Biomim.*, 2017, pp. 282–289.

[134] C. D. Onal and D. Rus, "Autonomous undulatory serpentine locomotion utilizing body dynamics of a fluidic soft robot," *Bioinspiration & Biomimetics*, vol. 8, no. 2, pp. 026003, Mar. 2013.

[135] A. A. Transeth, K. Y. Pettersen, and P. Liljebäck, "A survey on snake robot modeling and locomotion," *Robotica*, vol. 27, no. 7, pp. 999–1015, Dec. 2009.

[136] M. Mori and H. Hirose, "Locomotion of 3d snake-like robots–shifting and rolling control of active cord mechanism acm-r3–," *J. Robot. Mechatron.*, vol. 18, no. 5, pp. 521–528, 2006.

[137] Y. Yang, M. Zhang, D. Li, and Y. Shen, "Graphene-Based Light-Driven Soft Robot with Snake-Inspired Concertina and Serpentine Locomotion," *Advanced Materials Technologies*, vol. 4, no. 1, pp. 1800366, 2019.

[138] V. Venkiteswaran and S. Misra, "Towards gradient-based actuation of magnetic soft robots using a six-coil electromagnetic system," *in Proc. IEEE/RSJ Int. Conf. Intell. Robots Syst.*, 2020, pp. 8633–8639.

[139] S. Ernst, F. Ouyang, C. Linder, K. Hertting, F. Stahl, J. Chun, H. Hachiya, D. Bansch, M. Antz, and K. Kuck, "Initial experience with remote catheter ablation using a novel magnetic navigation system: magnetic remote catheter ablation," *Circulation*, vol. 109, no. 12, pp. 1472–1475, 2004.

[140] T. Gildea, P. Mazzone, D. Karnak, M. Meziane, and A. Mehta, "Electromagnetic navigation diagnostic bronchoscopy: a prospective study," *Am. J. Respir. Crit. Care Med.*, vol. 174, no. 9, pp. 982–989, 2006.

[141] E. B. Joyee and Y. Pan, "A fully three-dimensional printed inchworm-inspired soft robot with magnetic actuation," *Soft Robot.*, vol. 6, no. 3, pp. 333–345, 2019.

[142] S. Zheng, T. Park, M. Hoang, G. Go, C. Kim, J. Park, E. Choi, and A. Hong, "Ascidian-inspired soft robots that can crawl, tumble, and pick-and-place objects," *IEEE Robot. Autom. Lett.*, vol. 6, no. 2, pp. 1722–1728, 2021.

[143] S. Tottori, L. Zhang, F. Qiu, K. K. Krawczyk, A. Franco-Obregón, and B. J. Nelson, "Magnetic helical micromachines: fabrication, controlled swimming, and cargo transport," *Adv. Mater.*, vol. 24, no. 6, pp. 811–816, 2012.

[144] H. Deng, K. Sattari, Y. Xie, P. Liao, Z. Yan, and J. Lin, "Laser reprogramming magnetic anisotropy in soft composites for reconfigurable 3d shaping," *Nat. Commun.*, vol. 11, no. 1, pp. 1–10, 2020.

[145] J. Zhang, Z. Ren, W. Hu, R. H. Soon, I. C. Yasa, Z. Liu, and M. Sitti, "Voxelated three-dimensional miniature magnetic soft machines via multimaterial heterogeneous assembly," *Sci. Robot.*, vol. 6, no. 53, 2021.

[146] M. Sitti, H. Ceylan, W. Hu, J. Giltinan, M. Turan, S. Yim, and E. Diller, "Biomedical applications of untethered mobile milli/microrobots," *P. IEEE*, vol. 103, no. 2, pp. 205–224, 2015.

[147] S. R. Goudu, I. C. Yasa, X. Hu, H. Ceylan, W. Hu, and M. Sitti, "Biodegradable untethered magnetic hydrogel milli-grippers," *Adv. Funct. Mater.*, vol. 30, no. 50, pp. 2004975, 2020.

[148] U. Bozuyuk, O. Yasa, I. Yasa, H. Ceylan, S. Kizilel, and M. Sitti, "Light-triggered drug release from 3d-printed magnetic chitosan microswimmers," *ACS Nano*, vol. 12, no. 9, pp. 9617–9625, 2018.

[149] H. Ceylan, I. C. Yasa, O. Yasa, A. F. Tabak, J. Giltinan, and M. Sitti, "3d-printed biodegradable microswimmer for theranostic cargo delivery and release," *ACS Nano*, vol. 13, no. 3, pp. 3353–3362, 2019.

[150] M. Baumgartner, F. Hartmann, M. Drack, D. Preninger, D. Wirthl, R. Gerstmayr, L. Lehner, G. Mao, R. Pruckner, S. Demchyshyn, and

L. Reiter, "Resilient yet entirely degradable gelatin-based biogels for soft robots and electronics," *Nat. Mater.*, vol. 19, no. 10, pp. 1102–1109, 2020.

[151] S. Miyashita, S. Guitron, K. Yoshida, S. Li, D. Damian, and D. Rus, "Ingestible, controllable, and degradable origami robot for patching stomach wounds," *in Proc. IEEE Int. Conf. Robot. Auto.*, 2016, pp. 909–916.

[152] J. Hughes and D. Rus, "Mechanically programmable, degradable & ingestible soft actuators," *in Proc. IEEE/RSJ Int. Conf. Soft Robot.*, 2020, pp. 836–843.

[153] M. Thomazine, R. Carvalho, and P. Sobral, "Physical properties of gelatin films plasticized by blends of glycerol and sorbitol," *J. Food Sci.*, vol. 70, no. 3, pp. E172–E176, 2005.

[154] G. V. N. Rathna, "Gelatin hydrogels: enhanced biocompatibility, drug release and cell viability," *J. Mater. Sci.*, vol. 19, no. 6, pp. 2351–2358, 2008.

[155] N. Suderman, M. Isa, and N. Sarbon, "The effect of plasticizers on the functional properties of biodegradable gelatin-based film: A review," *Food Biosci.*, vol. 24, pp. 111–119, 2018.

[156] V. Kadiri, C. Bussi, A. Holle, K. Son, H. Kwon, G. Schütz, M. Gutierrez, and P. Fischer, "Biocompatible magnetic micro- and nanodevices: fabrication of fept nanopropellers and cell transfection," *Adv. Mater.*, vol. 32, no. 25, pp. 2001114, 2020.

[157] Y. Kim, G. Parada, S. Liu, and X. Zhao, "Ferromagnetic soft continuum robots," *Sci. Robot.*, vol. 4, no. 33, pp. eaax7329, 2019.

[158] D. Son, H. Gilbert, and M. Sitti, "Magnetically actuated soft capsule endoscope for fine-needle biopsy," *Soft robot.*, vol. 7, no. 1, pp. 10–21, 2020.

[159] W. Hu, G. Z. Lum, M. Mastrangeli, and M. Sitti, "Small-scale soft-bodied robot with multimodal locomotion," *Nature*, vol. 554, no. 7690, 2018.

[160] M. Eshaghi, M. Ghasemi, and K. Khorshidi, "Design, manufacturing and applications of small-scale magnetic soft robots," *Extreme Mech. Lett.*, vol. 44, 2021.

[161] C. Majidi, "Soft-matter engineering for soft robotics," *Adv. Mater. Technol.*, vol. 4, no. 2, 2019.

[162] B. J. Nelson, I. K. Kaliakatsos, and J. J. Abbott, "Microrobots for minimally invasive medicine," *Annu. Rev. Biomed. Eng.*, vol. 12, 2010.

[163] M. Sitti, "Miniature soft robots—road to the clinic," *Nat. Rev. Mater.*, vol. 3, no. 6, 2018.

[164] M. Tonutti, D. S. Elson, G.-Z. Yang, A. W. Darzi, and M. H. Sodergren, "The role of technology in minimally invasive surgery: state of the art, recent developments and future directions," *Postgrad Med. J.*, vol. 93, no. 1097, 2017.

[165] T. Wang, W. Hu, Z. Ren, and M. Sitti, "Ultrasound-guided wireless tubular robotic anchoring system," *IEEE Robot. Autom. Lett.*, vol. 5, no. 3, 2020.

[166] V. K. Venkiteswaran, D. K. Tan, and S. Misra, "Tandem actuation of legged locomotion and grasping manipulation in soft robots using magnetic fields," *Extreme Mech. Lett.*, vol. 93, no. 1097, 2017.

[167] C. Ahn, X. Liang, and S. Cai, "Bioinspired design of light-powered crawling, squeezing, and jumping untethered soft robot," *Adv. Mater. Technol.*, vol. 4, no. 7, 2019.

[168] H. Deng, K. Sattari, Y. Xie, P. Liao, Z. Yan, and J. Lin, "Laser reprogramming magnetic anisotropy in soft composites for reconfigurable 3d shaping," *Nat. Commun.*, vol. 11, no. 71, 2020.

[169] S. Wu, W. Hu, Q. Ze, M. Sitti, and R. Zhao, "Multifunctional magnetic soft composites: a review," *Multifunctional Materials*, vol. 3, no. 4, 2020.

[170] V. K. Venkiteswaran, L. P. Samaniego, J. Sikorski, and S. Misra, "Bio-inspired terrestrial motion of magnetic soft millirobots," *IEEE Robot. Autom. Lett.*, vol. 4, no. 2, 2019.

[171] Y. Kim, H. Yuk, R. Zhao, S. A. Chester, and X. Zhao, "Printing ferromagnetic domains for untethered fast-transforming soft materials," *Nature*, vol. 558, no. 7709, 2018.

[172] J. Zhang, Z. Ren, W. Hu, R. H. Soon, I. C. Yasa, Z. Liu, and M. Sitti, "Voxelated three-dimensional miniature magnetic soft machines via multimaterial heterogeneous assembly," *Sci. Robot.*, vol. 6, no. 53, 2021.

[173] S. Zhang, Z. Cui, Y. Wang, and J. den Toonder, "Metachronal - cilia for on-chip integrated pumps and climbing robots," *ACS Appl. Mater. Interfaces*, vol. 13, no. 17, 2021.

[174] L. Pancaldi, L. Noseda, A. Dolev, A. Fanelli, D. Ghezzi, A. J. Petruska, and M. S. Sakar, "Locomotion of sensor-integrated soft robotic devices inside sub-millimeter arteries with impaired flow conditions," *Adv. Intell. Syst.*, 2022.

[175] C. Wang, V. R. Puranam, S. Misra, and V. K. Venkiteswaran, "A snake-inspired multi-segmented magnetic soft robot towards medical applications," *IEEE Robot. Autom. Lett.*, vol. 7, no. 2, 2022.

[176] S. Noh, S. Jeon, E. Kim, U. Oh, D. Park, S. H. Park, S. W. Kim, and H. Choi, "A biodegradable magnetic microrobot based on gelatin methacrylate for precise delivery of stem cells with mass production capability," *Small*, 2020.

[177] T. Xu, J. Zhang, M. Salehizadeh, O. Onaizah, and E. Diller, "Millimeter-scale flexible robots with programmable three-dimensional magnetization and motions," *Sci. Robot.*, vol. 4, no. 29, 2019.

[178] X. Zhang, G. Chen, Y. Yu, L. Sun, and Y. Zhao, "Bioinspired adhesive and antibacterial microneedles for versatile transdermal drug delivery," *Research*, 2020.

[179] M. Baby, V. K. Periya, S. K. Sankaranarayanan, and S. C. Maniyeri, "Bioinspired surface activators for wet/dry environments through greener epoxy-catechol amine chemistry," *Appl. Surf. Sci.*, vol. 505, 2020.

[180] X.-C. Li, D.-Z. Hao, W.-J. Hao, X.-L. Guo, and L. Jiang, "Bioinspired hydrogel–polymer hybrids with a tough and antifatigue interface via one-step polymerization," *ACS Appl. Mater. Interfaces*, vol. 12, no. 45, 2020.

[181] M. P. Murphy, B. Aksak, and M. Sitti, "Gecko-inspired directional and controllable adhesion," *Small*, vol. 5, no. 2, 2009.

[182] L. Xi, L. Shi, X. Wan, B. Dai, M. Yang, Z. Gu, X. Shi, L. Jiang, and S. Wang, "A spider-silk-inspired wet adhesive with supercold tolerance," *Adv. Mater.*, vol. 33, no. 14, 2021.

[183] Y. Lee, S. Chun, D. Son, X. Hu, M. Schneider, and M. Sitti, "A tissue adhesion-controllable and biocompatible small-scale hydrogel adhesive robot," *Adv. Mater.*, vol. 34, no. 13, 2022.

[184] V. K. Venkiteswaran and S. Misra, "Towards gradient-based actuation of magnetic soft robots using a six-coil electromagnetic system," in *Proc. IEEE/RSJ Int. Conf. Intell. Robot. Syst. (IROS)*, Oct. 2020.

[185] R. Bansil and B. S. Turner, "The biology of mucus: Composition, synthesis and organization," *Adv. Drug Deliv. Rev.*, vol. 124, 2018.

[186] J. D. Smart, "The basics and underlying mechanisms of mucoadhesion," *Adv. Drug Deliv. Rev.*, vol. 57, no. 11, 2005.

[187] J. Varshosaz, N. Tavakoli, and F. Roozbahani, "Formulation and in vitro characterization of ciprofloxacin floating and bioadhesive extended-release tablets," *Drug Deliv.*, vol. 13, no. 4, 2006.

[188] M. F. Maitz, "Applications of synthetic polymers in clinical medicine," *Biosurface and Biotribology*, vol. 1, no. 3, 2015.

[189] de Souza, M. P. Chaves, R. M. Sábio, T. de Cassia Ribeiro, A. M. D. Santos, A. B. Meneguin, and M. Chorilli, "Highlighting the impact of chitosan on the development of gastroretentive drug delivery systems," *J. Biol. Macromol.*, vol. 159, 2020.

[190] L. Sun, J. Sun, L. Chen, P. Niu, X. Yang, and Y. Guo, "Preparation and characterization of chitosan film incorporated with thinned young apple polyphenols as an active packaging material," *Carbohydr. Polym.*, vol. 163, 2017.

[191] Y. Wu, X. Dong, J. kang Kim, C. Wang, and M. Sitti, "Wireless soft millirobots for climbing three-dimensional surfaces in confined spaces," *Sci. Adv.*, vol. 8, no. 21, 2022.

[192] C.-M. Lehr, J. A. Bouwstra, E. H. Schacht, and H. E. Junginger, "In vitro evaluation of mucoadhesive properties of chitosan and some other natural polymers," *Int. J. Pharm.*, vol. 78, no. 1-3, 1992.

[193] J. F. Fundo, M. A. Quintas, and C. L. Silva, "Influence of film forming solutions on properties of chitosan/glycerol films," 2011.

[194] N. E. Suyatma, L. Tighzert, A. Copinet, and V. Coma, "Effects of hydrophilic plasticizers on mechanical, thermal, and surface properties of chitosan films," *J. Agric. Food. Chem.*, vol. 53, no. 10, 2005.

[195] A. da Silva Costa, "Assessment of operative times of multiple surgical specialties in a public university hospital," *Einstein (Sao Paulo)*, vol. 15, 2017.

[196] A. G. Ranjbary, G. K. Saleh, M. Azimi, F. Karimian, J. Mehrzad, and J. Zohdi, "Superparamagnetic iron oxide nanoparticles induce apoptosis in ht-29 cells by stimulating oxidative stress and damaging dna," *Biol. Trace. Elem. Res.*, vol. 1, no. 11, 2022.

[197] M. Kammoun, M. Haddar, T. K. Kallel, M. Dammak, and A. Sayari, "Biological properties and biodegradation studies of chitosan biofilms plasticized with peg and glycerol," *Int. J. Biol.*, vol. 62, 2013.

[198] B. Li, J. Wang, Q. Gui, and H. Yang, "Drug-loaded chitosan film prepared via facile solution casting and air-drying of plain water-based chitosan solution for ocular drug delivery," *Bioact. Mater.*, vol. 5, no. 3, 2020.

[199] C. Tang, Y.-X. Guan, S.-J. Yao, and Z.-Q. Zhu, "Preparation of ibuprofen-loaded chitosan films for oral mucosal drug delivery using supercritical solution impregnation," *Int. J. Pharm.*, vol. 473, no. 1-2, 2014.

[200] J. L. Sparks, N. A. Vavalle, K. E. Kasting, B. Long, M. L. Tanaka, P. A. Sanger, K. Schnell, and T. A. Conner-Kerr, "Use of silicone

materials to simulate tissue biomechanics as related to deep tissue injury," *Adv. Skin Wound Care*, vol. 28, no. 2, 2015.

[201] P. Li, S. Jiang, Y. Yu, J. Yang, and Z. Yang, "Biomaterial characteristics and application of silicone rubber and pva hydrogels mimicked in organ groups for prostate brachytherapy," *J. Mech. Behav. Biomed. Mater.*, vol. 49, 2015.

[202] B. Jin, H. Song, R. Jiang, J. Song, Q. Zhao, , and T. Xie, "Programming a crystalline shape memory polymer network with thermo-and photo-reversible bonds toward a single-component soft robot," *Sci. Adv.*, vol. 4, no. 1, 2018.

[203] A. Lendlein, "Fabrication of reprogrammable shape-memory polymer actuators for robotics," *Sci. Robot.*, vol. 3, no. 18, 2018.

[204] B. T. Burruano, R. L. Schnaare, and D. Malamudd, "Synthetic cervical mucus formulation," *Contraception*, vol. 66, no. 2, 2002.

[205] L. M. Lichtenberger and J. J. Romerod, "Effect of ammonium ion on the hydrophobic and barrier properties of the gastric mucus gel layer: Implications on the role of ammonium in h. pylori-induced gastritis," *J. Gastroenterol. Hepatol.*, vol. 9, no. S1, 1994.

[206] L. Nie, A. Nusantara, V. Damle, M. Baranov, M. Chipaux, C. Reyes-San-Martin, T. Hamoh, C. Epperla, M. Guricova, P. Cigler, , and G. V. D. Bogaart, "Quantum sensing of free radicals in primary human dendritic cells," *Nano Lett.*, vol. 22, no. 4, 2021.

[207] N. Norouzi, A. C. Nusantara, Y. Ong, T. Hamoh, L. Nie, A. Morita, Y. Zhang, A. Mzyk, and R. Schirhagl, "Relaxometry for detecting free radical generation during bacteria's response to antibiotics," *Carbon*, vol. 199, 2022.

[208] A. Sigaeva, A. Hochstetter, S. Bouyim, M. Chipaux, M. Stejfova, P. Cigler, and R. Schirhagl, "Single-particle tracking and trajectory analysis of fluorescent nanodiamonds in cell-free environment and live cells," *Small*, vol. 2201395, 2022.

[209] F. P. Martine, A. C. Nusantara, M. Chipaux, S. K. Padamati, and R. Schirhagl, "Nanodiamond relaxometry-based detection of free-radical species when produced in chemical reactions in biologically relevant conditions," *ACS Sens.*, vol. 5, no. 12, 2020.

[210] A. Morita, T. Hamoh, F. P. P. Martinez, M. Chipaux, A. Sigaeva, C. Mignon, K. J. van der Laan, A. Hochstetter, and R. Schirhagl, "The fate of lipid-coated and uncoated fluorescent nanodiamonds during cell division in yeast," *Nanomaterials*, vol. 10, no. 3, 2020.

[211] O. A. Shenderova, A. I. Shames, N. A. Nunn, M. D. Torelli, I. Vlasov, and A. Zaitsev, "Synthesis, properties, and applications of fluorescent diamond particles," *J. Vac. Sci. Technol. B*, vol. 37, no. 3, 2019.

[212] K. Y. Ma, P. Chirarattananon, S. B. Fuller, and R. J. Wood, "Controlled flight of a biologically inspired, insect-scale robot," *Science*, vol. 340, no. 6132, pp. 603–607, 2013.

[213] Z. Zhakypov, K. Mori, K. Hosoda, and J. Paik, "Designing minimal and scalable insect-inspired multi-locomotion millirobots," *Nature*, vol. 571, no. 7765, pp. 381–386, 2019.

[214] C. Laschi, M. Cianchetti, B. Mazzolai, L. Margheri, M. Follador, and P. Dario, "Soft robot arm inspired by the octopus," *Advanced robotics*, vol. 26, no. 7, pp. 709–727, 2012.

[215] Y. Takishima, K. Yoshida, A. Khosla, M. Kawakami, and H. Furukawa, "Fully 3d-printed hydrogel actuator for jellyfish soft robots," *ECS Journal of Solid State Science and Technology*, vol. 10, no. 3, pp. 037002, 2021.

[216] Z. Shen, F. Chen, X. Zhu, K.-T. Yong, and G. Gu, "Stimuli-responsive functional materials for soft robotics," *Journal of Materials Chemistry B*, vol. 8, no. 39, pp. 8972–8991, 2020.

[217] Z. Yu, Y. Wang, J. Zheng, S. Sun, Y. Fu, D. Chen, W. Cai, D. Wang, H. Zhou, and D. Li, "Fast-response bioinspired near-infrared light-driven soft robot based on two-stage deformation," *ACS Applied Materials & Interfaces*, vol. 14, no. 14, pp. 16 649–16 657, 2022.

[218] G. Fusi, D. Del Giudice, O. Skarsetz, S. Di Stefano, and A. Walther, "Autonomous soft robots empowered by chemical reaction networks," *Advanced Materials*, vol. 35, no. 7, pp. 2209870, 2023.

[219] R. K. Katzschmann, J. DelPreto, R. MacCurdy, and D. Rus, "Exploration of underwater life with an acoustically controlled soft robotic fish," *Science Robotics*, vol. 3, no. 16, pp. eaar3449, 2018.

[220] J. Wang and A. Chortos, "Control strategies for soft robot systems," *Advanced Intelligent Systems*, vol. 4, no. 5, pp. 2100165, 2022.

[221] C. Yin, F. Wei, S. Fu, Z. Zhai, Z. Ge, L. Yao, M. Jiang, and M. Liu, "Visible light-driven jellyfish-like miniature swimming soft robot," *ACS Applied Materials Interfaces*, vol. 13, no. 39, pp. 47 147–47 154, 2021.

[222] G. R. Gossweiler, C. L. Brown, G. B. Hewage, E. Sapiro-Gheiler, W. J. Trautman, G. W. Welshofer, and S. L. Craig, "Mechanochemically active soft robots," *ACS applied materials & interfaces*, vol. 7, no. 40, pp. 22 431–22 435, 2015.

[223] N. Ebrahimi, C. Bi, D. J. Cappelleri, G. Ciuti, A. T. Conn, D. Faivre, N. Habibi, A. Hošovskỳ, V. Iacovacci, I. S. Khalil *et al.*, "Magnetic actuation methods in bio/soft robotics," *Advanced Functional Materials*, vol. 31, no. 11, pp. 2005137, 2021.

[224] H. Wang, Z. Zhu, H. Jin, R. Wei, L. Bi, and W. Zhang, "Magnetic soft robots: Design, actuation, and function," *Journal of Alloys and Compounds*, pp. 166219, 2022.

[225] Y. Kim, G. A. Parada, S. Liu, and X. Zhao, "Ferromagnetic soft continuum robots," *Science Robotics*, vol. 4, no. 33, pp. eaax7329, 2019.

[226] S. Lee, S. Lee, S. Kim, C.-H. Yoon, H.-J. Park, J.-y. Kim, and H. Choi, "Fabrication and characterization of a magnetic drilling actuator for navigation in a three-dimensional phantom vascular network," *Scientific reports*, vol. 8, no. 1, pp. 1–9, 2018.

[227] H. M. Le, T. N. Do, and S. J. Phee, "A survey on actuators-driven surgical robots," *Sensors and Actuators A: Physical*, vol. 247, pp. 323–354, 2016.

[228] A. Ghosh, C. Yoon, F. Ongaro, S. Scheggi, F. M. Selaru, S. Misra, and D. H. Gracias, "Stimuli-responsive soft untethered grippers for drug delivery and robotic surgery," *Frontiers in Mechanical Engineering*, vol. 3, pp. 7, 2017.

[229] G. Li, X. Chen, F. Zhou, Y. Liang, Y. Xiao, X. Cao, Z. Zhang, M. Zhang, B. Wu, S. Yin *et al.*, "Self-powered soft robot in the mariana trench," *Nature*, vol. 591, no. 7848, pp. 66–71, 2021.

[230] F. Ahmed, M. Waqas, B. Jawed, A. M. Soomro, S. Kumar, A. Hina, U. Khan, K. H. Kim, and K. H. Choi, "Decade of bio-inspired soft robots: A review," *Smart Materials and Structures*, vol. 31, no. 7, pp. 073002, 2022.

[231] L. G. M. M. Hu, W. and M. Sitti, "Small-scale soft-bodied robot with multimodal locomotion," *Nature*, vol. 554, no. 7690, pp. 81–85, 2018.

[232] M. Guo, Y. Wu, S. Xue, Y. Xia, X. Yang, Y. Dzenis, Z. Li, W. Lei, A. T. Smith, and L. Sun, "A highly stretchable, ultra-tough, remarkably tolerant, and robust self-healing glycerol-hydrogel for a dual-responsive soft actuator," *Journal of Materials Chemistry A*, vol. 7, no. 45, pp. 25 969–25 977, 2019.

[233] Z. Shen, F. Chen, X. Zhu, K.-T. Yong, and G. Gu, "Stimuli-responsive functional materials for soft robotics," *Journal of Materials Chemistry B*, vol. 8, no. 39, pp. 8972–8991, 2020.

[234] J. Fu, "Hydrogel properties and applications," *Journal of Materials Chemistry B*, vol. 7, no. 10, pp. 1523–1525, 2019.

[235] K. Otake, H. Inomata, M. Konno, and S. Saito, "Thermal analysis of the volume phase transition with n-isopropylacrylamide gels," *Macromolecules*, vol. 23, no. 1, pp. 283–289, 1990.

[236] H. G. Schild, "Poly (n-isopropylacrylamide): experiment, theory and application," *Progress in polymer science*, vol. 17, no. 2, pp. 163–249, 1992.

[237] F. Ongaro, S. Scheggi, C. Yoon, F. v. den Brink, S. H. Oh, D. H. Gracias, and S. Misra, "Autonomous planning and control of soft untethered grippers in unstructured environments," *Journal of micro-bio robotics*, vol. 12, pp. 45–52, 2017.

[238] J. C. Breger, C. Yoon, R. Xiao, H. R. Kwag, M. O. Wang, J. P. Fisher, T. D. Nguyen, and D. H. Gracias, "Self-folding thermo-magnetically responsive soft microgrippers," *ACS applied materials & interfaces*, vol. 7, no. 5, pp. 3398–3405, 2015.

[239] X. Du, H. Cui, T. Xu, C. Huang, Y. Wang, Q. Zhao, Y. Xu, and X. Wu, "Reconfiguration, camouflage, and color-shifting for bioinspired adaptive hydrogel-based millirobots," *Advanced Functional Materials*, vol. 30, no. 10, pp. 1909202, 2020.

[240] C. Siebenmorgen, A. Poortinga, and P. van Rijn, "Sono-processes: Emerging systems and their applicability within the (bio-) medical field," *Ultrasonics sonochemistry*, pp. 106630, 2023.

[241] Y. Zhai, H. Duan, X. Meng, K. Cai, Y. Liu, and L. Lucia, "Reinforcement effects of inorganic nanoparticles for double-network hydrogels," *Macromolecular Materials and Engineering*, vol. 300, no. 12, pp. 1290–1299, 2015.

[242] Y. Guan and Y. Zhang, "Pnipam microgels for biomedical applications: from dispersed particles to 3d assemblies," *Soft Matter*, vol. 7, no. 14, pp. 6375–6384, 2011.

[243] J. Jelken, S.-H. Jung, N. Lomadze, Y. D. Gordievskaya, E. Y. Kramarenko, A. Pich, and S. Santer, "Tuning the volume phase transition temperature of microgels by light," *Advanced Functional Materials*, vol. 32, no. 2, pp. 2107946, 2022.

[244] K. Kratz, T. Hellweg, and W. Eimer, "Influence of charge density on the swelling of colloidal poly (n-isopropylacrylamide-co-acrylic acid) microgels," *Colloids and Surfaces A: Physicochemical and Engineering Aspects*, vol. 170, no. 2-3, pp. 137–149, 2000.

[245] Y. K. Kim, E.-J. Kim, J. H. Lim, H. K. Cho, W. J. Hong, H. H. Jeon, and B. G. Chung, "Dual stimuli-triggered nanogels in response to temperature and ph changes for controlled drug release," *Nanoscale Research Letters*, vol. 14, pp. 1–9, 2019.

[246] L. Tang, L. Wang, X. Yang, Y. Feng, Y. Li, and W. Feng, "Poly (n-isopropylacrylamide)-based smart hydrogels: Design, properties and applications," *Progress in Materials Science*, vol. 115, pp. 100702, 2021.

[247] C. Siebenmorgen, G. Zu, D. Keskin, and P. van Rijn, "Dynamic covalent cross-linked nanogel-stabilized pickering emulsion for responsive microstructures," *Macromolecular Rapid Communications*, vol. 43, no. 15, pp. 2100766, 2022.

[248] N. Seddiki and D. Aliouche, "Synthesis, rheological behavior and swelling properties of copolymer hydrogels based on poly (n-isopropylacrylamide) with hydrophilic monomers," *Bulletin of the Chemical Society of Ethiopia*, vol. 27, no. 3, pp. 447–457, 2013.

[249] R. Regmi, S. R. Bhattarai, C. Sudakar, A. S. Wani, R. Cunningham, P. P. Vaishnava, R. Naik, D. Oupicky, and G. Lawes, "Hyperthermia controlled rapid drug release from thermosensitive magnetic microgels," *Journal of Materials Chemistry*, vol. 20, no. 29, pp. 6158–6163, 2010.

[250] D. Jiao, Q. Zhu, C. Li, Q. Zheng, and Z. Wu, "Programmable morphing hydrogels for soft actuators and robots: from structure designs to active functions," *Accounts of Chemical Research*, vol. 55, no. 11, pp. 1533–1545, 2022.

[251] Z. Chen, D. Zhao, B. Liu, G. Nian, X. Li, J. Yin, S. Qu, and W. Yang, "3d printing of multifunctional hydrogels," *Advanced Functional Materials*, vol. 29, no. 20, pp. 1900971, 2019.

[252] J. Li, C. Wu, P. Chu, and M. Gelinsky, "3d printing of hydrogels: Rational design strategies and emerging biomedical applications," *Materials Science and Engineering: R: Reports*, vol. 140, pp. 100543, 2020.

[253] A. Nishiguchi, H. Zhang, S. Schweizerhof, M. F. Schulte, A. Mourran, and M. Moller, "4d printing of a light-driven soft actuator with programmed printing density," *ACS applied materials & interfaces*, vol. 12, no. 10, pp. 12 176–12 185, 2020.

[254] E. Burdukova, H. Li, N. Ishida, J.-P. O'Shea, and G. V. Franks, "Temperature controlled surface hydrophobicity and interaction forces induced by poly (n-isopropylacrylamide)," *Journal of Colloid and Interface Science*, vol. 342, no. 2, pp. 586–592, 2010.

[255] Z. W. Tay, P. Chandrasekharan, A. Chiu-Lam, D. W. Hensley, R. Dhavalikar, X. Y. Zhou, E. Y. Yu, P. W. Goodwill, B. Zheng, C. Rinaldi *et al.*, "Magnetic particle imaging-guided heating in vivo using gradient fields for arbitrary localization of magnetic hyperthermia therapy," *ACS nano*, vol. 12, no. 4, pp. 3699–3713, 2018.

[256] E. Khadem, M. Kharaziha, H. R. Bakhsheshi-Rad, O. Das, and F. Berto, "Cutting-edge progress in stimuli-responsive bioadhesives: from synthesis to clinical applications," *Polymers*, vol. 14, no. 9, pp. 1709, 2022.

[257] L. Han, Y. Zhang, X. Lu, K. Wang, Z. Wang, and H. Zhang, "Polydopamine nanoparticles modulating stimuli-responsive pnipam hydrogels with cell/tissue adhesiveness," *ACS applied materials & interfaces*, vol. 8, no. 42, pp. 29 088–29 100, 2016.

[258] B. A. Badeau and C. A. DeForest, "Programming stimuli-responsive behavior into biomaterials," *Annual review of biomedical engineering*, vol. 21, pp. 241–265, 2019.

[259] A. F. Peery and et al., "Burden and cost of gastrointestinal, liver, and pancreatic diseases in the united states: update 2024," *Gastroenterology*, vol. 168(5), pp. 1000–1024, 2025.

[260] Y. Wang and et al., "Global burden of digestive diseases: a systematic analysis of the global burden of diseases study, 1990 to 2019," *Gastroenterology*, vol. 165(3), pp. 773–783, 2023.

[261] B. Starfield and et al., "Contribution of primary care to health systems and health," *The Milbank Quarterly*, vol. 83(3), pp. 457–502, 2005.

[262] C. B. Forrest and et al., "Primary care gatekeeping and referrals: effective filter or failed experiment?" *British Medical Journal*, vol. 326(7391), pp. 692–695, 2003.

[263] D. Kringos and et al., "The strength of primary care in europe: an international comparative study," *British Journal of General Practice*, vol. 63(616), pp. e742–e750, 2013.

[264] World Health Organization, *Medical devices: managing the mismatch: an outcome of the priority medical devices project.* World Health Organization, 2010.

[265] W. G. Thompson and et al., "Irritable bowel syndrome in general practice: prevalence, characteristics, and referral," *Gut*, vol. 46(1), pp. 78–82, 2000.

[266] M. L. Schubert and et al., "Control of gastric acid secretion in health and disease," *Gastroenterology*, vol. 134(7), pp. 1842–1860, 2008.

[267] J. D. Gardner and et al., "Increased gastric acid secretion as a possible cause of gerd," *Nature Reviews Gastroenterology and Hepatology*, vol. 7(3), pp. 125–126, 2010.

[268] W. M. De Vos and et al., "Gut microbiome and health: mechanistic insights," *Gut*, vol. 71(5), pp. 1020–1032, 2022.

[269] Q. Ci and et al., "Fe-doped carbon dots as nir-ii fluorescence probe for in vivo gastric imaging and ph detection," *Advanced Science*, vol. 10(7), pp. 2206271, 2023.

[270] W. Huang and et al., "In vivo quantitative photoacoustic diagnosis of gastric and intestinal dysfunctions with a broad ph-responsive sensor," *ACS nano*, vol. 13(8), pp. 9561–9570, 2019.

[271] T. Ghosh and et al., "Methods of measuring gastric acid secretion," *Alimentary Pharmacology Therapeutics*, vol. 33(7), pp. 768–781, 2011.

[272] M. Chiara and et al., "Non-invasive method for the assessment of gastric acid secretion," *Acta Bio Medica: Atenei Parmensis*, vol. 89(Suppl 8), pp. 53, 2018.

[273] W. H. Steinberg and et al., "Heidelberg capsule i: In vitro evaluation of a new instrument for measuring intragastric ph," *Journal of Pharmaceutical Sciences*, vol. 54(5), pp. 772–776, 1965.

[274] B. Jacobson and R. S. Mackay, "A ph-endoradiosonde," *The Lancet*, vol. 269(6981), pp. 1224, 1957.

[275] X. Zhang and et al., "Bioinspired oral delivery devices," *Nature Reviews Bioengineering*, vol. 1(3), pp. 208–225, 2023.

[276] M. Rehan and et al., "Smart capsules for sensing and sampling the gut: status, challenges and prospects," *Gut*, vol. 73(1), pp. 186–202, 2024.

[277] W. Hu and et al., "Small-scale soft-bodied robot with multimodal locomotion," *Nature*, vol. 554(7690), pp. 81–85, 2018.

[278] J. Cui and et al., "Nanomagnetic encoding of shape-morphing micromachines," *Nature*, vol. 575(7781), pp. 164–168, 2019.

[279] S. Tottori and et al., "Magnetic helical micromachines: fabrication, controlled swimming, and cargo transport," *Advanced materials*, vol. 24(6), pp. 811–816, 2012.

[280] T. Xu and et al., "Millimeter-scale flexible robots with programmable three-dimensional magnetization and motions," *Science robotics*, vol. 4(29), pp. eaav4494, 2019.

[281] H. Xie and et al., "Reconfigurable magnetic microrobot swarm: Multimode transformation, locomotion, and manipulation," *Science robotics*, vol. 4(28), pp. eaav8006, 2019.

[282] C. Wang and et al., "Biocompatible film-coating of magnetic soft robots for mucoadhesive locomotion," *Advanced Materials Technologies*, vol. 8(12), pp. 2201813, 2023.

[283] T. Wang and et al., "Clinical translation of wireless soft robotic medical devices," *Nature Reviews Bioengineering*, pp. 1–16, 2024.

[284] S. S. Srinivasan and et al., "Robocap: Robotic mucus-clearing capsule for enhanced drug delivery in the gastrointestinal tract," *Science robotics*, vol. 7(70), pp. eabp9066, 2022.

[285] R. Mundaca-Uribe and et al., "Towards multifunctional robotic pills," *Nature Biomedical Engineering*, pp. 1–13, 2023.

[286] N. K. Mandsberg and et al., "Ingestible device for gastric fluid sampling," *Advanced Materials Technologies*, pp. 2400434, 2024.

[287] D. Son and et al., "Magnetically actuated soft capsule endoscope for fine-needle biopsy," *Soft robotics*, vol. 7(1), pp. 10–21, 2020.

[288] Y. Sun and et al., "Magnetically driven capsules with multimodal response and multifunctionality for biomedical applications," *Nature Communications*, vol. 15(1), pp. 1839, 2024.

[289] Y. P. Lai and et al., "Hybrid hydrogel-magnet actuated capsule for automatic gut microbiome sampling," *IEEE Transactions on Biomedical Engineering*, 2024.

[290] S. Park and et al., "Multiple sampling capsule robot for studying gut microbiome," *Advanced Intelligent Systems*, pp. 2300625, 2024.

[291] D. Li and et al., "Battery-free, wireless, and electricity-driven soft swimmer for water quality and virus monitoring," *Science Advances*, vol. 10(2), pp. eadk6301, 2024.

[292] J. Han and et al., "A magnetic soft robot with multimodal sensing capability by multimaterial direct ink writing," *Additive Manufacturing*, vol. 61, pp. 103320, 2023.

[293] S. Li and et al., "Bioresorbable, wireless, passive sensors for continuous ph measurements and early detection of gastric leakage," *Science Advances*, vol. 10(16), pp. eadj0268, 2024.

[294] M. Wehner and et al., "An integrated design and fabrication strategy for entirely soft, autonomous robots," *Nature*, vol. 536(7617), pp. 451–455, 2016.

[295] L. Masjosthusmann and et al., "Miniaturized variable stiffness gripper locally actuated by magnetic fields," *Advanced Intelligent Systems*, vol. 6(9), pp. 2400037, 2024.

[296] R. H. Soon and et al., "Pangolin-inspired untethered magnetic robot for on-demand biomedical heating applications," *Nature Communications*, vol. 14(1), pp. 3320, 2023.

[297] S. Beg and et al., "Quality standards in upper gastrointestinal endoscopy: a position statement of the british society of gastroenterology (bsg) and association of upper gastrointestinal surgeons of great britain and ireland (augis)," *Gut*, vol. 1886-1899, 2017.

[298] M. Rezapour and et al., "Retention associated with video capsule endoscopy: systematic review and meta-analysis," *Gastrointestinal endoscopy*, vol. 85(6), pp. 1157–1168, 2017.

[299] C. Thorndal and et al., "A systematic review of capsule aspiration in capsule endoscopy," *Annals of Translational Medicine*, vol. 12(1), pp. 12, 2023.

[300] F. Taktak and et al., "Rapid deswelling of pdmaema hydrogel in response to ph and temperature changes and its application in controlled drug delivery," *Afyon Kocatepe Üniversitesi Fen Ve Mühendislik Bilimleri Dergisi*, vol. 16(1), pp. 68–75, 2016.

[301] L. Kong and et al., "Constructing carbon-coated fe3o4 microspheres as antiacid and magnetic support for palladium nanoparticles for catalytic applications," *ACS applied materials interfaces*, vol. 35(42), 2011.

[302] L. Yin and et al., "Dissolvable metals for transient electronics," *Advanced Functional Materials*, vol. 24(5), pp. 645–658, 2014.

[303] J. Chen and et al., "An ingestible capsule for luminance-based diagnosis of mesenteric ischemia," *Science Robotics*, vol. 10(107), pp. eadx1367, 2025.

[304] N. Deirram and et al., "ph-responsive polymer nanoparticles for drug delivery," *Macromolecular Rapid Communications*, vol. 40(10), pp. 1800917, 2019.

[305] W. K. LEE and et al., "Impact of pfos exposure on murine fetal hematopoietic stem cells, associated with intrauterine metabolic

perturbation," *Environmental Science Technology*, vol. 59(11), pp. 5496–5509, 2025.

[306] Z. He and et al., "Exposure to ambient fine particulate matter impedes the function of spleen in the mouse metabolism of high-fat diet," *Journal of Hazardous Materials*, vol. 423, pp. 127129, 2022.

[307] Y. Song and et al., "Phosphocholine-induced energy source shift alleviates mitochondrial dysfunction in lung cells caused by geospecific pm2.5 components," *Proceedings of the National Academy of Sciences*, vol. 121(14), pp. e2317574121, 2024.

[308] B. Figliuzzi and et al., "Rise in optimized capillary channels," *Journal of Fluid Mechanics*, vol. 731, pp. 142–161, 2013.

[309] N. Ichikawa and et al., "Interface motion of capillary-driven flow in rectangular microchannel," *Journal of colloid and interface science*, vol. 280(1), pp. 155–164, 2004.

[310] J. Cai and et al., "Lucas–washburn equation-based modeling of capillary-driven flow in porous systems," *Langmuir*, vol. 37(5), pp. 1623–1636, 2021.

[311] P. Hu and et al., "Numerical investigation of tesla valves with a variable angle," *Physics of Fluids*, vol. 34(3), 2022.

[312] Q. M. Nguyen and et al., "Early turbulence and pulsatile flows enhance diodicity of tesla's macrofluidic valve," *Nature Communications*, vol. 12(1), pp. 2884, 2021.

[313] S. Li and et al., "Bioresorbable, wireless, passive sensors for continuous ph measurements and early detection of gastric leakage," *Science Advances*, vol. 10(16), pp. eadj0268, 2024.

[314] B. Hao and et al., "Focused ultrasound enables selective actuation and newton-level force output of untethered soft robots," *Nature Communications*, vol. 15(1), pp. 5197, 2024.

[315] R. Katzschmann and et al., "Dynamically closed-loop controlled soft robotic arm using a reduced order finite element model with state observer," in *In 2019 2nd IEEE international conference on soft robotics (RoboSoft)*. IEEE, 2019, pp. 717–724.

[316] Y. Hu and et al., "A real-time differentiable physical simulator for soft robotics," in *In 2019 International conference on robotics and automation (ICRA)*. IEEE, 2019, pp. 6265–6271.

[317] T. Jin and et al., "Triboelectric nanogenerator sensors for soft robotics aiming at digital twin applications," *Nature Communications*, vol. 11(1), pp. 5381, 2020.

[318] F. Fischer and et al., "Magneto-oscillatory localization for small-scale robots," *npj Robotics*, vol. 2(1), 2024.

[319] J. Sikorski and et al., "Introducing bigmag—a novel system for 3d magnetic actuation of flexible surgical manipulators," in *In 2017 IEEE International Conference on Robotics and Automation (ICRA)*. IEEE, 2017, pp. 3594–3599.

[320] X. Xia and et al., "Artificial intelligence-assisted multimode microrobot swarm behaviors," *ACS Nano*, vol. 19(13), pp. 12 883–12 894, 2025.

[321] D. Kim and et al., "A 5 mg micro-bristle-bot fabricated by two-photon lithography," *Journal of Micromechanics and Microengineering*, vol. 29(10), pp. 105006, 2025.

[322] Z. Ma and et al., "Femtosecond laser programmed artificial musculoskeletal systems," *Nature Communications*, vol. 11(1), pp. 4536, 2020.

[323] D. Qin and et al., "Soft lithography for micro-and nanoscale patterning," *Nature Protocols*, vol. 5(3), pp. 491, 2010.

[324] S. Yin and et al., "Wearable and implantable soft robots," *Chemical Reviews*, vol. 124(20), pp. 11 585–11 636, 2024.

[325] K. García and et al., "Zwitterionic-coated "stealth" nanoparticles for biomedical applications: recent advances in countering biomolecular corona formation and uptake by the mononuclear phagocyte system," *Small*, vol. 10(13), pp. 2516–2529, 2014.

[326] L. H. Reddy and et al., "Magnetic nanoparticles: design and characterization, toxicity and biocompatibility, pharmaceutical and

biomedical applications," *Chemical reviews*, vol. 112(11), pp. 5818–5878, 2021.

Acknowledgements

Writing this section feels refreshingly different from the rest of this dissertation. For once, I am not trying to define, demonstrate, argue, or persuade. Finishing a PhD is often described as a great achievement, and in some sense it is. Yet it also feels quietly ordinary, like closing one chapter and stepping into a longer, messier, and more interesting story. When I look back, what stays with me most is not the complexity of the work, but the people who made it meaningful. And so, instead of one more analysis, I choose a simpler focus: gratitude, to the many individuals who made this dissertation, and these years, possible.

My PhD journey began with an email to **Prof. Sarthak Misra**, who later became my doctoral promoter. Thank you for accepting me and supporting my CSC scholarship application, even though I contacted you rather late and we submitted the proposal at the very last minute, which reflects my working style over the past years. I appreciate your patience. I truly enjoyed the relaxed research atmosphere you created in the lab, which gave me space for creative thinking and for refining my work. Thank you for your guidance whenever I lost direction, and for your constant support throughout the journey, especially during my visiting period in Shanghai. I wish you continued success in your distinguished academic career and happiness in your family life.

The same initial email also connected me with **Dr. Venkat Kalpathy Venkiteswaran**, who has been my daily supervisor throughout the PhD. From the very beginning, you consistently provided detailed and constructive feedback that greatly improved my work, from the CSC proposal to every subsequent manuscript and document over the years. Your careful guidance helped me refine my thinking and writing, even though I still occasionally make elementary mistakes, which seem to be part of my style since childhood. Thank you for your continued support with experiments in the UT lab, for introducing me to colleagues and friends, and for your kindness and patience in both work and daily life. I genuinely enjoyed our weekly meetings, which were always productive and relaxing and also helped me improve my English skills. Working with you has been a great fortunate for me, and I am especially grateful for your offer of a postdoc-

toral position, which gave me great reassurance during the most stressful period of my PhD, particularly during the animal experiments in Shanghai. Even now, I fondly remember your video call on my first day after arriving, the marathon competition in Enschede, and our many conversations about everyday life. I wish you every success in your professorship and happiness in your family life.

This work would not have been possible without contributions of my collaborators. My sincere appreciation extends to **Prof. Romana Schirihal** and **Dr. Aldona Mzyk** from University Medical Center Groningen and University of Groningen for your valuable contributions to the biocompatibility tests. **Aldona**, I truly appreciate having been your officemate, and I am grateful for your kindness and help, from setting up my computer to "looking for Ed" on my very first day in the office. Sharing my achievements in robot design with you was a meaningful experience that initiated our collaboration, and it marked my first attempt to incorporate biological perspectives into my research, which greatly broadened my thinking. I also enjoyed our conversations and the sharing of thoughts about marriage, and I sincerely wish you a happy life with your husband in Denmark.

My acknowledgements also extend to **Prof. Patrick van Rijn** and **Dr. Clio Sibermorgen** from University Medical Center Groningen and University of Groningen for your valuable contributions to the hydrogel robot project. This collaboration represented a successful attempt to combine magnetic soft robotics with hydrogels. **Patrick**, thank you very much for your kindness and support throughout the project and beyond. **Clio**, working with you was a great pleasure, enriched by both scientific insight and personal warmth, and I sincerely wish you success in realizing what you truly seek.

A special thank you goes to **Prof. Xiangzhong Chen** from Fudan University for your consistent support during the animal experiments in the final project of my PhD. Your strong scientific background and research expertise gave me confidence throughout the project, and working with you was both effective and professional. I hope our outcomes will have a meaningful impact on the research field. I would also like to thank **Dr. Anatolii Abalymov** and **Hao Bao** for your support and companionship during my visiting period at Fudan University. I wish you all a bright future in academia.

Additionally, I extend my sincere thanks to **Prof. Zongwei Cai** and

Dr. Rui Shi from HongKong Baptist University for your valuable contributions to the original idea and for conducting the mass spectrometry work in my final PhD project. Without your contributions, this project would not have reached its current level or potential impact. **Rui**, being your friend has been both a privilege and a great fortune. You are always smart, efficient, humor and professional. I will never forget the period of animal experiments in Shanghai, and I am deeply grateful for your supportive and insightful words, which gave me the courage to carry through and complete the experiments. Our online conversations every night, often lasting more than an hour, remain unforgettable, even if they occasionally made our girls a little jealous. I will also always cherish the memories of playing padel together on winter nights in Zernike, even if it was more about fun than skill. I would also like to express my sincere appreciation to your wife, **Shenghua**, for her valuable contributions to the illustration figures in our paper, the final illustration in my thesis, and her suggestions on the design of my thesis cover. I wish you every success in your professorship in Shandong and a happy life with Shenghua. Finally, I sincerely hope that after work you will go home promptly, rather than calling me.

I also sincerely appreciate **Prod. David Gracias** and **Dr. Aishwarya Pantula** from Johns Hopkins University for your collaboration and insightful discussions since the first year of my PhD. Although the outcomes did not fully meet our initial expectations, the exchanges were intellectually valuable and contributed meaningfully to my research development.

I would also like to express my sincere appreciation to the members of my reading committee: **Prof. Paul Breedveld** from Delft University of Technology, **Prof. Gabriëlle Tuijthof** from University of Twente, and **Prof. Ajay Giri Prakash Kottapalli** from University of Groningen. I am very grateful for your valuable insights, constructive comments on my thesis, and your critical evaluation of my research. In addition, I would like to express my sincere gratitude to **Prof. Patrick van Rijn** from University Medical Center Groningen and University of Groningen, as well as to **Dr. Bahar Haghighat** from University of Groningen, for kindly agreeing to serve as members of my examining committee.

I am grateful to have been part of the Surgical Robotics Lab (SRL) and to have worked alongside some of the most talented roboticists. **Chuang**, thank you for all your help, companionship, and kindness. I will never

forget your warm welcome hotpot dinner and your help carrying my mattress in the rain on my first day in Groningen. Thank you as well for introducing me to the football team. Playing football every weekend and watching matches together became some of the most cherished memories of my time in Groningen. Traveling with you to watch football games was a completely new and refreshing experience for me. Even though you often provided the ideas and we had to organize the trips, I truly enjoyed all our journeys, including those to Madrid, Barcelona, Dortmund, Rotterdam, Twente, and Bremen. I wish you every success in your professorship in Liaoning, and I extend my best wishes to your wife, your child, and your family. **Zihan**, being your colleague and friend has been both a pleasure and a great fortune. You are someone who seems to know everyone and everything. I truly admire your passion for research; while browsing TikTok is entertainment for me, scrolling through research news seems to be yours. One truth I must acknowledge here, though you may never believe it, is that you were the first person to introduce me to Nature, Science, and Cell papers. Playing padel, pingpong and football with you over the past years has been both enjoyable and unforgettable. Our padel skills grew together, and in the end we reached the final and came very close to winning the championship. I wish you success in realizing what you desire in the near future, and a happy and fulfilling life in Suzhou. **Kaixuan**, having you at any activity or event was always a reassurance that ideas could be clearly expressed across a wide range of topics. Thank you for generously sharing your knowledge, as well as your TikTok updates, which brought a great deal of fun and relaxation to both work and daily life. I deeply admire your ability to stay focused on research without being distracted by external noise, a quality that is clearly reflected in your publications in the top journals. I also greatly appreciate the openness and warmth that you and **Mengyu** always showed whenever we rang the bell. I wish you every success in Shenzhen, Hong Kong and Italy, and a happy and healthy life with Mengyu and your family. **Zhuoyue**, thank you very much for agreeing to serve as the photographer for my defense. I have been deeply impressed by both your scientific abilities and your artistic skills. I truly enjoyed reading your papers, especially the figures, from which I learned a great deal. Playing snooker, pool, and foosball with you after lunch or work were some of the most relaxing and enjoyable moments over the years. Thank you and **Jie** for the delicious food and wonderful meals in

Groningen, as well as whenever we traveled to Leiden. I wish you and Jie every success with your PhD theses and a bright and promising future. **Adriana**, a big thank you for agreeing to serve as one of my paranymphs. It has been a real pleasure working with you, both as a supervisor and as a colleague. Having you in the lab has meant a lot to me. For a time, you were the only girl in the lab, and your presence made it cleaner, more organized, and more lively. Thank you for all the jokes and laughter you brought into our daily work. I truly appreciate your talent for conversation and gossip, which also helped me improve my spoken English in a fun and natural way. I wish you a smooth and successful PhD journey, and I also extend my best wishes to your parents for good health and happiness. **Laurens**, thank you for your original contributions to the hydrogel robot project, which ultimately resulted in a journal publication. It was an honor and a pleasure to supervise you during your master's thesis. I wish you every success in your future career. **Chris**, thank you for your exploration of the interesting ultrasonic QR code project. Although the outcomes did not fully meet our expectations, I truly appreciated the time we worked together in the lab. **Zhengya**, thank you for kindly sharing your iPhone charger with me in the office. **Yiyang**, thank you for sharing your life tips in Groningen. **Sumit**, you are undoubtedly one of the most sociable guy in the lab. I truly appreciate your friendliness and help every time I visited the UT lab. Running into you and sharing dinner in Madrid was an amazing experience. I wish you every success in both your academic and musical careers. **Mert**, your dedication impressed me from the very beginning, and I sincerely appreciate your kind help with machining the aluminum frames and sharing your Turkish pancake lunch with me. **Jakub**, thank you for your help with setting up the coils at UMCG, as well as for your thoughtful questions during group meetings. **Theodosia**, thank you for your help with the PacMag during every visit to the UT lab, as well as for sharing the technical recordings and experiences which helped me a lot setting up the coils at UMCG. **Michiel**, you are always gentle, friendly, and kind. Thank you for your help with the VSM magnetization of my samples. **Yu-Hsiang**, thank you for your friendly help at the UT lab. I always enjoyed our conversations whenever we met, and I sincerely appreciate your support and companionship during the conference in Delft. I wish you every success in your postdoctoral position in Germany. **Juan**, you were the only one who visited our UMCG lab and stayed in Groningen

for a full day. Your presentation during the lunch meeting was excellent. I hope you enjoyed the lunch foosball game, dinner, and pool. I also wish you a smooth and successful start to your postdoctoral position. **Yuxin**, talking with you in Mandarin at the UT lab always felt refreshingly different and comforting, and I truly enjoyed our conversations and gossip over time. Thank you for your support and for taking those wonderful photos during the conference in Delft. I wish you every success in completing your PhD thesis. **Simon**, you are no doubt one of the most athletic people I have ever met. Your marathon performances truly impressed me, and you may well be the fastest man the lab has ever had. Thank you for your help with printing and for showing me your magic flexible robotic arms. I look forward to a fruitful collaboration on the Flexmart project. **Lukas**, you may not be aiming to take over Simon's title as the fastest man, but I was surprised to discover just how fast you are as well. I was equally impressed by your big baby on the human-adaptable magnetic setup, and I truly enjoyed reading your original manuscript. Thank you for your humor and your thoughtful concern whenever we met. I wish you every success in completing your PhD thesis. **Nick**, thank you for sharing your experience with publishing in Science Robotics, which was very comforting to me after my own rejection. It also helped me better understand how challenging the process is and how strong your work truly is. Thank you as well for teaching me how to use the da Vinci surgical system. Having you in the lab has been a great privilege for me. **Antonio**, your work on light-actuated robots has impressed me every time in the group meetings. I wish you great success in creating new and innovative work in the future. **Jeanine**, thank you for your dedicated work in organizing meetings and events over the past years, and for helping me settle in on my first day as a postdoc. I wish you every success in your work in the new department. Finally, I am also grateful to the rest of the SRL fellows—**Islam**, **Christoff**, **Rob**, **Hugo**, **Franco**, **Amin**, **Fouzia**, **Miryam**, **Martijn**, **Wendy**, **Yolanda**, **Zhiyao**, **Abhinav**, **Tao**, **Sushmitha**—for your support, collaboration, and for creating a friendly and stimulating working environment in the lab.

I am also grateful to have been part of the Department of Biomaterials and Biomedical Technology (BBT) at the University Medical Center Groningen, which has given me many fond memories. **Fei**, We first got to know each other through pingpong and padel, but over the past years, fish-

ing with you during the summer became my favorite activity and something I always eagerly looked forward to. **Guang**, I have to say that the moment you took off your pants on the padel court left the strongest impression on me. What I appreciate even more, however, is your straightforward and bold personality. Thank you as well for your help with dissecting porcine organs, which enabled me to take my first step toward ex vivo experiments. **Tianqi**, being your neighbor in both the office and the apartment was a pleasure and great fortune. Thank you for your help and discussions on biomaterials and chemicals, especially regarding contact angle measurements. I will not forget the delicious food, games, and photos you shared during the festivals. I wish you and Haoyang every success and happiness in the future. **Yong**, I enjoyed playing badminton with you, which reminded me of my life during my master's studies. Thank you as well for your time and contributions to the friction coefficient measurements, which enriched the data presented in my paper. **Ruichen**, thank you for your initial help with the synthesis of the pH-responsive hydrogel, which saved a great deal of time on the project. **Fenghua**, you are always enthusiastic and sociable. I truly appreciate the meals, gossips, and laughter you brought over the past year. I wish you a happy family life and every success in realizing what you desire. **Meng**, I appreciate your help in providing ideas for my childhood friend. **Fan**, your skill in cooking fish impressed me. **Jiachen**, thank you for introducing the animal research company in Shanghai, and for the English lessons, which were always filled with fun and laughter. **Harsh**, You are always polite and gentle, and it was a great pleasure to work with you in the same office, even though it was only for a short period of time. **Helder**, thank you for ordering a ping-pong table for the department. I truly enjoyed the time we spent playing ping-pong together during the COVID-19 period. Your competitive spirit and strong focus in every ping-pong and padel game always made the matches fun and engaging. **Thomas**, thank you for introducing me to padel, which has become one of my favorite sports. **Torben**, the local snake and dalao, I truly enjoyed playing pool with you and your friends. Thank you for the fun moments and for your friendly energy whenever we met. **Adi**, you are always friendly and gentle. I truly appreciated our chats during breaks and the time we spent playing padel together. My gratitude also extends to the many individuals in the department—**Kaiqi and Yue**, **Guimei**, **Yanjing**, **Ali**, **Prashant**, **Brandon**, **Theo**, **Sidi**, **Dayuan**, **Huijie**, **Lei**, **Ke**,

Dize, **Siyu and Hao**, **Henny**, **Henk**, **Inge**, **Theo**, **Runrun**, **Yuewen**, **Yunayuan**, **Raquel**, **Monica**, **Anna**, **Jie**, **Ruoyu**, **Siran**, **Yaran**—for all the moments we shared in the department.

A special and big thank you goes to the amazing technical team of the department. Without their support, this thesis would not have been possible. **Ed**, I met you on my very first day in the department, and I still clearly remember your warm and humorous welcome, as well as your help in setting up my computer and accounts, which immediately made me feel at home. As time went on, I came to realize just how indispensable you are to the lab as its cable and electronics expert. You are always friendly and kind, and whenever I needed help, you were ready to lend a hand. We are truly fortunate to have you in our lab. I am deeply grateful for all the electronic setups you built for me, including the coil power supply, adhesion force tester, and button-controlled motor system, among many others. These contributions significantly accelerated my research progress and saved me a great deal of time. I truly enjoyed sharing stories and gossips with you. I also feel especially grateful to have the opportunity to express my appreciation before your retirement, and I now wish you a very happy, healthy, and well-deserved retirement, surrounded by your daughters and grandchildren. **Joop**, your table tennis skills always impressed me, and I was equally amazed by your motorbike and your part-time work as a football referee. I can easily imagine how handsome and carefree you must have been in your younger years. Thank you for all your help over the years, and for your kind and patient answers whenever I came to you with questions, especially regarding the profilometer and tensile tester. I also truly appreciated your humor and thoughtfulness whenever we met. I wish you an enjoyable remainder of your time in the department without me, followed by a happy, healthy, and well-deserved retirement. **Hans**, thank you for your kindness and friendliness, as well as for your help with the compression meter. I truly enjoyed listening to your adventures in China, and I greatly appreciated our conversations and your thoughtful concern whenever we met in the department. I wish you good health and a wonderful life, and you are always welcome to visit my hometown. Please feel free to contact me whenever you plan to travel to China again. **Willem**, thank you for the e-learning and training that enabled me to work safely and effectively in the department's laboratories. **Marja, Willy, Betsy and Jelly**, thank you all for your help with ordering supplies and han-

dling package deliveries. **Willy**, thank you for providing the souvenir from the department, which made my visit to Fudan University especially memorable. **Gesinda**, Thank you for providing the syringes and training for contact angle measurements, as well as for the lab cleaning reminders and practical tips. **Wytse**, thank you for helping me recover my reimbursement, which was very important after the research activities. You were always timely and professional, and everything was handled smoothly.

I would also like to thank my dear friends for their support in daily life and for the many cherished memories we have shared over the years:

Roger and **Xiaofang**, you have been the best neighbors and couple we could have asked for during our years in Groningen. We truly appreciate your kindness, laughter, and thoughtful care in daily life. **Roger**, your fluent Chinese amazed me from the very beginning and continued to impress me over time. Your eagerness to learn and dedication to new things are truly inspiring, and with such qualities, nothing seems impossible. Thank you to you and your parents for inviting us to those dinners, which were unforgettable and truly gezellig. I wish you great success in the future. **Xiaofang**, your dedication to work and your excellent communication skills impressed me greatly, and I wish you every success in completing your PhD thesis. I wish you both, your baby and parents a happy and healthy life in both China and Netherlands.

Xinpeng and **Mei**, you have felt more like relatives than friends to me in Groningen, and I was very fortunate to have had the chance to witness Amy's birth. Sharing every Spring Festival dinner together—traditionally a time spent with family in China—made those moments especially meaningful. The sumptuous meals and the sense of gezellig made Groningen feel much more like a hometown. I wish you both, together with Amy, a bright future and a happy life.

Rafael and **Monyque**, you are always so gentle and kind. We share many common interests, including our love for pets and sports, and I truly cherish the conversations and dinners we have every time you return from Brazil. Thank you for giving us the opportunity to take care of Webbie, which allowed us to fulfill a small dream of having a dog. Our time with him was filled with joy, photos, and many warm memories. I wish Web rest in peace, and I wish you both all the best in Groningen.

Xueyi and **Rong**, you are always kind and ready to help. Thank you for the wonderful meals and for introducing us to your friends. I truly

appreciate your companionship and competitive spirit while playing pool, padel, and basketball. I am also grateful for the meals and companionship during my trip to Guangzhou. The way you both overcame the challenges of your PhD journey was truly impressive. I wish you both success in achieving what you desire, and a happy and rich life in Guangzhou in the future.

Yikun and **Guiling**, thank you for the dinners, games, and gossip we have shared over the past years. **Yikun**, you are always kind, gentle, and reliable. **Guiling**, your defense was truly impressive and a joy to watch. I wish you both great success and a bright future in Singapore.

Praveen and **Junia**, the New Year's Eve we spent together in Cologne and the gathering on King's Day were truly memorable. Thank you so much for the jokes, gossip, and companionship during the beginning of our PhD journey. We could have shared even more wonderful memories if you had both stayed in Groningen for a longer period. I wish you great success and a happy life in Eindhoven and Enschede.

Boyan and **Yue**, you are always gentle and reliable. We share so many memorable moments, including our trip to the Paris Olympics, your wedding in Groningen, as well as countless times spent watching and playing football and tennis. I am grateful to you for entrusting Bobo and Miantuan to us during you leave, allowing us to fulfill a small dream of having cats during those busy years. I sincerely wish you both a bright future as clinicians and a happy life with your cats in Beijing.

Ming, **Xiaoxin** and **Yaoyao**, I truly love the warm and lively vibe of your family, which always made me feel gezellig. I cherish the many small memories from our outings together, as well as the football and padel games we shared, and I especially loved the barbecue day at your house, which was both delicious and wonderfully relaxed. **Yaoyao** is so cute and full of energy, and I always smiled when I remember that she called me "WangChen pap" upon seeing the resin Labubu. I wish you all a very happy life in Emmen.

Yun and **Minqi**, a big thank you for letting me own a car, which greatly improved our quality of life in the Netherlands. It is wonderful that we share many interests, which sets our friendship apart from others. When I recall our trip to Disneyland Paris and the Blackpink concert, your reliability and maturity always made us feel reassured. I also deeply appreciate the atmosphere you built within our football team, and I was

truly impressed by both your football skills and your incredible heading ability. I wish you both a life full of youth, happiness, and joy.

My gratitude also extends to the many individuals: **Xiangpan**, thank you for the regular football training every week. **Yuhao**, your professionalism and football skills were unlike anything I had ever seen. Thank you for the many conversations we shared and for your deep knowledge of football. I also truly appreciate your invitation and the VIP tickets to watch a match of Vitesse. I wish you great success in both your football career and the next chapter of your life. **Jiahao**, thank you for teaching me how to shoot with the instep when I was still very new to football. **Xin**, thank you for always passing the ball to me, and I hope everything goes well for you in the US. **Chenhui**, thank you for your kindness and for all your contributions to the football team. **Langjian**, thank you for sharing your tips and experience in stock investing. **Zhen**, thank you for organizing our table tennis activities. Your commitment and enthusiasm for the sport were truly impressive. **Yuzhu**, the powerful aesthetics of your table tennis playing truly amazed me. Thank you for your advice and help with my thesis printing. **Fuchen**, playing padel with you over the past year has been a great joy for me. Your skills have improved remarkably, and I hope we can win a championship together in the near future. **Xin**, your dedication to padel impressed me, and I hope you will continue to play often in Shanghai. **Wenqiang**, your basketball skills are impressive, but I am still waiting for you to beat me in tennis. **Siyuan**, collaborating with you was a great pleasure, and I look forward to fruitful outcomes in the near future. My sincere acknowledgment also extends to **Bo**, **Jin**, **Yiming**, **Xiupeng**, **LiangLiang**, **Tamas**, **Xingwen**, **Teng**, **Wenjian**, **Baoqiang**, **Xiaoyan**, **Matthijs**, **Arijit**, **Luis**, **Linda**, **Jacky**, **Jasmin**, and **Sophie** for all your support and companionship over the past years.

As I write the concluding words of this doctoral dissertation, I am filled with deep gratitude for the love, encouragement, and support of my family. **Grandma**, **Dad**, and **Mom**, I have finally achieved the highest academic degree—a dream you have held for me for over thirty years. This honor belongs not only to me, but also to you and to the values and education you have given me. This honor is also shared with **Yiling**, my love and fiancée, my best and brilliant friend. This thesis would not have been completed without your technical support, creative ideas, constructive suggestions, and gentle encouragement in our daily life. Growing with you, fighting

through every challenge side by side, has been the most exhilarating journeys of my life. Thank you for your unwavering companionship over the past twelve years, since we were nineteen. Our shared path, studying at the same universities and moving forward together, has often amazed others, but only we truly know and understand the quiet details of our shared life. Today, we have grown up, and we stand at the beginning of a new chapter, one that carries greater responsibilities and deeper commitments. There is no need to conclude anything here, because our story does not seek a conclusion. We have a whole lifetime ahead of us in which to understand, to grow, and to complete it together.